

TECHNISCHE UNIVERSITÄT MÜNCHEN  
Department Chemie, Lehrstuhl für Technische Chemie II

**Controlled Catalysis by the Electronic Charge Transfer at  
Metal-Support Interfaces: A Study of Gallium Nitride  
Supported Platinum Nanoparticles**

Sonja Agnes Wyrzgol

Vollständiger Abdruck der von der Fakultät für Chemie der Technischen Universität  
München zur Erlangung des akademischen Grades eines

**Doktors der Naturwissenschaften (Dr. rer. nat.)**

genehmigten Dissertation.

Vorsitzender:	Univ.-Prof. Dr. T. Brück
Prüfer der Dissertation:	1. Univ.-Prof. Dr. J. A. Lercher
	2. Univ.-Prof. Dr. M. Tromp, Ph.D.

Die Dissertation wurde am 03.07.2013 bei der Technischen Universität München eingereicht  
und von der Fakultät für Chemie am 08.10.2013 angenommen.

*„Tu erst das Notwendige,  
dann das Mögliche  
und plötzlich schaffst du das Unmögliche...!“*

Franz von Assisi

## **Acknowledgment**

In the following part, I would like to thank all the people, who helped and supported me in all respects. First of all, I would like to thank Prof. Dr. Johannes A. Lercher, who gave me the opportunity to be a part of his group and provided this interesting and interdisciplinary topic to me. Thank you for your confidence allowing me to guide my research work, as well as to participate on scientific conferences, for your critical advice, and for your support in discussions and financials. Exactly all these points helped me to extend my expertise in various areas like chemistry, engineering, and physics.

My special thanks go to Prof. Martin Stutzmann (Walter Schottky Institute) for facilitating fruitful collaboration and discussion. Thank you for your scientific contribution and your financial support at the end of my thesis.

Moreover, I am grateful to apl. Prof. Dr. Andreas Jentys, who agreed to supervise me during the last half of my thesis. Thank you for your interest in my work, your active cooperation, and advice.

Additionally, I would like to thank my project partner, Susanne Schäfer (Walter Schottky Institute). I am convinced that our special teamwork led to successful research and gave a personal impact on our work. Thank you for your contribution, motivation, and critical view. I enjoyed our internal meetings, our trips to the annual IGSSE Forum, winter school, MRS Meeting, and especially our beamtimes at BESSY II. We learned a lot about each other that enforces our friendship.

I would like to acknowledge the International Graduate School of Science and Engineering (IGSSE) of the TUM Graduate School for project funding and the possibility of a three-month stay abroad.

I am grateful to Xuebing Li for his assistance and help during the first period of my work.

I would like to thank Dr. Habil. Stefan Vajda for his cooperation and support during my stay at the Argonne National Laboratory. Thank you for your motivation, interest in my work, and scientific discussion.

Moreover, I am grateful to my colleagues, who shared the office with me. The personal occupation changed continuously during my work and I would like to thank everyone for his

or her personal contribution and support. Richard, Manuela, Frederik, Dechao, Manuel, Claudia, Despina, Linus, Christian, Jieli, Sebastian, Max, Pamina, Sarah, and Dani, thank you for the nice office climate. Thank you, Sarah and Dani, for your motivating and constructive support and your friendship.

Many thanks go to Sungsik Lee, Marcel Di Vece, Byeongdu Lee, and Sönke Seifert (Argonne National Laboratory, Yale University) for their supporting help at the APS beamline regarding practical work, experiments, and discussion. Especially, thank you, Sönke, for the trip to Chicago.

I would like to acknowledge all the people, who were involved in measurements at BESSY II of the Helmholtz-Zentrum Berlin. Thank you, Michael Hävecker, Detre Teschner, Raoul Blume, Tulio Rocha, Alexander Klyushin, Rosa Arrigo, and Axel Knop-Gericke (Fritz-Haber-Institut der Max-Planck-Gesellschaft) for your subject-specific and technical assistance at the setup, as well as your contribution to data evaluation and discussion. Special thanks go to Roberta Caterino, Sebastian Schöll, Moritz Hauf, Matthias Sachsenhauser, Markus Hofstetter, Martin Schmid, and Ian Sharp (Walter Schottky Institute, Helmholtz-Zentrum München, and Lawrence Berkeley National Laboratory) for their help during the beamtime.

Additionally, I would like to thank Marianne Hanzlik (Institute of Electron Microscopy, TUM) for introduction into transmission electron microscopy and her support during measurements.

I am grateful to Thomas Michel (Lehrstuhl I für Technische Chemie, TUM) for introduction into atomic force microscopy.

I would like to thank Florian Schweinberger and Martin Tschurl (Chair of Physical Chemistry, TUM) for discussion on micro-structured reactor technology and photochemistry.

Many thanks go to Prof. Gary L. Haller (Yale University) for scientific discussion.

Special thanks go to the team of the workshop for fine mechanics, to Otto Straßer, Albert Englert, Reinhold Merz, Roland Schwarz, Marc Schönberger, Harald Wunder, Robert Göring, and Michael Wanninger. Thank you for the constructions of reactors and setup parts, and your endless patience regarding optimization and repairing.

I am grateful to all students, who I supervised during his or her practical, Bachelor's, or Master's thesis. Thank you, Sarah Konrad, Irmgard Buchberger, Pankaj Madkikar, and Iulius



Markovits, for your research contribution and interest. Especially, thank you, Iulius, for your cooperation as student assistant and your decision doing your Master's thesis on this topic.

I would like to acknowledge Prof. Dr. Günther Rupprechter for giving me the opportunity to do my stay abroad at the Institute of Material Chemistry of Vienna University of Technology.

I would like to thank all group members for their kind response and especially Karin Föttinger and Andreas Haghofer for experimental introduction in sum frequency generation vibrational spectroscopy and interest in my work.

Moreover, I am grateful to Stefanie Maier, Bettina Federmann, Karen Schulz, Helen Brenner, Katharina Thies, Joana Figueiredo (Walter Schottky Institute), and Silke Schnaubelt (Department of Physics, TUM) for their administrative support. Thank you, Steffi, for your help organizing meetings and appointments, and especially for your kindness.

I would like to acknowledge Xaver Hecht, Martin Neukamm, and Andreas Marx for their support regarding technical, safety, and computing issues. Especially, thank you, Xaver, for your assistance in any technical problems and your availability whenever I needed your help.

Additionally, I am grateful to all senior scientists, postdoctoral, and doctoral candidates of the group of Lehrstuhl II für Technische Chemie for their support and teamwork.

Finally, I would like to thank my family and my boyfriend, who supported me in every intention and pushed me not to give up. Ich danke euch, Mama und Papa, dass ihr mich immer unterstützt habt und mir die Freiheit gegeben habt, das zu lernen was ich wollte. Danke euch, Peter und Edith, für eure Ehrlichkeit und Aufmunterung, aber auch für eure Kritik. Ich danke dir, Alex, für deine Liebe und Unterstützung. Ohne euch wäre ich niemals so weit gekommen.

## Table of Contents

<b>1</b>	<b>General Introduction.....</b>	<b>1</b>
1.1	Motivation.....	1
1.2	Scope of the Thesis .....	3
1.3	Metal Nanoparticles in Catalysis .....	4
1.3.1	Size- and Shape-Selectivity .....	5
1.3.2	Physical Properties .....	13
1.3.3	Oxidation, Reduction, and Sintering of Platinum Nanoparticles.....	16
1.4	Gallium Nitride as Wide Bandgap Semiconducting Support .....	21
1.4.1	Chemical and Physical Properties.....	23
1.4.2	Native Surface Oxide and Surface Cleaning .....	30
1.4.3	Metal-Semiconductor Interface .....	31
1.5	References.....	35
<b>2</b>	<b>Experimental Methods .....</b>	<b>41</b>
2.1	Catalyst Preparation .....	41
2.1.1	Chemicals and Materials .....	42
2.1.2	Platinum Nanoparticle Synthesis .....	42
2.1.3	Spin-coating.....	45
2.2	<i>Ex situ</i> Characterization.....	47
2.2.1	Transmission Electron Microscopy (TEM).....	47
2.2.2	Atomic Force Microscopy (AFM) .....	50
2.3	<i>In situ</i> Characterization.....	55
2.3.1	Grazing Incidence Small-angle X-ray Scattering (GISAXS).....	57
2.3.2	Grazing Incidence X-ray Absorption Spectroscopy (GIXAS) .....	62
2.3.3	X-ray Photoelectron Spectroscopy (XPS) .....	66
2.4	Catalytic Performance .....	76
2.4.1	Ethene Hydrogenation as Probe Reaction .....	76
2.4.2	Batch-Operated External Recycle Reactor .....	88
2.5	References.....	96
<b>3</b>	<b>Combined TPRx, in situ GISAXS and GIXAS Studies of Model Semiconductor-Supported Platinum Catalysts in the Hydrogenation of Ethene.....</b>	<b>102</b>
3.1	Introduction.....	102
3.2	Experimental.....	104
3.2.1	Combined TPRx and in situ GISAXS/GIXAS .....	104
3.2.2	Sample Preparation .....	106
3.2.3	<i>In situ</i> Experiments.....	108
3.3	Results and Discussion.....	109
3.3.1	Particle Size Analysis by TEM, AFM, and GISAXS .....	109
3.3.2	<i>In situ</i> Characterization under Reduction Conditions and at Elevated Temperatures.....	111
3.3.3	Hydrogenation of Ethene with Deuterium.....	115
3.4	Conclusion.....	120

---

3.5	References.....	122
<b>4</b>	<b>Platinum Nanoparticles on Gallium Nitride Surfaces: The Effect of Semiconductor Doping on Nanoparticle Reactivity.....</b>	<b>126</b>
4.1	Introduction.....	126
4.2	Experimental.....	127
4.2.1	Sample Preparation .....	127
4.2.2	High-Pressure X-ray Photoemission Spectroscopy .....	129
4.3	Results .....	134
4.4	Discussion.....	143
4.5	Conclusion .....	147
4.6	References.....	147
<b>5</b>	<b>Optoelectronic Control of the Catalytic Reactivity of GaN-Supported Pt Nanoparticles.....</b>	<b>151</b>
5.1	Introduction.....	151
5.2	Results and Discussion.....	152
5.3	Conclusion .....	157
5.4	Methods .....	158
5.4.1	Model Catalyst Preparation .....	158
5.4.2	Transmission Electron and Atomic Force Microscopy (TEM, AFM).....	159
5.4.3	Batch-operated Recycle Reactor Setup for Ethene Hydrogenation .....	159
5.4.4	Kinetic Data Evaluation .....	160
5.4.5	Charge transfer to Pt nanoparticles on GaN .....	161
5.5	References.....	163
<b>6</b>	<b>Summary &amp; Zusammenfassung.....</b>	<b>166</b>
6.1	Summary.....	166
6.2	Zusammenfassung.....	170
<b>7</b>	<b>Outlook.....</b>	<b>176</b>
7.1	Outlook .....	176
7.2	References.....	180
<b>8</b>	<b>Curriculum Vitae.....</b>	<b>181</b>
<b>9</b>	<b>List of Publications .....</b>	<b>183</b>
<b>10</b>	<b>List of Presentations .....</b>	<b>184</b>

# *Chapter 1*

## **General Introduction**

### **Abstract**

The general introduction includes the motivation and scope of this work, as well as the basic theory regarding nanometer-sized metal particles in catalysis and gallium nitride as supporting material. The effects of the particle size and shape on catalysis are discussed with their physical properties. The potential of gallium nitride as support is described for fundamental applications based on its chemical and physical properties. Finally, characteristics of the metal-semiconductor interface are summarized to understand strong metal-support interactions.

# 1 General Introduction

## 1.1 Motivation

Heterogeneous catalyzed reactions are essentially relevant for the chemical industry, facilitating processes with high efficiency regarding high product selectivity, low energy consumption, and low waste production.<sup>[1]</sup> The concept of environmentally compatible technologies using sustainable methods and raw materials is described by Green Chemistry.<sup>[2]</sup> Nearly 90% of fine chemicals are produced using large-scale catalysis.<sup>[3]</sup> For this purpose, solid catalysts are rationally developed to achieve a cost-effective catalytic activity with properties tuned especially for their corresponding function in the reaction. The catalytic properties can be influenced by the use of various materials containing small particles of suitable metals and supporting substrates, which interact with the catalytically active particles geometrically or electronically.<sup>[4]</sup> While the metal particles exhibit a well-defined particle size and geometry with high surface-to-volume ratios, as well as high fractions of low-coordinated sites, the support shows a stabilizing effect against particle sintering and modifies the particle reactivity due to metal-support interactions.<sup>[3, 5-9]</sup> Strong metal-support interactions (SMSI) were investigated in the past for e.g. titania-based catalysts, where reduction at high temperatures altered the catalytic activity of metal particles due to the particle encapsulation by reduced titania species, changing their electronic properties.<sup>[4, 10, 11]</sup> However, the indirect effect of the electronic impact of the support on the catalytic activity of the particles is still difficult to assess and to quantify. A detailed and systematic study of defined metal-support interfaces, their charge transfer behavior, and their consequence on the catalytic reactivity is required to understand the electronic interplay for an advanced catalyst development.

Using semiconducting supports with suitable energies of the valence and conduction bands, as well as the bandgap energy provide the potential for charge transfer between metal particles and the underlying support.<sup>[8, 12]</sup> Exactly such materials are utilized in heterogeneous photocatalysis, which are currently excessively studied regarding e.g. the use of direct sunlight converting solar energy into chemical energy with high efficiency. Selected photocatalysts were developed for the destruction of organic pollutants and toxic compounds in industrial wastewaters, the activation of C-H bonds for the selective oxidation of intermediates for fine chemicals, the recycling of the greenhouse gas carbon dioxide back into fuels, or for the overall water splitting for hydrogen evolution.<sup>[13-17]</sup> Titania-based materials

are mainly used as photocatalysts, but its wide bandgap (3.0-3.2 eV) allows only light absorption in ultraviolet range and therefore, this material is not suitable for applications with sunlight. Recent studies concentrated on bandgap engineering for narrowing the bandgap by doping or by introduction of surface structure disorders.<sup>[18, 19]</sup> Alternative photocatalysts were developed for the visible light-driven hydrogen production from water using an oxynitride solid solution of gallium nitride and zinc oxide loaded with ruthenium oxide or rhodium-chromium mixed oxide particles.<sup>[20, 21]</sup> The particle-semiconductor contact increased the photocatalytic efficiency due to the trapping of optically excited electrons by the particles, hindering a fast charge carrier recombination.<sup>[22]</sup> The ability of the particle-semiconductor interface for the transfer of photo-generated charge carriers shows the possibility to control catalytic properties of metal particles by the optical, above bandgap excitation of the underlying support.

The study of metal catalysts that facilitate a controlled charge transfer over the metal-support interface in both directions is essentially required to verify the influence of electronic changes of the catalytically active species on their reactivity. For this purpose, the semiconducting support has to be able to transport negative as well as positive charge carriers to the particle in contact. Gallium nitride surfaces have been the most suitable wide bandgap semiconductors (bandgap of 3.4 eV), which are commercially available with *n*- and *p*-type conductivity, providing the same crystal structure for both types of doping.<sup>[23]</sup> In addition to that, gallium nitride is frequently used in the optoelectronic technology and its high thermal stability provides the device application at high powers and temperatures.<sup>[24-26]</sup> Catalytically active metal particles can be chemically prepared from platinum, where controlled synthesis methods are used to yield size- and shape-selected particles with defined exposed metal surfaces. An identical set of such particles on both *n*- and *p*-type gallium nitride surfaces allow for the exclusion of particle effects as origin of a modified catalytic reactivity under optical excitation. Previous studies showed the possible transfer of electrons through the platinum-gallium nitride interface for sensor applications, e.g. the detection of small amounts of hydrogen or the detection of an electron current generated by the exothermic CO oxidation.<sup>[27, 28]</sup> Such catalyst systems seem to be well-suitable to investigate the electronic control of catalytic properties and the possibilities and limitations of catalysis on demand.

## 1.2 Scope of the Thesis

The comparative study of catalysts with a supporting semiconductor, which exhibits *n*- and *p*-type conductivity and thus, is able to revert the charge transfer, has been the scope of this thesis to elucidate the *in situ* control of catalytic activity of the metal particles by the photo-activation of the underlying support. The expertise in heterogeneous catalysis, chemical engineering, and semiconductor physics has been combined to develop materials, techniques, and methods to implement the challenge.

The investigation of gallium nitride-supported platinum particles as suitable catalysts has been the subject of the work and has contained the preparation of platinum particles with selected size and geometry, their deposition onto *n*- and *p*-type gallium nitride surfaces, as well as the catalyst characterization and testing in a prototype reaction. The colloidal platinum particle solutions have been synthesized by procedures that allowed the production of well-defined particles with a high yield. The polymer-capped particles have been analyzed in solution with transmission electron microscopy, while atomic force microscopy has been used to evaluate the particle size and the areal distribution after their deposition onto the support. The particles were applied onto the gallium nitride surfaces via spin-coating, resulting in planar, reproducible catalysts functionalized with maximal a particle monolayer. The polymer-capping has been subsequently evaporated from the particles after deposition by oxygen plasma, which facilitated a complete removal without agglomeration of the particles. After further heat treatment and activation processes, the catalysts have been prepared for their characterization and testing.

Due to the low metal coverage on the semiconductor surfaces, *in situ* synchrotron techniques have been required to study the particle and support behavior under reaction conditions, i.e. in reducing and oxidizing atmosphere, as well as during hydrogenation of ethene. Small-angle X-ray scattering and X-ray absorption spectroscopy in grazing incidence mode have been used to monitor particle shape changes in the presence of a reactive ambient and high temperatures, measuring simultaneously their X-ray absorption spectra and catalytic activity (Chapter 3). The electronic properties of the platinum particles and the underlying gallium nitride under X-ray illumination were investigated with high-pressure X-ray photoelectron spectroscopy; monitoring changes of the particle surface as a function of the *n*- and *p*-type doping of the support (Chapter 4). The modified catalytic activity of the particles with and without ultraviolet light illumination of their support has been tested in the hydrogenation of ethene to ethane using a batch-operated external recycle reactor setup, which allowed for

product detection even at small single-path conversions due to product accumulation over reaction time (Chapter 5).

The applied techniques and methods have been used to combine electronic with catalytic properties in dependence on the optical excitation of the support. An advanced charge transfer mechanism has been proposed that explained changes in the electron density on the platinum with the above bandgap excitation of gallium nitride. This consistent, systematic study has shown the possibility of the *in situ* control of catalytic properties via the directed charge transport at the metal-support interface.

### 1.3 Metal Nanoparticles in Catalysis

Generally, five steps have to be passed during a heterogeneous catalyzed reaction: the diffusion of reactants from the bulk gas phase onto the catalyst (film diffusion followed by pore diffusion in porous solids), the adsorption of reactants onto the surface, the surface reaction, the desorption of products from the surface, and finally the diffusion of products from the catalyst back into the bulk phase.<sup>[1, 3]</sup> At the same time, the catalyst establishes new routes for the reaction, lowers the activation barrier, and accelerates the reaction compared to the non-catalyzed pathway, preserving ideally its active sites (Figure 1-1).<sup>[3]</sup>

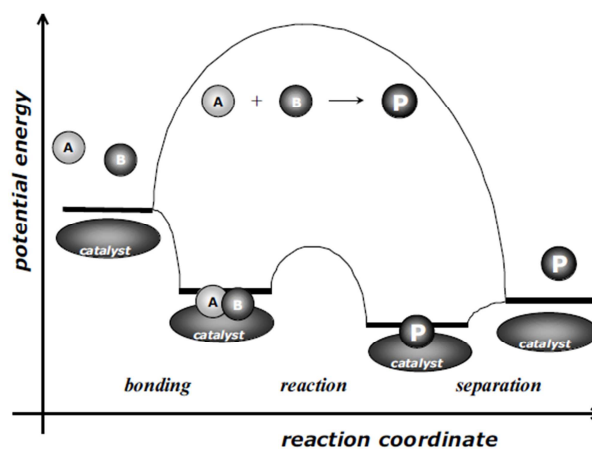


**Figure 1-1.** Potential energy diagram of the thermal, non-catalyzed and the heterogeneous catalyzed reaction of A and B to P. The reaction on the catalyst surface exhibits a lower activation energy.<sup>[3]</sup>

A large surface area is crucial for catalysis due to the reaction and accumulation of reactants on the catalyst surface. Therefore, nm-sized metal particles are mainly used as part of the



solid catalyst due to their high surface area and large portion of chemically unsaturated atoms.<sup>[3]</sup> Although small particles exhibit a high surface area, their catalytic reactivity tends not to increase with decreasing particle size due to the presence of the particle size effect, which appears normally at very small particle diameters. Moreover, not only the particle size but also the morphology plays a critical role in structure-sensitive reactions like the isomerization of light alkanes, hydrogenolysis, and dehydrocyclization.<sup>[29]</sup> Both the size and shape of metal particles influence their surface morphology and electronic properties, and thus, their active sites for the reaction. Additionally, the supporting material plays an important role regarding metal-support interactions and contributes to the formation of active sites, e.g. in bifunctional catalysts.

As a consequence, the understanding of parameters affecting the activity and selectivity of catalysts is important to design an optimal catalyst. Essential effects of small metal nanoparticles will be described in the following sections and will help to appreciate relationships between physical and chemical properties of the particles and their impact on catalysis.

### 1.3.1 Size- and Shape-Selectivity

The particle size effect impacts not only the catalytic activity but also the product selectivity and is dependent on the type of metal and type of reaction. For example, a decreasing turnover frequency (TOF) was found for Co particle sizes below 6 nm in the Fischer-Tropsch process (Figure 1-2 (a)), where strong irreversible bonding of CO on the unsaturated atoms was supposed to block active sites for the reaction.<sup>[30, 31]</sup> The catalyst for the selective hydrogenation of crotonaldehyde and cinnamaldehyde should preferably consist of large metal particles.<sup>[10, 32, 33]</sup> The selectivity towards the unsaturated alcohol was found to be enhanced by steric effects on large particles, where extended metal terraces prefer the adsorption of the carbonyl bond, which is subsequently hydrogenated. The reaction rate of the electron-transfer reaction between hexacyanoferrate(III) and thiosulfate was dependent on the fraction of edge and corner atoms of different Pt nanoparticle shapes (Figure 1-2 (b)).<sup>[34]</sup> Colloidal solutions of tetrahedral, “near spherical”, and cubic particles (5-7 nm) showed a decreasing reaction activity in the same order, which was supposed to originate from the high

number of surface edge and corner atoms of tetrahedral particles, and less edge atoms of cubic particles.

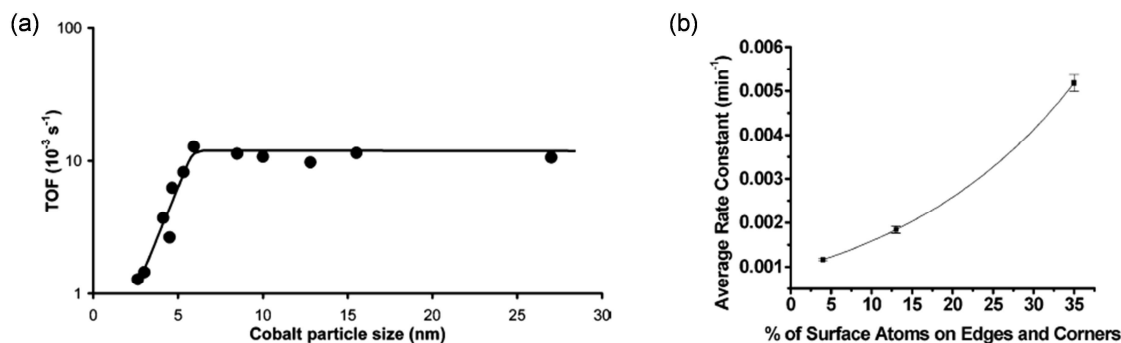


**Figure 1-2.** (a) TOFs versus Co particle size in the Fischer-Tropsch process ( $\text{H}_2/\text{CO} = 2$ , 1 bar, and 493 K).<sup>[30]</sup> (b) The average rate constant for the hexacyanoferrate(III)/thiosulfate reaction versus percentage of surface atoms on edges and corners of tetrahedral, “near spherical”, and cubic Pt colloidal solutions (318 K).<sup>[34]</sup>

The structure-sensitive reactions described above show reaction rates that are dependent on the structure of active sites of a metal surface. In general, reactions can be divided in structure-sensitive and structure-insensitive reactions.<sup>[35]</sup> The structure-sensitivity is mainly observed for reactions, where C-C bonds are formed or broken like for isomerization or hydrocracking, where low-coordinated metal sites are active. The most extensively studied structure-sensitive reaction is the ammonia synthesis, where the more open Fe(111) surface shows the highest activity for the cleavage of nitrogen.<sup>[35]</sup> In contrast to that, hydrogenation and dehydrogenation reactions are structure-insensitive, which involve the conversion of C-H bonds. The CO oxidation belongs to both types of reactions and the structure-sensitivity depends on the reaction conditions. For high CO partial pressures, the oxidation appears structure-insensitive, while it is structure-sensitive for low CO partial pressures.<sup>[29]</sup>

For the understanding of the structure-sensitivity phenomenon in catalysis, the morphology of a metal surface have to be considered, which contains various types of atoms with different coordination, e.g. chemically unsaturated terrace and step atoms, as well as kinks and adatoms (Figure 1-3). The metal particle surface is not fixed at ambient conditions, changing its topology dynamically with the environment. Surface relaxation and reconstruction occur in dependency on the pressure, presence of adsorbates, and surface reactions, which alter the particle shape kinetically.<sup>[35]</sup>

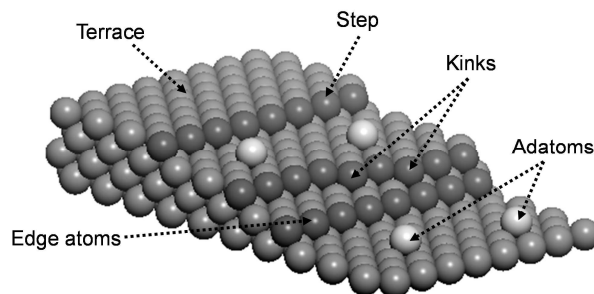


**Figure 1-3.** Scheme of a metal surface containing terraces, steps, kinks, edges, and adatoms.

In vacuum, the metal particle exhibits a defined equilibrium shape, the Wulff polyhedron.<sup>[36]</sup> The shape conforms to Wulff's theorem for isolated particles that describes the proportionality of the central distance to the facets and their corresponding surface energies. Due to the minimization of the total free surface energy, optimal equilibrium shapes are formed for the face-centered cubic (fcc) and body-centered cubic (bcc) metals. The Wulff polyhedron of fcc metals (e.g. Pt, Ni, Au) is a truncated octahedron that contains eight (111) and six (100) facets (Figure 1-4 (a)), while a dodecahedron with twelve rhombic (110) faces is the thermodynamically most stable shape of bcc metals (e.g. Fe, V, Mo). If the size of the equilibrated fcc metal particle decreases below 10 nm, (100) facets will disappear and an octahedral shape will be formed, exposing only (111) facets.<sup>[36]</sup>

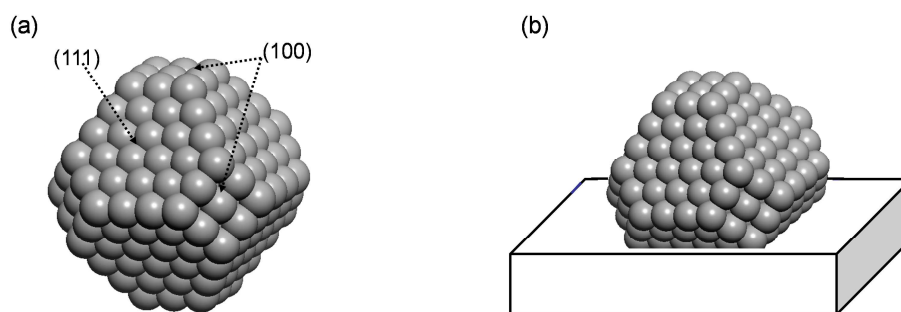


**Figure 1-4.** The Wulff polyhedron (truncated octahedron for fcc metals) for (a) the free equilibrated particle and (b) the supported particle.

After the deposition of a metal particle onto a solid surface, truncation at the interface occurs that is dependent on the particle-support interaction (Figure 1-4 (b)).<sup>[37]</sup> In this case, the equilibrium particle shape relates to the Wulff-Kaichew theorem, which includes the adhesion energy between the particle and the supporting surface.<sup>[36, 37]</sup> This theorem implies the same lattice parameters of the metal and the underlying surface, which is typically not true. The lattice mismatch causes stresses at the interface and a reduction of the interfacial area

becomes energetically more favored, decreasing the aspect ratio (width/height) of the ideal crystal shape.

The thermodynamically most stable Wulff polyhedrons expose distinct metal surfaces to minimize their net surface free energy. The arrangement of the surface atoms achieves different atom coordination. Fcc metal facets (111), (100), and (110) consist of surface atoms with a ninefold, eightfold, and sevenfold coordination, respectively (Figure 1-5). The surface free energy increases from the (111) to the (100), and finally to the (110) plane, where the stability of the surface decreases in the same order.<sup>[38]</sup> Additionally, the electronic properties are determined by the density of surface atoms and the metal work function decreases from the (111) and (110) to the (100) facet on metallic surfaces (without surface reconstruction).<sup>[39]</sup> Consequently, the (111) metal plane shows the most stable surface with the highest metal work function.

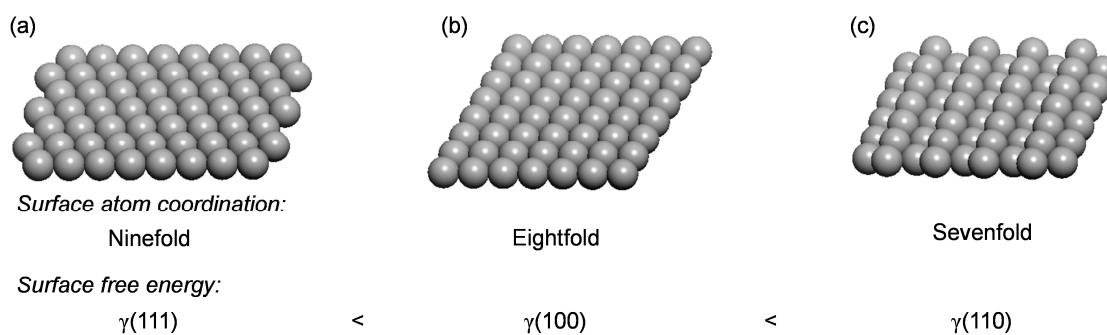


**Figure 1-5.** Model metal surfaces of fcc metals with (a) (111), (b) (100), and (c) (110) faces containing a ninefold, eightfold, and sevenfold atom coordination, respectively.

The presence of adsorbed molecules on the metal particle surface at high pressures promotes the energy minimization of the particle, leading to surface reconstruction and the rearrangement of the equilibrium particle shape. Adsorbates bind preferentially to low-coordinated surface sites of the particle and change the fraction of exposed facets. As the facets exhibit different atom coordination, the adsorption energy changes with the surface orientation. At high temperatures that are normally used in catalysis, a rounding of the particle shape occurs. Moreover, the deposition of metal particles onto supporting materials alters their geometry due to the interfacial strain.

Consequently, the particle shape is kinetically controlled under reaction conditions, which is affected by the presence of reactants, surface intermediates, and products, as well as by the interaction with the support.

In practice, the preparation of catalytically active, size- and shape-selected metal particles is challenging to yield high monodispersity. Various synthesis procedures have been developed and improved, which control the particle diameter and geometry in a well-defined way.

In this work, the metal nanoparticles have been solely prepared in solution by the reduction of the metal precursor with an appropriate reduction agent, followed by the growth of small metal nuclei to the final particle. The difference of the redox potentials between the metal and reducing agent is normally used to choose an effective agent for reduction (Table 1-1).<sup>[40, 41]</sup> Thus, an alcohol or hydrogen is used to reduce Rh- and Pt-precursors, while sodium borohydride and hydrazine is added for the reduction of Ni and Co ions. The increasing strength and amount of the reducing compound directs the particle size to small diameters, which was evaluated for e.g. Rh and Pt particles.<sup>[42, 43]</sup>

Besides the chemical reduction, metal particles can also be prepared by the thermolysis and photolysis of organometallic compounds.<sup>[44]</sup>

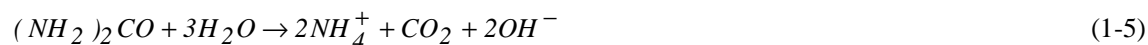
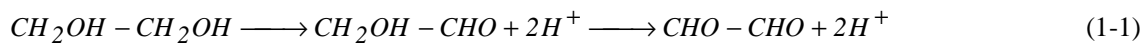
**Table 1-1.** Standard redox potentials  $E^\circ$  of different metals and reduction agents.<sup>[40, 41]</sup>

Component	Redox pair	Standard redox potential $E^\circ / \text{V}$
<i>Metals</i>	$\text{Rh}^{3+} + 3\text{e}^- \rightleftharpoons \text{Rh}^0$	+ 0.76
	$\text{Pt}^{4+} + 4\text{e}^- \rightleftharpoons \text{Pt}^0$	+ 0.74
	$\text{Ni}^{2+} + 2\text{e}^- \rightleftharpoons \text{Ni}^0$	- 0.23
	$\text{Co}^{2+} + 2\text{e}^- \rightleftharpoons \text{Co}^0$	- 0.28
<i>Reduction agents</i>	$\text{BH}_4^- + 8\text{OH}^- \rightleftharpoons \text{H}_2\text{BO}_3^- + 5\text{H}_2\text{O} + 8\text{e}^-$	- 1.24
	$\text{N}_2\text{H}_4 + 4\text{OH}^- \rightleftharpoons \text{N}_2 + 4\text{H}_2\text{O} + 4\text{e}^-$	- 1.17
	$\text{CH}_3\text{CH}_2\text{OH} \rightleftharpoons \text{CH}_3\text{CHO} + 2\text{H}^+ + 2\text{e}^-$	- 0.20 (pH 7) + 0.21 (pH 0)
	$\text{H}_2 \rightleftharpoons 2\text{H}^+ + 2\text{e}^-$	$\pm 0.00$

To avoid the agglomeration of particles in solution and to enhance the monodispersity, protecting polymers are usually added, which form a capping shell around the particles. Polymers like poly(ethylene oxide) (PEO), poly-2-ethylloxazoline (POX), polyethyleneimine (PIM), poly(methyl methacrylate) (PMMA), poly(4-styrenesulfonate) (PSS), and poly(*N*-vinyl-2-pyrrolidone) (PVP), as well as polymers functionalized with cyano or mercapto groups can be used.<sup>[42, 45]</sup> Additionally, huge organic molecules like octanethiol or poly(amido) amine dendrimers can also be applied as the protecting shell.<sup>[46, 47]</sup> These macromolecules provide a steric stabilization of the particles. An electrostatic protection by

the formation of an electric double layer around the particles is achieved by ionic molecules, e.g. halides or polyoxoanions. Surfactants with hydrophilic end groups and hydrophobic side chains combine both the electrostatic and steric stabilization.<sup>[48]</sup>

The ethylene glycol, which is utilized in the polyol method, acts as the reducing and protecting agent. The oxidation of ethylene glycol results in the corresponding aldehydes that are further oxidized to oxalic and glycolic acid (1-1 till 1-3).<sup>[48]</sup> The glycolate anion adsorbs on the metal and stabilizes the particles in solution against agglomeration. An alternative pathway is the abstraction of hydrogen, resulting in adsorbed CO on the metal (1-4). The problem of the preparation of such “unprotected” or rather solvent-capped nanoparticles is the accumulation of protons during the solvent oxidation, which decreases the pH and causes an early particle precipitation, yielding in polydispersity. The addition of urea prevents this particle sedimentation by keeping the pH at a constant value via hydrolysis (1-5).<sup>[49]</sup>



In this work, solely PVP was used as the protecting polymer for Pt particles, which interacts with the metal via charge transfer. A reversible charge transfer behavior between PVP and Pt particles (2-9 nm) was observed by UV-Raman spectroscopy, which was dependent on reduction and oxidation conditions (Figure 1-6).<sup>[50]</sup> The pyrrolidone ring adsorbs preferably via the carbonyl group onto the metal surface that consists of Pt<sup>2+</sup> with d<sup>8</sup> configuration and acceptor orbitals at oxidizing conditions. In opposite to that, repulsive interactions were found under reducing conditions, when metallic Pt is present on the particle surface. Consequently, the interaction between PVP and Pt is stronger for an oxidized particle surface.

The interaction between the carbonyl group from PVP and the metal was also confirmed for Ni particles (4 nm) by infrared spectroscopy and X-ray photoelectron spectroscopy.<sup>[51]</sup> The degradation of PVP was observed above 358 K in reducing atmosphere and the pyrrolidone ring adsorbs strongly on the metal via both the oxygen and nitrogen atom.<sup>[52]</sup>

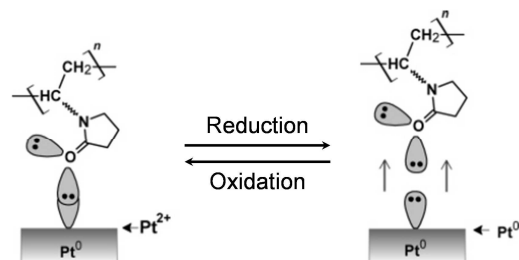


**Figure 1-6.** Donor-acceptor interaction between a Pt surface and PVP under reducing and oxidizing conditions.<sup>[50]</sup>

Generally, the metal-polymer interaction should be in an optimal range, not too strong and not too weak. A weakly coordinated polymer leads solely to large particles, while a strong adsorption hinders the reduction of the metal ions. An optimal interaction of Rh particles and the polymer was found when PVP and POX were used.<sup>[42]</sup> A lower molecular weight of the polymer and a higher polymer-to-metal ratio reduce the particle diameter.<sup>[43]</sup> The stability of the colloidal solutions increases with the decreasing solubility of the polymer in the storage solvent and the coagulation of PVP-capped Rh particles was observed in water due to the strong PVP-water interaction.<sup>[42]</sup>

The metal particle preparation by the reduction of the metal precursor in solution is described by the seeded growth method. The metal salt is reduced and forms small metallic seeds that grow subsequently to larger particles. These nuclei act as catalysts for the further reduction of metal ions on the seed surface (autocatalysis). The interplay between the nucleation and growth depends on the salt concentration and directs additionally the final particle size and shape.<sup>[53]</sup> This process is thermodynamically controlled and results in the thermodynamically most stable particle shapes in solution. For instance, shape-selective Rh particles can be prepared by a two-step synthesis approach, where small seeds are generated in the first step and a further Rh precursor addition leads to monodisperse cuboctahedral particles.<sup>[53]</sup> The size of these particles can be controlled by the Rh concentration that is added in the second step. The precursor addition rate defines the product particle shape and a slow addition favors the epitaxial growth of all facets, while branched multipods are formed at a fast addition. A low reaction temperature was found to enhance the anisotropic growth resulting in branched Rh particles. Contrary, isotropic Rh cubes were prepared at high temperature.<sup>[54]</sup>

In addition to the thermodynamically driven seeded growth method, a kinetically controlled polyol process can be applied for the formation of shape-selective, anisotropic particles. The

addition of a shape-directing compound promotes the crystal growth in a preferred direction. PVP-capped Rh cubes (~ 6 nm), as well as Pd nanobars (6 nm width) and nanorods (2 nm diameter) were prepared by the addition of trimethyl(tetradecyl) ammonium bromide (TTAB) and potassium bromide (KBr), respectively.<sup>[55, 56]</sup> The bromide ions were supposed to stabilize {100} and {110} facets, enhancing the growth of these surfaces by the oxidative etching. The chemisorption of Br<sup>-</sup> on small seeds at the beginning of the particle growth changes the surface free energies of the facets and the formation of thermodynamically favored particle geometries is kinetically hindered.

An advanced synthesis approach for well-defined Pt particle shapes was developed by Song *et al.*<sup>[57]</sup> and was used in this work. Both the particle shape and particle size can be tuned simultaneously during preparation. Silver ions act as the shape-directing compounds and enhance the particle growth in <100> direction. Final Pt particles expose solely {100} facets at low Ag<sup>+</sup> concentration, while a mixture of different shapes is formed without Ag<sup>+</sup> addition. The Ag<sup>+</sup> amount increases the fraction of {111} surfaces yielding cuboctahedra at medium and octahedra at high Ag<sup>+</sup> concentrations (Figure 1-7).

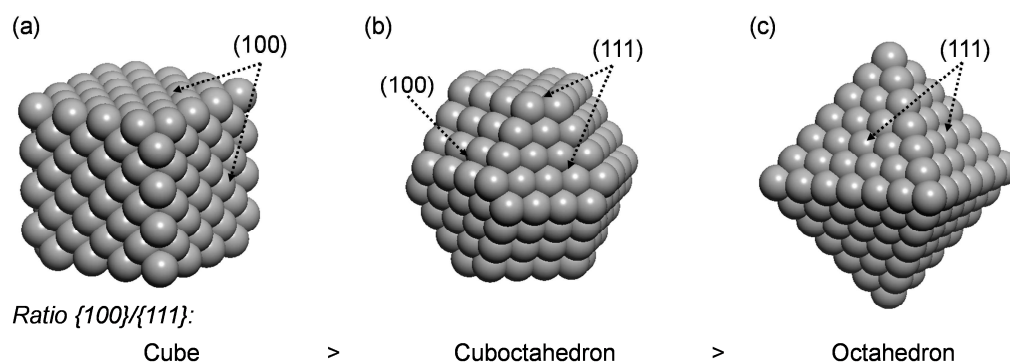


**Figure 1-7.** Fcc metal geometries: (a) cube, (b) cuboctahedron, and (c) octahedron with decreasing {100}/{111} ratio.

The authors proposed the adsorption of reduced Ag species like Ag<sub>4</sub><sup>2+</sup> and Ag<sup>0</sup> preferentially on {100} facets of small Pt seeds. The subsequent Pt precursor addition leads to the oxidation of the adsorbed Ag species and AgCl is formed, while Pt ions are simultaneously reduced to Pt<sup>0</sup> and accumulate on the seed's surface (1-6). The Ag containing side products can be completely removed from the particles by precipitation/redispersion and washing steps.<sup>[57]</sup>





The final particle diameter is controlled by the addition rate of the Pt precursor and PVP. If both reactants are added at once, small (4 nm) but irregular particles will be formed. The alternating addition of the Pt salt and the polymer within a time period of 16 min results in the particular particle shapes with high selectivity and a size of 10 nm, while larger, polycrystalline particles of 13 nm are formed after a slower addition of the polymer and the metal precursor.<sup>[57]</sup>

In summary, various parameters influence the size and geometry of metal particles and show the potential to control the nanoparticle properties during the synthesis regarding their performance in catalysis (Figure 1-8).

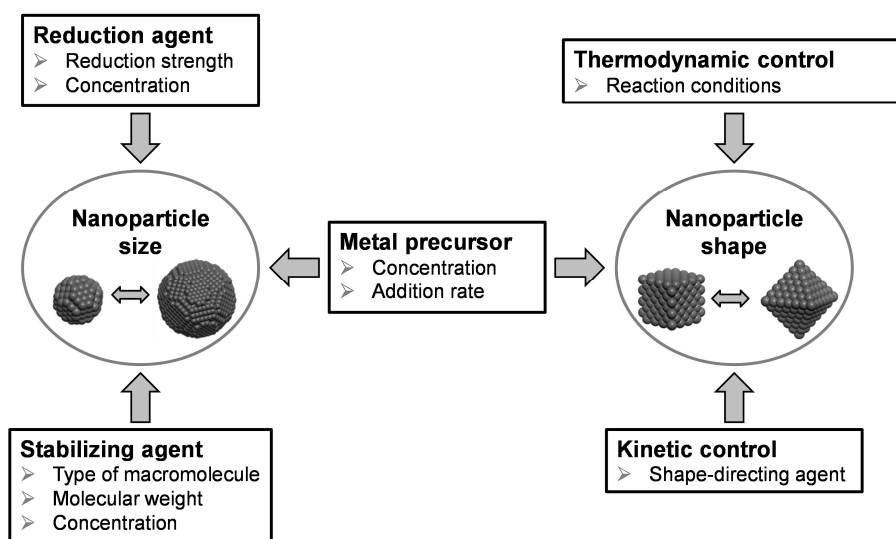


**Figure 1-8.** Main parameters that affect the size and shape of metal nanoparticles during their synthesis.

### 1.3.2 Physical Properties

The application of small metal particles in catalysis requires a detailed knowledge of their physical properties (electronic, optic, and magnetic), which differ significantly from the bulk metal properties, resulting in altered effects in catalysis.

The optical behavior of metal particles originates from their surface plasmon resonance that is not present in the bulk phase. The electromagnetic radiation induces a homogeneous polarization of the particles and conduction electrons oscillate coherently with the electric field, while the positively charged particle core appears immobile.<sup>[58, 59]</sup> The absorption

spectra of the particles can be generally described by the Mie theory, which defines the extinction by the sum of the light absorption and scattering.<sup>[60]</sup> The absorption bands in UV-vis spectra were found to be dependent on the particle size and shape. For instance, a blue shift of the absorption band maximum with decreasing particle size from 9 nm to 3 nm was observed for Au particles.<sup>[59]</sup> Moreover, a decreasing particle size leads to an increasing absorption band width.<sup>[61]</sup> The chemisorption of molecules on the particle surface causes a band shift and nucleophilic molecules act as electron donors, while electrophilic adsorbates withdraw electrons from the particle, leading to a blue and red shift of the absorption band, respectively.<sup>[61]</sup> UV-vis spectra of various particle shapes are significantly different and e.g. elongated structures exhibit two bands in their absorption spectra. A larger particle aspect ratio (width/height) leads to an increased distance between these bands.<sup>[58]</sup> In opposite to Au particles, Pt particles below 10 nm do not have surface plasmon resonances within the range of visible light (380-750 nm). However, huge Pt particles of 100 nm show absorption bands above 450 nm, due to the red shift with increasing particle size.<sup>[62]</sup>

In comparison to the optical properties, the magnetic behavior of metal particles is also significantly different from that of the bulk metal. The paramagnetic properties of bulk Pt are changed to superparamagnetic properties in PVP-capped nanoparticles below 4 nm. The magnetic moment increases with the decreasing particle diameter and correlates with an enhancement in magnetization.<sup>[63]</sup> Superparamagnetism was also found for Ni particles below 21 nm in contrast to the ferromagnetism in bulk Ni.<sup>[64]</sup> The magnetization of the particle surface and the interior was proposed to be nearly similar. However, a special spin polarization effect on the surface was observed for Pd particles below 3 nm, indicating a transition from conduction to atomic electron levels. This leads to a minimal saturation magnetization at a particle diameter of 3 nm.<sup>[64]</sup> The magnetic moment and susceptibility (degree of magnetization) are both size-dependent for superparamagnetic particles and both increase with increasing particle size.<sup>[63]</sup> Additionally, the formation of bimetallic particles enhances their magnetic properties, e.g. by CoPt alloying.<sup>[65]</sup>

The effect of the particle size on their thermodynamic properties like the specific heat and magnetic susceptibility originates from an electronic deviation compared to the corresponding bulk metal. The Young-Laplace equation shows directly the consequences of a decreasing size of spherical particles (Equation 1-1).

$$\Delta p = 2\gamma \frac{1}{R} \quad (\text{Equation 1-1})$$

Where  $\Delta p$  is the pressure difference on the particle surface,  $\gamma$  the surface tension, and  $R$  the particle radius.

A decrease in particle radius results in an increase of the pressure difference, which leads to strong forces at the surface. The interatomic interactions between surface atoms change with their electronic structure. This yields in a huge effect in small particles as they consist mainly of surface atoms. The band structure of the corresponding bulk phase is not valid anymore for particles of a critical diameter, which is typically  $< 1\text{-}2$  nm. The quantum size effect is responsible for the modified physical properties of very small particles (Figure 1-9).<sup>[66-68]</sup>

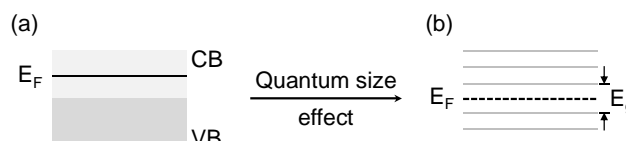


**Figure 1-9.** Scheme of the quantum size effect, which appears at the transition from (a) the bulk metal to (b) very small metal nanoparticle ( $< 1\text{-}2$  nm). The formation of a bandgap  $E_g$  occurs by the energy level separation of the valence and conduction band (VB and CB), while the Fermi level  $E_F$  lies within the bandgap.

The band structure of large particles or the bulk metal consists of very dense energy levels resulting in continuous bands, the valence and conduction band. The conduction band is filled with electrons up to the Fermi level. If the particle size decreases, less electronic states will be filled with electrons that reduce the number of conduction electrons and thus, the density of states at the Fermi level. Consequently, the energy levels are separated into discrete states and a bandgap appears between the valence and conduction band. The energy distance between the individual levels is called the Kubo gap, which depends inversely on the number of conduction electrons, resulting in a larger gap for smaller particles (Equation 1-2).<sup>[66, 67]</sup>

$$\delta = \frac{4E_F}{3N} \quad (\text{Equation 1-2})$$

Where  $\delta$  is the energy separation,  $E_F$  the Fermi level, and  $N$  the number of conduction electrons.

The thermal energy  $k_B T$  (25 meV at room temperature) limits the quantum size effect and small particles are metallic when  $k_B T$  exceeds  $\delta$ . Otherwise, the particles are nonmetallic and exhibit discrete electron states. If the energy to attach one electron to the quantum sized particle is beyond  $k_B T$  (Coulomb-charging effect), the odd-even particle effect will become

important. In this case, deviations in the heat capacity and magnetic susceptibility were found to be dependent on an even or odd number of electrons.<sup>[67, 68]</sup> The localization of valence electrons is increased with decreasing particle size and the d band center shifts towards higher energy for transition metal particles. The metal work function defines the energy that is at least required to remove one electron from the solid (energy difference between Fermi level and vacuum level) and increases for smaller particles (Equation 1-3).<sup>[69]</sup>

$$W_{Particle} = W_{Bulk} + \frac{5.4}{R} eV \quad (\text{Equation 1-3})$$

Where  $W$  is the metal work function and  $R$  the universal gas constant.

In summary, the particle size effect of very small metal particles dominates their optical, as well as their magnetic properties, and therefore, their reactivity in catalysis. The electron transfer or donor-acceptor behavior between chemisorbed molecules and the surface atoms is significantly different for such small particles. A clear prediction of the electronic states of monodisperse particles is fairly unfeasible. All colloidal particles have a certain particle size distribution and even the narrowest distribution cause variations in the electronic energy levels for every single particle.

### 1.3.3 Oxidation, Reduction, and Sintering of Platinum Nanoparticles

Various characterization methods and theoretical calculations have been used in the past to investigate the oxidation and reduction of Pt samples, which consisted of clean and defined surfaces, as well as supported particles. Generally, the gas molecules adsorb on the metal surfaces at pressures of  $10^{-9}$  bar at room temperature.<sup>[70]</sup> Therefore, clean surfaces are solely obtained under ultra-high vacuum (UHV) conditions. At higher pressures, adsorbed molecules like oxygen, water, and hydrocarbons are present on the metal surface. The oxidation of the Pt metal leads to Pt oxides with different stoichiometry and their reduction with hydrogen releases water (1-7 and 1-8).



Bulk Pt oxides exhibit different structures, the hexagonal  $\alpha$ -PtO<sub>2</sub>, the orthorhombic  $\beta$ -PtO<sub>2</sub>, the cubic Pt<sub>3</sub>O<sub>4</sub>, and the tetragonal PtO phase (Table 1-2). The enthalpies of formation show that PtO<sub>2</sub> is the thermodynamically most stable bulk oxide. The hexagonal  $\alpha$ -PtO<sub>2</sub> is preferred in contrast to  $\beta$ -PtO<sub>2</sub>, because the latter is only stable at very high oxygen pressures (200 bar).<sup>[71]</sup>

**Table 1-2.** Lattice constants, crystal structures, and enthalpies of formation for different bulk Pt oxides.<sup>[71, 72]</sup>

Oxide	Lattice constants / Å			Crystal structure	Enthalpy of formation <sup>(a)</sup>
					$\Delta H_f / \text{kJ mol}^{-1}$
$\alpha$ -PtO <sub>2</sub>	a = 3.100	c = 4.350		hexagonal	-198
$\beta$ -PtO <sub>2</sub>	a = 4.486	b = 4.537	c = 3.138	orthorhombic	-199
Pt <sub>3</sub> O <sub>4</sub>	a = 5.585			cubic	-137
PtO	a = 3.040	c = 5.3400		tetragonal	-73

<sup>(a)</sup> Calculated for T = 0 K and p = 0 bar.

The thermodynamic stability of the Pt bulk oxides is also reflected in the phase diagram, which shows  $\alpha$ -PtO<sub>2</sub> as the most stable phase at atmospheric oxygen pressure below 870 K and Pt<sub>3</sub>O<sub>4</sub> as the most stable oxide above 870 K (Figure 1-10). The decomposition of the oxide starts above 980 K. PtO is thermodynamically not favored et all.<sup>[71]</sup>

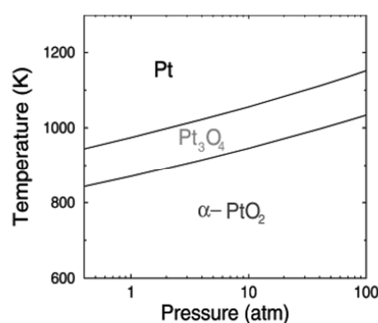


**Figure 1-10.** Phase diagram of bulk Pt oxides.  $\alpha$ -PtO<sub>2</sub> is the thermodynamically most stable phase at low temperatures and low oxygen pressures.<sup>[71]</sup>

The oxidation of the Pt surface occurs due to the preferential saturation of surface low-coordinated sites. The surface free energy is minimized by oxygen adsorption and surface oxide formation. DFT calculations on surface free energies of Pt surfaces in the presence of oxygen (1 bar) showed the dependency of the oxide coverage and oxide structure on the exposed Pt(111) and Pt(100) surface (Table 1-3).<sup>[71]</sup> The thermodynamically most stable oxide was  $\alpha$ -PtO<sub>2</sub> on Pt(111) (< 870 K) and a PtO-like structure on Pt(100) (< 970 K). The decomposition of adsorbed oxygen occurs above 1400 K and 1300 K on the Pt(111) and Pt(100) surface, respectively. The PtO-like monolayer is not stable anymore at higher oxygen coverage (3 ML) and a Pt<sub>3</sub>O<sub>4</sub>-like oxide layer is preferred on Pt(100). One monolayer of adsorbed oxygen atoms is not stable on both surfaces.<sup>[71]</sup> A subsurface oxidation was not observed on low-index surfaces like Pt(111), but it occurs for stepped Pt(557) surfaces. This was attributed to (100) ledges that allow oxygen atom insertion into deeper layers.<sup>[73]</sup>

**Table 1-3.** Temperature-dependent thermodynamically most stable Pt surfaces in the presence of 1 bar oxygen based on surface free energy calculations for Pt(111) and Pt(100).<sup>[71]</sup>

Surface	Temperature / K	Surface oxide species
<i>Pt(111)</i>	< 870	$\alpha$ -PtO <sub>2</sub> (1 ML)
	870-1400	0.25 ML O <sub>ads</sub>
	> 1400	Clean Pt(111)
<i>Pt(100)</i>	< 970	PtO-like oxide (1 ML)
	970-1300	0.50 ML O <sub>ads</sub>
	> 1300	Clean Pt(100)

In the case of Pt nanoparticles, an easier surface oxide formation occurs due to the huge fraction of chemically unsaturated atoms (steps, kinks, and edges). The amount of low-coordinated sites differs with the particle size, which varies the degree of oxidation. This was observed for alumina-supported Pt particles, which were oxidized in 500 mbar oxygen at 770 K.<sup>[74]</sup> PtO<sub>2</sub> was found to be the surface oxide on particles below 2 nm, while Pt<sub>3</sub>O<sub>4</sub> was observed on particles above 2 nm. Further heating in oxygen to 800 K led to the decomposition of the surface oxide, which was in contrast to other metal oxides like the oxides of Pd or Rh, where further oxide growth occurred. Moreover, the adsorption enthalpy for the chemisorption of oxygen increased with decreasing particle size (Equation 1-4).<sup>[75]</sup>

$$-\Delta H_{ads} [kJ (mol O_2)^{-1}] = 406 - \frac{81d}{nm} \quad (\text{Equation 1-4})$$

Where  $\Delta H_{ads}$  is the adsorption enthalpy and  $d$  the particle diameter.

Surface free energy calculations of ideal, cuboctahedral Pt particles showed a rounding of edges and corners at high oxygen coverage, which originated from the surface reconstruction by oxygen adsorption and mainly Pt(111) and Pt(110) facets were exposed.<sup>[76]</sup> Experimental results on Pt model catalysts (8 nm particles on alumina) confirmed the altered particle shape at oxidizing conditions.<sup>[77]</sup>

A more aggressive oxidation of Pt occurs during the oxygen plasma due to the presence of highly reactive compounds, as well as UV radiation. When Pt thin films (100 nm) were exposed to oxygen plasma (100 W, 0.1 mbar O<sub>2</sub>, 5 min), an oxide layer of about 2.7 nm was determined by X-ray photoelectron spectroscopy (XPS).<sup>[78]</sup> The samples in this work were treated with oxygen plasma at much harsher conditions (200 W, 1.4 mbar O<sub>2</sub>, 5 min) to remove the polymer-capping from the Pt particles and a significant oxidation of the Pt surface was expected (Chapter 4).

During the reduction of Pt particles with hydrogen different adsorption sites in atop, n-fold, and ontop position were found for the H atom after the dissociative adsorption of H<sub>2</sub>.<sup>[79]</sup> The hydrogen coverage determines the occupation of the special adsorption site and the n-fold coordination was found to be more stable at high pressures. In the case of very small supported Pt clusters (Pt<sub>4</sub>-Pt<sub>20</sub>), the basicity of the support increased the adsorption energy of hydrogen on Pt.<sup>[80]</sup> The temperature that is essential to reduce the metal is normally determined by the temperature-programmed reduction (TPR), where the sample is continuously heated in hydrogen to high temperatures and the formation of water is monitored simultaneously with the consumption of hydrogen at the reduction temperature. The temperature ramp during TPR affects the reduction temperature, which is higher for fast ramps, indicating low reduction rates.<sup>[81]</sup> The desorption of hydrogen from small, supported Pt clusters was observed at 450 K. The hydrogen species that was found to desorb at 575 K was assigned to spillover hydrogen, which originates from the metal-support interface.<sup>[82]</sup> Therefore, hydrogen is generally able to diffuse through the Pt particle.

High reduction temperatures above 800 K may lead to alloying of the supported Pt with the metal of the support, which was observed for e.g. Pt on alumina.<sup>[77, 83]</sup> Additionally, strong

metal-support interactions (SMSI) were found for reducible oxide supports like ceria, gallia, or titania after reduction at high temperatures.<sup>[10, 11, 83, 84]</sup> The decoration of the metal particle surface by partially reduced support oxide species was supposed to affect the accessibility of active sites, as well as their electronic properties.<sup>[85]</sup> The encapsulation of the Pt particles by gallia or titania suboxides can have a positive or negative effect on their catalytic behavior. The activity towards ethene or toluene hydrogenation was minimized by the SMSI effect, while an enhanced selectivity towards crotyl alcohol was detected in the crotonaldehyde hydrogenation.<sup>[10, 86-88]</sup>

High temperatures lead additionally to the sintering of metal particles, which occurs normally above the Tammann-temperature (half of the metal melting temperature). This would be 1021 K for Pt. However, significant sintering of small nanoparticles (2-3 nm) supported on alumina and silica was observed at much lower temperature of 873 K in oxygen.<sup>[89]</sup> Two limiting mechanisms are used to explain the metal particle sintering, the Ostwald ripening and the particle migration and coalescence.<sup>[90]</sup> The Ostwald ripening describes the separation of metal atoms or small metal clusters from the immobile fixed particles. Their subsequent migration from small to large particles occurs due to the lower chemical potential of atoms in large particles. Therefore, a change in the average diameter would linearly increase with the sintering time and a narrow size distribution changes to a bimodal and finally to a stationary distribution. In contrast to the Ostwald ripening, the particle migration and coalescence mechanism involves the mobility of the whole particle and coalescence into larger one. Here, a log normal size distribution is expected. Recent studies on the particle sintering of small, 2 nm-sized Pt particles showed a log normal distribution function for both mechanisms.<sup>[90]</sup> These results were assigned to the instability of very small particles that evaporate from the support during Ostwald ripening and disappear from the distribution. A transition between both mechanisms was found for the sintering of Pt particles, which was caused by the atmosphere. Ostwald ripening is usually not expected for Pt due to its low metal vapor pressure ( $10^{-20}$  mbar at 973 K). Therefore, particle migration and coalescence was observed at reducing conditions. In an oxidizing atmosphere, Ostwald ripening was found due to the formation of Pt oxides on the particle surface, which exhibit a higher vapor pressure compared to the metal, enhancing the escape of Pt atoms from the particle. However, hydrogen increases the mobility of Pt atoms on the support surface, which is utilized in physical vapor deposition techniques for the generation of particle islands. The regeneration of sintered catalysts can be performed with oxidation-reduction cycles at high temperatures



(775-875 K). The addition of chloride during the cycles was found to enhance the redispersion due to the formation of a mobile Pt complexes ( $[\text{PtO}_2\text{Cl}_2]^{2-}$ ).<sup>[91, 92]</sup>

## 1.4 Gallium Nitride as Wide Bandgap Semiconducting Support

The role of GaN in industry and in our daily life is reflected by its various applications in the advanced device technology. GaN extends possibilities due to its direct wide bandgap of 3.4 eV, which is in contrast to the widely used Si with an indirect bandgap of only 1.1 eV.

The most famous application of GaN is as light-emitting diodes (LEDs) with UV and blue light emission.<sup>[93]</sup> They are characterized by a high power, high performance, long lifetime, and a small size. After the availability of an efficient *p*-type doping, the development of GaN-based *p-n* junction LEDs was forwarded.<sup>[23, 24]</sup> The electric current flows from the *p*- to the *n*-type GaN during operation releasing energy with a wavelength according to the bandgap (electroluminescence) (Figure 1-11).<sup>[24]</sup> GaN-based LEDs emit blue light with a wavelength of 430 nm, while its alloy InGaN has contributions from green light. Recently, high-brightness LEDs facilitating the full light spectrum were investigated by the coating of blue LEDs with yellow phosphor ( $\text{Y}_3\text{Al}_5\text{O}_{15}:\text{Ce}$ ) and epoxy resin.<sup>[94]</sup> The replacement of standard electric bulbs is a current issue and white LEDs have a great potential for the application for general room lighting. So far, GaN is grown on the expensive sapphire substrate, which limits the use of the LED technology. Therefore, new developments in the growth methods improve the GaN growth on much cheaper and more available Si wafers, which showed cost savings of 75%.<sup>[95]</sup>

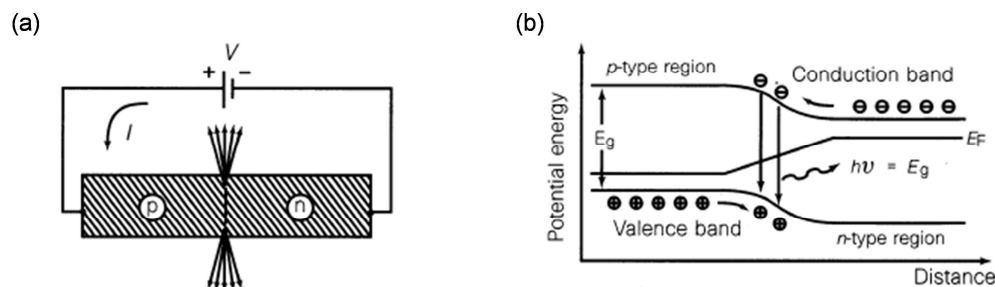


**Figure 1-11.** Operation mode of *p-n* junction LEDs. (a) Current flow from *p*- to *n*-type semiconductor with light emission at the *p-n* junction. (b) Potential energy diagram of the *p-n* junction with the valence and conduction bands, Fermi levels  $E_F$ , and charge recombination with light emission at the energy of the bandgap  $E_g$ .<sup>[24]</sup>

Another prevailing application of GaN is in “blue” lasers that are used in the Blu-ray technology. GaN-based laser diodes with a photoemission of 405 nm (violet) provide a smaller beam focus for a much denser optical data storage compared to the infrared lasers used for DVDs.<sup>[96]</sup> Additionally, GaN-based solar cells and devices can be used for space applications due to their stability against ionizing radiation.<sup>[97]</sup> Polar heterostructures like high-electron-mobility transistors (HEMT) pH sensors (AlGaIn/GaN), as well as white LEDs are used for communication systems with wireless data transmission.<sup>[98, 99]</sup> GaN metal-oxide-semiconductor field-effect transistors (MOSFETs) were investigated for a power supply appliance at very high temperature (523 K), high current, and high breakdown voltage.<sup>[100]</sup> The characteristics of GaN expand the operation area of MOSFETs in comparison to the Si-based devices. Besides the optoelectronic and electronic device applications, the biocompatibility of GaN provides new areas of organic/inorganic hybrid structures for biosensors. Self-assembled monolayers of organosilanes can be immobilized on GaN surfaces and act as linker for biomolecules, e.g. enzymes.<sup>[101]</sup> Small concentrations ( $\mu\text{M}$ ) of penicillin were detected with a biosensor containing a penicillinase monolayer linked by octadecyltrimethoxysilane (ODTMS) to the GaN-based substrate.<sup>[102]</sup> The main advantage of GaN is the energetic adjustment of the bandgap with the HOMO-LUMO (highest-occupied-molecular-orbital and lowest-unoccupied-molecular-orbital) energy states in organic molecules. This facilitates the charge transfer of electrons between the semiconducting surface and the organic molecules under optical excitation of GaN, which was monitored by the degradation of the ODTMS on *n*-type GaN surfaces.<sup>[103]</sup> The electronic devices can be optimized using quasi-one-dimensional structures containing *n*- and *p*-type, as well as *p-n* junction GaN nanorods and nanowires, which can be grown on Si substrates.<sup>[104, 105]</sup> They exhibit ideal crystal structures with a very low defect density.

The broad area of applications shows the indispensability of GaN for device technology. GaN is more suitable than Si for special applications due to its use at harsh conditions and alloying with other group III metals like Al and In, facilitating bandgap engineering. The defined control of the GaN doping with high carrier concentrations, its high stability, and biocompatibility establish advanced and novel options in industry and research.

The study of heterostructures composed of catalytically active metal particles and wide bandgap semiconductors is challenging for the combination of catalysis and device application. Generally, the oxide semiconductors with a wide bandgap similar to that of GaN are used in heterogeneous photocatalysis. ZnO and TiO<sub>2</sub> are commonly used as

photocatalysts, which exhibit bandgaps of 3.2 eV and 3.0-3.4 eV, respectively. However, the introduction of a controlled electrical conductivity is a major problem in such oxidic semiconductors.<sup>[106, 107]</sup> The undesired, background *n*-type conductivity is present due to native defects like oxygen vacancies and cation vacancies or interstitials. Consequently, the *p*-type doping is difficult to achieve, which results from poor material stability and reproducibility, inhomogeneous dopant distributions, and the formation of metal dopant oxide clusters on the surface. Especially, TiO<sub>2</sub> has three crystal phases, anatase, rutile, and brookite, which exhibit different electronic structures. A high-temperature treatment or high impurity concentration changes the crystal structure and anatase was found to be transformed to rutile in chromium-doped, *p*-type TiO<sub>2</sub>.<sup>[108]</sup> A well-defined strategy for semiconductor doping is generally not available and the addition of dopants during the synthesis affects the crystal growth, which may result in changed semiconductor properties. Therefore, impurity atoms are introduced subsequently after the semiconductor preparation by high-energy ion implementation, for example.<sup>[109]</sup> In contrast the ZnO and TiO<sub>2</sub>, GaN is well-explored regarding its *n*- and *p*-type doping and is used in this work as support for the metal nanoparticles. The following sections deal with important chemical and physical properties of GaN and with the interaction between metal particles and the semiconductor, which is crucial to understand the charge transfer at the metal-semiconductor interface.

### 1.4.1 Chemical and Physical Properties

The variety of applications shows the benefit of GaN regarding its electrical and optical properties. GaN belongs to the group III-V nitrides and is a direct wide bandgap semiconductor with a bandgap of  $E_g = 3.4$  eV, which corresponds to a wavelength of 365 nm.<sup>[110]</sup>

The electronic band structure originates from the large number of atoms and thus, from the large number of molecular orbitals that is present in the solid. The difference between the electronic states is quite small, resulting in continuous energy bands. The valence band is completely filled with electrons, while electrons are not present in the conduction band at 0 K. The Fermi level defines the chemical potential of electrons in the solid and is equal to the Fermi energy at 0 K, which describes the energy of the highest occupied state. Both bands overlap in metals providing electrical conductivity due to continuous electron transitions. Contrary to conductors, a forbidden energy gap without electronic states separates the valence

and conduction bands in semiconducting materials like GaN and electrical conductivity is only achieved by the excitation of electrons above the bandgap. Semiconductors with  $E_g < 1.6$  eV show an electrical conduction after thermal excitation, while in the case of semiconductors with  $E_g = 1.6$ -3.1 eV, electrons can be excited by visible light absorption. Wide bandgap materials like GaN with  $E_g > 3.1$  eV exhibit an electrical conductivity by the absorption of UV light, while solids with  $E_g > 4.0$  eV are insulators and are not conductive at all.<sup>[111]</sup>

The number of conduction electrons equals the number of positively charged holes in the case of intrinsic semiconductors, where the Fermi level is located at the bandgap center ( $E_F = E_C - E_V$ ) (Figure 1-12 (a)). The probability of electrons for a thermal excitation is defined by the Fermi-Dirac distribution, which is reduced to the Maxwell-Boltzmann equation at elevated temperatures ( $E - E_F > k_B T$ ) (Equation 1-5). Contrary, the hole probability in the valence band is described by  $f_h = 1 - f_e$  (Equation 1-6).<sup>[112]</sup> The concentration of electrons in the conduction band and holes in the valence band can be calculated with the assumption that both exhibit a particle behavior, using effective masses (Equation 1-7 and Equation 1-8).<sup>[112]</sup> The concentration of electrons is multiplied by that of the holes at thermal equilibrium conditions (Equation 1-9).<sup>[112]</sup>

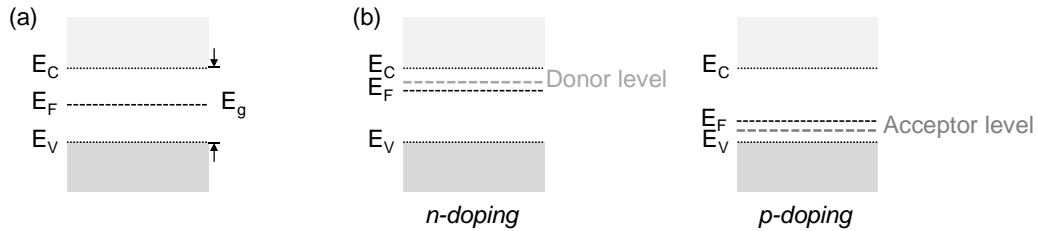


**Figure 1-12.** Band model of (a) an intrinsic and (b) an extrinsic semiconductor ( $n$ - and  $p$ -type) with the Fermi level  $E_F$ , bandgap  $E_g$  and the energy of the valence and conduction band edge  $E_V$ ,  $E_C$ .

Besides the intrinsic semiconductors, extrinsic ones provide an enhanced conductivity due to the insertion of donor or acceptor atoms resulting in  $n$ - or  $p$ -type conduction (Figure 1-12 (b)). The impurity atoms contain one valence electron more or less, which create a donor level right below the conduction band or an acceptor level just above the valence band, respectively. The Fermi level shifts towards the band of majority charge carriers, which are electrons for  $n$ -type and holes for  $p$ -type semiconductor. Undoped GaN shows always a background,  $n$ -type conductivity that originates from native defects.<sup>[113, 114]</sup> The replacement

of Ga atoms by Si results in *n*-type, while the doping with Mg forms *p*-type GaN. High majority charge carrier concentrations of  $10^{18} \text{ cm}^{-3}$  were obtained for both GaN substrates, which were used in this work. The Fermi level positions were determined by Auger peak position measurements and were  $E_C - 50 \text{ meV}$  in *n*-type and  $E_V + 250 \text{ meV}$  in *p*-type GaN.<sup>[115]</sup> In earlier studies, slightly different values were evaluated for the donor and acceptor levels in *n*- and *p*-type GaN, respectively, which were  $E_C - 22 \text{ meV}$  in *n*-type and  $E_V + 170 \text{ meV}$  in *p*-type GaN.<sup>[116, 117]</sup>

$$f_e \cong e^{-\frac{(E_F - E)}{k_B T}} \quad (\text{Equation 1-5})$$

$$f_h \cong e^{-\frac{(E - E_F)}{k_B T}} \quad (\text{Equation 1-6})$$

$$n = 2 \left( \frac{2\pi m_e k_B T}{h^2} \right)^{\frac{3}{2}} e^{-\frac{(E_F - E_C)}{k_B T}} \quad (\text{Equation 1-7})$$

$$p = 2 \left( \frac{2\pi m_h k_B T}{h^2} \right)^{\frac{3}{2}} e^{-\frac{(E_V - E_F)}{k_B T}} \quad (\text{Equation 1-8})$$

$$np = 4 \left( \frac{2\pi k_B T}{h^2} \right)^3 (m_e m_h)^{\frac{3}{2}} e^{-\frac{E_g}{k_B T}} \quad (\text{Equation 1-9})$$

Where  $f_e$  is the electron probability in conduction band,  $f_h$  the hole probability in valence band,  $E_F$  the Fermi level,  $E$  the energy of quantum state,  $k_B$  the Boltzmann constant,  $T$  the temperature,  $m_e$  and  $m_h$  the effective mass of electrons and holes,  $h$  the Planck constant, and  $E_C$  and  $E_V$  the energy of the conduction and valence band edge.

Semiconductors can be generally distinguished in materials with a direct or indirect bandgap (Figure 1-13). The electron momentum (*k*-vector) remains during the electron transition in a direct semiconductor, while it is changed in an indirect semiconductor by adding both the photon and phonon energy.<sup>[112]</sup> Therefore, only direct semiconductors like GaN can be used for effective radiation applications.

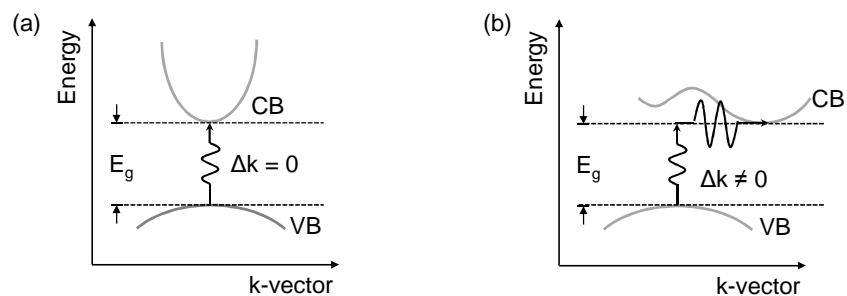


**Figure 1-13.** Schematic band structure of the (a) direct and (b) indirect photon absorption, which describes first the photon absorption followed by lattice vibrations. (With crystal momentum,  $k$ -vector, and the bandgap  $E_g$ ).

The crystal lattice of GaN exhibit either hexagonal wurtzite or cubic zinc blende structure (Figure 1-14). One Ga atom is tetragonally coordinated by four N atoms in both cases, while the layer arrangement changes from ABABAB in wurtzite to ABCABC in zinc blende. The wurtzite structure is the thermodynamically more stable phase, which does not contain inversion symmetry and ionic Ga-N bonds.<sup>[113]</sup>

GaN was synthesized for the first time by Johnson *et al.* in 1932.<sup>[118]</sup> The Ga metal was exposed to ammonia gas at high temperatures (ca. 1200 K) and GaN was formed under hydrogen evolution (1-9).

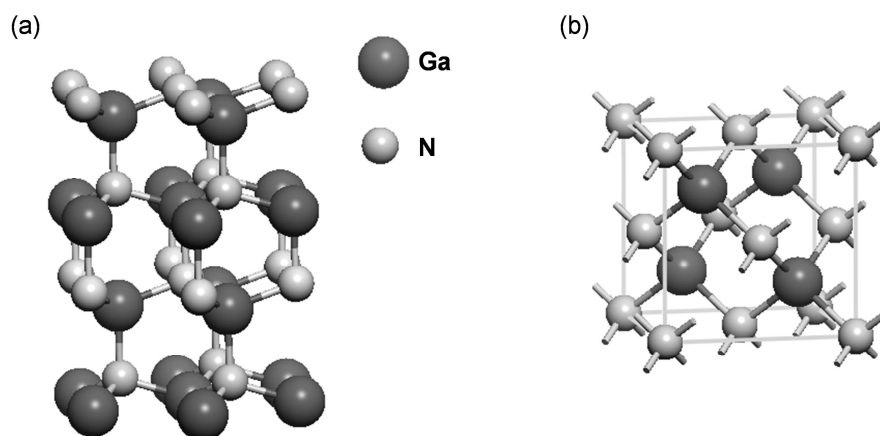


**Figure 1-14.** Crystal lattice of GaN in (a) the hexagonal wurtzite and (b) the cubic zinc blende structure.

Nowadays, GaN layers are prepared by the heteroepitaxial growth in high quality on substrate materials. Sapphire ( $\alpha$ -Al<sub>2</sub>O<sub>3</sub>) and silicon carbide (3C-SiO<sub>2</sub>) are generally used as suitable

substrates for the hexagonal and cubic GaN growth, respectively. The growth of thick epilayers is essential for a substantial quality due to the thermal and lattice mismatches between the substrate structure and GaN (Table 1-4).<sup>[113, 119]</sup> Sapphire is mainly used for the growth of wurtzite GaN, because it is a highly available and stable substrate.<sup>[113]</sup>

**Table 1-4.** Lattice constants of hexagonal and cubic GaN, the hexagonal  $\alpha$ -Al<sub>2</sub>O<sub>3</sub>, and cubic 3C-SiC.<sup>[113, 119]</sup>

Component	Lattice constants / Å		Crystal structure
<i>GaN (wurtzite)</i>	a = 3.189	c = 5.185	hexagonal
<i>GaN (zinc blende)</i>	a = 4.500		cubic
<i><math>\alpha</math>-Al<sub>2</sub>O<sub>3</sub></i>	a = 4.758	c = 12.991	hexagonal
<i>3C-SiC</i>	a = 4.360		cubic

Two methods can be applied for the epitaxial GaN growth, the plasma-assisted molecular beam epitaxy (PAMBE) and the metal organic chemical vapor deposition (MOCVD). The growth by MBE includes plasma-activated nitrogen and a beam of Ga metal at high temperatures (> 1200 K). MOCVD-grown GaN is formed from the trimethylgallium precursor and an ammonia plasma at similar temperatures (1-10).<sup>[113]</sup>



GaN surfaces terminated with Ga atoms exhibit different polarities, the Ga-face and N-face polarity (Figure 1-15). The Ga-faced surface shows negative charges with a polarization towards the interior of the epilayers, while an internal electric field builds up towards the surface. Contrary, the positive surface charges of the N-faced surface induce the opposite directions of the polarization and the electric field.<sup>[120]</sup>

The chemical behavior of GaN is dependent on its surface polarity, which correlates with the concentration of dangling bonds of the surface Ga atoms. Dangling bonds describe generally a fixed radical or an unsaturated valence of an immobilized atom in a solid.<sup>[111]</sup> Ga atoms on a Ga-faced surface contain one dangling bond, while three dangling bonds per Ga atom appear in N-face GaN (Figure 1-15). Thus, a higher reactivity is assigned to the larger number of dangling bonds on the surface. This is consistent with etching experiments, where Ga-faced GaN was found to be resistant and N-faced GaN was easily decomposed by KOH or NaOH. The surface polarity can be altered by the insertion of an AlN buffer layer during PAMBE

growth, resulting in the N-faced surface. MOCVD-grown GaN is solely Ga-faced, which exhibit a much smoother morphology than the N-face material.<sup>[121]</sup>

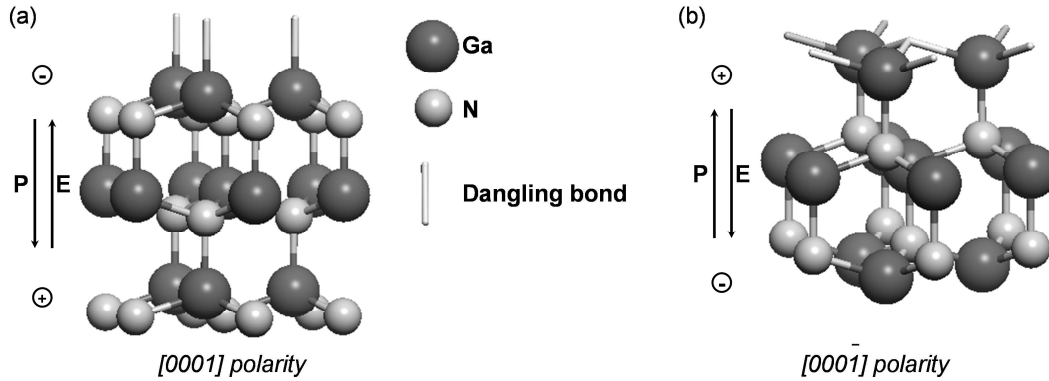


**Figure 1-15.** GaN surfaces with different polarity: (a) the Ga-face and (b) the N-face surface with opposite directions of the polarization  $P$  and the internal electric field  $E$ .

The fabrication of highly  $p$ -doped GaN was challenging in the past and Mg doping was established by a subsequent low-energy electron-beam irradiation (LEEBI) of GaN buffer layers.<sup>[23]</sup> This treatment provides a sufficient high carrier concentration of  $10^{18} \text{ cm}^{-3}$ . However, the control of structural defects like dislocations and vacancies or impurity atom contaminations with additional donor or acceptor levels play a crucial role in the growth of GaN films with reproducible and high quality.

In contrast to the bulk semiconductor, the topmost layers have significantly different structural and electronic properties. If the surface is not reconstructed, the interlayer distance between the first two layers will be smaller compared to that between the bulk layers (multilayer relaxation). The effect originates from low-coordinated atoms at the surface. The unsaturated valences or dangling bonds force the surface to reconstruct and lower its energy by bunching atoms into superstructures. The relaxation leads to fixed electronic states on the surface and results in energy levels within the bandgap, which are occupied or empty. The equilibrium charge carrier density and the chemical potential are consequently modified, forming the space charge region (SCR), where a bending of the valence and conduction bands occurs.<sup>[112]</sup> The Poisson equation describes the influence of the mobile charge on the electronic potential (Equation 1-10).<sup>[122]</sup>

$$\frac{d}{dx} \left( \epsilon_s(x) \frac{dV(x)}{dx} \right) = -\rho(x) \quad (\text{Equation 1-10})$$

Where  $x$  is the coordinate,  $\epsilon_s$  the dielectric permittivity,  $V$  the electronic potential, and  $\rho$  the charge density.



Four surface regimes are possible that will be discussed in the following for the  $n$ -type semiconductor in more detail (Figure 1-16). Flatband conditions are achieved at a surface electronic potential of  $V_s = 0$  and the charge carrier concentration is equilibrated. The accumulation regime shows a larger majority charge carrier density (electrons) at the surface, resulting in  $V_s > 0$ . The bands are bent towards lower energy within the SCR. Contrary, the depletion leads to a lower majority charge carrier concentration on the surface compared to the bulk material ( $V_b < V_s < 0$ ). The majority charge carrier concentration is still higher than the minority charge carrier concentration, showing an upward band bending at the surface. If the density of majority charges lowers the density of minority charge carriers, an inversion occurs that increases further the upward band bending and the SCR ( $V_s < V_b < 0$ ). Similar regimes appear in the  $p$ -type semiconductor, but with an opposite band bending to the described  $n$ -type.<sup>[122]</sup>

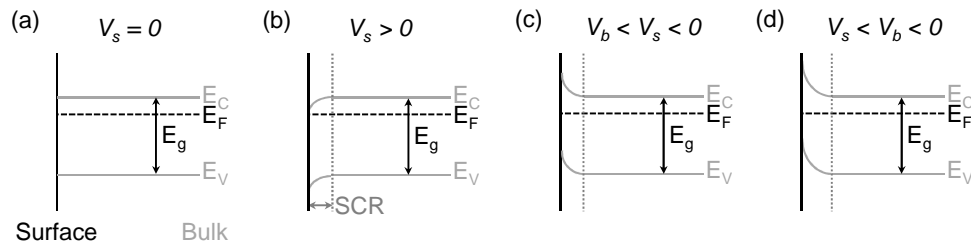


**Figure 1-16.** Electronic band structure of a  $n$ -type semiconductor in different surface regimes: (a) flatband, (b) accumulation, (c) depletion, (d) inversion. Where  $V_s$  and  $V_b$  is the electronic potential of the surface and bulk,  $E_g$  the bandgap,  $E_F$  the Fermi level,  $E_V$  and  $E_C$  the energy of the valence and conduction band edge, and  $SCR$  the space charge region.

The higher the surface state density and the higher the donor level energy, the larger is the band bending at the surface. Additionally, the surface polarity affects also the band bending and an intense upward bending was found for Ga-face GaN, while N-faced,  $n$ -type GaN showed a quite small downward band bending.<sup>[123]</sup> The changes in band bending with polarity were assigned to the surface charge compensation.

Additionally, surface dipoles can contribute to special surface effects that are more complicated when real surfaces are involved. In general, surface states and structural defects may act as deep level traps, which cancel free majority charges and disturb the semiconductor's available conductivity. Special surface states were supposed to be responsible for the typical yellow luminescence (2.2 eV) of  $n$ -type GaN, which is present in addition to its UV emission.<sup>[124, 125]</sup> The transition of electrons into an acceptor level is proposed, which originates from Ga vacancies and surface oxygen atoms. Contrary to  $n$ -type

GaN, *p*-type GaN do not show the significant yellow emission due to the filling of Mg atoms into Ga vacancies. However, the intensity of the yellow emission was found to be dependent on the excitation density and is negligible at current densities that are typical for LED or laser application.<sup>[125]</sup>

## 1.4.2 Native Surface Oxide and Surface Cleaning

A native oxide layer on GaN films was found after their growth by MBE.<sup>[126]</sup> The gallia structure exists mainly of monoclinic  $\beta$ -Ga<sub>2</sub>O<sub>3</sub>, which is the thermodynamically most stable modification. Additionally, some Ga oxynitride compounds were supposed to contribute to the oxide. Calculations of the oxygen adsorption on hexagonal GaN surfaces with different polarities showed the maximal oxygen coverage of 0.8 ML in air.<sup>[127]</sup> The adsorption energy for oxygen was endothermic for coverages above 0.8 ML on Ga-face, *n*-type GaN, while it becomes more exothermic at high coverage for the N-faced material. Initially, when less oxygen is available (0.25 ML), both surfaces exhibit a comparable activity for oxygen adsorption. The high oxygen affinity of N-face GaN was assigned to the higher density of available surface states, which originate from impurities and dangling bonds. A significantly lower density of states within the bandgap was found after the oxide layer formation. Different adsorption sites on Ga- and N-faced surfaces lead to either repulsive or attractive interactions with oxygen.<sup>[127]</sup> Experimental results of the oxidation of a clean GaN(0001) surface with O<sub>2</sub> at room temperature confirmed the calculated saturation coverage of 0.8 ML.<sup>[128]</sup> Further O<sub>2</sub> exposure leads to an increased oxygen uptake and the coverage reaches 2 ML at very high oxygen dosing. Two consecutive mechanisms for the oxidation of GaN were proposed based on O1s and Ga3p core level spectra (XPS). The dissociative chemisorption occurs at low O<sub>2</sub> pressures, while the Mott-Cabrera mechanism is supposed at higher dosing. The Mott-Cabrera mechanism describes a field-assisted diffusion of ionic species. An electric field in the oxide layer provides the electron tunneling from the GaN to oxygen ions, which results in further growth.<sup>[128]</sup>

The oxidation of bulk GaN was found to be kinetically hindered and oxygen adsorbs on-top of Ga atoms or on N vacancies, which does not disturb the bulk crystal lattice.<sup>[129]</sup> In comparison to other semiconductors like Si or GaAs, GaN shows a totally different oxidation behavior. GaN exhibits one single type of oxide, while various types of oxide are found on

GaAs. The presence of the native oxide adlayer contributes to the surface band bending and an increased band bending was found with increasing oxygen uptake, which originates from negative charges at the surface or at the interface.<sup>[130]</sup> A systematic thermal oxidation of GaN(0001) with dry oxygen at 1073 K resulted in an oxide layer with a thickness of maximal 3 nm.<sup>[131]</sup> A controlled oxidation of GaN surfaces at high temperature was found to improve the performance of Pt/GaN devices due to the reduction of the reverse bias leakage current.<sup>[132]</sup>

The cleaning of GaN surfaces from oxygen and carbon impurities can be performed by wet chemical etching, thermal desorption, annealing, or plasma treatment. Etching with HCl removes the surface oxide most effectively, while the treatment with HF followed by a subsequent thermal desorption eliminate mainly carbonaceous contaminants. The wet etching yields in adsorbed halogens on the surface that can be removed by hydrogen plasma at elevated temperatures. Carbon can also be eliminated by an UV/O<sub>3</sub> oxidation, but the formation of a surface oxide is simultaneously enhanced. Only the annealing in ammonia at 1073 K followed by the thermal desorption above 1173 K lead to atomically clean GaN surfaces, where GaN is partially sublimated.<sup>[133, 134]</sup>

Consequently, an oxide adlayer, as well as carbon and halogen contamination of the GaN surfaces cannot be avoided when the surfaces are handled in ambient air. These impurities affect the electronic properties of the semiconductor surface, leading to a complex situation at the metal-semiconductor interface. However, electron tunneling through the thin native oxide or the insulating impurity layer occurs, facilitating the transfer of charges at the Pt-GaN interface.<sup>[135]</sup>

### 1.4.3 Metal-Semiconductor Interface

In 1957, Schwab *et al.*<sup>[7]</sup> observed changes in the catalytic behavior of alumina-supported Ni catalysts during the dehydrogenation of formic acid, which was dependent on the doping of the underlying oxide support. The activation energy was reduced with lower *n*-type conductivity of the doped alumina. A subsequent study of Ni catalysts supported on ZnO showed the same results in the hydrogenation of ethene.<sup>[8]</sup> It was supposed that the electrochemical potential of electrons in the metal was altered by the contact with the

semiconducting oxide support. These observations indicate a possible charge transfer between the metal and the semiconductor, which is directed by the charge carrier concentration of the support. The transfer of charges at the metal-semiconductor interface was recently used to detect an electric current in TiO<sub>2</sub> and GaN, which was caused by the exothermic oxidation of CO on supported Pt (Figure 1-17).<sup>[28, 136]</sup> The obtained electron current was found to correlate with the TOF of CO oxidation, indicating an electron transfer from the metal to the semiconductor.

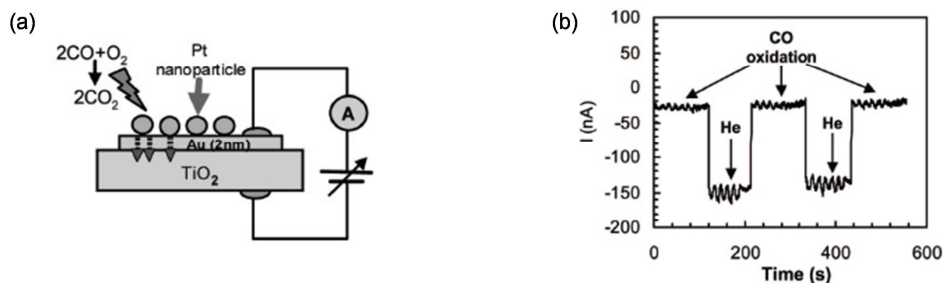


**Figure 1-17.** (a) Schematic illustration of the “hot” electron transfer from Pt nanoparticles to the Au/TiO<sub>2</sub> diode by the exothermic CO oxidation and (b) the current dependency on the gas exposure.<sup>[136]</sup>

In general, the metal-semiconductor interaction shows an ohmic or Schottky contact behavior. In contrast to the ohmic contact, the Schottky contact has rectifying properties, which are used in diode applications. The interfacial properties depend on the metal, the metal work function, the semiconductor bandgap, type of doping, and the dopant concentration. The tunneling of electrons dominates over the transition of electrons by thermionic emission for doping levels of  $> 10^{18} \text{ cm}^{-3}$ .<sup>[112, 137]</sup>

When the metal and semiconductor are not in contact, both exhibit a certain Fermi level. The Fermi levels are aligned after the formation of the Schottky contact due to the transfer of electrons from the semiconductor to the metal at thermal equilibrium (Figure 1-18). The metal-induced gap states (MIGS) are formed, which contain positively charged donor levels in the *n*-type and negatively charged acceptor levels in the *p*-type semiconductor. Within the SCR, the semiconductor surface is depleted by its majority carriers. The valence and conduction bands bend upwards for *n*-type and downwards for *p*-type doping. The band bending at the interface results in the Schottky barrier between the metal and the semiconductor that introduces the rectifying properties.<sup>[12, 112]</sup> The Schottky-Mott model describes an ideal, non-interactive metal-semiconductor interface with the maximal Schottky barrier height of 1.55 eV for Pt-GaN ( $\Phi_M = 5.65 \text{ eV}$  and  $\chi_{SC} = 4.10 \text{ eV}$ ) (Equation 1-11).<sup>[138]</sup>

$$\Phi_B = \Phi_M - \chi_{SC} \quad (\text{Equation 1-11})$$

Where  $\Phi_B$  is the Schottky barrier,  $\Phi_M$  the metal work function, and  $\chi_{SC}$  the electron affinity of the semiconductor.

The Schottky barrier can be determined from XPS, UPS, current- and capacitance-voltage measurements and was 1.1-1.8 eV for Pt-GaN.<sup>[138-142]</sup> The variations of the experimental results can be attributed to different preparation methods and the formation of interface dipoles. Recently, the model of a near-surface layer of process-induced electron states was discussed that leads to a voltage-dependent Schottky barrier height.<sup>[142]</sup> Different Schottky barriers were found for Pt on Ga-face and N-face GaN, which was assigned to spontaneous, polarization-induced surface charges.<sup>[123]</sup> The thermionic emission for a diode is described in Equation 1-12.<sup>[112]</sup>

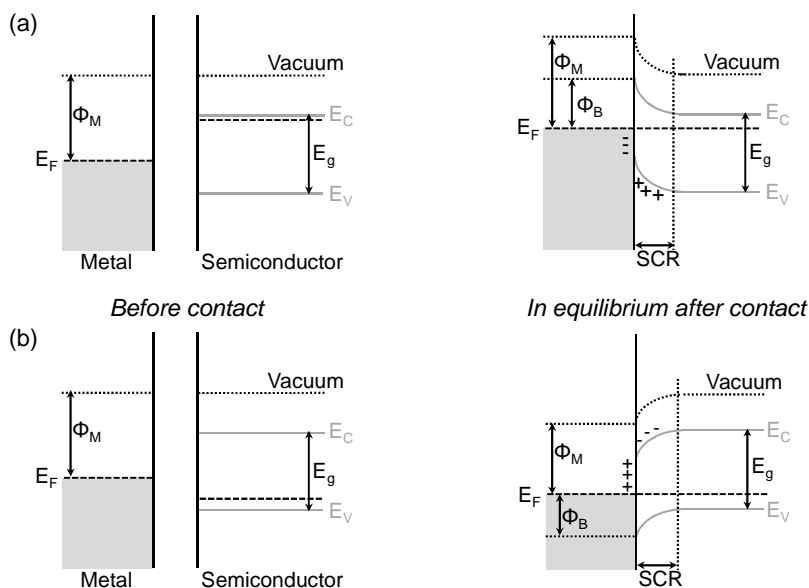


**Figure 1-18.** Metal-semiconductor interaction (Schottky contact) for (a) the  $n$ -type and (b) the  $p$ -type semiconductor before and after contact in thermal equilibrium with Fermi level  $E_F$ , valence and conduction band edge  $E_V$ ,  $E_C$ , bandgap  $E_g$ , metal work function  $\Phi_M$ , and Schottky barrier height  $\Phi_B$ .

$$I_0 = A^* T^2 e^{\frac{-\Phi_B}{k_B T}} \quad (\text{Equation 1-12})$$

Where  $I_0$  is the electron current,  $A^*$  the effective Richardson coefficient,  $T$  the temperature,  $\Phi_B$  the Schottky barrier, and  $k_B$  the Boltzmann constant.

The charge transfer of electrons between the  $n$ -type semiconductor and the metal can be estimated by the Schottky model. It can be applied to most of the diodes that contain metal films, where an infinite interface is assumed and the depletion length is independent of the

film thickness.<sup>[143]</sup> But the one-dimensional description cannot be used for semiconductor-supported metal particles < 10 nm. In this case, a three-dimensional model describes a finite interface and the depletion length decreases simultaneously with the particle radius.<sup>[143]</sup> The metal particle is smaller than the length of the SCR that would consequently lead to a strong electric field inside the particle due to localized negative charges at the interface after contact (Figure 1-19 (a)).<sup>[143]</sup> An advanced approach implies the uniform, stable distribution of electrons over the whole particle surface, which avoids the build-up of the electric field (Figure 1-19 (b)).<sup>[144]</sup>

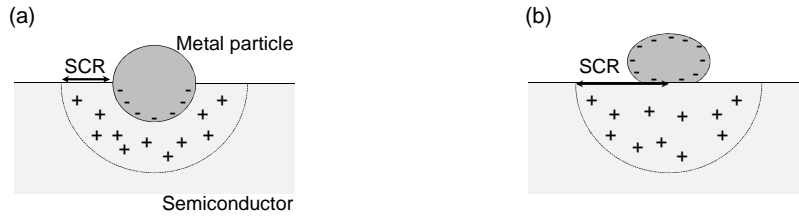


**Figure 1-19.** The charge distribution at the metal particle-*n*-type semiconductor interface for (a) the unstable conditions with an electric field inside the particle and (b) the stable conditions with the distribution of charges over the whole particle surface.

The amount of charge carriers that are transferred to the metal by the Schottky contact is smaller in the case of stable conditions and the number of transferred electrons to the metal and the depletion length can be calculated from Equation 1-13 and Equation 1-14.<sup>[144]</sup>

$$n_e \cong 4\pi\epsilon_0 r \frac{\Delta E_F}{e^2} \quad (\text{Equation 1-13})$$

$$l_{SCR} \cong \left( \frac{6\epsilon_0 r \Delta E_F}{e^2 N_d} \right)^{\frac{1}{3}} \quad (\text{Equation 1-14})$$

Where  $n_e$  is the number of electrons,  $r$  the particle radius,  $E_F$  the Fermi level,  $e$  the electron charge,  $l_{SCR}$  the depletion length, and  $N_d$  the donor concentration of the semiconductor.

In addition to the charge redistribution between the metal particle and the semiconductor after the Schottky contact formation, the optical excitation of the underlying semiconductor, for example, is supposed to induce an additional rearrangement of charge carriers at the metal-semiconductor interface and thus, at the metal particle surface, where catalytic surface reactions occur.

## 1.5 References

- [1] J. M. Thomas, W. J. Thomas, *Principles and Practice of Heterogeneous Catalysis*, Wiley-VCH: Weinheim, **1996**.
- [2] P. T. Anastas, J. C. Warner, *Green Chemistry: Theory and Practice*, Oxford University Press: New York, **1998**.
- [3] I. Chorkendorff, J. W. Niemantsverdriet, *Concepts of Modern Catalysis and Kinetics*, WILEY-VCH Verlag GmbH & Co. KGaA: Weinheim, **2003**.
- [4] Q. Fu, T. Wagner, *Surf. Sci. Rep.* **2007**, 62, 431.
- [5] G. Larsen, G. L. Haller, *Catal. Lett.* **1989**, 3, 103.
- [6] D. E. Resasco, G. L. Haller, *J. Catal.* **1983**, 82, 279.
- [7] G. M. Schwab, J. Block, W. Müller, D. Schultze, *Naturwissenschaften* **1957**, 44, 582.
- [8] G. M. Schwab, G. Mutzbauer, *Naturwissenschaften* **1959**, 46, 13.
- [9] J. de Graaf, A. J. van Dillen, K. P. de Jong, D. C. Koningsberger, *J. Catal.* **2001**, 203, 307.
- [10] M. Englisch, A. Jentys, J. A. Lercher, *J. Catal.* **1997**, 166, 25.
- [11] A. Dandekar, M. A. Vannice, *J. Catal.* **1999**, 183, 344.
- [12] W. Schottky, *Z. Phys.* **1939**, 113, 367.
- [13] S. S. Shinde, C. H. Bhosale, K. Y. Rajpure, *J. Mol. Catal. A-Chem.* **2011**, 347, 65.
- [14] B. Srinivas, P. A. K. Reddy, M. Rajesh, V. D. Kumari, M. Subrahmanyam, B. R. De, *Res. Chem. Intermediat.* **2011**, 37, 901.
- [15] Q. Zhang, Y. Li, E. A. Ackerman, M. Gajdardziska-Josifovska, H. Li, *Appl. Catal. A-Gen.* **2011**, 400, 195.
- [16] K. Maeda, K. Domen, *Chem. Mater.* **2010**, 22, 612.
- [17] R. Abe, *Bull. Chem. Soc. Jpn.* **2011**, 84, 1000.
- [18] R. Asahi, T. Morikawa, T. Ohwaki, K. Aoki, Y. Taga, *Science* **2001**, 293, 269.
- [19] C. Xiaobo, L. Lei, P. Y. Yu, S. S. Mao, *Science* **2011**, 331, 746.
- [20] K. Maeda, T. Takata, M. Hara, N. Saito, Y. Inoue, H. Kobayashi, K. Domen, *J. Am. Chem. Soc.* **2005**, 127, 8286.
- [21] K. Maeda, K. Teramura, D. L. Lu, T. Takata, N. Saito, Y. Inoue, K. Domen, *Nature* **2006**, 440, 295.
- [22] S. Sato, J. M. White, *Chem. Phys. Lett.* **1980**, 72, 83.
- [23] S. Nakamura, M. Senoh, T. Mukai, *Jpn. J. Appl. Phys.* **1991**, 30, L1708.
- [24] F. A. Ponce, D. P. Bour, *Nature* **1997**, 386, 351.
- [25] P. G. Neudeck, R. S. Okojie, L. Y. Chen, *P. IEEE* **2002**, 90, 1065.
- [26] J. L. Hudgins, G. S. Simin, E. Santi, M. A. Khan, *IEEE T. Power Electr.* **2003**, 18, 907.
- [27] M. Ali, V. Cimalla, V. Lebedev, H. Romanus, V. Tilak, D. Merfeld, P. Sandvik, O. Ambacher, *Sensor Actuat. B-Chem.* **2006**, 113, 797.
- [28] J. Y. Park, G. A. Somorjai, *J. Vac. Sci. Technol. B* **2006**, 24, 1967.
- [29] G. A. Somorjai, J. Carrazza, *Ind. Eng. Chem. Fundamen.* **1986**, 25, 63.
- [30] G. L. Bezemer, J. H. Bitter, H. Kuipers, H. Oosterbeek, J. E. Holewijn, X. D. Xu, F. Kapteijn, A. J. van Dillen, K. P. de Jong, *J. Am. Chem. Soc.* **2006**, 128, 3956.

- [31] J. P. den Breejen, P. B. Radstake, G. L. Bezemer, J. H. Bitter, V. Froseth, A. Holmen, K. P. de Jong, *J. Am. Chem. Soc.* **2009**, *131*, 7197.
- [32] M. Grass, R. Rioux, G. Somorjai, *Catal. Lett.* **2009**, *128*, 1.
- [33] A. Giroirfendler, D. Richard, P. Gallezot, *Catal. Lett.* **1990**, *5*, 175.
- [34] R. Narayanan, M. A. El-Sayed, *Nano Lett.* **2004**, *4*, 1343.
- [35] G. A. Somorjai, *Catal. Lett.* **1990**, *7*, 169.
- [36] C. Bréchnignac, P. Houdy, M. Lahmani, C. Henry, in *Nanomaterials and Nanochemistry*, Springer Berlin Heidelberg, **2007**, p. 3.
- [37] C. R. Henry, *Prog. Surf. Sci.* **2005**, *80*, 92.
- [38] T. K. Galeev, N. N. Bulgakov, G. A. Savelieva, N. M. Popova, *React. Kinet. Catal. L.* **1980**, *14*, 61.
- [39] S. Harada, *J. Phys. Soc. Jpn.* **1997**, *66*, 2921.
- [40] F. W. Küster, A. Thiel, *Rechentafeln für die Chemische Analytik*, de Gruyter: Berlin; New York, **2002**.
- [41] J. P. Chen, L. L. Lim, *Chemosphere* **2002**, *49*, 363.
- [42] G. W. Busser, J. G. van Ommen, J. A. Lercher, *J. Phys. Chem. B* **1999**, *103*, 1651.
- [43] T. Teranishi, M. Hosoe, T. Tanaka, M. Miyake, *J. Phys. Chem. B* **1999**, *103*, 3818.
- [44] A. Roucoux, J. Schulz, H. Patin, *Chem. Rev.* **2002**, *102*, 3757.
- [45] T. Teranishi, I. Kiyokawa, M. Miyake, *Adv. Mater.* **1998**, *10*, 596.
- [46] F. Dassenoy, K. Philippot, T. Ould-Ely, C. Amiens, P. Lecante, E. Snoeck, A. Mosset, M. J. Casanove, B. Chaudret, *New J. Chem.* **1998**, *22*, 703.
- [47] D. S. Deutsch, G. Lafaye, D. X. Liu, B. Chandler, C. T. Williams, M. D. Amiridis, *Catal. Lett.* **2004**, *97*, 139.
- [48] C. Bock, C. Paquet, M. Couillard, G. A. Botton, B. R. MacDougall, *J. Am. Chem. Soc.* **2004**, *126*, 8028.
- [49] H. S. Oh, J. G. Oh, Y. G. Hong, R. K. Sharma, Y. G. Shul, H. Kim, *Res. Chem. Intermediat.* **2008**, *34*, 853.
- [50] Y. Borodko, S. M. Humphrey, T. D. Tilley, H. Frei, G. A. Somorjai, *J. Phys. Chem. C* **2007**, *111*, 6288.
- [51] G. G. Couto, J. J. Klein, W. H. Schreiner, D. H. Mosca, A. J. A. de Oliveira, A. J. G. Zarbin, *J. Colloid Interf. Sci.* **2007**, *311*, 461.
- [52] M. M. Koebel, L. C. Jones, G. A. Somorjai, *J. Nanopart. Res.* **2008**, *10*, 1063.
- [53] S. M. Humphrey, M. E. Grass, S. E. Habas, K. Niesz, G. A. Somorjai, T. D. Tilley, *Nano Lett.* **2007**, *7*, 785.
- [54] J. D. Hoefelmeyer, K. Niesz, G. A. Somorjai, T. D. Tilley, *Nano Lett.* **2005**, *5*, 435.
- [55] Y. W. Zhang, M. E. Grass, J. N. Kuhn, F. Tao, S. E. Habas, W. Y. Huang, P. D. Yang, G. A. Somorjai, *J. Am. Chem. Soc.* **2008**, *130*, 5868.
- [56] Y. J. Xiong, H. G. Cai, B. J. Wiley, J. G. Wang, M. J. Kim, Y. N. Xia, *J. Am. Chem. Soc.* **2007**, *129*, 3665.
- [57] H. Song, F. Kim, S. Connor, G. A. Somorjai, P. D. Yang, *J. Phys. Chem. B* **2005**, *109*, 188.
- [58] S. Link, M. A. El-Sayed, *Int. Rev. Phys. Chem.* **2000**, *19*, 409.
- [59] D. Philip, *Spectrochim. Acta A* **2008**, *71*, 80.
- [60] S. K. Ghosh, T. Pal, *Chem. Rev.* **2007**, *107*, 4797.



- [61] A. Henglein, *J. Phys. Chem.* **1993**, *97*, 5457.
- [62] N. C. Bigall, T. Hartling, M. Klose, P. Simon, L. M. Eng, A. Eychmuller, *Nano Lett.* **2008**, *8*, 4588.
- [63] Y. Yamamoto, T. Miura, Y. Nakae, T. Teranishi, M. Miyake, H. Hori, *Physica B* **2003**, *329*, 1183.
- [64] H. Hori, T. Teranishi, Y. Nakae, Y. Seino, M. Miyake, S. Yamada, *Phys. Lett. A* **1999**, *263*, 406.
- [65] X. Y. Du, M. Inokuchi, N. Toshima, *J. Magn. Magn. Mater.* **2006**, *299*, 21.
- [66] C. N. R. Rao, G. U. Kulkarni, A. Govindaraj, B. C. Satishkumar, P. J. Thomas, *Pure Appl. Chem.* **2000**, *72*, 21.
- [67] W. P. Halperin, *Rev. Mod. Phys.* **1986**, *58*, 533.
- [68] Y. Volokitin, J. Sinzig, L. J. deJongh, G. Schmid, M. N. Vargaftik, I. I. Moiseev, *Nature* **1996**, *384*, 621.
- [69] D. M. Wood, *Phys. Rev. Lett.* **1981**, *46*, 749.
- [70] K. R. Lawless, *Rep. Prog. Phys.* **1974**, *37*, 231.
- [71] N. Seriani, W. Pompe, L. C. Ciacchi, *J. Phys. Chem. B* **2006**, *110*, 14860.
- [72] M. Salmeron, L. Brewer, G. A. Somorjai, *Surf. Sci.* **1981**, *112*, 207.
- [73] P. Legare, G. Lindauer, L. Hilaire, G. Maire, J. J. Ehrhardt, J. Jupille, A. Cassuto, C. Guillot, J. Lecante, *Surf. Sci.* **1988**, *198*, 69.
- [74] C. B. Wang, H. K. Lin, S. N. Hsu, T. H. Huang, H. C. Chiu, *J. Mol. Catal. A-Chem.* **2002**, *188*, 201.
- [75] C. B. Wang, C. T. Yeh, *J. Catal.* **1998**, *178*, 450.
- [76] N. Seriani, F. Mittendorfer, *J. Phys-Condens. Mat.* **2008**, *20*, 184023.
- [77] K. Hayek, H. Goller, S. Penner, G. Rupprechter, C. Zimmermann, *Catal. Lett.* **2004**, *92*, 1.
- [78] Z. Y. Li, P. Beck, D. A. A. Ohlberg, D. R. Stewart, R. S. Williams, *Surf. Sci.* **2003**, *529*, 410.
- [79] M. K. Oudenhuijzen, J. A. van Bokhoven, J. T. Miller, D. E. Ramaker, D. C. Koningsberger, *J. Am. Chem. Soc.* **2005**, *127*, 1530.
- [80] D. C. Koningsberger, M. K. Oudenhuijzen, J. de Graaf, J. A. van Bokhoven, D. E. Ramaker, *J. Catal.* **2003**, *216*, 178.
- [81] J. Barbier, D. Bahloul, P. Marecot, *J. Catal.* **1992**, *137*, 377.
- [82] J. T. Miller, B. L. Meyers, F. S. Modica, G. S. Lane, M. Vaarkamp, D. C. Koningsberger, *J. Catal.* **1993**, *143*, 395.
- [83] S. Penner, D. Wang, D. S. Su, G. Rupprechter, R. Podloucky, R. Schlogl, K. Hayek, *Surf. Sci.* **2003**, *532*, 276.
- [84] G. L. Haller, D. E. Resasco, *Adv. Catal.* **1989**, *36*, 173.
- [85] A. Y. Stakheev, Y. M. Shulga, N. A. Gaidai, N. S. Telegina, O. P. Tkachenko, L. M. Kustov, K. M. Minachev, *Mendeleev Commun.* **2001**, *11*, 186.
- [86] F. Dominguez, G. Carruyo, R. Andrade, R. Solano, D. Rodriguez, J. Sanchez, G. Arteaga, *Catal. Lett.* **2008**, *123*, 207.
- [87] N. A. Gaidai, R. V. Kazantsev, N. V. Nekrasov, Y. M. Shulga, I. N. Ivleva, S. L. Kiperman, *React. Kinet. Catal. L.* **2002**, *75*, 55.

- [88] E. Gebauer-Henke, J. Grams, E. Szubiakiewicz, J. Farbotko, R. Touroude, J. Rynkowski, *J. Catal.* **2007**, *250*, 195.
- [89] R. W. McCabe, C. Wong, H. S. Woo, *J. Catal.* **1988**, *114*, 354.
- [90] A. K. Datye, Q. Xu, K. C. Kharas, J. M. McCarty, *Catal. Today* **2006**, *111*, 59.
- [91] H. Lieske, G. Lietz, H. Spindler, J. Völter, *J. Catal.* **1983**, *81*, 8.
- [92] G. Lietz, H. Lieske, H. Spindler, W. Hanke, J. Völter, *J. Catal.* **1983**, *81*, 17.
- [93] S. Nakamura, T. Mukai, M. Senoh, *Jpn. J. Appl. Phys.* **1991**, *30*, L1998.
- [94] S. L. Nguyen, T. N. N. Nguyen, V. T. Chau, M. C. Dang, *Adv. Nat. Sci.: Nanosci. Nanotechnol.* **2010**, *1*, 025015.
- [95] <http://bridgelux.com/media-center/category/press-releases/>.
- [96] A. A. Bergh, *Phys. Status Solidi A* **2004**, *201*, 2740.
- [97] <http://www.ostendo.com/gan/applications.php#solar>.
- [98] S. Kang, H. T. Wang, F. Ren, M. Hlad, B. P. Gila, C. R. Abernathy, S. J. Pearton, C. Li, Z. N. Low, J. Lin, J. W. Johnson, P. Rajagopal, J. C. Roberts, E. L. Piner, K. J. Linthicum, *J. Electron. Mater.* **2008**, *37*, 550.
- [99] <http://www.physorg.com/news183300565.html>.
- [100] Y. Niiyama, T. Shinagawa, S. Ootomo, H. Kambayashi, T. Nomura, S. Kato, *Furukawa Review* **2009**, *36*, 1.
- [101] B. Baur, G. Steinhoff, J. Hernando, O. Purrucker, M. Tanaka, B. Nickel, M. Stutzmann, M. Eickhoff, *Appl. Phys. Lett.* **2005**, *87*, 263901.
- [102] M. Stutzmann, J. A. Garrido, M. Eickhoff, M. S. Brandt, *Phys. Status Solidi A* **2006**, *203*, 3424.
- [103] J. Howgate, S. J. Schoell, M. Hoeb, W. Steins, B. Baur, S. Hertrich, B. Nickel, I. D. Sharp, M. Stutzmann, M. Eickhoff, *Adv. Mater.* **2010**, *22*, 2632.
- [104] F. Furtmayr, M. Vielemeyer, M. Stutzmann, J. Arbiol, S. Estrade, F. Peiro, J. R. Morante, M. Eickhoff, *J. Appl. Phys.* **2008**, *104*, 034309.
- [105] F. Furtmayr, M. Vielemeyer, M. Stutzmann, A. Laufer, B. K. Meyer, M. Eickhoff, *J. Appl. Phys.* **2008**, *104*, 074309.
- [106] G. W. Tomlins, J. L. Routbort, T. O. Mason, *J. Appl. Phys.* **2000**, *87*, 117.
- [107] C. Liu, A. Wenzel, B. Rauschenbach, E. Alves, A. D. Sequeira, N. Franco, M. F. da Silva, J. C. Soares, X. J. Fan, *Nucl. Instrum. Meth. B* **2001**, *178*, 200.
- [108] A. M. Ruiz, G. Sakai, A. Cornet, K. Shimano, J. R. Morante, N. Yamazoe, *Sensor Actuat. B-Chem.* **2003**, *93*, 509.
- [109] G. Liu, L. Z. Wang, H. G. Yang, H. M. Cheng, G. Q. Lu, *J. Mater. Chem.* **2010**, *20*, 831.
- [110] H. P. Maruska, J. J. Tietjen, *Appl. Phys. Lett.* **1969**, *15*, 327.
- [111] A. F. Holleman, E. Wiberg, *Lehrbuch der Anorganischen Chemie*, De Gruyter: New York, Berlin, **1995**.
- [112] C. Kittel, *Introduction to Solid State Physics*, John Wiley & Sons, Inc.: New York, **2005**.
- [113] S. Strite, H. Morkoc, *J. Vac. Sci. Technol. B* **1992**, *10*, 1237.
- [114] J. Neugebauer, C. G. Van de Walle, *Phys. Rev. B* **1994**, *50*, 8067.
- [115] G. Ecke, M. Niebelschütz, R. Kosiba, U. Rossow, V. Cimalla, J. Liday, P. Vogrincic, J. Pezoldt, V. Lebedev, O. Ambacher, *J. Electr. Eng.* **2006**, *57*, 354.

- [116] W. Götz, N. M. Johnson, C. Chen, H. Liu, C. Kuo, W. Imler, *Appl. Phys. Lett.* **1996**, *68*, 3144.
- [117] W. Götz, N. M. Johnson, J. Walker, D. P. Bour, R. A. Street, *Appl. Phys. Lett.* **1996**, *68*, 667.
- [118] W. C. Johnson, J. B. Parsons, M. C. Crew, *J. Phys. Chem.* **1932**, *36*, 2651.
- [119] W. J. Fan, M. F. Li, T. C. Chong, J. B. Xia, *Solid State Commun.* **1996**, *97*, 381.
- [120] A. R. Smith, R. M. Feenstra, D. W. Greve, J. Neugebauer, J. E. Northrup, *Phys. Rev. Lett.* **1997**, *79*, 3934.
- [121] M. Stutzmann, O. Ambacher, M. Eickhoff, U. Karrer, A. L. Pimenta, R. Neuberger, J. Schalwig, R. Dimitrov, P. J. Schuck, R. D. Grober, *Phys. Status Solidi B* **2001**, *228*, 505.
- [122] L. Kronik, Y. Shapira, *Surf. Sci. Rep.* **1999**, *37*, 1.
- [123] U. Karrer, O. Ambacher, M. Stutzmann, *Appl. Phys. Lett.* **2000**, *77*, 2012.
- [124] I. Shalish, Y. Shapira, L. Burstein, J. Salzman, *J. Appl. Phys.* **2001**, *89*, 390.
- [125] W. Grieshaber, E. F. Schubert, I. D. Goepfert, R. F. Karlicek, M. J. Schurman, C. Tran, *J. Appl. Phys.* **1996**, *80*, 4615.
- [126] K. Prabhakaran, T. G. Andersson, K. Nozawa, *Appl. Phys. Lett.* **1996**, *69*, 3212.
- [127] T. K. Zywietz, J. Neugebauer, M. Scheffler, *Appl. Phys. Lett.* **1999**, *74*, 1695.
- [128] O. Janzen, C. Hahn, W. Mönch, *Eur. Phys. J. B* **1999**, *9*, 315.
- [129] N. J. Watkins, G. W. Wicks, Y. L. Gao, *Appl. Phys. Lett.* **1999**, *75*, 2602.
- [130] M. A. Garcia, S. D. Wolter, T. H. Kim, S. Choi, J. Baier, A. Brown, M. Losurdo, G. Bruno, *Appl. Phys. Lett.* **2006**, *88*, 013506.
- [131] S. D. Wolter, J. M. DeLucca, S. E. Mohny, R. S. Kern, C. P. Kuo, *Thin Solid Films* **2000**, *371*, 153.
- [132] O. Weidemann, E. Monroy, E. Hahn, M. Stutzmann, M. Eickhoff, *Appl. Phys. Lett.* **2005**, *86*, 083507.
- [133] L. L. Smith, S. W. King, R. J. Nemanich, R. F. Davis, *J. Electron. Mater.* **1996**, *25*, 805.
- [134] S. W. King, J. P. Barnak, M. D. Bremser, K. M. Tracy, C. Ronning, R. F. Davis, R. J. Nemanich, *J. Appl. Phys.* **1998**, *84*, 5248.
- [135] Q. Z. Liu, S. S. Lau, *Solid State Electron.* **1998**, *42*, 677.
- [136] J. Y. Park, H. Lee, J. R. Renzas, Y. Zhang, G. A. Somorjai, *Nano Lett.* **2008**, *8*, 2388.
- [137] W. Mönch, *J. Vac. Sci. Technol. B* **1999**, *17*, 1867.
- [138] L. Wang, M. I. Nathan, T. H. Lim, M. A. Khan, Q. Chen, *Appl. Phys. Lett.* **1996**, *68*, 1267.
- [139] K. M. Tracy, P. J. Hartlieb, S. Einfeldt, R. F. Davis, E. H. Hurt, R. J. Nemanich, *J. Appl. Phys.* **2003**, *94*, 3939.
- [140] K. Suzue, S. N. Mohammad, Z. F. Fan, W. Kim, O. Aktas, A. E. Botchkarev, H. Morkoc, *J. Appl. Phys.* **1996**, *80*, 4467.
- [141] A. C. Schmitz, A. T. Ping, M. A. Khan, Q. Chen, J. W. Yang, I. Adesida, *Semicond. Sci. Tech.* **1996**, *11*, 1464.
- [142] O. Cojocari, H. L. Hartnagel, *J. Vac. Sci. Technol. B* **2006**, *24*, 2544.
- [143] T. Ioannides, X. E. Verykios, *J. Catal.* **1996**, *161*, 560.
- [144] V. P. Zhdanov, *Surf. Sci.* **2002**, *512*, L331.

# Chapter 2

## Experimental Methods

### Abstract

The following section describes the experimental methods, which were used to synthesize and characterize the GaN-based Pt catalysts. A new preparation procedure was developed for the deposition of metal particles onto semiconductor surfaces. *Ex situ* techniques like transmission electron microscopy and atomic force microscopy were used to evaluate the metal particle size and shape in solution, as well as their distribution on the GaN surface after deposition. *In situ* synchrotron methods like small-angle X-ray scattering, X-ray absorption, and X-ray photoelectron spectroscopy were performed to study the particle shape changes, metal oxidation state, and the Pt-GaN interface under reactive conditions like reduction, oxidation, and ethene hydrogenation. A special reactor was operated in the external recycle mode to test the Pt-GaN catalysts in the hydrogenation of ethene to ethane with and without the optical excitation of the semiconductor support.

## 2 Experimental Methods

### 2.1 Catalyst Preparation

The general procedure to prepare the Pt-GaN catalysts involved the synthesis of polymer-protected Pt particles in solution, their spin-coating onto the cleaned, *n*- and *p*-type GaN surfaces, and the subsequent oxygen plasma treatment for the evaporation of the polymer (Figure 2-1). A further heating to moderate temperature established sufficient adhesion strength between the particles and the semiconductor.

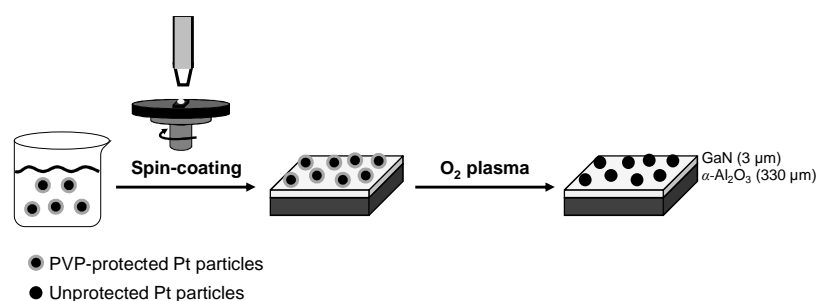


**Figure 2-1.** Model catalyst preparation: Spin-coating of PVP-protected Pt particles onto GaN surfaces and oxygen plasma treatment for polymer removal.

Poly(*N*-vinyl-2-pyrrolidone) (PVP) was used as the polymer to prevent the agglomeration of the particles in solution and its amount controlled the final nanoparticle size. The colloidal solutions exhibited various Pt particle sizes and shapes with defined Pt concentrations, which were spin-coated onto the GaN surfaces. The spin-coating provided an alternative deposition method for planar catalysts, which yielded homogeneous and reproducible particle distributions of a monolayer. The amount of deposited metal could be tuned by the metal concentration in solution, as well as the spin-coating parameters. Particle agglomeration and multilayer deposition was only observed for very high-concentrated particle solutions. The oxygen plasma was adjusted to ensure the complete removal of the polymer capping, which was determined by thermal deposition spectroscopy. The activation of the particles by the reduction in hydrogen was performed *in situ* or *ex situ*, which was dependent on the sample application and/or characterization.

## 2.1.1 Chemicals and Materials

All chemicals and materials were utilized without further purification (Table 2-1).

**Table 2-1.** Chemicals and materials used for the catalyst preparation.

Compound	Purity	Company
Hexachloroplatinic acid solution	8 wt% in water	Sigma-Aldrich
Poly( <i>N</i> -vinyl-2-pyrrolidone) ( $M_w = 40\,000$ and $55\,000\text{ g mol}^{-1}$ )	-	
1-Propanol	99.7%	
Acetone	$\geq 99.5\%$	
<i>n</i> -Hexane	-	
Silver nitrate	$> 99\%$	
Ethanol	99%	Merck
2-Propanol	$\geq 99.5\%$	
Nitric acid	$> 65\%$ in water	Fluka
Ethylene glycol	$\geq 99.5\%$	
Hydrochloric acid	32% in water	Riedel-de Haën
MOCVD <i>n</i> -type GaN (Si concentration: $2 \times 10^{18}\text{ cm}^{-3}$ )	-	Lumilog Group St Gobain Crystals
PAMBE <i>p</i> -type GaN (Mg concentration: $4 \times 10^{17}\text{ cm}^{-3}$ )	-	TopGaN Blue Laser Technologies
MOCVD <i>p</i> -type GaN (Mg concentration: $5 \times 10^{17}\text{ cm}^{-3}$ )	-	Fraunhofer-Institut für Angewandte Festkörperphysik

## 2.1.2 Platinum Nanoparticle Synthesis

Two different approaches were applied to synthesize polymer-capped, size- and shape-selected Pt particles. The reduction of the metal precursor by an alcohol or hydrogen was used to prepare particles with a defined particle size, while different particle geometries of comparable diameters were achieved by the polyol method.

Spherical, 2 nm-sized Pt particles were prepared by the alcohol/hydrogen reduction that was modified from the method of Busser *et al.*<sup>[1]</sup>. An aqueous solution (bidistilled water  $> 18.2\text{ M}\Omega\text{-cm}$ , 20 ml) of hexachloroplatinic acid (0.057 mmol) and PVP (2.0 mmol monomer,  $M_w = 40\,000\text{ g mol}^{-1}$ ) was stirred at 373 K for 2 h to achieve sufficient interactions between the Pt ions and the polymer. Subsequently, 1-propanol (130 ml) was added as

reducing agent at the same temperature and the solvent was evaporated after stirring for 48 h at 373 K. The formed brown residue was washed with ethanol (20 ml) and finally re-dispersed in ethanol (20 ml, Pt concentration of 2.85 mmol l<sup>-1</sup>).

The particle size was tuned by changing the amount of PVP, the amount of reduction agent, and the kind of reduction agent (methanol, ethanol, 1-propanol) (Table 2-2). The diameter was determined by transmission electron microscopy (TEM, description in 2.2.1) and was found to decrease with decreasing Pt to PVP molar ratio (from 1:35 to 1:70) and with increasing concentration of 1-propanol (from alcohol to water volume ratio of 6.5:1, 10:1, to 20:1). A slightly higher particle size was observed when methanol was used.

**Table 2-2.** Synthesis parameters for spherical, size-selected Pt particles during the alcohol/hydrogen reduction. The average particle size was determined by TEM.

Pt to PVP molar ratio	Reduction agent	Alcohol to water volume ratio	Average particle size / nm
1:10	1-Propanol	6.5:1	2.0 ± 0.4
1:35	1-Propanol	6.5:1	2.0 ± 0.3
1:70	1-Propanol	6.5:1	1.7 ± 0.3
1:35	Ethanol	6.5:1	2.0 ± 0.4
1:35	Methanol	6.5:1	2.2 ± 0.4
1:35	1-Propanol	10:1	1.9 ± 0.3
1:35	1-Propanol	20:1	1.6 ± 0.3
1:35	Hydrogen	6.5:1	1.2 ± 0.3

The same synthesis procedure was modified to yield very small particles of 1 nm using hydrogen for the reduction of the Pt precursor, which has a higher reduction strength than the alcohol. The synthesis setup was flushed initially with nitrogen gas (1 bar) during the interaction period in water at 373 K for 2 h. Subsequently, hydrogen (1 bar) was introduced via bubbling through the solution for 41 h at 343 K before cooling to room temperature and flushing again with nitrogen after the reaction. All further steps for the particle separation were performed like described for the reduction with alcohol.

Large, 7 nm-sized Pt particles without a specific shape were prepared by the polyol process according to Rioux *et al.*<sup>[2]</sup> Ethylene glycol (2.5 ml) was heated to 473 K and solutions of PVP (1.125 mmol monomer) in ethylene glycol (3 ml) and hexachloroplatinic acid (0.094 mmol) in ethylene glycol (1.5 ml) were alternately added every 30 s. The mixture was refluxed at 473 K for 5 min and the particles were precipitated with acetone (21 ml) and

separated by centrifugation (4000 rpm, 293 K, 45 min). The residue was re-dispersed in ethanol (20 ml, Pt concentration of  $4.69 \text{ mmol l}^{-1}$ ).

Another polyol method was used to achieve shape-selected, large particles with cubic, cuboctahedral, and octahedral geometry and a mean particle size of 8-13 nm. The addition of silver nitrate directed the particle growth along the  $\langle 100 \rangle$  direction, resulting in particle geometries with solely  $\{111\}$  facets at high silver ion concentrations.<sup>[3]</sup> Ethylene glycol (2.5 ml) was refluxed at 473 K for 5 min before silver nitrate ( $1.0 \times 10^{-3}$  mmol for cubes,  $1.0 \times 10^{-2}$  mmol for cuboctahedra, and  $3.0 \times 10^{-2}$  mmol for octahedra) was added. Ethylene glycol solutions of PVP (1.125 mmol monomer,  $M_w = 40\,000 \text{ g mol}^{-1}$ , 3 ml) and hexachloroplatinic acid (0.094 mmol, 1.5 ml) were alternately added to the silver nitrate solution every 30 s for 17 min. The mixture was refluxed for 5 min and centrifuged (4000 rpm, 283 K, 30 min) to remove silver chloride. The particles were precipitated from the supernatant by adding acetone (23 ml) and separated by centrifugation (3000 rpm, 283 K, 5 min). The particles were dispersed in ethanol (3 ml) in an ultrasonic bath (15 min) and *n*-hexane (9 ml) was added to wash out residual silver ions. The particles were separated again by centrifugation (3000 rpm, 283 K, 5 min). This washing procedure was repeated for additional two times and the particles were finally re-dispersed in ethanol (3 ml, Pt concentration of  $31.3 \text{ mmol l}^{-1}$ ). The yield of cubes, cuboctahedra, and octahedra was 90%, 51%, and 74%, respectively (Table 2-3).

The synthesis of particles with cuboctahedral geometry was repeated with a decreasing amount of silver nitrate ( $5.5 \times 10^{-3}$  mmol) and higher molecular weight of PVP ( $M_w = 55\,000 \text{ g mol}^{-1}$ ) to increase the yield of cuboctahedra from 51% to > 88%.

**Table 2-3.** Particle size and yield of large, shape-selected Pt particles prepared by the polyol process using defined silver nitrate amounts to control the shape. The analysis was performed with TEM.

Particle shape	Silver nitrate / $\times 10^{-3}$ mmol	Average particle size / nm	Shape yield
Cubes	1.0	$7.6 \pm 0.8$	90% Cubes, 10% Tetrahedra
Cuboctahedra	10	$9.7 \pm 0.9$	51% Cuboctahedra, 23% Tetrahedra, 16% Octahedra, 10% Polyhedra
	5.5	$8.1 \pm 0.9$	98% Cuboctahedra, 2% Polyhedra
	5.5	$8.9 \pm 0.7$	88% Cuboctahedra, 12% Tetrahedra
Octahedra	30	$12.7 \pm 1.6$	74% Octahedra, 13% Cuboctahedra, 8% Tetrahedra, 5% Polyhedra



### 2.1.3 Spin-coating

Colloidal particle solutions were deposited onto *n*- and *p*-type GaN surfaces by spin-coating. For cleaning, the GaN substrates were washed in acetone (ultrasonic bath, 10 min) and rinsed with 2-propanol. Typically, Ga-faced *n*- and *p*-type GaN surfaces were used except for some samples, where N-faced *n*-type GaN catalysts were prepared e.g. for X-ray photoemission experiments. Pt solutions with defined metal concentrations in ethanol (Table 2-4) were dropped onto the GaN surfaces (50  $\mu\text{l}$  for GaN edge length  $> 5 \times 5$  mm and 20  $\mu\text{l}$  for  $< 5 \times 5$  mm) and spin-coated at 3000 rpm for 60 s. The excess solvent was evaporated by heating the samples to 363 K for 5 min and the PVP-capping was removed afterwards by oxygen plasma with an oxygen pressure of 1.4 mbar at 200 W for 5 min (TePla 100-E, Technics Plasma GmbH). The samples were moderately heated to 423 K in nitrogen (100 mbar) or in vacuum for 15 min to increase the adhesion between the particles and GaN. The spin-coating rotation speed of 3000 rpm and rotation time of 60 s were found to provide a homogeneous and reproducible particle distribution on the GaN surface, which was probed by atomic force microscopy (consider 2.2.2). The particle adhesion was tested under mechanical strain and high adhesive forces were found between Pt and GaN.<sup>[4]</sup>

**Table 2-4.** Pt-GaN catalysts prepared by spin-coating.

Pt particles	Pt concentration for spin-coating / mol l <sup>-1</sup>	GaN surface (edge length / mm)	Pt coverage on GaN surface / %ML <sup>(a)</sup>
Spheres (1.8 nm)	$2.5 \times 10^{-4}$	<i>n</i> -type (8 × 8)	1.6
Spheres (2.0 nm)	$6.2 \times 10^{-4}$	<i>n</i> -type (5 × 5)	2.0
		<i>p</i> -type (3.5 × 3.5)	2.5
Unshaped (6.7 nm)	$6.6 \times 10^{-4}$	<i>n</i> -type (8 × 8)	1.6
Cubes (7.6 nm)	$2.4 \times 10^{-3}$	<i>n</i> -type (5 × 5)	16
		<i>p</i> -type (3.5 × 3.5)	17
Cuboctahedra (8.1 nm)	$2.4 \times 10^{-3}$	<i>n</i> -type (5 × 5) <sup>(b)</sup>	16
		<i>p</i> -type (2 × 4)	17
Cuboctahedra (8.9 nm)	$2.4 \times 10^{-3}$	<i>n</i> -type (9 × 9)	7.4
		<i>p</i> -type (9 × 9)	8.7

<sup>(a)</sup> The percentage of a monolayer (%ML) was calculated combining the particle size and shape and the particle coverage (calculation described in 2.2.2). <sup>(b)</sup> Ga-face and N-face *n*-type GaN substrates were used.

The spin-coating process includes generally four stages (Figure 2-2). First, a droplet of the colloidal solution is pipetted onto the substrate surface, which spreads out into a film during spinning and most of the suspension is spun off. The steady state is reached as soon as both the centrifugal and viscous shear forces are equilibrated and the volumetric flow rate  $Q$  becomes constant. At a sufficiently small film thickness, the evaporation of the solvent is dominant, which increases simultaneously the particle concentration of the film.<sup>[5, 6]</sup>

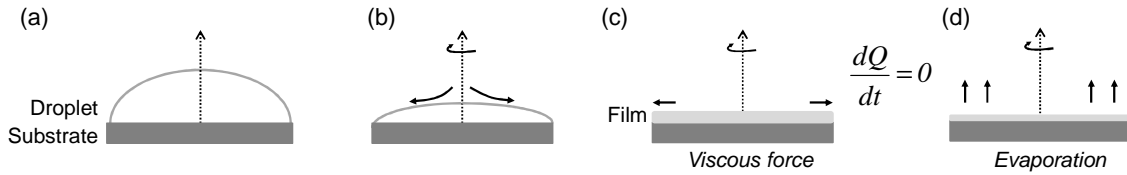


**Figure 2-2.** Spin-coating process including (a) droplet dispersion on the substrate, (b) droplet spreading during acceleration, (c) steady state dominated by viscous force, and (d) steady state dominated by film evaporation.

The steady state period that is dominated by the viscous force affects mainly the final particle distribution on the substrate. As the film thickness is reduced to the size range of the particles, the capillary forces arise that may lead to particle aggregation. The film thickness decreases with increasing spin-coating time at a constant rotation speed (Equation 2-1).<sup>[5]</sup>

$$h(t) = \frac{h_0}{\sqrt{1 + 4Kh_0^2 t}} \quad \text{with} \quad K = \frac{1}{3} Re_F \left( \frac{\Omega L}{U} \right)^2 \quad (\text{Equation 2-1})$$

Where  $h(t)$  is the film thickness at time  $t$ ,  $h_0$  the initial film thickness,  $Re_F$  the Reynolds number of the film,  $\Omega$  the rotation rate,  $U$  the horizontal fluid velocity, and  $L$  the horizontal fluid length.

The acceleration by gravity is significantly small in comparison to the centrifugal force and can be neglected. The dynamics of the film formation and thinning are generally dependent on various effects, e.g. the momentum, mass, and energy transport, which increase the complexity of an empirical process description. Additionally, radial striations can appear at certain conditions and avoid the formation of a uniform film. This is attributed to gradients in the surface tension (Marangoni effect), when the evaporative convection becomes the dominant force.<sup>[7]</sup>

In summary, spin-coating presents an alternative procedure to e.g. Langmuir-Blodgett films to deposit metal particles onto planar surfaces, preparing array-like surfaces functionalized with a particle monolayer under well-controlled conditions.

## **2.2 *Ex situ* Characterization**

The properties of the Pt-GaN catalysts like the Pt nanoparticle size before and after deposition onto GaN, as well as the areal distribution of the particles over the surface were analyzed with *ex situ* methods. Transmission electron microscopy was performed in vacuum, while the samples were measured in environmental atmosphere by atomic force microscopy.

### **2.2.1 Transmission Electron Microscopy (TEM)**

The colloidal, PVP-capped Pt solutions were analyzed with TEM (JEOL JEM-2010, Institute of Electron Microscopy, TUM) with an electron acceleration voltage of 120 kV. Various magnifications (100 000-300 000) were used to determine the particle size and shape. The micrographs were collected with a CCD camera. The particle solution was diluted with ethanol and dispersed in an ultrasonic bath (15 min) prior to the deposition onto copper grids (10  $\mu$ l), which were coated with a 2 nm carbon film (Quantifoil Micro Tools GmbH). The average particle size was evaluated from 150-500 particles using the software ImageJ. The diameter of the Pt particles was measured from their longest edge, while the central cubic edge was evaluated for octahedral particles.

The instrumental assembly of a TEM consists of an electron gun, condenser lenses, the sample object, an objective, as well as intermediate and projective lenses, a fluorescence screen, and the camera for imaging (Figure 2-3). The electron beam is generated by e.g. the thermionic emission of electrons from a cathode (tungsten wire) and the electrons are accelerated towards the anode while passing the Wehnelt cylinder for focusing, which provide a high beam intensity and refinement. The Schottky or field emission can be alternatively applied for the formation of the electron beam, which is normally used in electron microscopes with high resolution. After generation, the electron beam passes condenser lenses, which transform the bunched electron crossover onto the sample and facilitate the

variation of the spot size. A condenser aperture is inserted to reduce the beam intensity with a simultaneous increase in beam coherence. The objective lens after the sample focuses the transmitted electrons, while an objective aperture shields highly scattered electrons. The microscope resolution and contrast are both determined by the objective lens/aperture system. The following intermediate and projective lenses are used to adjust the optical magnification. The sample image is projected onto a fluorescence screen and finally collected with the camera. An electron acceleration voltage of 100-200 kV is usually used, while high-voltage instruments reach up to 3 MV, facilitating a much better transmission and resolution. The whole system requires high vacuum conditions ( $10^{-7}$  mbar) to prevent the interaction between electrons and gas molecules.<sup>[8, 9]</sup>

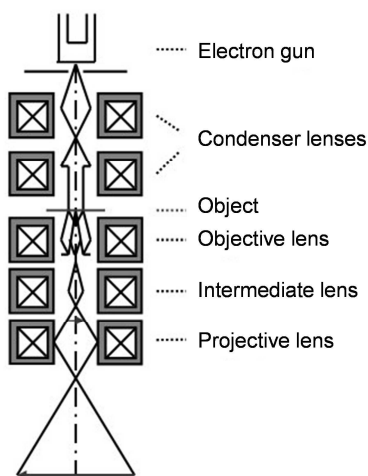


**Figure 2-3.** Assembly of a transmission electron microscope containing an electron gun, the sample object, and various electromagnetic lenses.<sup>[9]</sup>

The interaction of the electron beam with the sample determines the contrast of the TEM image. The electrons can be scattered on the atomic electron shell or on the nucleus. In the first case, inelastic scattering leads to an energy loss of the electrons, while the direction is not changed. The latter describes the elastic scattering without the loss of energy but with a significantly altered direction. The degree of scattering is affected by the sample mass or by the thickness and determines the contrast. Hence, the thinner the sample or the lower the atomic number of the contained elements, the poorer is the contrast. The quality of an image is obtained by an optimal adjustment of the electromagnetic lens system, which avoids optical errors like the spherical and chromatic aberration or astigmatism by minimizing the focal width. The TEM images are collected in two different modes. The insertion of an aperture into the back focal plane of the objective lens blocks a high fraction of diffracted electrons,

providing bright-field images of transmitted electrons. Contrary, dark-field images originate from the entity of scattered electrons.<sup>[8]</sup>

TEM is a suitable method to image small metal particles in the nm size range. As only a very small part of the sample is displayed and analyzed, a number of images have to be collected from different locations on the copper grid. Hundreds of particles should be counted for the evaluation of an average particle diameter and for the particle distribution. Additionally, the agglomeration of particles in solution cannot be totally excluded, when only isolated particles are imaged. The particle size, shape, and areal distribution after the deposition onto the GaN surfaces cannot be measured with TEM due to the GaN sample thickness. However, the so-called TEM windows (TEMwindows.com) facilitate transmission measurements of spin-coated metal particles. The windows consist of silica or silicon nitride and are etched from the back side to a thin film of 50 nm to establish transparency (Figure 2-4). Unfortunately, the windows are not of GaN and interactions between Pt and SiO<sub>2</sub> or Si<sub>3</sub>N<sub>4</sub> during spin-coating are different than the interaction between Pt and GaN, and the areal particle distributions cannot be compared.

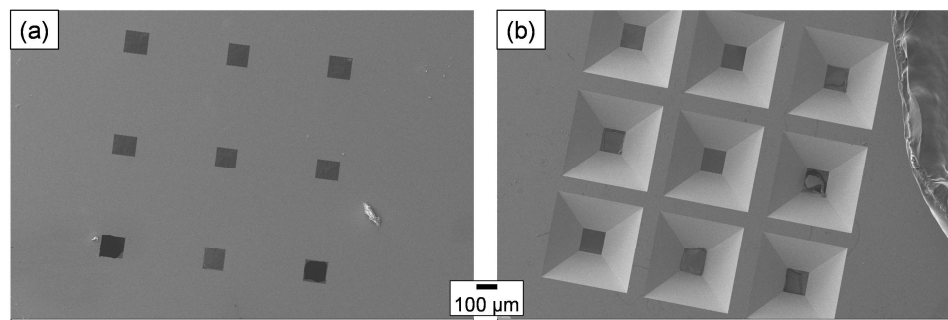


**Figure 2-4.** SEM images of silica-based TEM windows from (a) the top view with the thin film containing windows and (b) the bottom view showing the structures from etching.

In contrast to the copper grids, the TEM windows provide a high thermal stability, facilitating the imaging of the particles after an *ex situ* treatment at high-temperature oxidizing or reducing conditions. Cubic, cuboctahedral, and octahedral Pt particles showed a rounding of edges at 573 K in nitrogen and synthetic air (80 Vol% N<sub>2</sub>, 20 Vol% O<sub>2</sub>). A partial sintering of the particles was found after their exposure to hydrogen atmosphere at 773 K.

## 2.2.2 Atomic Force Microscopy (AFM)

The areal particle distribution, the Pt coverage, and the particle height after the spin-coating of the particles onto the GaN surfaces were analyzed with AFM (Veeco Multimode AFM with Nanoscope IIIa or V controller, Institute of Electron Microscopy, Department of Chemistry or Walter Schottky Institute, Technische Universität München). AFM probes of silicon were used with a resonance frequency of 204-497 kHz, a force constant of 10-130 N m<sup>-1</sup>, and a typical tip radius below 7 nm (Nanosensors). AFM images of different sizes from 1 × 1 μm to 5 × 5 μm were recorded at a scanning frequency of 1 Hz and with 512 or 256 data points per line. The image evaluation was performed with the software WSxM.<sup>[10]</sup> Several images were collected from different sample positions in the central to edge region of the GaN surface. The number of particles per GaN area and the particle height were subsequently averaged from all images. With AFM, the catalyst samples were chosen for *in situ* characterization or reaction testing, which exhibit solely isolated particles on the GaN surface. The catalysts with octahedral Pt particles showed only aggregated particles and thus, these samples were not used for further analysis.

The average particle height obtained with AFM was slightly lower than the particle size determined with TEM. Therefore, we assumed a truncation of the particles of one third and two thirds of the particle is exposed on the GaN surface. Additionally, the individual particle shape was supposed to be preserved after spin-coating and oxygen plasma. This assumption was supported by TEM images of Pt cubes deposited onto GaN nanowires after oxygen plasma treatment. The nanowires were scratched from their substrate and could be analyzed with high-resolution TEM (Figure 2-5).

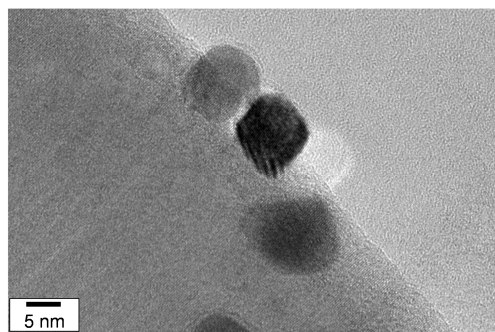


**Figure 2-5.** High-resolution TEM image of Pt cubes on GaN nanowires (recorded by S. Schäfer at the Lawrence Berkeley Laboratory).

The number of particles per GaN area was used to calculate the Pt coverage in percentage of a monolayer (%ML) based on the Pt atom densities on Pt(111) and Pt(100) facets of  $1.5 \times 10^{15} \text{ cm}^{-2}$  and  $1.3 \times 10^{15} \text{ cm}^{-2}$ , respectively.<sup>[11, 12]</sup> The number of Pt surface atoms was also estimated from the areal particle coverage. The number of atoms and surface atoms per particle were determined considering the respective particle shape.

Small, spherical and large, unshaped Pt particles were calculated based on the results from grazing incidence small-angle X-ray scattering (GISAXS) (Chapter 3), which provided exact values for the particle height and diameter. The small particles were found to be ellipsoidal, while the larger particles showed a flat, cuboidal particle shape. The particle volume was estimated for both geometries according to Equation 2-2 and Equation 2-3. The number of Pt atoms per particle was calculated using the Pt metal density ( $21.4 \text{ g cm}^{-3}$ ) and the Pt molar mass ( $195.08 \text{ g mol}^{-1}$ ) (Equation 2-4). The surface area of the ellipsoidal and cuboidal particle was determined by Equation 2-5 and Equation 2-6, respectively. The number of surface Pt atoms per particle was subsequently determined from the particle surface area and the atom density on the Pt(111) or Pt(100) facet (Equation 2-7). The base area of the cuboidal particle was subtracted because it does not contribute to the exposed surface.

$$V_{\text{Ellipsoid}} = \frac{1}{2} \left( \frac{4}{3} \pi h \left( \frac{d}{2} \right)^2 \right) \quad (\text{Equation 2-2})$$

$$V_{\text{Cuboid}} = hd^2 \quad (\text{Equation 2-3})$$

$$N_{\text{Particle}} = \frac{\rho_{\text{Pt}} V_{\text{Particle}}}{M_{\text{Pt}}} N_A \quad (\text{Equation 2-4})$$

$$S_{\text{Ellipsoid}} = \pi \left( \frac{d}{2} \right)^2 \left( 1 + \frac{2h}{d} \frac{\arcsin(\varepsilon)}{\varepsilon} \right) \quad \text{with} \quad \varepsilon = \sqrt{1 - \left( \frac{d}{2h} \right)^2} \quad (\text{Equation 2-5})$$

$$S_{\text{Cuboid}} = d^2 + 4dh \quad (\text{Equation 2-6})$$

$$N_{\text{Surface}} = S_{\text{Ellipsoid}} A_{\text{Pt}(111)} \quad \text{or} \quad N_{\text{Surface}} = S_{\text{Cuboid}} A_{\text{Pt}(100)} \quad (\text{Equation 2-7})$$

Where  $V$  is the particle volume,  $h$  the particle height,  $d$  the particle diameter,  $N$  the number of atoms,  $\rho$  the density,  $M$  the molar mass,  $N_A$  the Avogadro constant,  $S$  the particle surface area, and  $A$  the Pt surface density of the Pt(111) and Pt(100) facet.

The number of atoms and surface atoms of the particle for other samples that were not measured with GISAXS were calculated considering model particle shapes (Figure 2-6).

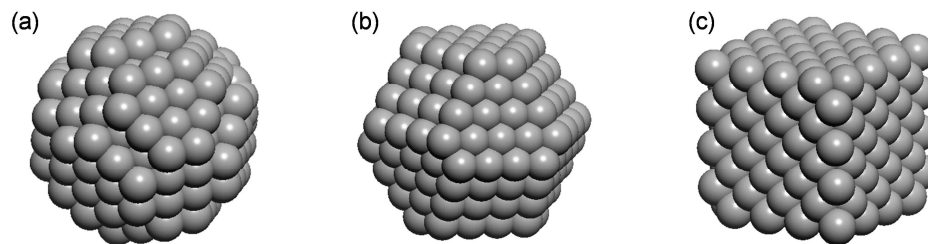


**Figure 2-6.** Model geometries of (a) spherical, (b) cuboctahedral, and (c) cubic particles. These shapes do not show the number of atoms that correspond to the particle sizes in this study.

The cuboctahedral particles were analyzed with the model equations from Benfield using the cluster edge length, which describes the number of atomic shells around one single metal atom (Equation 2-8 to Equation 2-10).<sup>[13]</sup> Small, spherical particles exhibit roughly an icosahedral shape and were calculated with the same equations as cuboctahedral particles. The average particle size from TEM was used to determine the cluster edge length and only two thirds of the particle was proposed to be exposed.

$$N_{Particle} = \frac{2}{3} \left[ \frac{1}{3} (2m - 1) (5m^2 - 5m + 3) \right] \quad (\text{Equation 2-8})$$

$$m = \frac{1}{2} \left( \frac{d_{Particle}}{d_{Pt\ atom}} + 1 \right) \quad (\text{Equation 2-9})$$

$$N_{Surface} = \frac{2}{3} (10m^2 - 20m + 12) \quad (\text{Equation 2-10})$$

Where  $N_{Particle}$  is the number of atoms per particle,  $N_{Surface}$  the number of surface atoms of the particle,  $m$  the cluster edge length,  $d_{particle}$  the particle diameter, and  $d_{Pt\ atom}$  the Pt atom diameter.

The number of atoms and surface atoms of cubic Pt particles were calculated using the number of atoms for one cubic plane that was extrapolated to the three-dimensional shape (Equation 2-11 and Equation 2-12). Two thirds of a particle was assumed to be exposed.

The Pt particle coverage on the GaN surfaces was calculated from AFM images and was used to determine the total Pt coverage of the catalyst and the total Pt surface coverage in %ML (Table 2-5). The Pt coverage and Pt surface coverage were utilized to normalize the kinetic results for a direct comparison of the different catalysts.



$$N_{Particle} = \frac{2}{3} \frac{d_{Particle}^3}{d_{Pt\ atom}} A_{Pt(100)} \quad (\text{Equation 2-11})$$

$$N_{Surface} = 4d_{Particle}^2 A_{Pt(100)} - 8 \frac{d_{Particle}}{d_{Pt\ atom}} \quad (\text{Equation 2-12})$$

Where  $N_{Particle}$  is the number of atoms per particle,  $N_{Surface}$  the number of surface atoms of the particle,  $d_{Particle}$  the particle diameter,  $d_{Pt\ atom}$  the Pt atom diameter, and  $A_{Pt(100)}$  the Pt atom density of the Pt(100) facet.

**Table 2-5.** Calculated atoms and surface atoms per particle, average particle coverage, total Pt coverage on GaN, and surface Pt coverage for spherical, cubic, and cuboctahedral Pt nanoparticles.

Particle shape	Atoms per particle (surface atoms)	GaN surface	Particles on GaN <sup>(c)</sup> / $\mu\text{m}^{-2}$	Pt coverage on GaN / %ML	Surface Pt coverage / %ML
Spheres (2.0 nm)	106 (65)	<i>n</i> -type	$2776 \pm 291$	$2.0 \pm 0.2$	$1.2 \pm 0.1$
		<i>p</i> -type	$3545 \pm 365$	$2.5 \pm 0.3$	$1.5 \pm 0.2$
Cubes (7.6 nm)	13685 (2785)	<i>n</i> -type	$177 \pm 78$	$16.1 \pm 7.1$	$3.3 \pm 1.5$
		<i>p</i> -type	$184 \pm 12$	$16.8 \pm 1.1$	$3.4 \pm 0.2$
Cuboctahedra (8.1 nm)	6882 (1321)	<i>n</i> -type	$347 \pm 55$	$15.9 \pm 2.5$	$3.1 \pm 0.5$
		<i>n</i> -type <sup>(b)</sup>	$361 \pm 122$	$16.6 \pm 5.6$	$3.2 \pm 1.1$
		<i>p</i> -type	$367 \pm 101$	$16.8 \pm 4.6$	$3.2 \pm 0.9$
Cuboctahedra (8.9 nm)	9127 (1604)	<i>n</i> -type	$122 \pm 17$	$7.4 \pm 1.0$	$1.3 \pm 0.2$
		<i>p</i> -type	$143 \pm 12$	$8.7 \pm 0.8$	$1.5 \pm 0.1$

<sup>(a)</sup> Determined from TEM. <sup>(b)</sup> N-face *n*-type GaN. <sup>(c)</sup> Determined from AFM.

In general, AFM belongs to the group of scanning probe microscopes that exhibits a very high resolution at the atomic scale. The very small and sharp probe scans the sample surface resulting in images based on the force interactions between the tip and the sample. Therefore, the topography, surface charge, resistance, as well as the chemical and magnetic properties of the surface can be monitored by scanning probe microscopy. The measurement environment can be vacuum, air, or a liquid, which extends the field of application for e.g. biology. The experimental assembly contains a cantilever with a tip that is deflected from its initial position due to the force interaction with the surface (Figure 2-7). The deflection changes of the tip are measured by a reflected laser beam from the cantilever that is directed to a position sensitive detector (PSD), which consists of two photodiodes. The alteration of the laser position induces voltage changes on the diodes that create an output signal by their difference normalized by their sum. The signal is differentially amplified and transformed into a three-dimensional topographical map of the sample. The scanning of the tip over the surface is arranged by the sample movement with a piezoelectric element.<sup>[14]</sup>

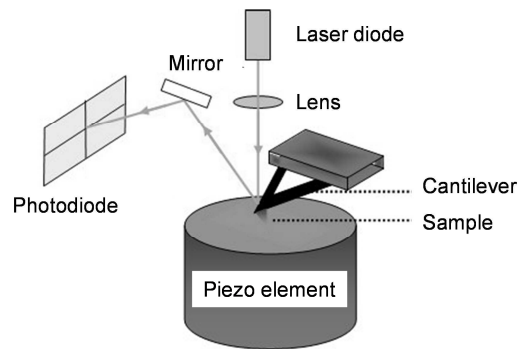


**Figure 2-7.** Experimental assembly of an atomic force microscope with the piezoelectric element for sample movement, the tip and cantilever, the laser diode, and the photodiodes for detection.<sup>[14]</sup>

AFM can be performed in two operation modes, the static (contact mode) or dynamic (non-contact mode and tapping mode) (Figure 2-8). The tip is in contact with the surface during the static operation. The cantilever deflection displays directly the topography during the measurement with a constant sample height. If the scanning occurs with a constant force, the cantilever bending will be fixed and the piezoelectric controller will change the output signal to the sample height. In this mode, the sample can be damaged due to strong forces. Sensitive samples should be imaged in dynamic mode, where the probe is not in direct contact with the surface. The cantilever is mounted to the actuator during the non-contact operation, which facilitates the external excitation of the tip vibration. The tip oscillates above its resonance frequency with an amplitude below 10 nm and the forces between the tip and the sample cause the damping of these vibrations. Changes in the amplitude and phase (amplitude modulation) or in the frequency (frequency modulation) generate the feedback signal for imaging. An intermediate solution between the contact and non-contact operation is implemented when working in the tapping mode. The tip oscillates near its resonance frequency with an amplitude of 100-200 nm and attaches the surface for a very short time. The amplitude is adjusted to a constant value to control the signal. The advantage of this operation is clearly its application for sensitive samples and imaging with higher resolution.<sup>[14, 15]</sup>

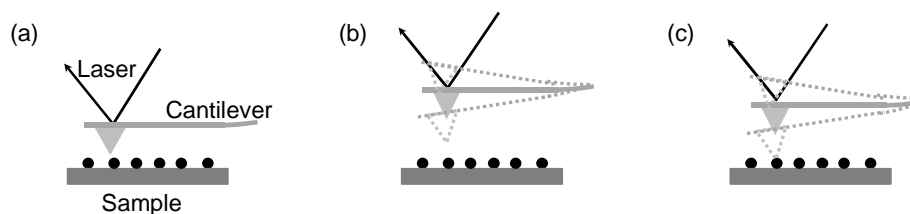


**Figure 2-8.** Operation modes of AFM: (a) the contact mode, (b) the non-contact mode, and (c) the tapping mode.

Some problems may occur during the measurements when the surface structures are mobile or when they cause tip contaminations. As a result, the image quality and resolution is limited, especially in the lateral direction. Usually, a real AFM probe does not consist of one single atom at the end of the tip, but has a finite expansion and radius of curvature in the nm range. Consequently, sharp edges on the sample surface cannot be resolved. However, a high accuracy can be obtained for the height of the surface structures. The resulting sample map is always composed of the structure of the surface folded with the structure of the tip. Therefore, tip artifacts like the double tip can be imaged that does not relate to the real sample surface but to the contaminated tip. Small, supported nanoparticles that were used in this work contaminated the AFM probes very quickly and the initially observed small dots expanded into large dots with the scanning time. Anyway, the particle height and their density on the surface could be successfully mapped with high accuracy.

### 2.3 *In situ* Characterization

The catalyst characterization under realistic reaction conditions at elevated temperatures and high pressures is not only important for the rational catalyst development and the optimization but also for the understanding of the surface reaction pathways and mechanisms. Consequently, *in situ* techniques became essential in heterogeneous catalysis and their combination delivers complementary information for an advanced description of the catalyst reactivity. The addition of methods for the simultaneous product analysis completes the insight into the complex catalytic systems by operando studies. Only bridging the “pressure gap” by the application of *in situ* high-pressure methods does not fulfill the requirements on the view of the catalyst at work. Indeed, the surface-sensitive analysis of more realistic catalysts instead of ideal single crystals is a basic approach to narrow the “materials gap”, minimizing the discrepancy between the surface science and catalysis. Moreover, the design of experimental cells is challenging regarding their ability to facilitate spectroscopic as well as catalytic data at defined conditions. The gradients in temperature and concentration should be diminished by an optimal reactor cell design considering particular requirements of the applied *in situ* technique.<sup>[16]</sup>

Various methods were developed for *in situ* applications and testing of catalysts for relevant industrial processes. The reactant or product adsorption, elementary reaction steps, and surface pathways were explored by *in situ* infrared (IR) spectroscopy e.g. for the NO<sub>x</sub>

storage-reduction, the high-selective oxidative dehydrogenation of alkanes, and the alkylation.<sup>[17-19]</sup> In general, IR spectroscopy is a powerful method, which monitors important intermediates during the reaction on the surface.<sup>[20]</sup> *In situ* X-ray absorption spectroscopy (XAS) including extended X-ray absorption fine structure (EXAFS) and X-ray absorption near edge structure (XANES) reveals the near-neighbor coordination and electronic state of the probed atoms. High-pressure and time-resolved experiments could be realized by the energy-dispersive and quick EXAFS.<sup>[21]</sup> Catalysts for the SO<sub>x</sub> storage, alkane hydrogenolysis, methanol oxidation, and selective oxidation were investigated by *in situ* XAS.<sup>[22-25]</sup> Additionally, studies during the aqueous-phase reactions, as well as during the formation of metal catalysts were performed.<sup>[26-28]</sup> *In situ* high-pressure X-ray photoelectron spectroscopy (XPS) was developed to probe the surface composition of gas and liquid surfaces.<sup>[29]</sup> Some catalysts for oxidation and hydrogenation were analyzed regarding their structural surface properties under reaction conditions.<sup>[30-32]</sup> The particle size and shape of supported catalysts with a low particle coverage can be simultaneously investigated with grazing incidence small-angle X-ray scattering (GISAXS). Therefore, the stability and growth of particles could be followed *in situ* at different catalytic conditions.<sup>[33-35]</sup> One suitable method for the research of interfaces of solid-gas, solid-liquid, and liquid-liquid systems is the vibrational sum frequency generation (SFG) spectroscopy that uses a second-order nonlinear optical process. The chemical species at the interface and their orientation during the reaction can be probed at high pressures and temperatures.<sup>[36, 37]</sup> Studies on single crystals and model catalysts, which represented nearly a real surface, were used to compare the molecule adsorption on the surface at ultra-high vacuum conditions and at high pressures.<sup>[38-42]</sup> Besides the spectroscopic techniques, microscopic methods were also applied for the *in situ* surface characterization. Scanning tunneling microscopy (STM) and TEM were both used for sample imaging in a reactive atmosphere with a high atomic resolution.<sup>[43, 44]</sup>

The combined application of methods in one single experiment with a simultaneous detection of the catalytic activity provided a more advanced view of the catalyst under working conditions. *In situ* X-ray diffraction (XRD), XAS, and mass spectrometry were combined to probe the catalyst behavior during the synthesis of methanol.<sup>[45]</sup> Recently, a straightforward combination of GISAXS and temperature-programmed reaction (TPRx) was investigated for various model catalysts in the epoxidation of propene, the oxidative decomposition of methanol, and the dehydrogenation of cyclohexene.<sup>[46-49]</sup> In this work, exactly the same setup was used and extended by XAS to monitor the Pt particle shape changes and stability simultaneously with the changes in the electronic state of Pt at elevated temperatures under

reduction with deuterium and ethene hydrogenation (Chapter 3). To study the chemical composition of the Pt particle and GaN surface under reaction, *in situ* XPS was applied in this work at high pressures in a reducing and oxidizing atmosphere (Chapter 4).

### 2.3.1 Grazing Incidence Small-angle X-ray Scattering (GISAXS)

The sample morphology like the particle size and shape, as well as the particle size distribution was investigated under reaction conditions with GISAXS (Beamline 12-ID-C, Advanced Photon Source, Argonne National Laboratory, Argonne, USA). Small, spherical and large, unshaped Pt nanoparticles supported on *n*-type GaN were measured in helium with increasing temperature to 673 K, during the temperature-programmed reduction with deuterium, and during the hydrogenation of ethene with deuterium at 373 K. The reaction products were detected on-line by a differentially pumped mass spectrometer (Pfeiffer Vacuum Prisma QMS 200). The sample was placed into a self-designed reaction cell that facilitated spectroscopy and the real-time product analysis.<sup>[49]</sup> Changes in the particle size and shape were collected as a function of temperature and time in two-dimensional GISAXS patterns (scattering vector  $q$  in x, y, and z direction) with the X-ray energy of 11.5 keV and a MarCCD detector (1024 × 1024 pixel). The quantitative analysis was performed by taking cuts in  $q_{xy}$  and  $q_z$  direction for the lateral and vertical particle information, respectively. The Guinier analysis was applied assuming a spherical particle shape and a narrow size distribution.<sup>[50]</sup> Hence, the radii of gyration were determined from plots of the logarithm of the scattering intensity versus  $q^2$  in the small-angle region. Horizontal ( $R_{gH}$ ) and vertical ( $R_{gV}$ ) radii of gyration resulted in the particle diameter and height ( $2.58 \times R_{gH}$  and  $R_{gV}$ ). Finally, the aspect ratio,  $R_{gH}$  divided by  $R_{gV}$ , was calculated during the heating and/or reaction. The background scattering from *n*-type GaN was measured and subtracted from the data sets, which were evaluated with the software IgorPro 5.05A that was featured with a GISAXS toolkit (B. Lee at 12ID SAXS, APS). Further experimental details are described in Chapter 3.

In general, X-ray scattering experiments reveal different properties of the sample that depends on the applied angle range (Figure 2-9). As the information is collected in reciprocal space, the large-scale electron density fluctuations are analyzed at very low angles. The Guinier regime represents the asymptotic behavior of the form factor close to the origin of the reciprocal space, providing data on the particle size and polydispersity at small angles. The

information on the particle shape, smoothness of interfaces, and internal surface-to-volume ratios is obtained from the asymptotic behavior at intermediate and wider angles (Porod regime). The scattering intensity decays in this region with  $q^{-n}$ , while  $n$  is characteristic for the particle shape and becomes 3 for a cylinder and 2 for a hemisphere. Finally, powder diffraction or rather the scattering on lattice atoms is analyzed at very large angles.<sup>[51, 52]</sup>

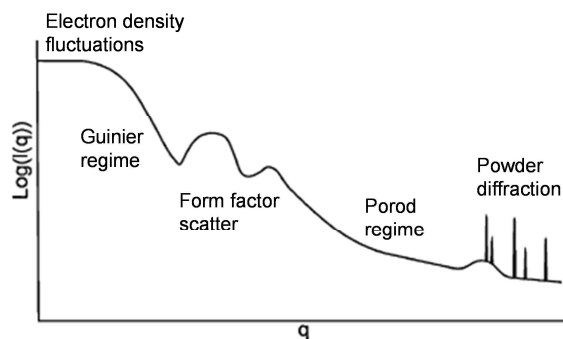


**Figure 2-9.** Scheme of the X-ray scattering regimes with scattering intensity  $\log(I(q))$  versus wave vector  $q$ .<sup>[51]</sup>

The probing of nanostructures with conventional X-ray sources is limited to objects of 100-200 nm, while smaller structures can be analyzed with synchrotron radiation. Moreover, the surface sensitivity can be enhanced by the grazing incidence geometry (reflection mode) instead of the transmission mode (Figure 2-10). The incident beam (wave vector  $k_i$ ) approaches the sample surface at a low constant angle (out-of-plane  $\alpha_i$ , in-plane  $\theta_i$ ), which is close to the critical angle of total external reflection ( $\alpha_c$ ), and is scattered by the structures on the substrate surface. The scattered beam (wave vector  $k_f$ ) with its characteristic small angles (out-of-plane  $\alpha_f$ , in-plane  $2\theta_f$ ) is then detected as a two-dimensional scattering pattern with the wave vector transfer components parallel ( $q_y$ ) and perpendicular ( $q_z$ ) to the sample normal (Equation 2-13). A T-shaped beam stop permits the absorption of the direct and reflected beam, while the scattered beam is detected.<sup>[52, 53]</sup>

$$q = k_f - k_i \quad (\text{Equation 2-13})$$

Where  $q$  is the wave vector transfer, and  $k_i$ ,  $k_f$  the wave vector of the incident and scattered beam, respectively.

The rotation of the sample by its normal facilitates information about the particle symmetry and the orientation of the incident beam with respect to the in-plane crystallographic directions. The absolute values of the wave vector transfer are expressed by the angular coordinates of the scattered beam (Equation 2-14 to Equation 2-16).<sup>[52]</sup> The area of the

reciprocal space is only a few  $\text{nm}^{-1}$  as all contributed angles are small. Therefore, all scattering vectors can be simplified by Equation 2-17 to Equation 2-19.<sup>[52]</sup>

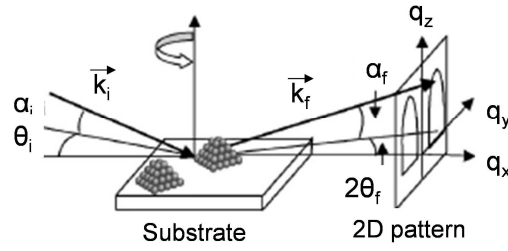


**Figure 2-10.** Experimental geometry of grazing incidence small-angle X-ray scattering of particles supported on a substrate with the incident wave vector  $k_i$ , the out-of-plane and in-plane angles  $\alpha_i$ ,  $\theta_i$  of the incident beam, the scattered wave vector  $k_f$ , the out-of-plane and in-plane angles  $\alpha_f$ ,  $2\theta_f$  of the scattered beam, and the wave vector transfer in reciprocal space in all directions  $q_x$ ,  $q_y$ ,  $q_z$ . The substrate can be rotated around its surface normal.<sup>[53]</sup>

$$q_x = \frac{2\pi}{\lambda} [\cos(2\theta_f)\cos(\alpha_f) - \cos(\alpha_i)] \quad (\text{Equation 2-14})$$

$$q_y = \frac{2\pi}{\lambda} [\sin(2\theta_f)\cos(\alpha_f)] \quad (\text{Equation 2-15})$$

$$q_z = \frac{2\pi}{\lambda} [\sin(\alpha_f) + \sin(\alpha_i)] \quad (\text{Equation 2-16})$$

$$q_x \cong 0 \quad (\text{Equation 2-17})$$

$$q_y = \frac{2\pi}{\lambda} 2\theta_f \quad (\text{Equation 2-18})$$

$$q_z = \frac{2\pi}{\lambda} \alpha_f \quad (\text{Equation 2-19})$$

Where  $q$  is the wave vector transfer in x, y, and z direction,  $\lambda$  the X-ray wave length,  $2\theta_f$  the in-plane angle and  $\alpha_f$  the out-of-plane angle of the scattered beam, and  $\alpha_i$  the out-of-plane angle of the incident beam.

The sample surface behaves like a mirror at low incident angles, which leads to multiple scattering and the reflection and refraction has to be considered. The beam is completely reflected at  $\alpha_i < \alpha_c$ , while the transmitted beam penetrates into the bulk at  $\alpha_i > \alpha_c$ . Therefore, the adjustment of the incident angle to small values above  $\alpha_c$  allows the variation in the scattering depth. Typically, the critical angle is  $0.1\text{-}0.5^\circ$ . The maximum of the off-specular diffuse scattering appears at  $\alpha_i = \alpha_c$ , the Yoneda peak. The contrast is given by electron density variations and the refractive index of the particles and the surrounding determines the dielectric constant contrast (Equation 2-20).<sup>[52]</sup>

$$\Delta n^2 = n_p^2 - n_m^2 \quad (\text{Equation 2-20})$$

Where  $\Delta n^2$  is the dielectric constant contrast,  $n_p$  and  $n_m$  are the refractive index of the particle and medium, respectively.

Generally, the coherent and incoherent scattering contributes to the scattering intensity that is described by the Born Approximation (Equation 2-21). The coherent term includes the particle form factor and a two-dimensional interference function, while the incoherent term describes the correlation between the particle sizes or rather the diffuse scattering.<sup>[53]</sup>

$$I(q) = S(q_y) \times \left| \overline{F}(q_y) \right|^2 + \sum_m \Phi_m(q) \times e^{-iqr_m} \quad (\text{Equation 2-21})$$

Where  $I(q)$  is the scattering intensity,  $q$  the wave vector transfer,  $S(q_y)$  the interference function,  $F(q_y)$  the average particle form factor,  $\Phi_m$  the particle size correlation function, and  $r_m$  the vector of the particle separation.

The theoretical description of a single scattering within the Born Approximation has to be extended to the distorted wave Born Approximation (DWBA), because multiple scattering appears. The DWBA-based particle form factor includes the interference between four scattering events, while the particle shape is no longer a simple Fourier transform of the real shape (Figure 2-11).<sup>[52, 53]</sup>

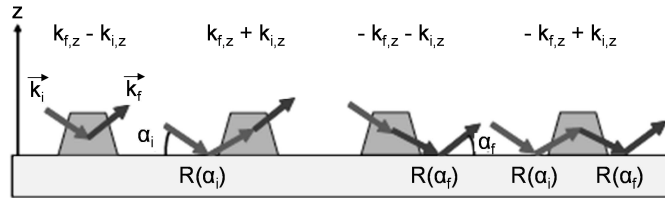


**Figure 2-11.** Multiple scattering contribution in the distorted wave Born Approximation on supported particles with the incident and scattered wave vectors  $k_i$ ,  $k_f$ , angles  $\alpha_i$ ,  $\alpha_f$ , and Fresnel reflection coefficients  $R(\alpha_i)$ ,  $R(\alpha_f)$ .<sup>[52]</sup>

The particle form factor is determined by the four scattering possibilities, which involve the reflection of the incident and/or the scattered beam on the support surface or not weighted by the Fresnel reflection coefficients (Equation 2-22).<sup>[52, 53]</sup>



$$F(q_y, k_{i,z}, k_{f,z}) = F(q_y, k_{f,z} - k_{i,z}) + R(\alpha_i)F(q_y, k_{f,z} + k_{i,z}) + R(\alpha_f)F(q_y, -k_{f,z} - k_{i,z}) + R(\alpha_i)R(\alpha_f)F(q_y, -k_{f,z} + k_{i,z}) \quad (\text{Equation 2-22})$$

Where  $F(q_y)$  is the particle form factor,  $q_y$  the wave vector transfer in y direction,  $k_{i,z}$  and  $k_{f,z}$  the incident and scattered wave vectors in z direction,  $\alpha_i$  and  $\alpha_f$  the out-of-plane angles of the incident and scattered beam, and  $R(\alpha_i)$  and  $R(\alpha_f)$  the Fresnel coefficients for the reflection of the incident and scattered beam, respectively.

A careful quantitative analysis of the two-dimensional GISAXS patterns is required that includes appropriate background corrections. However, the background should be generally minimized due to the small angles and the vicinity of the direct and scattered beam. But huge background signals can be produced by the sample, the beam divergence, the optical beamline elements and windows, and the air environment. Improving the beamline itself and applying an advanced *in situ* reaction cells can both reduce and filter unwanted scattering contributions. Nevertheless, suitable models have to be applied for the data fitting to distinguish between the scattering from the nanostructures and the underlying support. If a constant surface roughness is expected, the blank surface can be subtracted from sample data like was applied in this study. Alternatively, the so-called anomalous GISAXS can be used to decouple the scattering of the particles and the substrate, where the data are collected at various X-ray energies around the absorption edge of the desired element.<sup>[54]</sup>

The particle size distribution, the lateral and vertical diameters, and the distance between the particles can be analyzed from cuts through the GISAXS patterns in lateral and vertical direction. The Guinier analysis used in the small-angle region assumes monodisperse, spherical particles (Equation 2-23).<sup>[51]</sup> The radius of gyration is calculated in the parallel and perpendicular direction to the sample normal, resulting in the corresponding diameter and height of the particles, respectively (Equation 2-24).<sup>[51]</sup>

$$I(q) \approx e^{-q^2 \frac{R_g}{3}} \quad (\text{Equation 2-23})$$

$$r_p = \sqrt{\frac{3}{5}} R_g \quad (\text{Equation 2-24})$$

Where  $I(q)$  is the intensity,  $q$  the wave vector transfer,  $R_g$  the radius of gyration, and  $r_p$  is the particle radius.

GISAXS allows for measuring in real-time and provides statistical information of a large sample area, which is according to the X-ray beam size. The sample had to be perfectly positioned in the X-ray beam that avoids the background scattering. The background

subtraction and correction was important to reconstruct the real particle structure from the reciprocal space.

### 2.3.2 Grazing Incidence X-ray Absorption Spectroscopy (GIXAS)

The oxidation state of small, spherical and large, unshaped Pt particles on *n*-type GaN was analyzed simultaneously during GISAXS experiments with GIXAS (Beamline 12-ID-C, Advanced Photon Source, Argonne National Laboratory, Argonne, USA). In particular, the grazing incidence X-ray absorption near edge structure (GIXANES) was collected from the Pt L<sub>3</sub> edge before and after reduction and ethene hydrogenation with deuterium at elevated temperature. The qualitative analysis of the white line compared to the reference Pt foil, as well as the quantitative shift of the absorption edge were evaluated to determine the oxidation state of Pt. The measurement in reflection mode required the signal detection by fluorescence (4-element Ge fluorescence detector) instead of transmission, and provided sufficient surface sensitivity for probing the low coverage of particles on the GaN surface. The X-ray penetration depth during the measurement was 2 nm. Due to the long acquisition time of about 17 min for XANES, one point of the Pt edge at energy of 11.57 keV was *in situ* monitored during the reduction and reaction. The change in the absorbance intensity represented the change of the white line and *in situ* changes of the electron density were recorded. The data analysis of the XANES region was performed with XANDA dactyloscope.<sup>[55]</sup> The extended X-ray absorption fine structure (EXAFS) was not collected due to the poor resolution of oscillations above the Pt edge. A further description of the experimental details is given in Chapter 3.

XAS is generally used for the short-range structural information of a sample. Atomic coordination numbers and interatomic distances provide the determination of the metal dispersion and particle size. Additionally, the types of neighboring atoms are obtained leading to the analysis of the electronic state. The synchrotron radiation is typical in XAS due to the broad energy range and high intensity.

Based on the photoelectric effect in XAS, a photoelectron is emitted when the incident X-ray photon energy exceeds the binding energy of a core level electron, resulting in a sudden increase in the absorption coefficient, the absorption edge (Figure 2-12 (a)). The photoelectron leaves a core hole and contains excess energy. The excited atom tends to relax

to the ground state either by X-ray fluorescence or by the Auger effect (Figure 2-12 (b-c)). An electron from a high-energy level refills the core hole and emits X-rays or another photoelectron, the Auger-electron. Both the fluorescence and Auger-electrons are characteristic for each element, facilitating the analysis of the sample composition.<sup>[56]</sup>

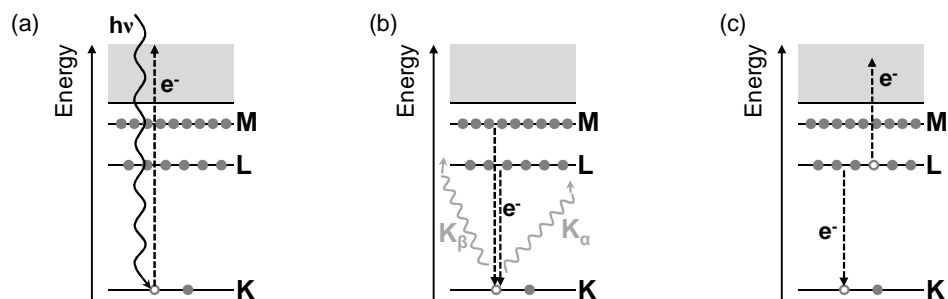


**Figure 2-12.** The photoelectric effect: (a) X-ray absorption with the emission of a photoelectron leaving a core hole and (b) relaxation of the core hole by X-ray fluorescence with the emission of X-ray photons and/or (c) the relaxation by the Auger effect with the emission of an Auger electron.

The neighboring atoms cause the backscattering of the ejected photoelectron, which interacts with itself by constructive or destructive interference (Figure 2-13). This leads to oscillations in the spectrum above the absorption edge, which are dependent on the environmental coordination shells around the absorbing atom. If more atoms are involved into the scattering process, multiple scattering will occur before the photoelectron returns to its original atom.<sup>[56]</sup>

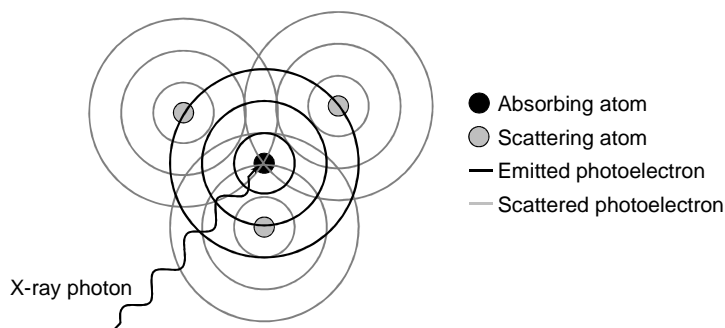


**Figure 2-13.** Scattering effect in X-ray absorption spectroscopy. The emitted photoelectron from the absorbing atom is scattered back on neighboring atoms (scattering atoms).

The energy dependency of the X-ray absorption coefficient is measured around the absorption edge providing two regimes in the spectrum. XANES includes the edge region, while EXAFS contains the oscillations above the edge (Figure 2-14). The electronic properties are determined from XANES and the local environment of the absorbing atoms is evaluated from

EXAFS. XANES is especially suitable for samples with low concentrations due to its huge signal. However, the quantitative interpretation is very difficult and requires ab initio calculations in the real-space, including the multiple-scattering formalism, which connects the X-ray absorption with the electronic states in XAS.<sup>[57]</sup>

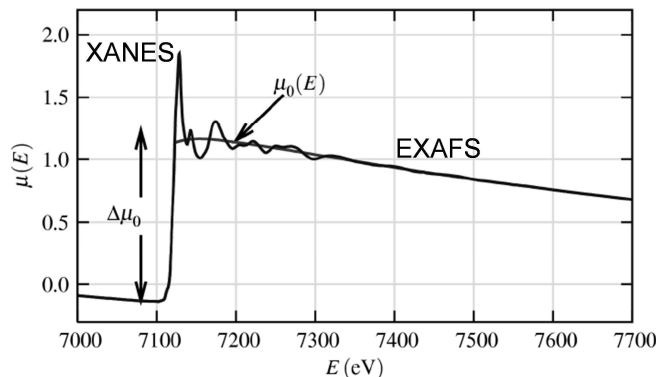


**Figure 2-14.** X-ray absorption spectrum of iron oxide (FeO) with two regimes, XANES and EXAFS, the smooth background function  $\mu_0(E)$ , and absorption edge step  $\Delta\mu_0$ .<sup>[56]</sup>

The XAS signal can be collected in both the transmission and fluorescence mode. High-concentrated samples are usually measured in transmission, which requires an exactly defined sample thickness. Contrary, X-ray fluorescence facilitates experiments of samples that contain low element concentrations. The combination of the grazing incidence geometry with fluorescence enhances the surface sensitivity of XAS and the Pt-GaN catalysts could be probed. Two parameters are essential for fluorescence measurements due to the contribution of additional fluorescence lines and scattered X-rays. First, a solid angle is needed to increase the signal. The fluorescence detector is located with an angle of  $90^\circ$  to the incident beam and  $45^\circ$  to the sample due to isotropic and anisotropic behavior of the fluorescence and scattered X-rays, respectively. Secondly, the energy discrimination allows the suppression of the background, while collecting solely the favored fluorescence line. A physical approach includes the assembly of a filter (Z-1 filter) and a set of slits (Soller slits) that remove some background contributions. Alternatively, the unwanted fluorescence and scattering can be removed electronically by a solid-state germanium detector.<sup>[56]</sup>

The X-ray absorption coefficient is strongly affected by the atomic number leading to an enhanced contrast between different elements (Equation 2-25).<sup>[56]</sup>

$$\mu(E) \approx \frac{\rho Z^4}{ME^3} \quad (\text{Equation 2-25})$$

Where  $\mu(E)$  is the X-ray absorption coefficient,  $\rho$  the atom density,  $Z$  the atomic number,  $M$  the atomic mass, and  $E$  is the energy.

The XAS intensity depends on the experimental geometry and is described by the Lambert Beer's law for absorption (Equation 2-26), while the fluorescence intensity contains extended terms due to the detection of the core hole refilling by fluorescence (Equation 2-27).<sup>[56]</sup>

$$I_t = I_0 e^{-\mu(E)d} \quad (\text{Equation 2-26})$$

$$I_f = I_0 \frac{\varepsilon \Delta\Omega}{4\pi} \frac{\mu_\chi(E)}{\mu_{tot}(E) + \mu_{tot}(E_f)} \left[ 1 - e^{-[\mu_{tot}(E) + \mu_{tot}(E_f)]d} \right] \quad (\text{Equation 2-27})$$

Where  $I_t$  is the transmitted intensity,  $I_0$  the initial intensity,  $\mu(E)$  the absorption coefficient,  $d$  the sample thickness,  $I_f$  the fluorescence intensity,  $\varepsilon$  the fluorescence efficiency,  $\Delta\Omega$  the solid angle,  $E_f$  the energy of fluorescent X-rays, and  $\mu_\chi(E)$  and  $\mu_{tot}(E)$  is the element and total absorption coefficient, respectively.

The X-ray energy is further transformed into the wave vector  $k$  due to the wave-like behavior of the photoelectrons (Equation 2-28). The EXAFS oscillations are plotted versus the wave vector to analyze the local atom environment. Moreover, the oscillations are normally weighted by  $k^2$  or  $k^3$  for amplification.<sup>[56, 58]</sup>

$$k = \sqrt{\frac{8\pi m_e (E - E_0)}{h^2}} \quad (\text{Equation 2-28})$$

Where  $k$  is the wave vector,  $m_e$  the electron mass,  $E$  the X-ray energy,  $E_0$  the energy of the core level, and  $h$  is the Plank constant.

The EXAFS signal is normalized to one single absorption event, which includes the absorption coefficient of the isolated atom without the presence of near neighbors (Equation 2-29). Finally, the EXAFS equation (Equation 2-30) describes the signal quantitatively and is used for modeling in various software programs. The scattering amplitude and phase-shift functions can be calculated by e.g. the FEFF program or determined by model compounds. The Fourier transform of the wave vector into the distance facilitates the separation of the frequencies and the investigation of the number of neighbors, their distance, and disorder.

This detailed physical description fails in the region of low wave vectors and thus, XANES cannot be evaluated with the EXAFS equation.<sup>[56, 58]</sup>

$$\chi(k) = \frac{\mu(k) - \mu_0(k)}{\mu_0(k)} \quad (\text{Equation 2-29})$$

$$\chi(k) = \sum_j \frac{N_j S_0^2 f_j(k) e^{-\frac{2R_j}{\lambda(k)}} e^{-2k^2 \sigma_j^2}}{k R_j^2} \sin[2kR_j + \delta_j(k)] \quad (\text{Equation 2-30})$$

Where  $\chi(k)$  is the EXAFS,  $\mu(k)$  the experimental absorption coefficient,  $\mu_0(k)$  the absorption coefficient of the isolated atom,  $k$  the wave vector, the sum over  $j$  atomic shells,  $N_j$  the coordination number,  $S_0^2$  the amplitude reduction term,  $f_j(k)$  the scattering amplitude function,  $R_j$  the distance between the atoms,  $\lambda(k)$  the photoelectron mean free path,  $\sigma^2$  is the disorder in the distance or the Debye-Waller factor, and  $\delta_j(k)$  the phase-shift function.

The X-ray absorption process takes only place when unoccupied states are available for the transition. Therefore, XAS probes the density of empty states near the Fermi level that is in contrast to X-ray photoemission spectroscopy, where the density of the filled states is analyzed. For instance, the Pt L<sub>3</sub> edge at 11.564 keV represents the transition 2p<sub>3/2</sub> → 5d<sub>5/2</sub> and 5d<sub>3/2</sub> that is the white line in XANES. Especially for small Pt particles, only the 2p<sub>3/2</sub> → 5d<sub>5/2</sub> transition contributes to the absorption edge, because the 5d<sub>3/2</sub> states are fully occupied by the band narrowing.<sup>[59]</sup> Thus, Pt L<sub>3</sub> edge spectra exhibit the information on the density of empty d band states in the valence band. Additionally, XANES is sensitive to the orbital hybridization when molecules like hydrogen or oxygen adsorb on the metal or the crystal-field is changed by an altered coordination. The 1s orbital of hydrogen or rather the 2p orbital of oxygen are mixed with the d levels of Pt and alter the white line area and intensity, as well as the edge energy. The appearance of pre-edge peaks indicate the presence of highly localized electronic states that correlate with the hybridization and finally, with the coordination chemistry. XANES of model compounds facilitate definitely an almost quantitative analysis by the determination of valence states ratios.<sup>[56, 59]</sup>

### 2.3.3 X-ray Photoelectron Spectroscopy (XPS)

The chemical composition of the metal particles and the GaN surfaces was investigated *in situ* by XPS (ISISS beamline, BESSY II, Helmholtz-Zentrum Berlin, Germany). Small spherical,

large cubic, and large cuboctahedral Pt particles on *n*- and *p*-type GaN (Ga-face and N-face *n*-type) were analyzed during the temperature-programmed reduction in vacuum and hydrogen at temperatures up to 800 K and during the oxidation with oxygen at 725 K. The as-prepared samples that were treated with the oxygen plasma were used directly for the *in situ* reduction experiments, while the samples were reduced *ex situ* in hydrogen at 773 K for 3 h, transported to the beamline in nitrogen atmosphere, and oxidized *in situ* during the oxidation measurements. Additionally, a Pt foil was analyzed after the treatment with the oxygen plasma and was used to compare evolved Pt species of the foil with that of the particles. Core level spectra of O1s, N1s, C1s, Pt4f, and Ga3d were acquired with the constant photon energy of 270 eV, which corresponds to the fixed penetration depth of 0.8 nm, providing high surface-sensitivity. The escape depth was increased to 1.6 nm at the photon energy of 850 eV to compare the Pt species on the surface and in deeper layers. The reduction of the photoelectron scattering at high pressures was provided by the differentially pumped electrostatic lens system. The base pressure of the reaction chamber was  $10^{-7}$  mbar, which leads to the contamination of the sample surface by oxygen, water, carbon, and hydrocarbons. The gas pressure was adjusted to 0.5 mbar during *in situ* experiments. The quantitative analysis was performed with the CASA XPS software and peak positions, line widths, and relative peak areas were evaluated. The fitting parameters were optimized after the Shirley background subtraction and Pt4f core level spectra were analyzed using the Doniach-Sunjic asymmetric functions, the fixed spin-orbit coupling of 3.3 eV, the Pt4f<sub>5/2</sub>:Pt4f<sub>7/2</sub> ratio of 3:4, and a full width at half maximum of  $1.0 \pm 0.1$  eV for all Pt species. The relative fraction of the metallic Pt species was monitored during the thermal reduction, the reduction with hydrogen, as well as during the oxidation. The composition of the Pt particle surface was compared for the different sizes and shapes of the *n*- and *p*-type GaN samples. More experimental details are specified in Chapter 4.

XPS is generally applied for the surface studies of solid materials in heterogeneous catalysis, where the elemental composition, phase dispersion, and electronic properties are probed with high surface-sensitivity. The photoemission process is based on the photoelectric effect that emits photoelectrons from the core levels (Figure 2-12). The kinetic energy of the ejected photoelectrons is dependent on their mean free path, which determines a maximal surface-sensitivity of 0.5 nm at the kinetic energy of 50 eV (Figure 2-15).<sup>[60]</sup> The penetration depth can be altered by changing the electron kinetic energy or the angle between the sample surface and the detector.

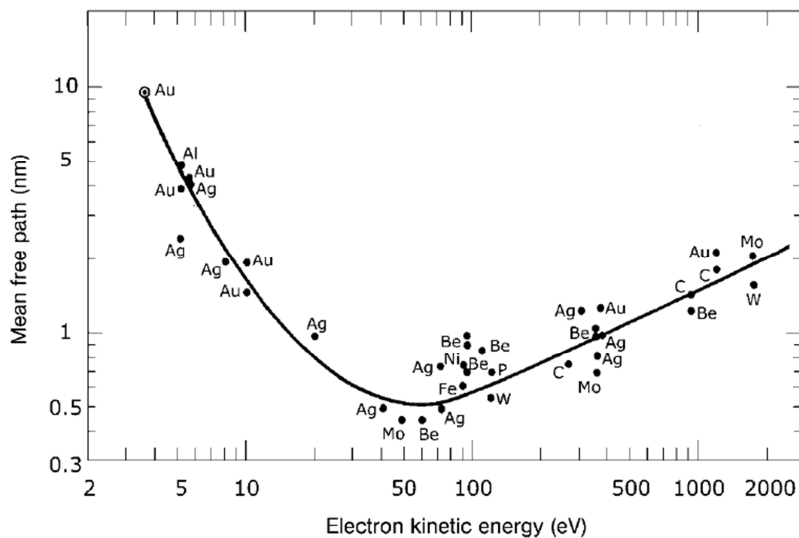


**Figure 2-15.** Electron mean free path versus the electron kinetic energy. An optimal surface-sensitivity of 0.5 nm is observed for the kinetic energy of 50 eV.<sup>[60]</sup>

The excitation of the sample by X-ray photons releases core level photoelectrons facilitating the information on the chemical environment of the atom. In contrast to the excitation with X-rays in XPS, ultraviolet irradiation leads to the ejection of photoelectrons from valence orbitals and the element bonding or work function is probed (ultraviolet photoelectron spectroscopy, UPS). Additionally, the Auger effect occurs, which results in secondary photoelectrons with a fixed and low kinetic energy (Figure 2-12 (c)). The Auger effect is the basis of the Auger electron spectroscopy (AES) that is used for elemental analysis.

The XPS setup that was used in this work contains the synchrotron source, which is focused onto the sample surface (Figure 2-16 (a)). The sample is mounted into a quartz glass holder between two metallic plates, which exhibits the electrical contact between the spectrometer and the sample. For heating, the sample backside was irradiated with a laser. After X-ray radiation, the emitted photoelectrons are directed into a hemispherical energy analyzer, which filters the electrons regarding their kinetic energy by the application of a particular pass energy.<sup>[61]</sup>

The electron kinetic energies are measured with respect to the Fermi level of the detector due to the electrical contact (Figure 2-16 (b)). Therefore, the work function of the spectrometer has to be considered in the evaluation of the core level binding energy (Equation 2-31).<sup>[61, 62]</sup>



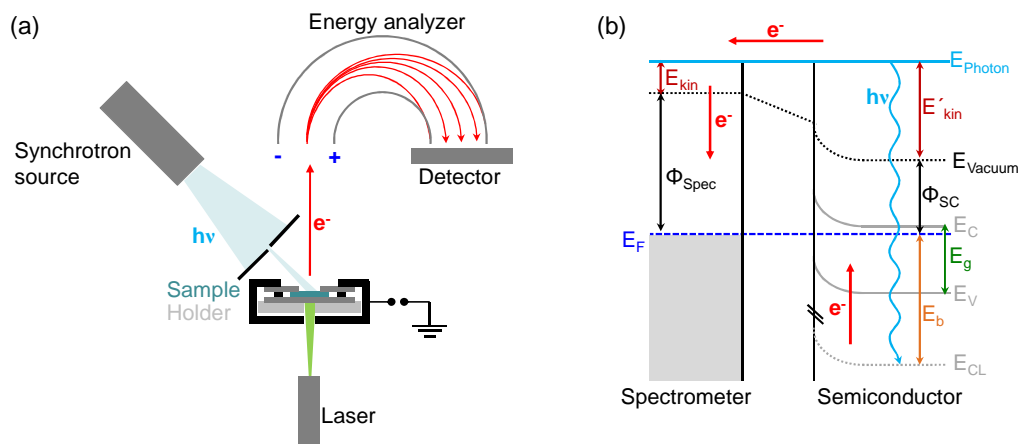


**Figure 2-16.** Illustration of (a) the XPS setup components with the quartz glass holder, the laser heating, and the hemispherical analyzer. (b) The electrical contact between an  $n$ -type semiconducting sample and the spectrometer is provided by the energetic alignment of the electronic band structure.

$$E_{kin} = h\nu - E_b - \Phi_{Spec} \quad (\text{Equation 2-31})$$

Where  $E_{kin}$  is the electron kinetic energy,  $h\nu$  the photon energy,  $E_b$  the core level binding energy, and  $\Phi_{Spec}$  the work function of the spectrometer.

When a wide bandgap semiconductor is measured with XPS, sample charging may occur, which originates from the minor electron conductivity that cannot compensate the core hole after photoemission. Thus, the remained positive potential decelerates the outgoing photoelectrons, which results in a lower kinetic energy and simultaneously in a higher binding energy. The charging effect can be confused with a chemical shift, leading to wrong interpretations of the spectra. In the case of charging, all core level spectra are normalized to a reference compound that can be the C1s peak.<sup>[62]</sup> In this work, metallic contacts were evaporated onto the GaN surfaces to ensure the electrical contact with the detector and charging was not observed.

One important parameter for the analysis of the samples by XPS is the chemical shift of the core level binding energy. A shift to higher energies is expected with an increasing oxidation state, because the remained electrons in the excited atom are more attracted by the positively charged nucleus. Theoretically, the frozen orbital model (Koopmann's theorem) is applied for the photoemission process, which defines similar orbital energies before and after the removal of one core level electron. But this is not true in reality due to the appearance of relaxation and secondary electron emission processes. Consequently, two states contribute to the core level binding energy, the initial and final state of an atom with  $N$  and  $N-1$  electrons,

respectively (Figure 2-17). The chemical shift includes the binding energies of both states and the initial state can overwhelm the final state or the other way round, which leads to different interpretations (Equation 2-32). As a result, the simple ESCA (electron spectroscopy for chemical analysis) approach cannot be generalized for all photoemission experiments.<sup>[61-63]</sup>

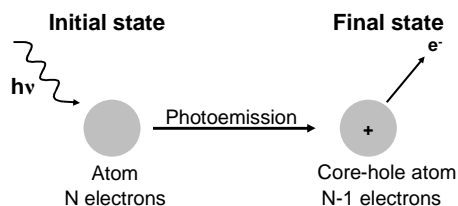


**Figure 2-17.** Scheme of the initial and final state of an atom before and after X-ray photoemission.

$$E_b \cong E_f(N-1) - E_i(N) \quad (\text{Equation 2-32})$$

Where  $E_b$  is the measured core level binding energy,  $E_f(N-1)$  and  $E_i(N)$  are the core level binding energies of the atom with  $N-1$  and  $N$  electrons in the final and initial state, respectively.

The surface core level shifts (SCLS) originate from the difference of the initial and final state and they describe electronic differences of bulk and surface atoms. Bulk atoms are able to compensate the core hole after photoemission, while the atoms on the surface cannot compensate the positive charge. The distribution of the electrons in localized  $d$  orbitals is crucial for the description of the binding energy shifts. SCLS to higher energy occur typically for metallic surface atoms with less than a half-filled  $d$  band, while shifts to lower energies appear for metals with more than half-filled  $d$  orbitals.<sup>[62]</sup> The shift to higher binding energy was observed e.g. for cesium atoms on the surface and the quantity of the shift could be estimated by the Born-Haber cycle (Figure 2-18).<sup>[64]</sup>

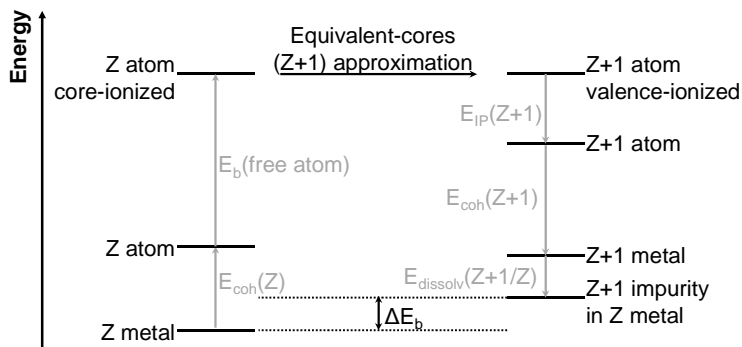


**Figure 2-18.** Born-Haber cycle for the photoemission process with the atomic number  $Z$ , the cohesive energy  $E_{coh}$ , the core level binding energy of the free atom  $E_b(\text{free atom})$ , the ionization potential  $E_{IP}$ , the solvation energy  $E_{dissolv}$ , and the core level binding energy of the metal  $E_b$ .

Additionally, adsorbate-induced SCLS of transition metals are explained by the dominant final state effects. The adsorbate-induced electron abstraction from or donation into the d band of the metal or adsorbate-induced electron relaxation was supposed to change the binding energy of the metal core level. Due to the Coulomb interaction between the valence and the core level electrons, the effect of adsorbed molecules that interact only with the valence orbitals can be detected with XPS.<sup>[62]</sup> A larger positive shift in the binding energy of Pt was observed when CO is adsorbed in comparison to hydrogen, because CO interacts more intense with the Pt d orbitals.<sup>[65]</sup> This shift is caused by the final state effect, where CO is weaker bonded to the excited Pt atom, which is chemically equivalent to the Au atom. Similar adsorbate-induced SCLS were also found for CO and oxygen on Pd<sup>[66]</sup> and for various electronegative and -positive adsorbates on Pt.<sup>[67]</sup>

Small metal particles below 1-2 nm show binding energy shifts to higher values compared to the bulk metal. Such shifts are assigned to the pronounced final state effect, where the core hole cannot be screened anymore by the conduction electrons in the small particle. In addition, an initial state effect contributes partially to the observed shift, which originates from the zero energy reference. The zero point refers to the Fermi edge of the main ingredient like the support and not to the Fermi level of the small metal particle. Due to the lattice contraction in small particles, a broadening of the core level peaks can be observed with decreasing particle size. The core hole can be generally balanced by electrons from neighboring atoms (polarization by extra-atomic relaxation), which can be atoms from the particle itself or from the support. Therefore, the particle-support interactions determine both the direction and the quantity of the core level binding energy shift.<sup>[62, 68-70]</sup>

Dominant final state effects lead also to shake-up and shake-off peaks, which may appear additionally to core level peaks in a spectrum at higher binding energies.<sup>[61]</sup> In this case, the photoelectron loses energy to electrons, which are excited into higher empty bonding (shake-up) or nonbonding (shake-off) states. Other ghost peaks can be detected as well, originating from misaligned instrumental components or from high pressures, where additional photoelectrons are formed by the X-ray interaction with gas molecules.<sup>[31, 62]</sup>

The investigation of the core level spectra at elevated temperatures or in gaseous environment at high pressures reveals the clarification of possible X-ray-induced damage or changes of the sample, which may result in wrong interpretations. For example, the reduction of Au particles supported on TiO<sub>2</sub> was observed in oxygen atmosphere, where the beam-induced formation of oxygen vacancies on TiO<sub>2</sub> caused a subsequent oxygen spillover from the particles to the support.<sup>[71, 72]</sup>

The core level peak intensity in XPS is among others a function of the X-ray photon penetration depth and thus, of the probed atom concentration (Equation 2-33).<sup>[61]</sup> Additionally, the ionization cross-section is included that describes the probability of an electron for the emission process and varies for different atoms.

$$I = F_X S(E_k) \sigma(E_k) \int_0^{\infty} n(z) e^{-\frac{z}{\lambda(E_k) \cos \theta}} dz \quad (\text{Equation 2-33})$$

Where  $I$  is the peak intensity,  $F_X$  the photon flux,  $S(E_k)$  the detector efficiency or transmission function,  $\sigma(E_k)$  the cross-section,  $n(z)$  the atom concentration,  $z$  the X-ray penetration depth,  $\lambda(E_k)$  the electron mean free path, and  $\theta$  the take-off angle (angle between the photoelectron and the surface normal).

The line shape of the core level peaks contains normally the convolution of the Gaussian function with Lorentzian contributions, which model the measurement process and the natural line shape, respectively. Additionally, the line asymmetry becomes more important for d metals like Pt due to the increased density of electronic states at the Fermi level. The asymmetry originates from the intrinsic anisotropy of the photoemission process, which is induced by the many-electron interaction of conduction electrons with photons that are formed from filling the core hole with electrons. The Doniach-Sunjic asymmetry is used as an equivalent to the Lorentzian function for the peak fitting of the Pt4f core level spectra in this work (Equation 2-34).<sup>[73, 74]</sup>

$$Y(\varepsilon) \cong \frac{\Gamma(1-\alpha)}{\left(\varepsilon^2 + \gamma^2\right)^{\frac{1-\alpha}{2}}} \cos \left[ \frac{\pi\alpha}{2} + (1+\alpha) \tan^{-1} \left( \frac{\varepsilon}{\gamma} \right) \right] \quad (\text{Equation 2-34})$$

Where  $Y(\varepsilon)$  is the line shape,  $\Gamma$  the gamma function,  $\alpha$  the asymmetry factor,  $\varepsilon$  the relative energy referred to the maximal energy without the lifetime broadening, and  $\gamma$  is the natural line width.

The quantitative interpretation of the core level spectra requires the chemical and physical understanding of the sample during photoemission and modeling of the spectral envelope by an exact peak fitting. One peak may consist of various underlying lines resulting from different chemical states of the probed element. Parameters like the peak width and relative intensity ratios are set to fixed values to direct the fitting for analysis. Additionally, a suitable background correction has to be applied that arises from energy loss processes and inelastic scattering.<sup>[75]</sup> In this work, the Shirley background was used with an iterative algorithm for subtraction.

The high-pressure XPS setup of the ISSS beamline at BESSY II contained a synchrotron soft X-ray beam with a high photon flux of up to  $6 \times 10^{10}$  photons  $s^{-1}$  and a spot size of ca.  $150 \times 80 \mu\text{m}$ , which hit the sample surface with an angle of  $55^\circ$  (Figure 2-19).<sup>[76]</sup>

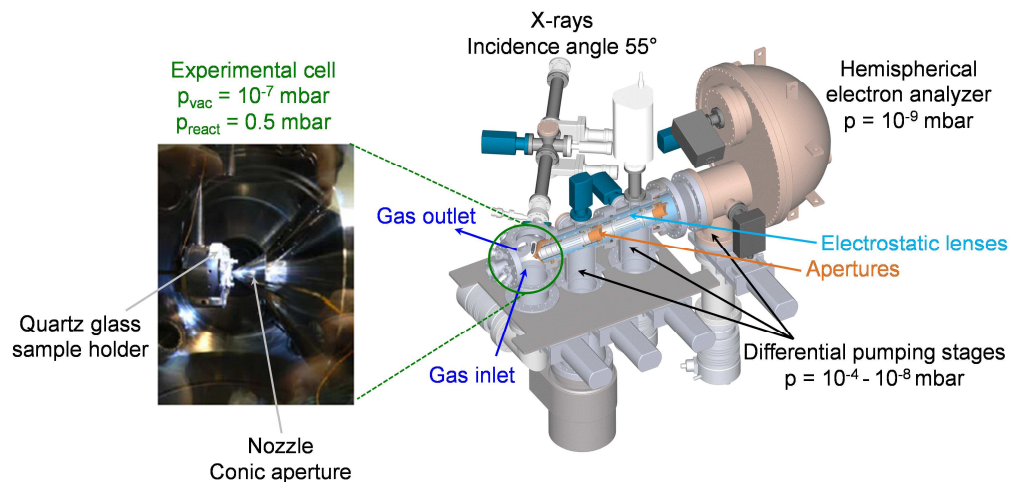


**Figure 2-19.** Illustration of the high-pressure XPS setup at the ISSS beamline (BESSY II).<sup>[76]</sup>

The quartz glass sample holder was mounted directly in front of the conic aperture (nozzle), which transferred the emitted photoelectrons into the differentially pumping system (Figure 2-19). An arrangement of electrostatic lenses was used for focusing the photoelectron to the hemispherical analyzer (SPECS) (Figure 2-20). This setup configuration was essential to minimize the contributions of the photoelectron scattering on gas molecules at high pressures.<sup>[29, 77, 78]</sup> The sample could be transferred into the experimental chamber via a load-lock system, providing a base pressure of  $10^{-7}$  mbar inside the experimental cell.

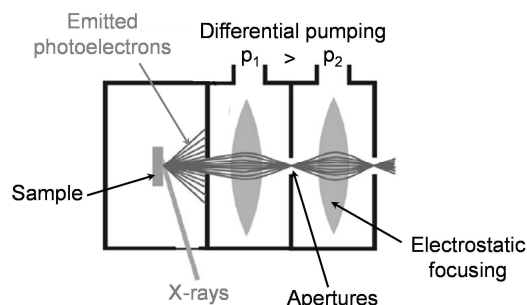


**Figure 2-20.** The principle of focusing the emitted photoelectrons by electrostatic lenses in the differentially pumping stages.<sup>[78]</sup>

The Pt4f core level spectra were used in this study to evaluate the surface composition of the particles in dependency on the electrical doping of the underlying GaN. Therefore, the present Pt species in the spectrum had to be carefully assigned to the right Pt oxidation state, which was performed on the basis of previous XPS results. Various Pt catalysts and single crystals were investigated and different Pt species were observed that were e.g. metallic Pt, electron-deficient Pt, Pt with adsorbed oxygen atoms, and oxidized Pt with oxidation states of Pt<sup>+2</sup>-Pt<sup>+4</sup> (Table 2-6).<sup>[79-87]</sup> The Pt4f core level spectrum contains generally a peak doublet, which results from the spin-orbit splitting with the electron momentum of  $j = l + s$ . The doublet describes the Pt4f<sub>7/2</sub> and Pt4f<sub>5/2</sub> peak according to the orbital momentum of  $l = 3$  for the f orbital and the electron spin momentum of  $s = \pm 1/2$ . The intensity ratio for Pt4f<sub>7/2</sub>:Pt4f<sub>5/2</sub> is 4:3 due to the multiplicity of  $2j + 1$ .<sup>[61]</sup>

**Table 2-6.** Core level binding energies of the Pt4f<sub>7/2</sub> peak for various Pt species of different samples.

Species	Pt4f <sub>7/2</sub> / eV	Sample	Treatment
Pt <sup>0</sup>	71.2	Pt(111)	<sub>[79,80]</sub>
	71.2	PtO <sub>2</sub> -Pt(111)	1 bar O <sub>2</sub> , 900 K <sup>[79]</sup>
	71.2	PtO <sub>2</sub> ·xH <sub>2</sub> O-Pt(111)	HNO <sub>3</sub> , 370 K <sup>[79]</sup>
	71.6	30 wt.% Pt/C	Commercial <sup>[81]</sup>
	71.0	1 wt.% Pt/TiO <sub>2</sub> nanowires	Impregnation (4 nm Pt) <sup>[82]</sup>
	71.1	Pt/SiO <sub>2</sub> /Si(001)	O <sub>2</sub> plasma (3 nm Pt) <sup>[83]</sup>
	71.0	1 wt.% Pt/CeO <sub>2</sub>	Combustion <sup>[84]</sup>
	71.0	1 wt.% Pt/CeO <sub>2</sub>	1 bar air, 1073 K <sup>[84]</sup>
	70.7	Oxidized Pt foil	HNO <sub>3</sub> , 298 K <sup>[85]</sup>
	70.7	Oxidized Pt foil	Electrochemical oxidation <sup>[85]</sup>
Pt <sup>δ+</sup>	71.4	1 wt.% Pt/KL zeolite	Impregnation <sup>[86]</sup>
	71.9	1 wt.% Pt/KL zeolite	Ion exchange <sup>[86]</sup>
Pt-O <sub>ads</sub>	71.2	O <sub>ads</sub> -Pt(111)	10 <sup>-6</sup> mbar O <sub>2</sub> , 298 K <sup>[79]</sup>
	71.8	Oxidized Pt foil	HNO <sub>3</sub> , 298 K <sup>[85]</sup>
	71.6	Oxidized Pt foil	Electrochemical oxidation <sup>[85]</sup>
Pt <sup>2+</sup>	72.3	PtO	<sub>[80]</sub>
	72.9	30 wt.% Pt/C	Commercial <sup>[81]</sup>
	72.4	1 wt.% Pt/TiO <sub>2</sub> nanowires	Impregnation (3.7 nm Pt) <sup>[82]</sup>
	72.2	Pt/SiO <sub>2</sub> /Si(001)	O <sub>2</sub> plasma (3 nm Pt) <sup>[83]</sup>
	73.4	Pt/ZrO <sub>2</sub> /Si(001)	O <sub>2</sub> plasma (3 nm Pt) <sup>[83]</sup>
	71.9	1 wt.% Pt/CeO <sub>2</sub>	Combustion <sup>[84]</sup>
	72.9	1 wt.% Pt/CeO <sub>2</sub>	1 bar air, 1073 K <sup>[84]</sup>
	73.4	Oxidized Pt foil	HNO <sub>3</sub> , 298 K <sup>[85]</sup>
	73.3	Oxidized Pt foil	Electrochemical oxidation <sup>[85]</sup>
	Pt <sup>3+/Pt<sup>8/3+</sup></sup>	73.6	Pt-PtO <sub>x</sub> /Si(100)
Pt <sup>4+</sup>	74.1	Bulk PtO <sub>2</sub>	<sub>[79]</sub>
	74.4	Pt(OH) <sub>4</sub> -Pt(111)	Electrochemical oxidation <sup>[79]</sup>
	74.5	30 wt.% Pt/C	Commercial <sup>[81]</sup>
	74.2	1 wt.% Pt/TiO <sub>2</sub> nanowires	Impregnation (3.7 nm Pt) <sup>[82]</sup>
	73.8	Pt/SiO <sub>2</sub> /Si(001)	O <sub>2</sub> plasma (3 nm Pt) <sup>[83]</sup>
	74.5	Pt/ZrO <sub>2</sub> /Si(001)	O <sub>2</sub> plasma (3 nm Pt) <sup>[83]</sup>
	74.3	1 wt.% Pt/CeO <sub>2</sub>	Combustion <sup>[84]</sup>
	74.6	1 wt.% Pt/CeO <sub>2</sub>	1 bar air, 1073 K <sup>[84]</sup>
	74.2	Oxidized Pt foil	HNO <sub>3</sub> , 298 K <sup>[85]</sup>
	74.1	Oxidized Pt foil	Electrochemical oxidation <sup>[85]</sup>

## 2.4 Catalytic Performance

### 2.4.1 Ethene Hydrogenation as Probe Reaction

The catalytic activity of GaN-supported Pt particles was tested in the hydrogenation of ethene to ethane, which shows a high sensitivity towards small amounts of metal. As ethene reacts with hydrogen solely on metallic surfaces, the reaction occurs only on Pt and not on GaN, facilitating the study of charge transfer effects between the support and the metal. The small sample area of the GaN substrate with an edge length of  $0.9 \times 0.9$  cm limits the overall Pt coverage and thus, the catalytic yield on ethane. The reaction conditions were adjusted to gain a high reaction rate and the reaction setup was designed to increase the ethene conversion to detectable levels. The kinetic studies were performed at moderate temperatures of 335-355 K and the reactant gas mixture consisted of an ethene to hydrogen ratio of roughly 1 to 60 with 8 mbar ethene and 470 mbar hydrogen balanced with nitrogen to atmospheric pressure. The excess of hydrogen was used to obtain a fast hydrogenation rate according to the assumption of reaction orders of one for hydrogen and a negative order for ethene.<sup>[88-90]</sup> Moreover, a high hydrogen concentration was supposed to prevent the particle deactivation by the deposition of carbonaceous contaminants during reaction. The activation of the Pt-GaN catalysts between each temperature-dependent kinetic measurement was essential to get reproducible results. Therefore, the activated Pt-GaN catalysts could be compared for the *n*- and *p*-type GaN support at different temperatures with and without the optical excitation of the support.

The following procedure was typically performed for the activation between each kinetic experiment. Hydrogen (1 bar) was continuously directed over the catalyst at 425 K for 6 h before cooling down the reactor to the reaction temperature (335-355 K). The reactant gas mixture was continuously introduced until a constant flow was observed. Afterwards, the reactor setup was switched to batch-operation and the accumulation of ethane was monitored over the reaction time (detailed setup description in section 2.4.2).

The kinetic experiments under irradiation of the GaN support were performed with the same procedure, and only the optical source was switched on during the recycling mode. A UV lamp (Benda, 6 W) with a constant wavelength of 254 nm was used to illuminate the Pt-GaN catalysts through a UV light transparent window. The UV light-induced decomposition of the gas molecules was not detected at 254 nm, which facilitated the assignment of the different catalytic reactivity with and without illumination to the effect from the *n*- and *p*-type doping



of GaN. The dissociation of ethene and hydrogen by the radiation with high-energy photons was observed at wavelengths of 193 nm and 85 nm, respectively.<sup>[91, 92]</sup>

To verify the catalytic conversion of the blank GaN surfaces in comparison to the samples functionalized with Pt particles, reference surfaces of *n*- and *p*-type GaN were prepared by exactly the same preparation method as the Pt-GaN samples. PVP ( $1.4 \times 10^{-6}$  mol) in ethanol (50  $\mu$ l) was spin-coated onto GaN and the samples were heated for solvent evaporation, treated with the oxygen plasma, and finally heated in vacuum. The reference samples did not show catalytic activity towards the hydrogenation of ethene. However, a small concentration of ethane was detected in the setup even without any sample, which was maximal 3% of the nanoparticle activity. This background reaction was subtracted from the Pt-GaN samples for all data shown within this work.

The conversion of ethene to ethane was evaluated from ethane accumulation curves during recycling of the gas mixture (Equation 2-35). The catalytic activity was determined by the TOF of accumulated ethane molecules under differential conditions (ethene conversion < 10%) (Equation 2-36). The number of accumulated ethane molecules per second was calculated by the reaction rate that was estimated from the slope, where the ethane concentration was plotted versus the recycle time (Equation 2-37).

$$X(C_2H_4)_t = \frac{c(C_2H_6)_t}{c(C_2H_6)_t + c(C_2H_4)_t} \quad (\text{Equation 2-35})$$

$$TOF = \frac{N(C_2H_6)_{acc}}{N_{Surface Pt}} \quad (\text{Equation 2-36})$$

$$N(C_2H_6)_{acc} = V_R r N_A \quad \text{with} \quad r = \frac{dc(C_2H_6)}{dt} \quad (\text{Equation 2-37})$$

Where  $X$  is the conversion of ethene,  $c$  the concentration of ethane or ethene,  $t$  the recycle time,  $TOF$  the turnover frequency,  $N(C_2H_6)_{acc}$  the number of accumulated ethane molecules per s,  $N_{Surface Pt}$  the number of Pt surface sites per sample,  $V_R$  the recycle reactor volume,  $r$  the reaction rate, and  $N_A$  is the Avogadro constant.

The temperature-dependent TOFs allowed the determination of the apparent activation energies by means of the Arrhenius equation (Equation 2-38). Mass transport limitations by the film diffusion of the gas molecules from the gas phase onto the metal surface were not observed within the used temperature range of 335-355 K.

$$\begin{aligned} TOF &= A_0 e^{\frac{-E_{a,app}}{RT}} \\ \ln(TOF) &= \ln(A_0) - \frac{E_{a,app}}{R} \frac{1}{T} \\ E_{a,app} &= -mR \end{aligned} \quad (\text{Equation 2-38})$$

Where  $TOF$  is the turnover frequency,  $A_0$  the pre-exponential factor,  $E_{a,app}$  the apparent activation energy,  $R$  the universal gas constant,  $T$  the temperature, and  $m$  is the slope.

The hydrogenation of ethene to ethane (2-1) is normally used as a model reaction for the understanding of the hydrogenation of olefins on metal surfaces, as well as for the testing of model catalysts in heterogeneous catalysis.<sup>[93]</sup>



Although ethene hydrogenation is one of the simplest reactions, the relevant mechanistic pathways are still unclear. Various experimental and theoretical approaches were investigated in the last 55 years to elucidate the key intermediates and adsorbed hydrocarbons on Pt crystal surfaces and Pt nanoparticles (Table 2-7).<sup>[41, 89, 90, 94-118]</sup>

**Table 2-7.** Summary of the experimental and theoretical results of the last 55 years, showing the reactive surface species, key intermediates, and rate-determining steps in the hydrogenation of ethene on Pt catalysts (chronologically ordered from 1956 to 2011).

Sample	Method	Feature results
Pt/support <sup>(a)</sup> [89]	Kinetics	Irreversible step: $C_2H_4^* + H^* \rightarrow C_2H_5^*$
Pt/Al <sub>2</sub> O <sub>3</sub> <sup>[94]</sup>	IR <sup>(b)</sup>	$\pi$ -C <sub>2</sub> H <sub>4</sub> as key intermediate (203 K)
Pt(111) <sup>[95]</sup>	TPD <sup>(c)</sup>	T < 300 K: di- $\sigma$ -C <sub>2</sub> H <sub>4</sub> , T > 300 K: *CCH <sub>3</sub>
O/Pt(111)		T < 250 K: di- $\sigma$ - and $\pi$ -C <sub>2</sub> H <sub>4</sub> , T > 250 K: decomposition (H <sub>2</sub> , H <sub>2</sub> O, CO <sub>2</sub> )
Pt(111) <sup>[90]</sup>	LEED/TDS <sup>(d)</sup>	*CCH <sub>3</sub> as spectator
Pt(111) <sup>[96]</sup>	TPD <sup>(c)</sup>	C <sub>2</sub> H <sub>4</sub> self-hydrogenation (150 K)
H/Pt(111)		Lower barrier for C <sub>2</sub> H <sub>4</sub> self-hydrogenation (150 K) *CCH <sub>3</sub> /CH <sub>x</sub> as active species
Pt/Al <sub>2</sub> O <sub>3</sub> <sup>(e)</sup> [97]	IR <sup>(b)</sup>	*CCH <sub>3</sub> at 300 K
Pt(111) <sup>[98]</sup>	Kinetics	*CCH <sub>3</sub> (65 mbar C <sub>2</sub> H <sub>4</sub> , 65 mbar H <sub>2</sub> , 300 K)
(5×20)Pt(100)		More *CCH <sub>3</sub> (65 mbar C <sub>2</sub> H <sub>4</sub> , 65 mbar H <sub>2</sub> , 300 K) *CCH <sub>3</sub> as poison
Pt(111) <sup>[99]</sup>	Theory <sup>(f)</sup>	rds: $C_2H_4^* + H^* \rightarrow C_2H_5^*$ *CCH <sub>3</sub> as spectator
Pt(110) <sup>[100]</sup>	EELS <sup>(g)</sup>	di- $\sigma$ - and $\pi$ -C <sub>2</sub> H <sub>4</sub> (93 K)
H/Pt(110)		Mainly $\pi$ -C <sub>2</sub> H <sub>4</sub> and physisorbed C <sub>2</sub> H <sub>4</sub> (93 K)
Pt(111) <sup>[101]</sup>	Theory <sup>(h)</sup>	Decomposition: $CH_2CH_2^* \rightarrow *CHCH_3 \rightarrow *CCH_3 \rightarrow *CHCH_2 \rightarrow *CHCH \rightarrow *CCH \rightarrow *C_2 \rightarrow 2C^*$
K/Pt(111)		Stabilization of H* and H-rich species
Pt(111) <sup>[102]</sup>	Theory <sup>(i)</sup>	di- $\sigma$ -C <sub>2</sub> H <sub>4</sub> most stable adsorption mode
Pt(110)		di- $\sigma$ - and $\pi$ -C <sub>2</sub> H <sub>4</sub> stable adsorption mode
Pt/CabOSil <sup>[103]</sup>	Kinetics	T < 273 K: Noncompetitive adsorption T > 273 K, C <sub>2</sub> H <sub>4</sub> < 95 mbar: Competitive adsorption Irreversible step: $C_2H_5^* + H^* \rightarrow C_2H_6$
Pt(111) <sup>[41, 104]</sup>	SFG <sup>(j)</sup>	$\pi$ -C <sub>2</sub> H <sub>4</sub> as key intermediate *CCH <sub>3</sub> as spectator
Pt(111) <sup>[105]</sup>	IRAS <sup>(k)</sup>	*CCH <sub>3</sub> for H-transfer to physisorbed C <sub>2</sub> H <sub>4</sub> (< 200 K, vac)
Pt(111) <sup>[106]</sup>	IRAS <sup>(k)</sup>	di- $\sigma$ - and $\pi$ -C <sub>2</sub> H <sub>4</sub> (112 K, vac)
CCH <sub>3</sub> /Pt(111)		Less $\pi$ -C <sub>2</sub> H <sub>4</sub> (112 K, vac)
Pt(111) <sup>[107]</sup>	Kinetics <sup>(l)</sup>	Physisorbed C <sub>2</sub> H <sub>4</sub> as key intermediate
H/Pt(111)		More physisorbed C <sub>2</sub> H <sub>4</sub> on surface *CCH <sub>3</sub> as poison
(1×2)Pt(110) <sup>[108]</sup>	Calorimetry	*CCH <sub>3</sub> most stable species (300 K)
Pt(111) <sup>[109]</sup>	Theory <sup>(f)</sup>	*CCH <sub>3</sub> destabilization on low-coordinated sites
Pt/SiO <sub>2</sub> <sup>[110]</sup>	Theory <sup>(m)</sup>	rds: $C_2H_5^* + H^* \rightarrow C_2H_6$

Pt(111) <sup>[111]</sup> CCH <sub>3</sub> /Pt(111)	IRAS <sup>(k)</sup>	di- $\sigma$ -C <sub>2</sub> H <sub>4</sub> and *CCH <sub>3</sub> (1 mbar C <sub>2</sub> H <sub>4</sub> , 65 mbar H <sub>2</sub> , 220-320 K) only *CCH <sub>3</sub> (1 mbar C <sub>2</sub> H <sub>4</sub> , 65 mbar H <sub>2</sub> , 220-320 K) Rate independent of di- $\sigma$ -C <sub>2</sub> H <sub>4</sub> and *CCH <sub>3</sub>
Pt <sub>7</sub> and Pt <sub>10</sub> <sup>[112]</sup>	Theory <sup>(n)</sup>	rds: C <sub>2</sub> H <sub>5</sub> * + H* $\rightarrow$ C <sub>2</sub> H <sub>6</sub>
Pt/Al <sub>2</sub> O <sub>3</sub> <sup>[113]</sup>	IR <sup>(b)</sup>	C <sub>2</sub> H <sub>5</sub> * as key intermediate (H <sub>2</sub> /N <sub>2</sub> flow, C <sub>2</sub> H <sub>4</sub> pulses, 432-473 K)
Pt/support <sup>(a,o)[114]</sup>	XANES	Small particles: *CCH <sub>3</sub> (300 K, 250 mbar C <sub>2</sub> H <sub>4</sub> ) Large particles: di- $\sigma$ - and $\pi$ -C <sub>2</sub> H <sub>4</sub> (300 K, 330 mbar C <sub>2</sub> H <sub>4</sub> )
Pt/SBA-15 <sup>(p)[115]</sup>	IR <sup>(b)</sup>	Small particles: di- $\sigma$ -C <sub>2</sub> H <sub>4</sub> , $\pi$ -C <sub>2</sub> H <sub>4</sub> , and *CCH <sub>3</sub> (298 K, atm) Large particles: less $\pi$ -C <sub>2</sub> H <sub>4</sub> and mainly *CCH <sub>3</sub> (298 K, atm)
Pt(111) <sup>[116]</sup> N/Pt(111)	IRAS <sup>(k)</sup>	di- $\sigma$ -C <sub>2</sub> H <sub>4</sub> (90 K) di- $\sigma$ - and $\pi$ -C <sub>2</sub> H <sub>4</sub> (90 K)
Pt(111) <sup>[117]</sup> Pt(211)	Theory <sup>(n)</sup>	*CCH <sub>3</sub> most stable species *CCH <sub>3</sub> most stable species
Pt <sup>[118]</sup>	Theory <sup>(q)</sup>	*CCH <sub>3</sub> (33 mbar C <sub>2</sub> H <sub>4</sub> , 200 mbar H <sub>2</sub> , 336 K) Fast step: $\pi$ -C <sub>2</sub> H <sub>4</sub> * + H* $\rightarrow$ C <sub>2</sub> H <sub>5</sub> * $\rightarrow$ C <sub>2</sub> H <sub>6</sub> No single rds

<sup>(a)</sup> Silica, silica-alumina, and alumina as supports. <sup>(b)</sup> Infrared spectroscopy. <sup>(c)</sup> Temperature-programmed desorption. <sup>(d)</sup> Low energy electron diffraction and thermal desorption spectroscopy. <sup>(e)</sup> 1.9 nm Pt particles. <sup>(f)</sup> Atomic superposition and electronic delocalization molecular orbital theory. <sup>(g)</sup> Electron energy loss spectroscopy. <sup>(h)</sup> First-principle calculations and hierarchical multiscale methodology. <sup>(i)</sup> Extended Hückel calculations. <sup>(j)</sup> Vibrational sum frequency generation spectroscopy. <sup>(k)</sup> Infrared reflection absorption spectroscopy. <sup>(l)</sup> Reactants deposited by molecular beam. <sup>(m)</sup> Monte Carlo simulations. <sup>(n)</sup> Density functional theory. <sup>(o)</sup> 0.6-3.0 nm particles. <sup>(p)</sup> 1.7-7.1 nm particles. <sup>(q)</sup> First-principle calculations and hierarchical multiscale methodology.

The adsorption of ethene on Pt was found to be sensitive to the reaction conditions and three adsorption modes were observed, the di- $\sigma$ -, the  $\pi$ -bound, and a weakly adsorbed or physisorbed ethene (Table 2-7). Calculations revealed that the di- $\sigma$ -bound ethene species was the most stable adsorption geometry at low temperatures on Pt(111), while both the di- $\sigma$ - and  $\pi$ -bonded ethene were stabilized on the more open surface Pt(110) (Figure 2-21).<sup>[102]</sup>

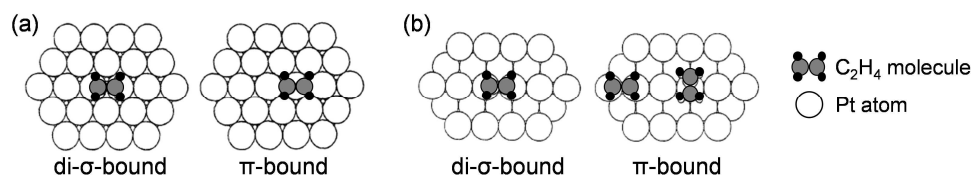


**Figure 2-21.** Adsorption geometries of ethene on the (a) Pt(111) and (b) Pt(110) surface at low temperature.<sup>[102]</sup>

The adsorption of ethene occurs via attractive and repulsive interactions between the d orbitals of Pt and the HOMO,  $\pi$  and LUMO,  $\pi^*$  of ethene (Figure 2-22).<sup>[102]</sup> The free ethene contains  $sp^2$  hybrid orbitals that change to  $sp^3$  orbitals due to adsorption. The altered hybridization is true for both the di- $\sigma$ - and  $\pi$ -bound ethene, but it is more pronounced for di- $\sigma$ -bonded ethene. Thus, the energy gap between the bonding and antibonding orbitals of ethene becomes smaller. The interaction of ethene with Pt includes the two-electron attraction (filled Pt d orbitals and empty ethene  $\pi^*$  orbital, as well as empty Pt d orbitals and occupied ethene  $\pi$  orbital). Simultaneously, the four-electron repulsion occurs between filled d orbitals of Pt and the occupied  $\pi$  orbital of ethene.

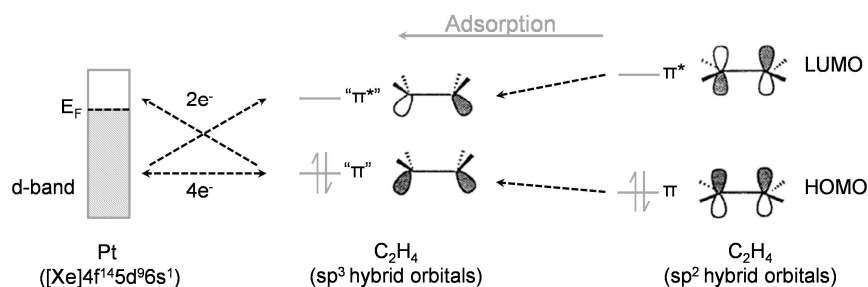


**Figure 2-22.** Relevant orbitals for the ethene-Pt interaction during the adsorption of ethene onto the Pt surface with the two-electron attraction and four-electron repulsion between empty and occupied Pt d orbitals and the  $\pi$  (HOMO) and  $\pi^*$  orbital (LUMO) of ethene.<sup>[102]</sup>

After the adsorption of ethene and hydrogen onto the Pt surface, the next step includes the reaction of the adsorbed ethene with the surface metal hydride (adsorbed in 3-fold hollow sites), forming the surface ethyl species (2-2, the star marks the adsorption onto the Pt surface).



Considering one single active site on Pt, the formation of the surface ethyl may occur via the H migration onto adsorbed ethene or via the ethene insertion into the Pt-H bond. In the case of ethene insertion, the coplanar arrangement of the Pt, H, and C atoms leads to the formation of a four-center transition state and finally, to the surface ethyl (Figure 2-23 (a)). The involved orbitals in the transition state consist of the Pt  $d_{x^2-y^2}$  orbital, the s orbital of H, and the  $\pi$  orbital of ethene, which leads to repulsive interactions between H and  $C_\beta$  as a result of their symmetry, preventing the C-H bond formation (Figure 2-23 (b)). The mixing with the  $\pi^*$

orbital of ethene enhances the attractive interactions that facilitates the H-C<sub>β</sub> bond formation.<sup>[119]</sup>

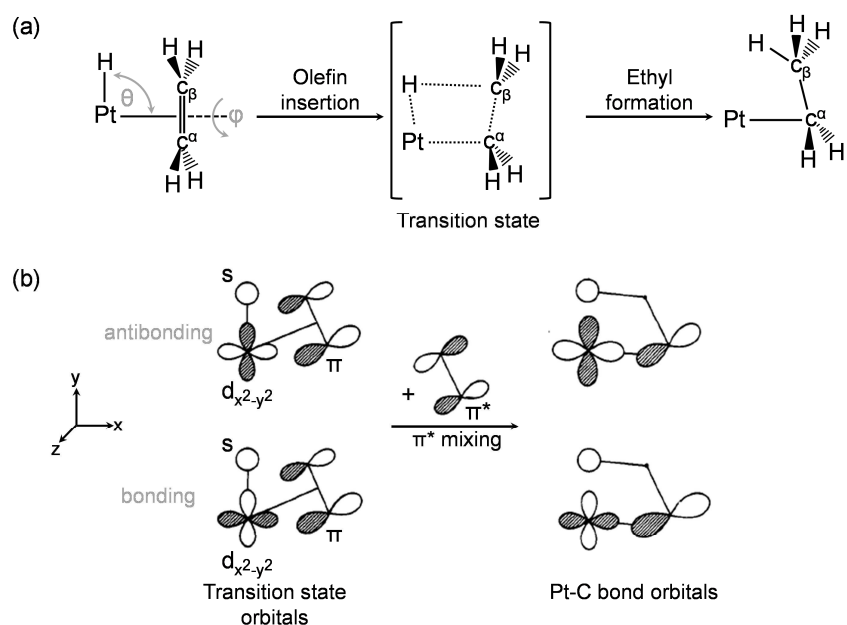


**Figure 2-23.** Schematic illustration of (a) the ethene insertion into the Pt-H bond via a four-center transition state for the formation of the surface ethyl and (b) the involved orbitals.<sup>[119]</sup>

The description of the orbitals during the first hydrogenation step becomes different in the case of a Pt surface with two or more vicinal Pt atoms. The transition state shows a five-center complex with a long C<sub>β</sub>-H bond that is stabilized by a second Pt atom (Figure 2-24 (pale grey highlighted orbitals)) In addition to the bonding orbitals, the antibonding σ orbital between C<sub>β</sub> and H contributes to the stabilization of the transition state. The bonding orbital between Pt and C<sub>α</sub> does not change its energy by the transition state formation (Figure 2-24 (dark grey highlighted orbital)).<sup>[99]</sup>

In the next elementary step, the surface ethyl reacts with the Pt hydride to ethane that desorbs from the surface (2-3).



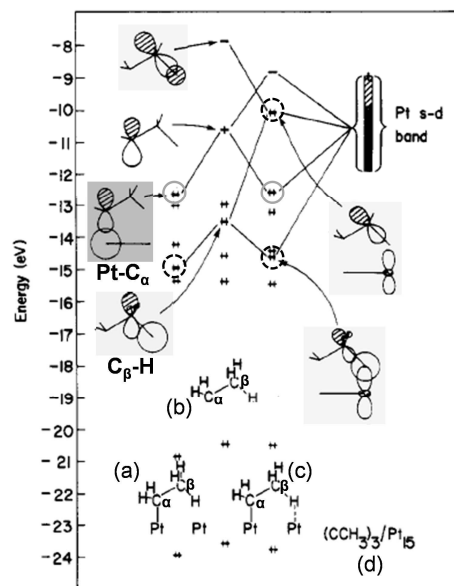


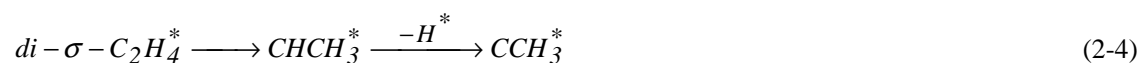
**Figure 2-24.** Orbital diagram for the hydrogenation of ethene to ethyl on an ethylidyne-covered Pt surface with (a) the surface ethyl, (b) the free ethyl radical of the transition state, (c) the five-center transition state of the ethyl formation, and (d) the ethylidyne-covered Pt surface.<sup>[99]</sup>

In an early kinetic study, the first hydrogenation step was found to be irreversible, which was in contrast to a later kinetic investigation, where the second hydrogenation step was proposed to be irreversible.<sup>[89, 103]</sup> Moreover, previous calculations revealed that the formation of the surface ethyl on Pt(111) was rate-determining, while recent theoretical studies on Pt/SiO<sub>2</sub> and small Pt clusters showed the slowest rate for the hydrogenation of the surface ethyl to ethane.<sup>[99, 110, 112]</sup> In the most current theoretical study on Pt, the authors proposed that there is no single rate-determining step in ethene hydrogenation and both hydrogenation steps contribute to the overall reaction rate.<sup>[118]</sup> However, the surface coordination of the adsorbed ethene on Pt was found to play a crucial role in the reaction kinetics. Both the ethyl species and the  $\pi$ -bonded ethene were proposed to be the key intermediates and the reaction rate was found to be independent on the concentration of the di- $\sigma$ -bound ethene.<sup>[41, 94, 104, 111, 113, 118]</sup> The coadsorption of oxygen, hydrogen, and/or nitrogen atoms on the Pt surface promoted the concentration on the weakly bound ethene that can be the  $\pi$ -bonded or physisorbed species.<sup>[95, 96, 107, 116]</sup> In contrast to that, hydrocarbon fragments like ethylidyne were found to destabilize the  $\pi$ -bonded ethene, resulting in lower concentrations.<sup>[106]</sup> The concentration of the di- $\sigma$ - and  $\pi$ -bound ethene, as well as the ethylidyne on the Pt surface of nanoparticles was dependent on their particle size and particles below 1 nm showed solely the ethylidyne species on the surface at room temperature, while particles of 2-3 nm exhibited additionally to ethylidyne the

di- $\sigma$ - and  $\pi$ -bonded ethene.<sup>[114, 115]</sup> Larger particles of 7 nm contained again mainly ethylidyne and less amounts of  $\pi$ -bound ethene. These findings were investigated by XANES and IR experiments in two groups<sup>[114, 115]</sup>, who tested different particle size ranges. Consequently, ethylidyne was observed on small and large particles in significant concentrations, and the di- $\sigma$ - and  $\pi$ -bonded ethene was only detected on moderate-sized particles. This is inconsistent with theoretical calculations<sup>[109]</sup>, where a destabilization of ethylidyne was found to occur on low-coordinated sites that are present on small particles. A high ethylidyne concentration was supposed to exist on large particles (> 7 nm) that exhibit extended Pt facets, where ethylidyne is much more stable. However, the particles consist of various shapes and different fractions of Pt facets, which alter the stabilization of the di- $\sigma$ - and  $\pi$ -bound ethene and thus, their concentrations.<sup>[102]</sup>

The decomposition of ethene and the formation of ethylidyne on metal surfaces as a ( $2 \times 2$ )-ordered overlayer (3-fold hollow sites<sup>[120]</sup>) was observed in most of the studies that include different reaction conditions, temperatures, and ethene partial pressures (Table 2-7).<sup>[41, 90, 95-99, 101, 104-109, 111, 114, 115, 117, 118]</sup> Although a large number of studies were performed for ethene hydrogenation, the role of ethylidyne is still unknown, which may act as an active species, a spectator, or a poison of active sites. From 1995s on, powerful *in situ* techniques like SFG and IRAS facilitated the detection of ethylidyne on Pt, but its concentration did not correlate with the obtained reaction rate, which indicated ethylidyne as a spectator species.<sup>[41, 104, 105, 111]</sup>

In general, the decomposition of ethene on Pt(111) leads to different hydrocarbon species that dissociate further to adsorbed carbon atoms. Ethylidyne was proposed to arise from the isomerization of the di- $\sigma$ -bonded ethene to ethylidene, which subsequently dehydrogenates to ethylidyne (2-4).<sup>[101, 118]</sup> In contrast to the isomerization of ethene, recent DFT calculations suggested that the ethylidyne is formed via the dehydrogenation of ethene to vinyl, followed by the re-hydrogenation to ethylidene, and the dehydrogenation to ethylidyne (2-5).<sup>[117]</sup> However, the ethylidyne formation starts from the di- $\sigma$ -coordinated ethene in both cases.



The change of the electron density of the Pt(111) surface by the insertion of K atoms resulted in higher activation energies for the C-H and C-C bond cleavage, which led simultaneously to the stabilizing of adsorbed hydrogen and hydrogen-rich carbonaceous species.<sup>[101]</sup> The charge



transfer from K to Pt was supposed to yield to a more ionic Pt-hydrocarbon bond and only adsorbates were stabilized that could admit the negative charge.

The hydrogenation of ethene to ethane on Pt seems to be structure-insensitive, which resulted in similar TOFs for e.g. supported PVP-protected Pt particles with different sizes (5-9 nm) and shapes (cubes, polyhedral).<sup>[121]</sup> Kinetic studies on various Pt facets showed comparable hydrogenation activities and hence, low-coordinated sites were supposed to be the active sites in ethene hydrogenation, because only these sites are equal for different metal surfaces.<sup>[104]</sup> However, an altered reaction rate was obtained for the hydrogenation of the surface ethyl to ethane, when the Pt-ethyl bond strength varied by surface heterogeneities.<sup>[113]</sup> Consequently, an alteration in the electron density on Pt may change the kinetics in ethene hydrogenation. The catalytic activity over Pt varies in a broad range with TOFs of  $10^{-2}$ - $10^4$  s<sup>-1</sup>, which is strongly dependent on the reaction conditions (Table 2-8).<sup>[88, 90, 94, 107, 111, 121-128]</sup>

For the ethene hydrogenation on Pt(111) at atmospheric pressure, high temperatures (333-385 K), and a C<sub>2</sub>H<sub>4</sub>:H<sub>2</sub> ratio of 1:10, very high TOFs in the order of  $10^3$ - $10^4$  s<sup>-1</sup> were determined.<sup>[123]</sup> Lower TOFs in the range of 1-20 s<sup>-1</sup> were measured for Pt nanoparticles on different supports.<sup>[88, 121, 128]</sup> Especially, Pt particles that were capped with different polymers showed variations in their activity, which was related to the altered interaction between Pt and the polymer and thus, to the variation in available active sites for reaction, while the intrinsic activity remained the same.<sup>[128]</sup> Pt particle arrays showed similar TOFs to commercially synthesized supported Pt catalysts.<sup>[125]</sup>

The activation energies for the hydrogenation of ethene to ethane range between 30 kJ mol<sup>-1</sup> and 67 kJ mol<sup>-1</sup> for experiments that were performed above room temperature and at atmospheric pressure (Table 2-8). An increase in activation energy from 40 kJ mol<sup>-1</sup> to 85 kJ mol<sup>-1</sup> was observed for the reaction on Pt(111), when the surface was poisoned with CO. In contrast to the Pt surface, the Pt nanoparticle array was found to be resistant against CO poisoning, because additional active sites were available at the Pt-support interface.<sup>[122]</sup>

**Table 2-8.** Kinetic results of various Pt catalysts at different reaction conditions.

Catalyst	Reaction conditions						TOF / s <sup>-1</sup>	Kinetic orders	
	p / mbar			T / K	E <sub>a</sub> / kJ mol <sup>-1</sup>	T / K		C <sub>2</sub> H <sub>4</sub>	H <sub>2</sub>
	C <sub>2</sub> H <sub>4</sub>	H <sub>2</sub>	total						
Pt(111) <sup>[90]</sup>	13	26	143	300-373	45	333	6.8	-0.6	1.3
	13	130	143				65		
Pt(111) <sup>[122]</sup>	13	130	1000	400-523	40	400	90	-	-
					85 <sup>(a)</sup>		0.03 <sup>(a)</sup>		
Pt(111) <sup>[111]</sup>	1.3	65	100	200-300	37	-	-	-	-
Pt(111) <sup>[107]</sup>	-	-	vac <sup>(b)</sup>	190-233	25	227	-	-0.8	1.2
Pt(111) <sup>[123]</sup>	100	900	1000	245-385	46	385	2000	-	-
						333	~250		
Pt foil <sup>[123]</sup>	100	900	1000	270-335	33	333	900	-	-
Pt array <sup>(c)[122, 124]</sup>	13	130	1000	313-423	43	400	660	-0.9	1.2
					48 <sup>(d)</sup>		10 <sup>(d)</sup>		
Pt arrays <sup>[125]</sup>	13	130	1000	313-413	47 <sup>(e)</sup>	300	5 <sup>(e)</sup>	-	-
					56 <sup>(f)</sup>		11 <sup>(f)</sup>		
Pt array <sup>(g)[126]</sup>	16	984	1000	-	-	298	140 <sup>(h)</sup>	-	-
							30 <sup>(i)</sup>		
Pt/SiO <sub>2</sub> <sup>[127]</sup>	30	200	1000	318-366	67	-	-	-	-
Pt/Al <sub>2</sub> O <sub>3</sub> <sup>[94]</sup>	<260	>90	-	-	-	203	0.03	-	-
Pt/CabOSil <sup>[88]</sup>	33	195	1000	223-336	36	336	20	-0.4	1.1
PVP-Pt/ MCF-17 <sup>[121]</sup>	13	130	1000	-	33 <sup>(j)</sup>	298	5 <sup>(j)</sup>	-	-
					30 <sup>(k)</sup>		6 <sup>(k)</sup>		
Polymer-Pt/SBA-15 <sup>(l)[128]</sup>									
TTAB-Pt	13	130	1000	-	42	293	1	-	-
PVP-Pt							13		
OA-Pt							20		

<sup>(a)</sup> Poisoned with CO (1 mbar). <sup>(b)</sup> Reactants deposited by molecular beam. <sup>(c)</sup> Array of 15 × 28 nm Pt islands with interparticle distance of 100 nm on alumina. <sup>(d)</sup> Poisoned with CO (0.4 mbar). <sup>(e)</sup> Array of 28 nm Pt islands on silica. <sup>(f)</sup> Array of 25 nm sized Pt nanowires on silica. <sup>(g)</sup> Array of 15 × 50 nm Pt islands with interparticle distance of 200 nm on silica. <sup>(h)</sup> Initial rate. <sup>(i)</sup> Steady-state rate. <sup>(j)</sup> 9 nm PVP-capped Pt nanocubes (Pt:PVP = 1:20). <sup>(k)</sup> 5 nm PVP-capped Pt nanocubes (Pt:PVP = 1:20). <sup>(l)</sup> 1.5 nm polymer-capped Pt particles.

The reaction order in ethene increased from negative values at low partial pressures (< 100 mbar) to zero at higher partial pressures for Pt/SiO<sub>2</sub> at 350 K.<sup>[127]</sup> Consequently, the reaction rate decreased with an increasing partial pressure of ethene (< 100 mbar). The opposite was observed for the hydrogen partial pressures, where the reaction rate increased

with an increasing partial pressure at 350 K, resulting in a reaction order of 0.5 for hydrogen, which led to the assumption of weakly adsorbed hydrogen and a competitive adsorption of ethene and hydrogen on the Pt surface (Equation 2-39).<sup>[127]</sup>

$$r = k\sqrt{K_H p_H} (1 - \Theta_E)\Theta_E \quad (\text{Equation 2-39})$$

Where  $r$  is the reaction rate,  $k$  the rate constant,  $K_H$  the equilibrium constant for the hydrogen adsorption,  $p_H$  the hydrogen partial pressure, and  $\Theta_E$  is the ethene coverage.

Equation 2-40 defines a maximal reaction rate at an ethene coverage of 0.5. Both lower and higher ethene concentrations on the Pt surface would lead to a decreased catalytic activity. In this work, the lowest tested ethene partial pressure was 8 mbar that corresponds still to a higher coverage than 0.5. Additionally, the zero order reaction kinetics in ethene at high ethene partial pressures indicated a limited ethene coverage and all surface sites are not accessible.<sup>[127]</sup>

In the most kinetic studies, the hydrogenation was performed at low ethene partial pressures and with excess hydrogen, which resulted in reaction orders of -0.4 to -0.9 for ethene and around 1 for hydrogen.<sup>[88, 90, 107, 122]</sup>

If a Langmuir-Hinshelwood mechanism is assumed, both reactants have to adsorb onto the metal surface. The competitive adsorption of hydrogen and ethene was supposed to occur at temperatures above 273 K and at ethene partial pressures < 95 mbar, which facilitate Langmuir isotherms for the dissociative adsorption of hydrogen and the associative adsorption of ethene (Equation 2-40 and Equation 2-41).<sup>[89, 103, 107]</sup>

$$\Theta_H = \frac{\sqrt{K_H p_H}}{1 + \sqrt{K_H p_H} + K_E p_E} \quad (\text{Equation 2-40})$$

$$\Theta_E = \frac{K_E p_E}{1 + \sqrt{K_H p_H} + K_E p_E} \quad (\text{Equation 2-41})$$

Where  $\Theta_H$  and  $\Theta_E$  is the hydrogen and ethene coverage,  $K_H$  and  $K_E$  is the adsorption constant of hydrogen and ethene, and  $p_H$  and  $p_E$  is the hydrogen and ethene partial pressure.

All elementary steps are summarized in the competitive Horiuti-Polanyi mechanism, which includes the stepwise hydrogenation of ethene to surface ethyl and finally to ethane (2-6).<sup>[129]</sup>



From the computational, spectroscopic, and kinetic results a reaction network is established that shows a modified Horiuti-Polanyi mechanism (Figure 2-25). Hydrogen is dissociatively adsorbed onto Pt, while ethene adsorbs in di- $\sigma$ - and  $\pi$ -coordination. The slower reaction pathway includes the decomposition of di- $\sigma$ -bound ethene and ethylidyne acts as a spectator. The dominant pathway is the stepwise hydrogenation of  $\pi$ -bonded ethene to surface ethyl and ethane.<sup>[104, 117, 118]</sup>

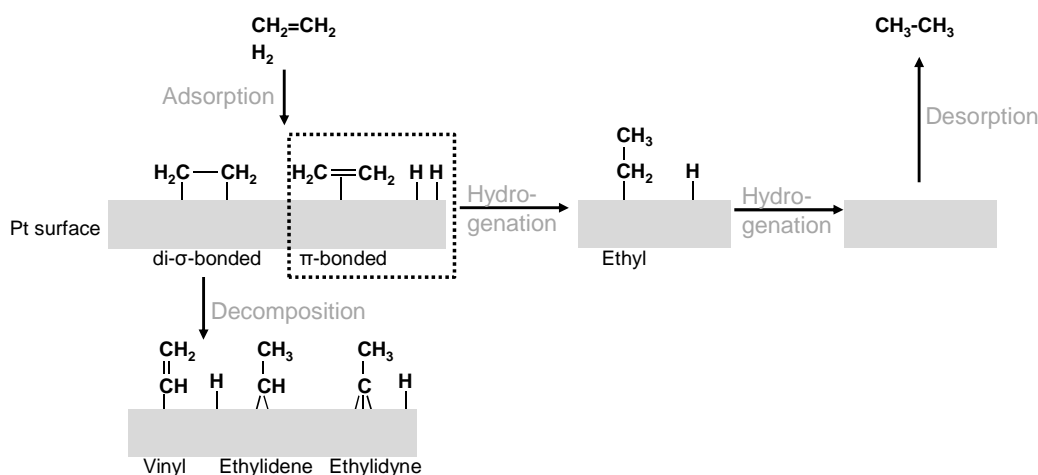


**Figure 2-25.** The modified Horiuti-Polanyi mechanism for hydrogenation of ethene, which includes the hydrogenation route to ethane via the  $\pi$ -bound ethene and the decomposition pathway to ethylidyne via di- $\sigma$ -bound ethene.

## 2.4.2 Batch-Operated External Recycle Reactor

The hydrogenation of ethene was performed in a batch-operated external recycle reactor setup that was especially designed to test the Pt-GaN catalysts with and without illumination (Figure 2-26 (a)). Hydrogen and ethene were used after purification by passing oxygen and moisture traps, while nitrogen was directly used to balance the gas to atmospheric pressure. The gas mixture was adjusted with mass flow controllers and the reactants were mixed in the tubing prior to the reactor. The reactor contained a quartz glass window, which was

transparent for UV light (Figure 2-26 (b)). An adapted heating unit allowed for reactor heating from the back side. The gas mixture passed the micro-pump that was switched on during recirculation. The gas composition was subsequently analyzed with a gas chromatograph (GC). The UV source was mounted above the reactor window with a fixed distance of 10 cm.

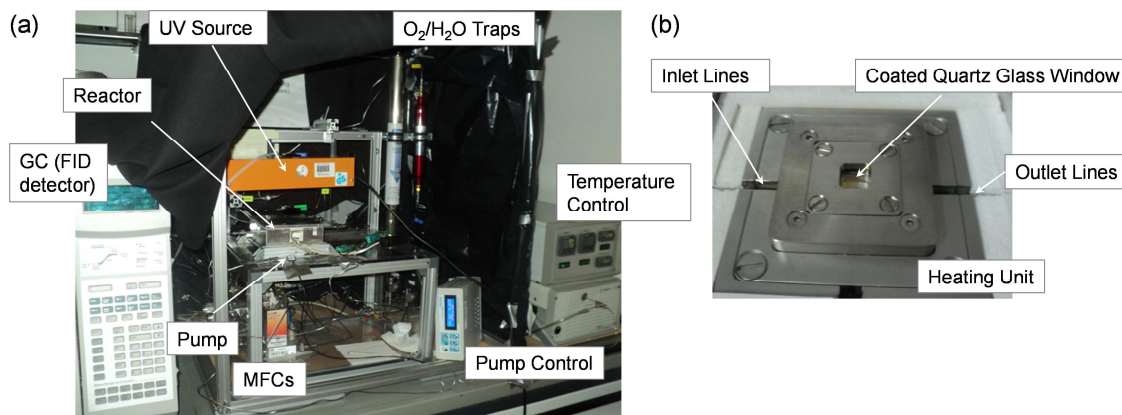


**Figure 2-26.** Image of (a) the reaction setup for ethene hydrogenation including oxygen/moisture traps, mass flow controllers (MFCs), reactor, recycling pump, gas chromatograph, UV lamp, and the control units for the pump and temperature, and (b) the stainless steel reactor with the coated quartz glass window and heating unit.

The flow scheme of the setup shows all connections and lines, and the electronically switched six-port valve V-10 with the sample loop for the gas loading onto the capillary column (Figure 2-27). The setup was filled with the reactant gas mixture in continuous flow until a constant concentration was achieved. The operation was changed to recycle mode by closing the valve V-8 simultaneously with switching the valve V-9 from the exhaust to reactor, and the micro-pump was turned on. The mass flow controllers were shut down and the valves V-5 till V-7 were closed during recirculation. The valves V-1 till V-4 allow for purging all mass flow controllers and all tubes with nitrogen. The gas volume of the sample loop (V-10) was flushed with the carrier gas during GC injection onto the capillary column for separation prior to the analysis with the flame ionization detector (FID). After injection, V-10 switched back and the reaction mixture was diluted with the carrier gas nitrogen.

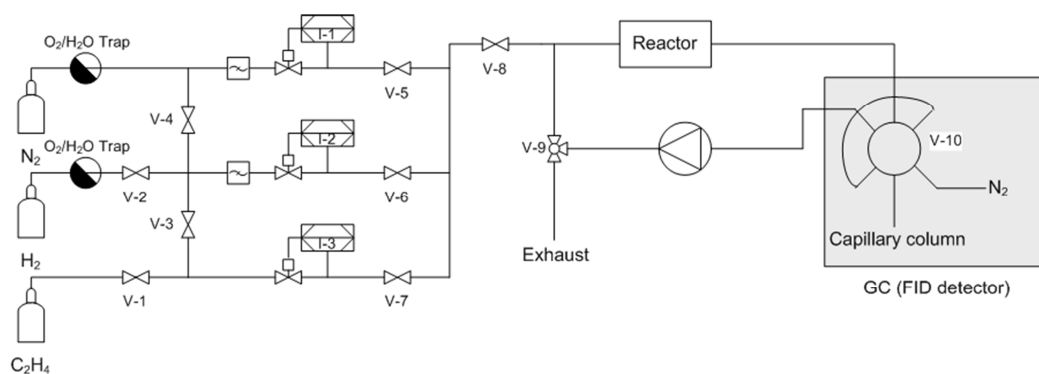


**Figure 2-27.** Flow scheme of the recycle reactor setup with the ball valves (V-1 till V-9), mass flow controllers (I-1 till I-3), and the electronic six-port valve with the sample loop (V-10).

The sample reactor was a sandwich-like stainless steel unit with a quartz glass window that was mounted above the sample (Figure 2-28). The gas was directed from the left- to the right-hand side via lines and dispersed over the catalyst surface with a V-shaped part. The chamber depth was similar to the GaN thickness (333  $\mu\text{m}$ ). The inner side of the top plate contained a channel for the o-ring sealing, where the o-ring was pressed onto the polished bottom plate by screwing. The same principle was applied to seal the quartz glass window and the gas chamber. The dead volume of 330  $\mu\text{l}$  was assumed to be present above the sample, but external diffusion limitations were not observed in the experimental data. The cell temperature was controlled by a thermocouple that was placed below the catalyst chamber. The temperature difference between the thermocouple and the catalyst surface was measured with an additional thermocouple on top of the sample and was determined to be only  $\sim 1\%$  in the relevant temperature range (Figure 2-29).

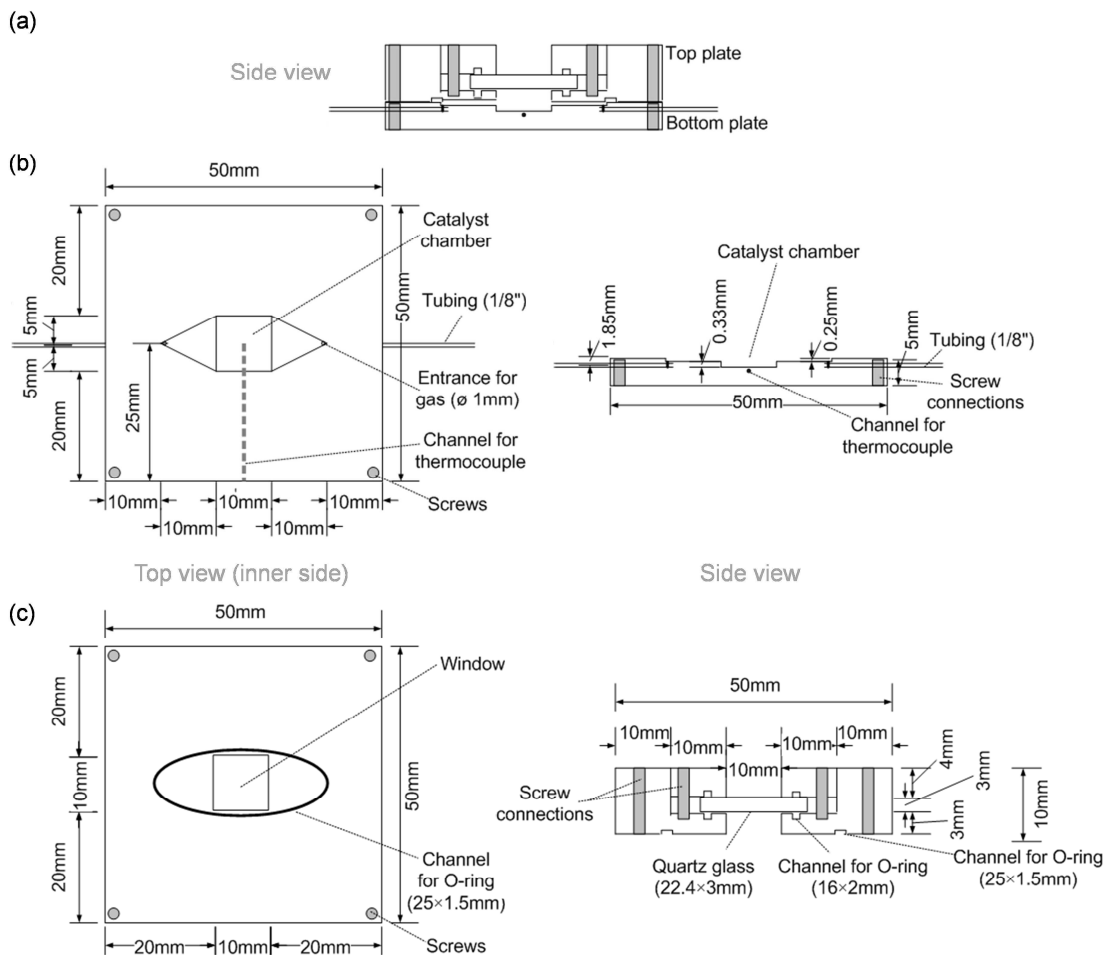


**Figure 2-28.** Design drawing of (a) the stainless steel, sandwich reactor from the side view, which contains (b) the bottom plate with the catalyst chamber and gas tubing and (c) the top plate with the quartz glass window and O-ring sealing.

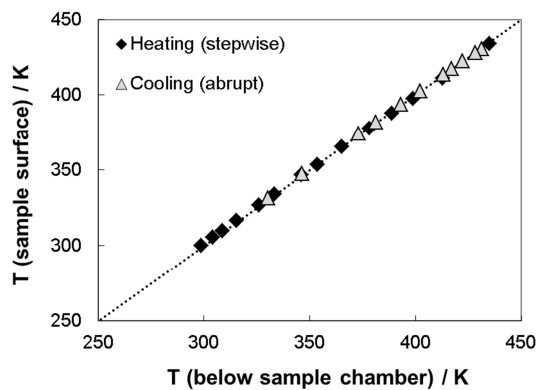


**Figure 2-29.** Plot of the temperature on the sample surface versus the temperature of the thermocouple that was placed below the catalyst chamber.

The product analysis was performed with GC using a HP-PLOT Al<sub>2</sub>O<sub>3</sub> KCl capillary column for the separation of ethene and ethane at low temperature (323 K) and a FID was used for detection. A mixture of ethene or ethane diluted with nitrogen to a total flow of 13 ml min<sup>-1</sup> was used for calibration in the range of 0.4-1.9 Vol% ethene and 0.3-1.5 Vol% ethane.

All specifications and parameters of the individual setup units are summarized in Table 2-9. The reactor temperature was limited to 473 K due to the material of the o-rings. The complete tightness of the setup was only reached when the pump connections were glued with the stainless steel tubes with a cyanoacrylate glue (LOCTITE 496). The evaporation of the glue was not detected.

**Table 2-9.** Specifications and parameters of individual setup units.

Setup unit	Properties	Company
<b>Gases</b>	purity	Westfalen AG
nitrogen/hydrogen/ethene	5.0/5.0/3.5	
<b>Gas purifiers</b>		
All-Pure O <sub>2</sub> trap	-	Alltech
O <sub>2</sub> /moisture trap	-	Supelco
<b>Mass flow controllers</b>	capacity / ml min <sup>-1</sup>	Bronkhorst
nitrogen/hydrogen/ethene	13.16/30.00/3.00	
software	FlowDDE FLOW-BUS	
<b>Sandwich reactor</b>	stainless steel, chamber volume: 56 µl	Self-constructed
quartz glass	broadband antireflection coating	LINOS Photonics
o-rings	Viton <sup>®</sup> (max. 473 K)	RALICKS
<b>Heating unit</b>		
Ultramic600 Heater	AlN (77.5 W cm <sup>-2</sup> ), thermocouple Type “K”	Watlow
Micro-pump mp5	piezoelectric membrane pump frequency 250 Hz, amplitude 250 V back pressure 250 mbar, flow max. 18 ml min <sup>-1</sup> (air)	Bartels Mikrotechnik
<b>Gas chromatograph</b>		HP 6890 Series
six-port valve	323 K, sample loop 10 µl, load & injection time 30 s	VICI Valco
injection/inlet	573 K, flow 8.3 ml min <sup>-1</sup> , split ratio 3	Instruments
capillary column	323 K, flow 1.7 ml min <sup>-1</sup> , HP-PLOT Al <sub>2</sub> O <sub>3</sub> KCl (50 m × 0.32 mm × 5 µm)	
FID	473 K, H <sub>2</sub> 35 ml min <sup>-1</sup> , air 350 ml min <sup>-1</sup>	
Software	GC ChemStation	Agilent Technologies
UV lamp	254 nm, 6 W, 600 µW cm <sup>-2</sup> (15 cm distance)	Benda



In a typical experiment, the sample was mounted into the reactor and flushed continuously with nitrogen ( $13 \text{ ml min}^{-1}$ ) for 15 min at 355 K. Afterwards, hydrogen ( $13 \text{ ml min}^{-1}$ ) was introduced and the sample was heated from 355 K to 425 K within 1 h by a stepwise heating of 10 K every 7 min. After 6 h at 425 K, the reactor was cooled down in hydrogen for 20 min before the gas was changed to the reactant mixture ( $\text{N}_2$   $6.9 \text{ ml min}^{-1}$ ,  $\text{H}_2$   $6.0 \text{ ml min}^{-1}$ , and  $\text{C}_2\text{H}_4$   $0.1 \text{ ml min}^{-1}$ ) at 400 K and GC analysis was started. The catalyst was cooled in the reactant mixture until the reaction temperature (335-355 K) was reached at a constant gas flow (additional 2 h). Finally, the batch-operated recycle mode was applied by switching the valves and the micro-pump. The UV lamp was additionally turned on during illumination experiments.

Two theoretical approaches were used to describe the batch-operated external recycle reactor, the model of a batch reactor and an external recycle reactor. The batch reactor model displayed the accumulation of ethane over the recirculation time (Equation 2-42).<sup>[130]</sup> Considering the literature value for the kinetic order in ethene of -0.6 for Pt(111)<sup>[90]</sup>, the reaction rate (Equation 2-43) and the conversion of ethene to ethane was calculated. As an example, the experimental conversion of cuboctahedral Pt particles on *n*-type GaN at 355 K was compared with the theoretical conversion, showing a good agreement of the theoretical model with the experiment (Figure 2-30).

$$c(\text{C}_2\text{H}_4)_0 \frac{dX}{dt} = -r \quad (\text{Equation 2-42})$$

$$r = -kc(\text{C}_2\text{H}_4)^{-0.6} \quad (\text{Equation 2-43})$$

Where  $c$  is the concentration,  $X$  the conversion,  $t$  the time,  $r$  the reaction rate, and  $k$  the reaction rate constant.

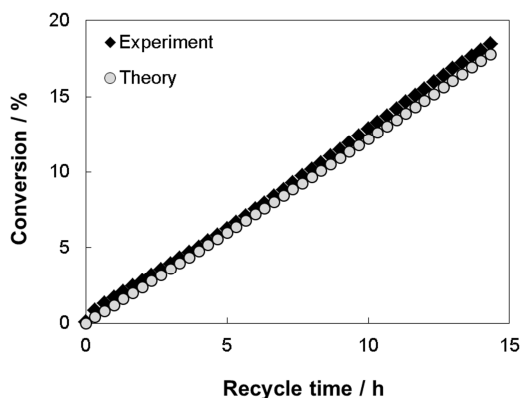


**Figure 2-30.** Experimental and theoretical conversion of ethene to ethane for Pt cuboctahedral particles on *n*-type GaN at 355 K during the recirculation.

Additionally, the model of an external recycle reactor was applied, because the reaction gas was removed by the GC injection and nitrogen was introduced afterwards, which diluted the reaction gas over the recirculation time. The degree of dilution was dependent on the number of injections, which was constant for all measurements. In general, an external recycle reactor contains the catalyst bed and an external loop with a pump for the recirculation of a fluid fraction back to the reactor entrance.<sup>[130, 131]</sup> The mass balance through an external recycle reactor is typically determined for the reactor and the reservoir, while the reaction takes only place in the reactor (Equation 2-44). The concentration of the reactant in the reactor and in the reservoir is similar under differential conditions that provide a constant reaction rate (Equation 2-45). The mass balance results in Equation 2-46, which is used to define the differential operation of the recycle reactor.<sup>[132]</sup> For the setup used in this work with a reactor volume of 0.4 ml, a reservoir volume of 2.4 ml, and a pump flow rate of  $\sim 7 \text{ ml min}^{-1}$ , the concentration difference of ethene was very small with  $10^{-8} \text{ mol l}^{-1}$ , which indicated the operation at differential conditions and the term  $V_R/Q$  became small ( $10^{-4} \text{ h}$ ). Therefore, the reaction rate was calculated with only one reactor volume that is noted as  $V_R$  in the following calculations.

$$\int_0^{V_R} r dV_R = \frac{d}{dt} \int c_R dV_R + V_T \frac{dc_T}{dt} \quad (\text{Equation 2-44})$$

$$r = \left( \frac{V_R + V_T}{V_R} \right) \frac{dc_T}{dt} \quad (\text{Equation 2-45})$$

$$c_T - c_e = - \frac{V_R}{Q} \left( \frac{V_T}{V_R + V_T} \right) r \quad (\text{Equation 2-46})$$

Where  $V_R$  is the reactor volume,  $r$  the reaction rate,  $c_R$  the concentration in the reactor,  $V_T$  the reservoir volume,  $c_T$  the concentration in the reservoir,  $c_e$  the concentration in the reactor effluent,  $Q$  the volumetric flow rate, and  $V_R$  and  $V_T$  is the volume of the reactor and the reservoir.

During recirculation, ethene was not only consumed by the hydrogenation but also by the gas sampling and dilution with nitrogen. To determine the dilution by sampling, the ethene concentration was monitored in the absence of reaction and the mass balance could be described by Equation 2-47 that defines the reaction rate in Equation 2-48. Finally, the initial ethene concentration was diluted exponentially with the dilution rate, which was defined as the flow rate divided by the recycle reactor volume (Equation 2-49).<sup>[130, 131]</sup>

$$\text{Accumulation} = \text{Input} - \text{Output} + \text{Generation}$$

$$V_R \frac{dc(C_2H_4)_i}{dt} = Fc(C_2H_4)_{if} - Fc(C_2H_4)_i + V_R r \quad (\text{Equation 2-47})$$

$$r = \frac{F}{V_R} (c(C_2H_4)_i - c(C_2H_4)_{if}) \quad \text{with} \quad D = \frac{F}{V_R} \quad (\text{Equation 2-48})$$

$$c(C_2H_4)_t = c(C_2H_4)_0 e^{-Dt} \quad (\text{Equation 2-49})$$

Where  $V_R$  is the recycle reactor volume,  $c(C_2H_4)_i$  the ethene concentration in the reactor,  $c(C_2H_4)_{if}$  the ethene concentration fed to the reactor entrance,  $c(C_2H_4)_0$  the initial ethene concentration,  $c(C_2H_4)_t$  the ethene concentration at time  $t$ ,  $F$  the flow rate,  $t$  the time,  $r$  the reaction rate, and  $D$  is the dilution rate.

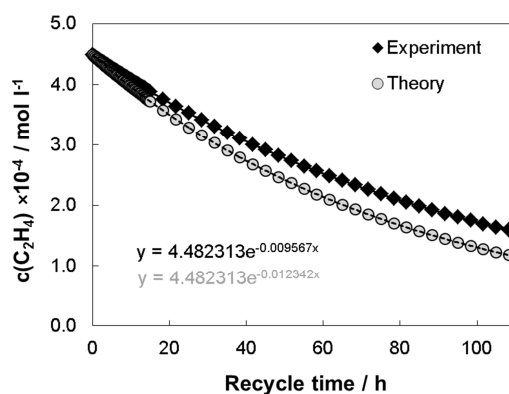


**Figure 2-31.** Comparison of the experimental and theoretical dilution of ethene during recycling in absence of reaction. The experimental curve was averaged from fifty individual measurements.

The theoretical and experimental decrease of the ethene concentration over recycle time were compared using the following parameters: the recycle reactor volume (sandwich-like reactor and all lines) was 2.43 ml, the flow rate was calculated from the volume of the sample loop of 10  $\mu\text{l}$  and the number of GC injections per hour of 3  $\text{h}^{-1}$  and yielded  $3 \times 10^{-5} \text{ l h}^{-1}$ , which led to the dilution rate of  $0.012 \text{ h}^{-1}$ . Several experimental runs were averaged and used to calculate the experimental dilution rate. The experimental dilution of ethene was less pronounced than the theoretical dilution, which originated from lower values for the experimental dilution rate (Figure 2-31). As the flow rate of  $3 \times 10^{-5} \text{ l h}^{-1}$  was always constant, the theoretical recycle reactor volume had to be corrected by 30% to 3.14 ml to reach the experimental dilution rate. Therefore, all kinetic data were evaluated using the experimentally obtained reactor volume.

## 2.5 References

- [1] G. W. Busser, J. G. van Ommen, J. A. Lercher, *J. Phys. Chem. B* **1999**, *103*, 1651.
- [2] R. M. Rioux, H. Song, J. D. Hoefelmeyer, P. Yang, G. A. Somorjai, *J. Phys. Chem. B* **2005**, *109*, 2192.
- [3] H. Song, F. Kim, S. Connor, G. A. Somorjai, P. D. Yang, *J. Phys. Chem. B* **2005**, *109*, 188.
- [4] Y. Wang, *Preparation and Properties of Platinum Nanoparticles on Wide Bandgap Semiconductor Surfaces*, Master's Thesis, Walter Schottky Institute, Technische Universität München, **2009**.
- [5] Y. Zhao, J. S. Marshall, *Phys. Fluids* **2008**, *20*, 043302.
- [6] B. D. Washo, *IBM J. Res. Dev.* **1977**, *21*, 190.
- [7] T. J. Rehg, B. G. Higgins, *Aiche J.* **1992**, *38*, 489.
- [8] L. Reimer, H. Kohl, *Transmission Electron Microscopy: Physics of Image Formation*, Springer Science+Business Media, LLC: New York, **2008**.
- [9] <http://www.ch.tum.de/em/emlabor/methoden/tem-funktion.htm>.
- [10] I. Horcas, R. Fernandez, J. M. Gomez-Rodriguez, J. Colchero, J. Gomez-Herrero, A. M. Baro, *Rev. Sci. Instrum.* **2007**, *78*, 013705.
- [11] Y. Y. Yeo, L. Vattuone, D. A. King, *J. Chem. Phys.* **1997**, *106*, 392.
- [12] B. N. Grgur, N. M. Markovic, P. N. Ross, *Can. J. Chem.* **1997**, *75*, 1465.
- [13] R. E. Benfield, *J. Chem. Soc. Faraday T.* **1992**, *88*, 1107.
- [14] <http://www.ch.tum.de/em/emlabor/methoden/afm-funktion.htm>.
- [15] F. J. Giessibl, *Rev. Mod. Phys.* **2003**, *75*, 949.
- [16] H. Topsøe, *J. Catal.* **2003**, *216*, 155.
- [17] C. Sedlmair, K. Seshan, A. Jentys, J. A. Lercher, *J. Catal.* **2003**, *214*, 308.
- [18] E. Heracleous, A. A. Lemonidou, J. A. Lercher, *Appl. Catal. A-Gen.* **2004**, *264*, 73.
- [19] A. E. Palomares, G. EderMirth, J. A. Lercher, *J. Catal.* **1997**, *168*, 442.
- [20] J. A. Lercher, V. Veefkind, K. Fajerweg, *Vib. Spectrosc.* **1999**, *19*, 107.
- [21] T. Shido, R. Prins, *Curr. Opin. Solid St. M.* **1998**, *3*, 330.
- [22] H. Dathe, A. Jentys, J. A. Lercher, *J. Phys. Chem. B* **2005**, *109*, 21842.
- [23] D. C. Koningsberger, M. K. Oudenhuijzen, J. de Graaf, J. A. van Bokhoven, D. E. Ramaker, *J. Catal.* **2003**, *216*, 178.
- [24] A. Knop-Gericke, M. Hävecker, T. Schedel-Niedrig, R. Schlögl, *Top. Catal.* **2001**, *15*, 27.
- [25] R. Schlögl, A. Knop-Gericke, M. Hävecker, U. Wild, D. Frickel, T. Ressler, R. E. Jentoft, J. Wienold, G. Mestl, A. Blume, O. Timpe, I. Uchida, *Top. Catal.* **2001**, *15*, 219.
- [26] A. P. Markusse, B. F. M. Kuster, D. C. Koningsberger, G. B. Marin, *Catal. Lett.* **1998**, *55*, 141.
- [27] A. Jentys, B. J. McHugh, G. L. Haller, J. A. Lercher, *J. Phys. Chem.* **1992**, *96*, 1324.
- [28] E. Bus, R. Prins, J. A. van Bokhoven, *Phys. Chem. Chem. Phys.* **2007**, *9*, 3312.
- [29] D. F. Ogletree, H. Bluhm, E. D. Hebenstreit, M. Salmeron, *Nucl. Instrum. Meth. A* **2009**, *601*, 151.

- [30] H. Bluhm, M. Hävecker, A. Knop-Gericke, E. Kleimenov, R. Schlögl, D. Teschner, V. I. Bukhtiyarov, D. F. Ogletree, M. Salmeron, *J. Phys. Chem. B* **2004**, *108*, 14340.
- [31] D. Teschner, A. Pestryakov, E. Kleimenov, M. Hävecker, H. Bluhm, H. Sauer, A. Knop-Gericke, R. Schlögl, *J. Catal.* **2005**, *230*, 186.
- [32] D. Teschner, A. Pestryakov, E. Kleimenov, M. Hävecker, H. Bluhm, H. Sauer, A. Knop-Gericke, R. Schlögl, *J. Catal.* **2005**, *230*, 195.
- [33] R. E. Winans, S. Vajda, B. Lee, S. J. Riley, S. Seifert, G. Y. Tikhonov, N. A. Tomczyk, *J. Phys. Chem. B* **2004**, *108*, 18105.
- [34] R. E. Winans, S. Vajda, G. E. Ballentine, J. W. Elam, B. Lee, M. J. Pelling, S. Seifert, G. Y. Tikhonov, N. A. Tomczyk, *Top. Catal.* **2006**, *39*, 145.
- [35] S. Vajda, R. E. Winans, J. W. Elam, B. Lee, M. J. Pelling, S. Seifert, G. Y. Tikhonov, N. A. Tomczyk, *Top. Catal.* **2006**, *39*, 161.
- [36] G. Rupprechter, H. Unterhalt, M. Morkel, P. Galletto, L. J. Hu, H. J. Freund, *Surf. Sci.* **2002**, *502*, 109.
- [37] G. A. Somorjai, K. C. Chou, M. Yang, *e-J. Surf. Sci. Nanotech.* **2004**, *2*, 106.
- [38] G. Rupprechter, H. Unterhalt, M. Morkel, P. Galletto, T. Dellwig, H. J. Freund, *Vacuum* **2003**, *71*, 83.
- [39] G. Rupprechter, *Phys. Chem. Chem. Phys.* **2001**, *3*, 4621.
- [40] K. M. Bratlie, G. A. Somorjai, *J. Phys. Chem. C* **2007**, *111*, 6837.
- [41] P. S. Cremer, X. C. Su, Y. R. Shen, G. A. Somorjai, *J. Am. Chem. Soc.* **1996**, *118*, 2942.
- [42] S. Baldelli, A. S. Eppler, E. Anderson, Y. R. Shen, G. A. Somorjai, *J. Chem. Phys.* **2000**, *113*, 5432.
- [43] B. J. McIntyre, M. Salmeron, G. A. Somorjai, *J. Catal.* **1996**, *164*, 184.
- [44] P. L. Hansen, J. B. Wagner, S. Helveg, J. R. Rostrup-Nielsen, B. S. Clausen, H. Topsøe, *Science* **2002**, *295*, 2053.
- [45] J. D. Grunwaldt, A. M. Molenbroek, N. Y. Topsøe, H. Topsøe, B. S. Clausen, *J. Catal.* **2000**, *194*, 452.
- [46] S. Vajda, S. Lee, K. Sell, I. Barke, A. Kleibert, V. von Oeynhausen, K.-H. Meiwes-Broer, A. F. Rodriguez, J. W. Elam, M. M. Pelling, B. Lee, S. Seifert, R. E. Winans, *J. Chem. Phys.* **2009**, *131*, 121104.
- [47] L. M. Molina, S. Lee, K. Sell, G. Barcaro, A. Fortunelli, B. Lee, S. Seifert, R. E. Winans, J. W. Elam, M. J. Pelling, I. Barke, V. von Oeynhausen, Y. Lei, R. J. Meyer, J. A. Alonso, A. F. Rodriguez, A. Kleibert, S. Giorgio, C. R. Henry, K.-H. Meiwes-Broer, S. Vajda, *Catal. Today* **2011**, *160*, 116.
- [48] S. Lee, B. Lee, F. Mehmood, S. Seifert, J. A. Libera, J. W. Elam, J. Greeley, P. Zapol, L. A. Curtiss, M. J. Pelling, P. C. Stair, R. E. Winans, S. Vajda, *J. Phys. Chem. C* **2010**, *114*, 10342.
- [49] S. Lee, B. Lee, S. Seifert, S. Vajda, R. E. Winans, *Nucl. Instrum. Meth. A* **2011**, *649*, 200.
- [50] A. Guinier, G. Fournet, C. B. Walker, K. L. Yudowitch, *Small Angle Scattering of X-rays*, Wiley: New York, **1955**.
- [51] G. Sankar, W. Bras, *Catal. Today* **2009**, *145*, 195.
- [52] G. Renaud, R. Lazzari, F. Leroy, *Surf. Sci. Rep.* **2009**, *64*, 255.

- [53] C. Revenant, F. Leroy, R. Lazzari, G. Renaud, C. R. Henry, *Phys. Rev. B* **2004**, *69*, 035411.
- [54] B. Lee, S. Seifert, S. J. Riley, G. Tikhonov, N. A. Tomczyk, S. Vajda, R. E. Winans, *J. Chem. Phys.* **2005**, *123*, 074701.
- [55] <http://www.desy.de/~klmn/xanda.html>.
- [56] M. Newville, *Fundamentals of XAFS*, Consortium for Advanced Radiation Sources, University of Chicago: Chicago, **2003**.
- [57] J. J. Rehr, A. L. Ankudinov, *Coordin. Chem. Rev.* **2005**, *249*, 131.
- [58] G. Vlaic, D. Andreatta, P. E. Colavita, *Catal. Today* **1998**, *41*, 261.
- [59] D. E. Ramaker, B. L. Mojet, M. T. G. Oostenbrink, J. T. Miller, D. C. Koningsberger, *Phys. Chem. Chem. Phys.* **1999**, *1*, 2293.
- [60] G. A. Somorjai, *Introduction to Surface Chemistry and Catalysis*, Wiley: New York, **1994**.
- [61] J. W. Niemantsverdriet, *Spectroscopy in Catalysis*, WILEY-VCH Verlag GmbH & Co. KGaA: Weinheim, **2007**.
- [62] T. L. Barr, *Modern ESCA - The principles and practice of X-ray photoelectron spectroscopy*, CRC Prss, Inc., **1994**.
- [63] P. H. Citrin, G. K. Wertheim, *Phys. Rev. B* **1983**, *27*, 3176.
- [64] M. Domke, T. Mandel, C. Laubschat, M. Prietsch, G. Kaindl, *Surf. Sci.* **1987**, *189*, 268.
- [65] K. Dückers, K. C. Prince, H. P. Bonzel, V. Chab, K. Horn, *Phys. Rev. B* **1987**, *36*, 6292.
- [66] G. Comelli, M. Sastry, G. Paolucci, K. C. Prince, L. Olivi, *Prog. Surf. Sci.* **1990**, *35*, 71.
- [67] G. Apai, R. C. Baetzold, P. J. Jupiter, A. J. Viescas, I. Lindau, *Surf. Sci.* **1983**, *134*, 122.
- [68] E. Costanzo, G. Faraci, A. R. Pennisi, S. Ravesi, A. Terrasi, G. Margaritondo, *Solid State Commun.* **1992**, *81*, 155.
- [69] W. Eberhardt, P. Fayet, D. M. Cox, Z. Fu, A. Kaldor, R. Sherwood, D. Sondericker, *Phys. Rev. Lett.* **1990**, *64*, 780.
- [70] M. G. Mason, *Phys. Rev. B* **1983**, *27*, 748.
- [71] P. Jiang, S. Porsgaard, F. Borondics, M. Köber, A. Caballero, H. Bluhm, F. Besenbacher, M. Salmeron, *J. Am. Chem. Soc.* **2010**, *132*, 2858.
- [72] L. K. Ono, B. R. Cuenya, *J. Phys. Chem. C* **2008**, *112*, 4676.
- [73] S. Hüfner, G. K. Wertheim, J. H. Wernick, *Solid State Commun.* **1975**, *17*, 417.
- [74] S. Doniach, M. Sunjic, *J. Phys. C Solid State* **1970**, *3*, 285.
- [75] [www.casaxps.com/help\\_manual/manual\\_updates/peak\\_fitting\\_in\\_xps.pdf](http://www.casaxps.com/help_manual/manual_updates/peak_fitting_in_xps.pdf).
- [76] [www.fhi-berlin.mpg.de/acnew/groups/electronicstructure/pages/methods/pages/electronicstructure\\_group\\_methods\\_xps.pdf](http://www.fhi-berlin.mpg.de/acnew/groups/electronicstructure/pages/methods/pages/electronicstructure_group_methods_xps.pdf).
- [77] D. F. Ogletree, H. Bluhm, G. Lebedev, C. S. Fadley, Z. Hussain, M. Salmeron, *Rev. Sci. Instrum.* **2002**, *73*, 3872.
- [78] M. Salmeron, R. Schlögl, *Surf. Sci. Rep.* **2008**, *63*, 169.
- [79] M. Peuckert, H. P. Bonzel, *Surf. Sci.* **1984**, *145*, 239.

- [80] C. R. Parkinson, M. Walker, C. F. McConville, *Surf. Sci.* **2003**, 545, 19.
- [81] A. S. Arico, A. K. Shukla, H. Kim, S. Park, M. Min, V. Antonucci, *Appl. Surf. Sci.* **2001**, 172, 33.
- [82] Z. L. Liu, B. Guo, L. Hong, H. X. Jiang, *J. Photoch. Photobio. A* **2005**, 172, 81.
- [83] L. K. Ono, B. Yuan, H. Heinrich, B. R. Cuenya, *J. Phys. Chem. C* **2010**, 114, 22119.
- [84] P. Bera, K. R. Priolkar, A. Gayen, P. R. Sarode, M. S. Hegde, S. Emura, R. Kumashiro, V. Jayaram, G. N. Subbanna, *Chem. Mater.* **2003**, 15, 2049.
- [85] K. S. Kim, N. Winograd, R. E. Davis, *J. Am. Chem. Soc.* **1971**, 93, 6296.
- [86] A. Arcoya, X. L. Seoane, J. M. Grau, *Appl. Surf. Sci.* **2003**, 205, 206.
- [87] K. Kuribayashi, S. Kitamura, *Thin Solid Films* **2001**, 400, 160.
- [88] R. D. Cortright, S. A. Goddard, J. E. Rekoske, J. A. Dumesic, *J. Catal.* **1991**, 127, 342.
- [89] G. C. Bond, *T. Faraday Soc.* **1956**, 52, 1235.
- [90] F. Zaera, G. A. Somorjai, *J. Am. Chem. Soc.* **1984**, 106, 2288.
- [91] J. J. Lin, D. W. Hwang, Y. T. Lee, X. M. Yang, *J. Chem. Phys.* **1998**, 109, 2979.
- [92] A. P. Clark, M. Brouard, F. Quadrini, C. Vallance, *Phys. Chem. Chem. Phys.* **2006**, 8, 5591.
- [93] M. Neurock, R. A. van Santen, *J. Phys. Chem. B* **2000**, 104, 11127.
- [94] Y. Soma, *J. Catal.* **1982**, 75, 267.
- [95] H. Steininger, H. Ibach, S. Lehwald, *Surf. Sci.* **1982**, 117, 685.
- [96] D. Godbey, F. Zaera, R. Yeates, G. A. Somorjai, *Surf. Sci.* **1986**, 167, 150.
- [97] T. P. Beebe, J. T. Yates, *J. Phys. Chem.* **1987**, 91, 254.
- [98] A. L. Backman, R. I. Masel, *J. Vac. Sci. Technol. A* **1988**, 6, 1137.
- [99] A. B. Anderson, S. J. Choe, *J. Phys. Chem.* **1989**, 93, 6145.
- [100] E. Yagasaki, R. I. Masel, *Surf. Sci.* **1990**, 226, 51.
- [101] E. A. Carter, B. E. Koel, *Surf. Sci.* **1990**, 226, 339.
- [102] P. Sautet, J. F. Paul, *Catal. Lett.* **1991**, 9, 245.
- [103] J. E. Rekoske, R. D. Cortright, S. A. Goddard, S. B. Sharma, J. A. Dumesic, *J. Phys. Chem.* **1992**, 96, 1880.
- [104] P. S. Cremer, G. A. Somorjai, *J. Chem. Soc. Faraday T.* **1995**, 91, 3671.
- [105] F. Zaera, *Langmuir* **1996**, 12, 88.
- [106] J. Kubota, S. Ichihara, J. N. Kondo, K. Domen, C. Hirose, *Surf. Sci.* **1996**, 357, 634.
- [107] H. Öfner, F. Zaera, *J. Phys. Chem. B* **1997**, 101, 396.
- [108] M. A. Natal-Santiago, S. G. Podkolzin, R. D. Cortright, J. A. Dumesic, *Catal. Lett.* **1997**, 45, 155.
- [109] S. J. Choe, S. M. Park, D. H. Park, D. S. Huh, *B. Korean Chem. Soc.* **1998**, 19, 733.
- [110] D. Duca, G. La Manna, M. R. Russo, *Phys. Chem. Chem. Phys.* **1999**, 1, 1375.
- [111] T. Ohtani, J. Kubota, J. N. Kondo, C. Hirose, K. Domen, *J. Phys. Chem. B* **1999**, 103, 4562.
- [112] T. Miura, H. Kobayashi, K. Domen, *J. Phys. Chem. B* **2000**, 104, 6809.
- [113] W. Wasylenko, H. Frei, *J. Phys. Chem. B* **2005**, 109, 16873.
- [114] E. Bus, D. E. Ramaker, J. A. van Bokhoven, *J. Am. Chem. Soc.* **2007**, 129, 8094.
- [115] R. M. Rioux, J. D. Hoefelmeyer, M. Grass, H. Song, K. Niesz, P. Yang, G. A. Somorjai, *Langmuir* **2008**, 24, 198.

- [116] J. Yin, M. Trenary, R. Meyer, *J. Phys. Chem. C* **2010**, *114*, 12230.
- [117] Y. Chen, D. G. Vlachos, *J. Phys. Chem. C* **2010**, *114*, 4973.
- [118] M. Saliccioli, Y. Chen, D. G. Vlachos, *Ind. Eng. Chem. Res.* **2011**, *50*, 28.
- [119] D. L. Thorn, R. Hoffmann, *J. Am. Chem. Soc.* **1978**, *100*, 2079.
- [120] J. Silvestre, R. Hoffmann, *Langmuir* **1985**, *1*, 621.
- [121] C.-K. Tsung, J. N. Kuhn, W. Huang, C. Aliaga, L.-I. Hung, G. A. Somorjai, P. Yang, *J. Am. Chem. Soc.* **2009**, *131*, 5816.
- [122] K. S. Hwang, M. C. Yang, J. Zhu, J. Grunes, G. A. Somorjai, *J. Mol. Catal. A-Chem.* **2003**, *204*, 499.
- [123] M. A. Quinlan, *Ph.D. Thesis: Structural Sensitivity Studies of Ethylene Hydrogenation on Platinum and Rhodium Surfaces*, Materials and Chemical Sciences Division, Lawrence Berkeley Laboratory, University of California, **1996**.
- [124] J. Grunes, J. Zhu, E. A. Anderson, G. A. Somorjai, *J. Phys. Chem. B* **2002**, *106*, 11463.
- [125] A. M. Contreras, J. Grunes, X. M. Yan, A. Liddle, G. A. Somorjai, *Catal. Lett.* **2005**, *100*, 115.
- [126] P. W. Jacobs, F. H. Ribeiro, G. A. Somorjai, S. J. Wind, *Catal. Lett.* **1996**, *37*, 131.
- [127] J. H. Sinfelt, *J. Phys. Chem.* **1964**, *68*, 856.
- [128] J. N. Kuhn, C.-K. Tsung, W. Huang, G. A. Somorjai, *J. Catal.* **2009**, *265*, 209.
- [129] I. Horiuti, M. Polanyi, *T. Faraday Soc.* **1934**, *30*, 1164.
- [130] O. A. Hougen, K. M. Watson, *Chemical Process Principles. Part Three: Kinetics and Catalysis*, John Wiley & Sons: New York, **1947**.
- [131] R. J. Wijngaarden, A. Kronberg, K. R. Westerterp, *Industrial Catalysis - Optimizing Catalysts and Processes*, WILEY-VCH: Weinheim, **1998**.
- [132] J. M. Smith, *Chemical Engineering Kinetics*, McGraw-Hill Inc.: New York, **1981**.



# Chapter 3

## **Combined TPRx, *in situ* GISAXS and GIXAS Studies of Model Semiconductor-Supported Platinum Catalysts in the Hydrogenation of Ethene**

### **Abstract**

The preparation, characterization, and catalytic reactivity of GaN supported Pt catalyst in the hydrogenation of ethene are presented, highlighting the use of *in situ* characterization of the material properties during sample handling and catalysis by combining temperature-programmed reaction with *in situ* grazing incidence small-angle X-ray scattering and X-ray absorption spectroscopy. The catalysts are found to be sintering resistant at elevated temperatures as well as during reduction and hydrogenation reactions. In contrast to Pt particles of approximately 7 nm diameter, smaller particles of 1.8 nm in size are found to dynamically adapt their shape and oxidation state to the changes in the reaction environment. These smaller Pt particles also showed an initial deactivation in ethene hydrogenation, which is paralleled by the change in the particle shape. The subtle temperature-dependent X-ray absorbance of the 1.8 nm sized Pt particles indicates that subtle variations in the electronic structure induced by the state of reduction by electron tunneling over the Schottky barrier between the Pt particles and the GaN support can be monitored.

### **3 Combined TPRx, in situ GISAXS and GIXAS Studies of Model Semiconductor-Supported Platinum Catalysts in the Hydrogenation of Ethene**

#### **3.1 Introduction**

Supported and unsupported noble metal particles are used as highly efficient catalysts in a wide range of reactions including catalytic reforming, steam reforming as well emission reduction catalysts to name only three large volume applications. An arsenal of characterization techniques has been developed over the last decade for *in situ* studying properties of such catalysts during action. Of those techniques, X-ray absorption, X-ray photoelectron spectroscopy, X-ray diffraction and scattering are among the most widely used for supported metal particles.<sup>[1-8]</sup> As each specific technique also has limitations, the use of complementary analysis techniques is highly desirable.

In this work we combine the *in situ* measurements of small-angle X-ray scattering (GISAXS) and X-ray absorption (GIXAS) in grazing incidence geometry with temperature-programmed reaction (TPRx) in a single experiment. The novelty of this experimental approach lies in combining the highly surface-sensitive grazing incidence X-ray scattering and X-ray absorption with temperature-programmed reaction. This combination allows for making a direct correlation between catalyst size and shape, its oxidation state, and catalytic performance under reaction conditions in a single experiment. GISAXS provides detailed morphological information about the metal particles, independent of composition or coverage. XANES reveals the electronic state of the particles, while EXAFS provides information about the structure and composition. By using the coordination number obtained from EXAFS analysis, the particle size of well-defined, non-oxidized small particles can be estimated. However, for (partially) oxidized or asymmetrical particles GISAXS is the only X-ray technique to elucidate the detailed shape and its change during catalyst treatments. Combining GISAXS and GIXAS and TPRx in one suite sets the direction for the extraction of extremely detailed information about metal particles of nanometric dimensions in a reaction environment.

The small size of catalytically active metal particles (ranging in diameter from less than a nanometer to few nanometers) provides not only a high efficiency with respect to the fraction of usable (accessible) metal atoms; the small size also leads to a high fraction of coordinatively strongly unsaturated sites. Such sites are usually by far more active than the

majority of the surface metal atoms. In addition to the size of these particles, their shape may determine the arrangements of metal atoms at the surface and both may influence surface states and the overall electronic properties, which all influence activity and selectivity for a particular catalytic reaction.<sup>[9]</sup> Different routes have been explored to prepare particles varying in size and geometry.<sup>[10-12]</sup> However, even for a given chemical composition, size and shape of the metal particle, the chemical nature of the support as well as its acidity and basicity significantly impacts its stability against sintering and its electronic properties.<sup>[13]</sup>

In this context, semiconducting supports may influence the electronic structure of nanoparticles via charge transfer and because the semiconductor surface charge density can be altered by thermal, electrical or optical induction, it would add unseen and hitherto unexplored flexibility for small devices. The fact, that a semiconducting material is able to affect a supported metallic species electronically and therefore alters the catalytic reaction, was first observed by Schwab *et al.*<sup>[14]</sup> They found a lower activation energy in the dehydrogenation of formic acid, when the alumina supported Ni catalyst was doped with NiO that caused a lower *n*-character of the support. The authors proposed a “synergetic amplification” by the reduction of the Fermi level of metallic layers in contact with a semiconducting oxide and therefore an electron transfer from the metal into the support. This effect leads to a decrease of activation energy and subsequently to the increase of the catalytic activity. Similar enhancement of catalytic performance was observed for oxide-supported metal catalysts in methanol synthesis<sup>[15]</sup>, in the hydrogenation of ethene and CO<sup>[16, 17]</sup>, as well as in the selective hydrogenation of cyclohexane, cyclopropane, and propene.<sup>[18, 19]</sup> The contact between a metal layer and a semiconductor surface can be described by the Schottky model that assumes a charge separation at the metal-semiconductor interface and a band bending at the interface in the semiconductor.<sup>[20]</sup> Doping of the semiconductor causes a charge accumulation or depletion of charge in the metal. In this case, a charge accumulation appeared at the interface in the metal leading to a strong electric field inside the particle and a high instability. The Schottky model can be applied to deposited metal layers as well as to nanometer sized metal particles that were in contact to a semiconducting surface.<sup>[21]</sup> The charge separation at the metal semiconductor interface cause an uniform charge distribution over the whole particle surface changing its catalytic behavior. This approach may alter the electronic density of surface atoms by an accumulation or depletion of electrons on the metal particle surface potentially changing its catalytic behavior. Thus, conceptually, wide bandgap semiconductors, e.g., TiO<sub>2</sub> or GaN may offer the possibility for indirect electronic control of

the catalytic action. Due to the contact between metal and semiconductor a Schottky diode can be formed and electrons have to overcome the Schottky barrier for transfer. A transfer of hot electrons from the metal surface into the semiconductor generated by the CO oxidation was detected by Park and Somorjai using Pt-TiO<sub>2</sub> as well as Pt-GaN diodes.<sup>[22]</sup> Furthermore, Pt-GaN heterostructures have been used as chemical sensors for hydrogen with high sensitivity.<sup>[23]</sup>

This study of model catalysts containing Pt nanoparticles that were spin-coated to *n*-type GaN aims the understanding and differentiating geometric and electronic effects on the catalytic behavior in a well-controlled reaction environment as a first step in this direction.

## 3.2 Experimental

### 3.2.1 Combined TPRx and in situ GISAXS/GIXAS

The experiments were performed using a dedicated setup developed at the Sector 12 ID at the Advanced Photon Source of the Argonne National Laboratory.

#### 3.2.1.1 Grazing Incidence Small-Angle X-ray Scattering (GISAXS)

Grazing incidence small angle X-ray scattering (GISAXS) was used to determine cluster size and shape. This technique has been proved to be very powerful to study particles at surfaces and their transformations under reactive gas environment at the nanometer as well as the sub-nanometer scale.<sup>[24-29]</sup> GISAXS is sensitive to the particles in the surface region, and in addition to particle size it provides particle size distribution, interparticle distance, and average aspect ratio of metal particles.<sup>[24, 26-28]</sup> The GISAXS experiments were performed with X-rays of 11.5 keV energy in a reaction cell of unique design. The cell was sealed with Kapton windows and mounted on a computer controlled goniometer. A 1024 × 1024 pixel two-dimensional MarCCD detector was used for recording the GISAXS images from the sample. GISAXS data were collected as a function of reaction temperature and time. The two-dimensional X-ray images were analyzed by taking cuts in the  $q_{xy}$  direction for horizontal information and in the  $q_z$  direction for vertical information. Scattering vectors  $q$  are calculated from  $(4\pi/\lambda) \sin\theta$  where  $\theta$  is the scattering half angle and  $\lambda$  is the wavelength of the X-rays. Based on the narrow distribution of the platinum nanoparticles and assuming a spherical

shape, the data were analyzed by Guinier analysis<sup>[30]</sup>, providing the horizontal and vertical particle radii of gyration  $R_{gH}$  and  $R_{gV}$ , respectively. The diameter and height of the nanoparticles can be calculated from the radii of gyration as  $2.58 \times R_{gH}$  and  $R_{gV}$ , respectively. The aspect ratio of the particles can be calculated as  $R_{gH}/R_{gV}$ .

### 3.2.1.2 Grazing Incidence X-ray Absorption (GIXAS)

XAS (XANES/EXAFS) is a powerful technique that is able to monitor changes in oxidation state and local coordination environment of metal nanoparticles during the course of the catalytic reaction.<sup>[31]</sup> Unlike conventional approach, GIXAS provides information of near surface region especially when the incident beam is below critical angle. Therefore, GIXAS shows enhanced surface sensitivity which allows monitoring chemical change in samples with a fraction of a monolayer coverage. GIXAS data were collected by a 4-element Ge fluorescence detector mounted parallel to the sample surface as a function of reaction temperature and time. The collected data were analyzed using the IFEFFIT interactive software package (with ATHENA and ARTEMIS graphical interfaces).<sup>[32]</sup>

### 3.2.1.3 Temperature-Programmed Reaction (TPRx)

During the GISAXS/GIXAS measurements, simultaneous reactivity measurements were also conducted (Figure 3-1). The reactants used were gases at 1%  $C_2H_4$  in He and 99.7%  $D_2$ , and the ratio for  $C_2H_4$  and  $D_2$  was kept 1:2 by preparing the mixture in a remotely controlled gas-mixing unit consisting of calibrated mass flow controllers (Brooks model SLA5850). The reaction cell was operated in a continuous flow mode (1 bar,  $50 \text{ ml min}^{-1}$  gas flow). The products were analyzed using a differentially pumped mass spectrometer (Pfeiffer Vacuum Prisma QMS 200), the turnover rates (TOR) were calculated using calibrated gas mixtures and the count of deposited Pt particles. The catalyst temperature was controlled with a ceramic heater (Momentive Performance Materials Inc.) allowing heating up to 900 K. The sample temperature was measured with a K-type thermocouple attached to the edge of the heater surface. To achieve thermal equilibrium between the heater and sample during the application of a temperature ramp, a low heating rate ( $< 6 \text{ K min}^{-1}$ ) was used. The uncertainty

in the mass spectrometer signal is estimated to be  $\sim 2\%$  of the ion current, based on standard deviation of 5-25 points under steady reaction conditions. With an assumption of a better than 10% determination of the total metal loading in this study, this error translates into about estimated 10% uncertainty in the calculation of the total Pt atom based turnover rates.

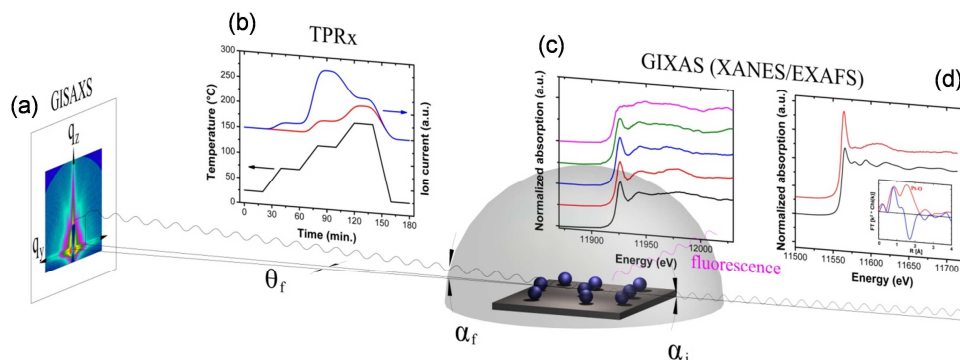


**Figure 3-1.** Schematic of the combined temperature-programmed reaction, grazing incidence X-ray scattering, and X-ray absorption approach. The insets illustrate the capabilities offered by this combination of techniques: (a) two-dimensional *in situ* GISAXS pattern that allows for the determination of particle size and shape and to study particle stability, (b) monitoring of product evolution with temperature/time, (c) series of XANES spectra collected during *in situ* reduction of small gold nanoparticles, and (d) example of a quick EXAFS scan on Pt<sub>10</sub> clusters revealing fully oxidized Pt.

## 3.2.2 Sample Preparation

### 3.2.2.1 Materials

Chloroplatinic acid solution (8 wt. % in water), Poly(*N*-vinyl-2-pyrrolidone) (PVP40), 1-propanol (99.7%) and acetone ( $\geq 99.5\%$ ) were purchased from Sigma-Aldrich; ethanol (99%), and 2-propanol ( $\geq 99.5\%$ ) from Merck, nitric acid ( $> 65\%$  in water) and ethylene glycol ( $\geq 99.5\%$ ) from Fluka, and hydrochloric acid (32% in water) from Riedel-de Haën. The chemicals were used without further purification. MOCVD *n*-type GaN (donor concentration of Si:  $2 \times 10^{18} \text{ cm}^{-3}$ ) was received from Lumilog Group St Gobain Crystals.

### 3.2.2.2 Platinum Nanoparticle Preparation

Small platinum particles with an average size of 1.8 nm were prepared by the alcohol reduction method.<sup>[11]</sup> An aqueous solution (bidistilled water  $> 18.2 \text{ M}\Omega \text{ cm}$ , 20 ml) containing

chloroplatinic acid solution (0.057 mmol) and poly(N-vinyl-2-pyrrolidone) (PVP) (2.0 mmol monomer) was stirred at 373 K for 2 h before 1-propanol (130 ml) was added as reduction agent. The solvent was evaporated after 48 h at 373 K. The formed brown residue was then re-dispersed in ethanol (20 ml).

Large platinum particles with an average size of 6.7 nm were synthesized using the polyol process.<sup>[33]</sup> Ethylene glycol solutions of PVP (1.125 mmol monomer, 3 ml) and chloroplatinic acid (0.094 mmol, 1.5 ml) were alternatingly added to ethylene glycol (2.5 ml) every 30 s at 473 K. The mixture was refluxed for 5 min before precipitation with acetone (21 ml) and centrifugation (4000 rpm, 293 K, 45 min). The residue was re-dispersed in ethanol (20 ml).

### 3.2.2.3 Spin-coating of Platinum Nanoparticles onto *n*-type GaN Surfaces

All substrates were pre-treated with aqua regia (HCl:HNO<sub>3</sub> of 3:1) for 10 min at 353 K, cleaned in acetone (ultrasonic bath, 10 min), and rinsed with 2-propanol. Subsequently after cleaning, Pt dispersions with defined Pt concentration in ethanol ( $2.5 \times 10^{-4}$  mol l<sup>-1</sup> Pt for 1.8 nm particles and  $6.6 \times 10^{-4}$  mol l<sup>-1</sup> Pt for 6.7 nm particles) were pipetted (50 μl) onto the *n*-type GaN surface (8 × 8 mm) and spin-coated at 3000 rpm for 60 s.<sup>[34]</sup> The samples were heated for 5 min to 363 K for solvent evaporation. Afterwards, the PVP-capping was removed by oxygen plasma with an oxygen pressure of 1.4 mbar for 5 min (TePla 100-E, Technics Plasma GmbH). To increase the adhesive forces between particles and substrate, the samples were heated at 423 K for 15 min in nitrogen atmosphere (100 mbar). For our *in situ* GISAXS study of particle reduction in deuterium, oxygen plasma treated samples were used. In contrast, for the *in situ* GISAXS experiments of the deuterium-ethene reaction, the samples were reduced in advance in hydrogen atmosphere (100 ml min<sup>-1</sup>) for 30 min at 373 K (temperature ramp of 5 K min<sup>-1</sup>), followed by flushing with synthetic air (20 ml min<sup>-1</sup>) for 30 min at room temperature.

### 3.2.2.4 *Ex situ* Sample Characterization by Transmission Electron Microscopy (TEM) and Atomic Force Microscopy (AFM)

The average particle sizes of PVP-protected Pt colloids in ethanol were analyzed by TEM (JEOL JEM 2010, 120 kV, magnification of 200 000 and 250 000). The evaluated particle

sizes were averaged from 500 small and 150 large particles, respectively. The errors for the TEM particle size were calculated from the standard deviation of 500 small and 150 large particles, respectively. For the evaluation of the particle distribution on *n*-type GaN, AFM images were taken with a Veeco Multimode AFM using a Nanoscope IIIa SPM controller in the tapping mode. AFM probes (204-497 kHz, 10-130 N m<sup>-1</sup>, tip radius < 7 nm) were purchased from Nanosensors. 1 × 1 μm images were recorded with 256 data points per line at a scanning frequency of 1 Hz. The analysis was performed with the WSxM software.<sup>[35]</sup> Two images each from the sample center and the edge region were collected for four samples in total. The average particle height and the number of particles per μm<sup>2</sup> were analyzed. The average particle height was determined by the AFM software for each image resulting in eight images for similar Pt coverage with small and large particles, respectively. The errors in the average particle height were calculated by the standard deviation of the average particle size of the eight images.

### 3.2.3 *In situ* Experiments

During the TPRx/GISAXS/GIXAS measurements the reactants used were gases at 1% C<sub>2</sub>H<sub>4</sub> in He and 99.7% D<sub>2</sub>. Deuterium was chosen based on the following considerations. In the case of C<sub>2</sub>H<sub>6</sub> and using electron impact ionization, C<sub>2</sub>H<sub>4</sub><sup>+</sup> ( *m/z* = 28) is the base peak, at 5 times of the intensity of the C<sub>2</sub>H<sub>6</sub><sup>+</sup> parent ion peak (*m/z* = 30), the intensity of the latter potentially not offering a sufficiently intense signal. As far as *m/z* = 28 is considered, the ion signal from traces of nitrogen (*m/z* = 28) present in the reactant gases may interfere and consequently corrupt data. When using deuterium, the C<sub>2</sub>H<sub>2</sub>D<sub>2</sub><sup>+</sup>, C<sub>2</sub>H<sub>4</sub>D<sup>+</sup> fragment ions of the product C<sub>2</sub>H<sub>4</sub>D<sub>2</sub> contribute to the *m/z* = 30 signal. Another significant advantage of monitoring the *m/z* = 30 signal is that there is virtually no background for this *m/z* in the mass spectrum, unlike in the case of *m/z* = 32, which can originate from trace amounts of O<sub>2</sub>. In the hydrogenation experiments, the ratio of C<sub>2</sub>H<sub>4</sub> and D<sub>2</sub> was kept 1:2. In the case of the reduction experiments, identical concentration of deuterium (2%) was used. The *in situ* reaction cell was operated in a continuous flow mode at 1 bar pressure and 50 ml min<sup>-1</sup> of total gas flow in both experiments.



### 3.3 Results and Discussion

#### 3.3.1 Particle Size Analysis by TEM, AFM, and GISAXS

An average particle size of  $1.8 \pm 0.3$  nm (small) was determined by TEM for particles synthesized by alcohol reduction, while an average particle size of  $6.7 \pm 1.1$  nm (large) resulted from the polyol process (Figure 3-2 (a, b)). Moreover, particles prepared by the polyol method resulted in cubic or tetragonal particles. In addition to isolated particles, aggregates of particles were observed. The fraction of particle aggregates was 13% for small and 20% for large particles.

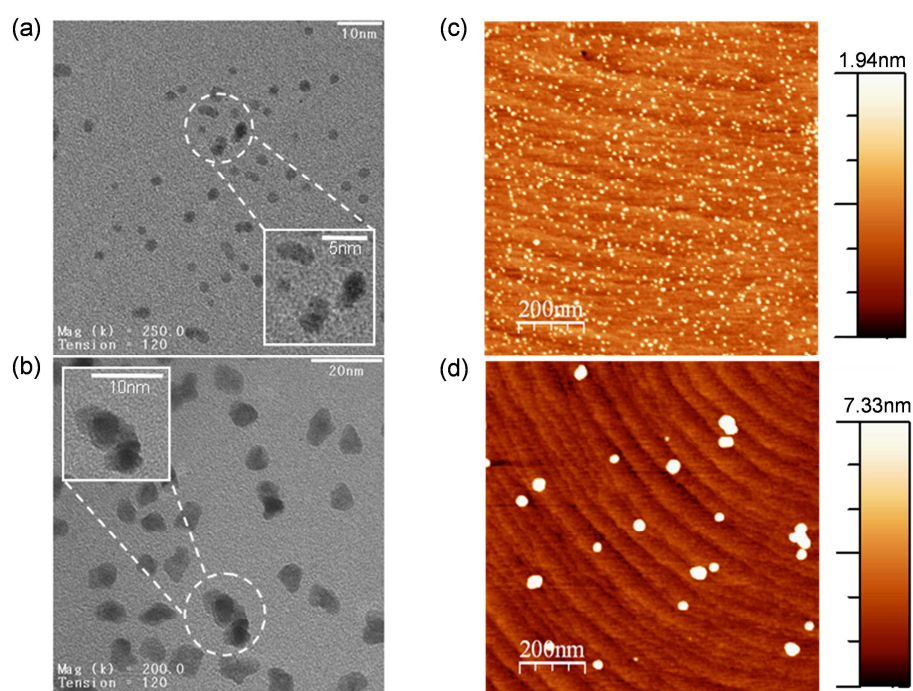


**Figure 3-2.** TEM micrographs of Pt nanoparticles prepared by (a) alcohol reduction with average particle size of  $1.8 \pm 0.3$  nm and (b) polyol method with average particle size of  $6.7 \pm 1.1$  nm. AFM images of spin-coated Pt nanoparticles on *n*-type GaN with particle sizes of (c)  $1.8 \pm 0.3$  nm and (d)  $6.7 \pm 1.1$  nm. The root mean square of blank *n*-type GaN was 0.1 nm.

After the determination of the particle size in dispersion, the particle distribution and coverage on the semiconductor substrate was investigated by AFM (Figure 3-2 (c, d)). An average number of 1324 particles per  $\mu\text{m}^2$  and 20 particles per  $\mu\text{m}^2$  were calculated for small and large particles, respectively. The coverage was calculated in percentage of a monolayer (%ML) relative to a Pt monolayer containing  $1.5 \times 10^{15}$  atoms  $\text{cm}^{-2}$  for Pt(111).<sup>[36]</sup> A Pt coverage of 1.6%ML was achieved for both particle sizes with a homogeneous distribution on

the surface. In contrast to TEM images, the cubic shape of the large particles was not detected by AFM due to limitations in lateral resolution.

From GISAXS data, the average horizontal and vertical radii of gyration  $R_{gH}$  and  $R_{gV}$  were obtained by Guinier plots (i.e., the logarithm of scattering intensity plotted against  $q_y^2$  and  $q_z^2$ ).<sup>[30]</sup> Note that Guinier analysis does not require an assumption of a particular shape. When assuming a spheroid particle, the lateral diameter and height of the Pt particles were both calculated from the radii of gyration  $R_{gH}$  and  $R_{gV}$  to be  $2.58 \times R_{gH}$  and  $2.58 \times R_{gV}$ , respectively. Since both TEM and AFM indicated a distribution of particle sizes and their aggregates, the horizontal cut of the GISAXS data was also analyzed using a lognormal distribution of the lateral diameter confirming a range of particle sizes (Figure 3-3). The uncertainty in the particle size is estimated to be  $\sim \pm 0.1$  nm, which is approximately 5 % of the particle size or better. The measurement accuracy in this region could be improved by applying anomalous GISAXS.<sup>[26]</sup> Anomalous small-angle X-ray scattering refers to an extension of the standard scattering experiments, in which the energy of the probing X-rays is tuned near the absorption edge of the interrogated element in the sample. By performing scattering experiments near the characteristic absorption edge of any given atom, it is possible to vary the contrast for scattering of that particular element. This approach solves a major problem with small-angle scattering, namely the lack of a quantitative background subtraction especially in the case of highly diluted samples and very small particles.

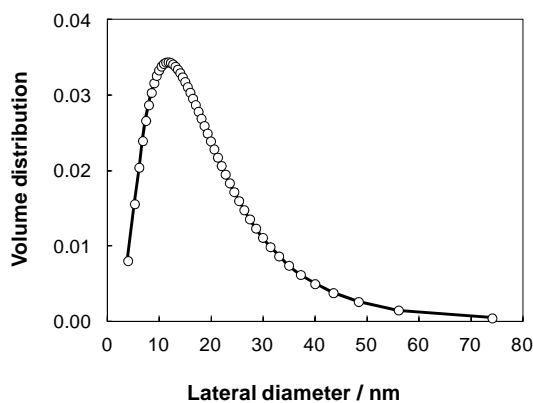


**Figure 3-3.** Result of the fit of the horizontal cut from the GISAXS pattern of the large Pt particle sample using lognormal distribution.

The results of TEM, AFM, and GISAXS analysis are summarized in Table 3-1, showing a good agreement.

**Table 3-1.** Pt concentration in ethanol dispersion and corresponding properties as evaluated by TEM, AFM, and GISAXS.

Pt content $\times 10^{-4}$ / mol l <sup>-1</sup>	TEM	AFM	GISAXS <sup>(a)</sup>		GISAXS <sup>(b)</sup>	
	average size / nm	average height / nm	average height / nm	average lateral diameter / nm	mean lateral diameter / nm	FWHM of distribution / nm
2.5	1.8 ± 0.3	1.8 ± 0.6	1.5 ± 0.1	2.0 ± 0.1	-	-
6.6	6.7 ± 1.1	7.9 ± 1.1	4.5 ± 0.1	5.3 ± 0.1	7.8 ± 0.7	8.7

<sup>(a)</sup> Determined from Guinier fit. <sup>(b)</sup> Determined from the fit of the horizontal cuts using lognormal distribution. In the case of the small particles, the particle size was too small for a lognormal fit. FWHM stands for full width at half maximum.

The stability of spin-coated Pt particles on the semiconductor surface was tested under gas and liquid flux and under mechanical strain. The average particle height and the Pt coverage were analyzed by AFM and changes such as particle aggregation were not observed. Additionally, the samples were analyzed after the GISAXS/GIXANES and TPRx experiments by AFM, without significant sample modifications.

### 3.3.2 *In situ* Characterization under Reduction Conditions and at Elevated Temperatures

In a combined X-ray scattering and X-ray absorption experiment the thermal stability and evolution of the shape of particles was studied together with the change in their oxidation state in the presence of deuterium. The samples were heated in a stepwise fashion in the presence of helium or D<sub>2</sub>. First, the reaction cell was filled with He at room temperature and GISAXS and GIXANES was recorded. Then, the temperature was increased to 373 K, the temperature later to be used during the hydrogenation of ethene. At this temperature GISAXS and GIXANES were recorded in He. Next, D<sub>2</sub> was introduced for 30 min and GISAXS and GIXANES were taken at regular time intervals. At the end of the 373 K step the flow of D<sub>2</sub> was replaced by He and GISAXS and GIXANES were recorded again. Subsequently, the temperature was increased in three steps up to 673 K to monitor shape changes and Pt particle stability. Finally, GISAXS and GIXANES were recorded after cooling back the sample to room temperature. Figure 3-4 shows a series of typical two-dimensional GISAXS images recorded during the heat treatment in He on large Pt particles. A small change in GISAXS pattern is observed at 573 K (Figure 3-4 (c)), indicative of an onset in particle shape change to form highly monodisperse objects.<sup>[28, 37]</sup>

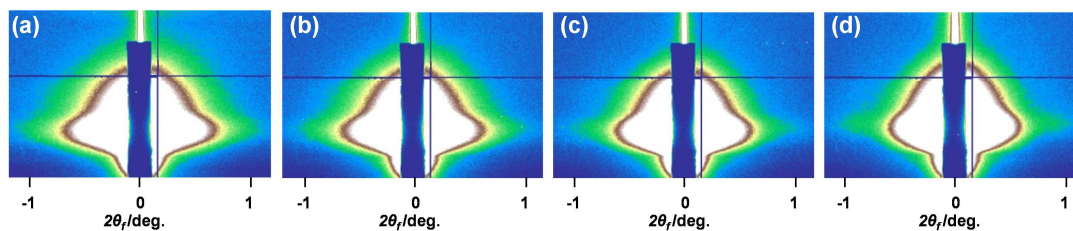


**Figure 3-4.** 2D GISAXS patterns of large Pt nanoparticles on *n*-type GaN at (a) 298 K, (b) 473 K, (c) 573 K, and (d) 298 K after temperature cycle in helium.

Figure 3-5 shows the horizontal cuts of the GISAXS images recorded as a function of temperature in the inert gas environment.

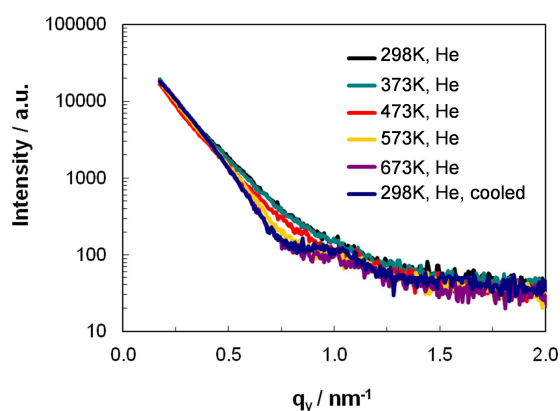


**Figure 3-5.** Background subtracted horizontal cuts of GISAXS data of large Pt nanoparticles on *n*-type GaN during heat treatment. The distinct feature in the horizontal cuts of GISAXS data at a scattering vector of  $1 \text{ nm}^{-1}$  is attributed to highly uniform particles above 573 K.<sup>[29, 38]</sup>

The mean particle height and particle width calculated from the vertical and horizontal cuts along with the corresponding aspect ratio are plotted for the complete treatment cycle (Figure 3-6 (a, b)). The as prepared large Pt particles have a slightly oblate shape (aspect ratio of  $\sim 1.2$ ), which does not change after the introduction of deuterium and up to temperatures reaching 473 K in He. At 573 K the particles become spherical. No change in particle size is observed at temperatures up to 673 K indicative of highly stable Pt particles. The particles retain their spherical shape after cooling back to room temperature.

The results obtained under identical treatment conditions for the small Pt particles are shown in Figure 3-6 (c, d). At the first, it is obvious that in contrast to the larger Pt particles, the shape of the smaller ones changes dynamically, following the changes in their environment. In He, the oblate particles flatten further, when the temperature is increased to 373 K. A subsequent substantial increase in the aspect ratio is observed upon the introduction of  $\text{D}_2$

indicating a strong interaction of deuterium with the small Pt particles. After the interruption of the  $D_2$  flow, the particles resume a similar shape as observed before the inlet of  $D_2$  indicating the reversible response of the particles to changes in the gas composition and temperature. The slight increase in the lateral diameter together with the slight decrease in the height of particles observed at the end of the heating cycle indicates the preservation of the volume of the particles. Thus, if at all, only a very small fraction of Pt particles underwent sintering during the treatment.

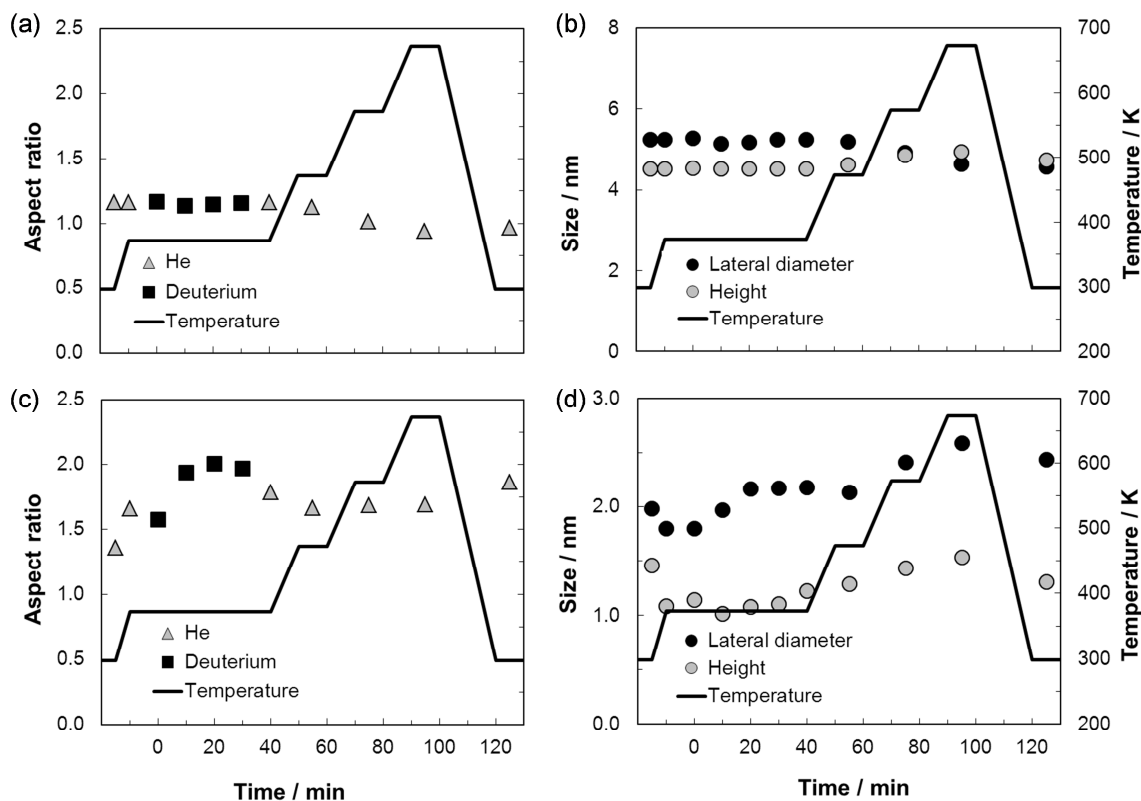


**Figure 3-6.** (a) Aspect ratio of large Pt nanoparticles on *n*-type GaN during helium and deuterium treatment and (b) the corresponding average lateral diameter and height of the nanoparticles. (c) Aspect ratio of small Pt nanoparticles on *n*-type GaN during helium and deuterium treatment and (d) the corresponding lateral diameter and height. The temperature cycle is shown as solid line.

The GIXANES spectra recorded before and after reduction are shown in Figure 3-7 and exhibit a decrease in the white line typical for the reduction of Pt particles.<sup>[39, 40]</sup> The position of the absorption edge of the Pt particles before reaction is shifted 2.4 eV as compared to the absorption edge position of the Pt foil, in agreement with a modest oxidation. The slight negative shift of 1.2 eV after reaction suggests the reduction of the Pt particles. It is important to note that the white line intensity of the GIXANES spectrum recorded after reduction does

not reach the value of the Pt metal reference foil spectrum. Recent studies indicate that this may be a genuine effect observed in reduced Pt nanoclusters attributed to chemisorbed hydrogen on the Pt surface, where the Pt-H bond creates empty antibonding states above the Fermi level that lead to an increase of the white line intensity.<sup>[41, 42]</sup>

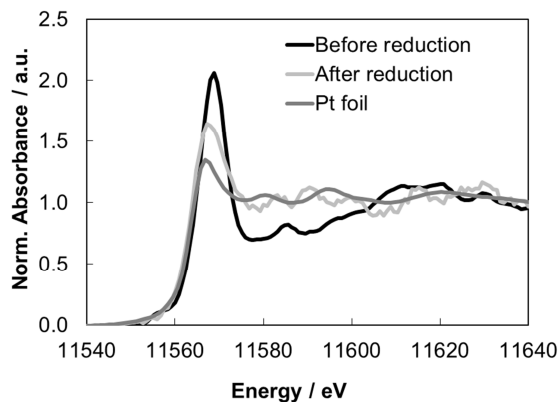


**Figure 3-7.** Normalized Pt  $L_3$  edge spectra of small Pt nanoparticles on *n*-type GaN and Pt foil recorded at 298 K in helium before and after reduction in deuterium. The GIXANES spectrum measured on Pt foils is included as reference. All recorded GIXANES spectra were analyzed using the XANES dactyloscope software and normalized to unity via average post-edge.

Metallic Pt was identified for the large Pt particles before and after deuterium treatment, as indicated by a very similar white line in comparison to the Pt foil (not shown). The larger Pt particles XANES consequently do not respond to the presence of a reducing atmosphere; the white line intensity remains at the value for the Pt metal foil and the absorption edge does not shift. It should be noted at this point that as compared to the small Pt particles the surface-to-volume ratio is an order of magnitude smaller. Therefore, the X-ray absorption spectrum is dominated by inner Pt atoms, which are metallic. Although similar reduction processes are expected with the oxidized surface of the large Pt particles, the thin oxide shell contributes too little to the total signal to provide a significant difference in the spectra.

The GISAXS and AFM studies demonstrate the high sintering resistance of the GaN-supported Pt particles making the system a suitable model catalyst for reactivity studies. Similar sintering resistance was observed for small oxide-supported Pt and Au clusters and Pt nanoparticles at temperatures reaching 673 K and higher.<sup>[43-46]</sup> The stability against migration is also reflected in the flat shape of the particles after preparation indicating a strong metal-semiconductor interaction. The dynamic changes of small Pt nanoparticles exposed to  $D_2$  is attributed to the change of the surface energy after the adsorption of deuterium and

subsequent reduction, which influences wetting.<sup>[47-50]</sup> The large particles become spherical above 573 K, which is attributed to Pt atom surface diffusion, because surface melting was not observed below 773 K for 8 nm Pt particles.<sup>[51]</sup> During reduction of small Pt particles, a reduction of the initially oxidized particles was observed, but a complete reduction of Pt species was not achieved under given experimental conditions. In contrast to the small particles, the oxidation state of large particles resembles metallic Pt and no changes in GIXANES were observed in the presence of D<sub>2</sub>. Because XANES is a bulk technique and not specifically surface sensitive, it cannot detect small fractions of oxidized metal species at the surface of a particle.<sup>[31]</sup> In the case of the small Pt particles, a considerable fraction of the Pt atoms are surface atoms.

We also observed that the *ex situ* oxidized samples of small particles had a nearly 30% larger particle size compared to that of the *in situ* reduced samples. The larger size is attributed to the presence of a significant oxygen content in the Pt particles in accordance with the literature<sup>[52]</sup> and observed here by GIXANES.

### 3.3.3 Hydrogenation of Ethene with Deuterium

For the hydrogenation of ethene over small and large Pt particles the samples were first reduced *ex situ* in H<sub>2</sub> at 373 K for 30 min. To study GISAXS during hydrogenation the temperature was increased in He to 373 K and the mixture of ethene and D<sub>2</sub> was introduced to the reaction cell. The reaction was followed for 30 min and the catalyst sample was cooled down to room temperature in reactant gas mixture. Then, He was introduced at room temperature. Figure 3-8 (a, b) and (c, d) shows the evolution of the shape for the large and small pre-reduced Pt particles, respectively. The large Pt particles did not change their size or shape. The aspect ratio of small particles slightly decreased upon the inlet of reactant mixture returning to the initial shape after the halt of reactant flow. This is perfectly in line with the dynamic changes of small particles.

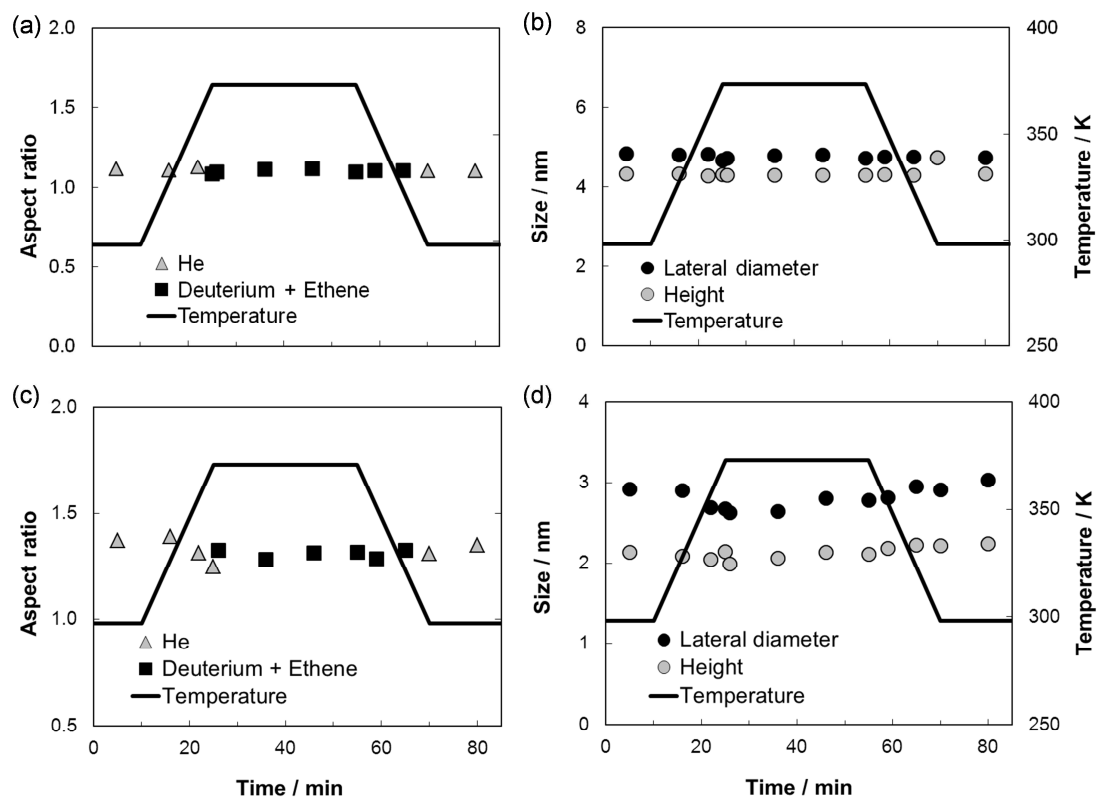


**Figure 3-8.** Aspect ratio and the corresponding lateral diameter and height during deuterium-ethene reaction of (a), (b) large and (c), (d) small Pt particles on *n*-type GaN. The temperature cycle is shown as solid line.

GIXANES spectra recorded for the two Pt samples are shown in Figure 3-9. The data exhibit a decreasing white line for small particles after the ethene deuteration, which indicates an increase in the degree of reduction of the small Pt particles.<sup>[39, 40]</sup> Again, the large Pt nanoparticles did not show any changes in their oxidation state before and after reaction. We attribute this to their low surface-to-volume ratio limiting the sensitivity of the method to pick up variations in the degree of surface reduction.



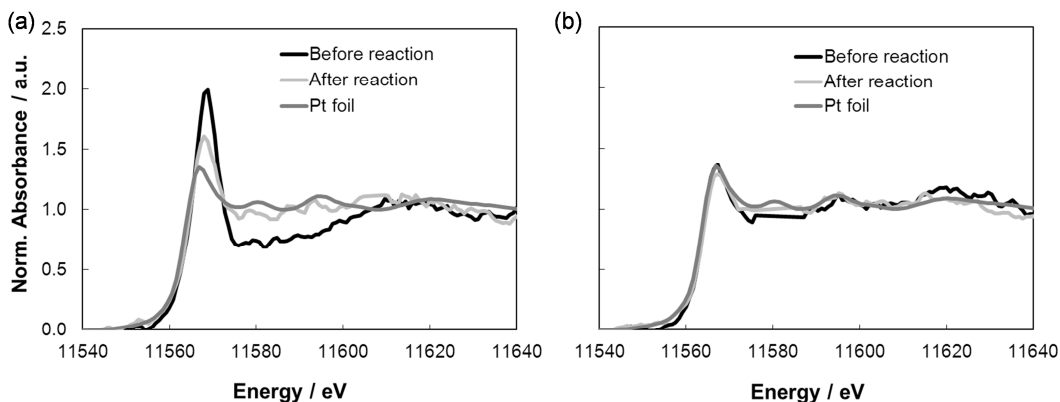


**Figure 3-9.** Normalized Pt  $L_3$  edge spectra of (a) small and (b) large Pt particles on *n*-type GaN and Pt foil recorded at 298 K in helium before and after deuterium-ethene reaction. Additional peaks were detected in XANES spectra for small and large particles in vicinity to the Pt edge due to sample charging, as is known for N K edge spectra of GaN.<sup>[53]</sup> These peaks were removed in the shown spectra for clarity.

To investigate the time evolution of the reduction of Pt particles, the absorbance of small Pt particles at 11.566 keV (absorption peak) was monitored during the reaction of ethene with  $D_2$  (Figure 3-10). During the temperature ramp from room temperature to 373 K the height of the white line decreased, which is ascribed to a reduction of the unoccupied states above the Fermi level with temperature. Plausibly, electron tunnelling over the Schottky barrier between the platinum oxide particle and GaN is increased at elevated temperatures. This may lead to a charging of the PtO particle and subsequent reduction of the white line intensity. The absorbance decreased only slightly during 30 min of reaction at 373 K and increased again with decreasing temperature, which is tentatively attributed to deuterium adsorption and/or temperature effect of the interactions of the support.<sup>[54, 55]</sup>

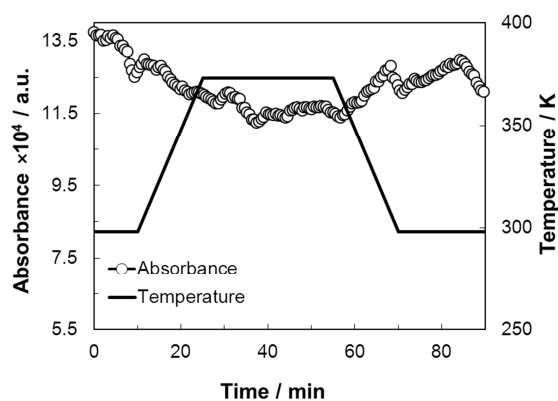


**Figure 3-10.** Absorbance at 11.566 keV monitored for small Pt particles on *n*-type GaN during ethene hydrogenation with deuterium. The temperature is plotted as solid line.

The comparison of the time evolution of the Pt white line absorption intensity during ethene hydrogenation at 373 K on large and small particles shows, as in the case of the pure reduction, a pronounced reduction of the small Pt particles in agreement with their predominantly high surface area (Figure 3-11).

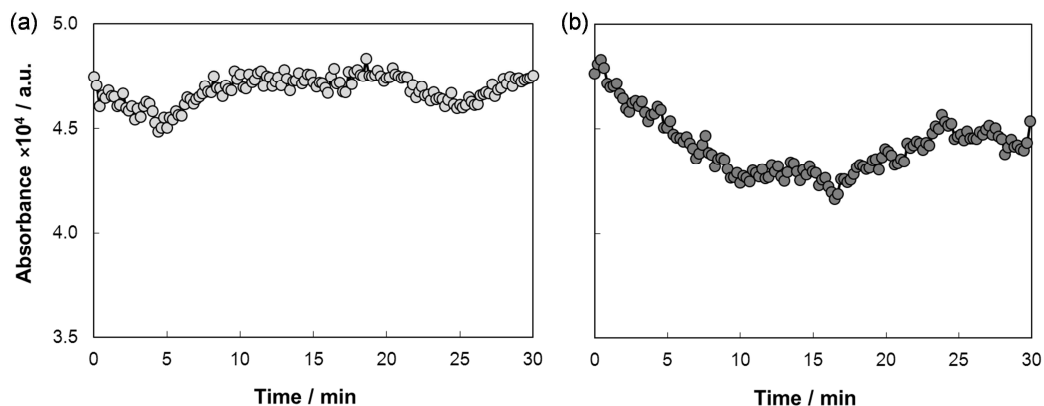


**Figure 3-11.** Absorbance at 11.556 keV monitored for (a) large and (b) small Pt particles on *n*-type GaN during reduction with deuterium at 373 K.

The catalytic activity of small and large GaN-supported Pt particles in ethene hydrogenation with deuterium was investigated by simultaneous TPRx using an on line mass spectrometer (Figure 3-12).<sup>[25, 27]</sup>

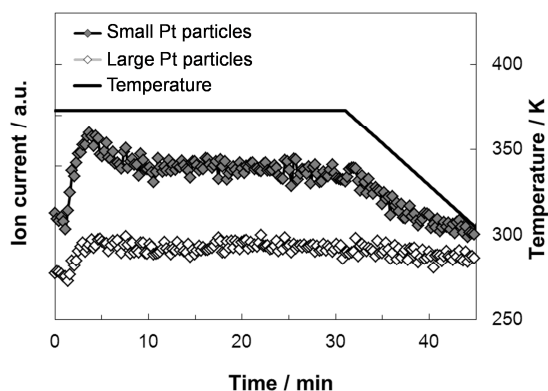


**Figure 3-12.** Ion current of ethane ( $C_2H_4D_2$ ,  $m/z = 30$ ) for small and large Pt nanoparticles on *n*-type GaN during deuterium-ethene reaction. The temperature is plotted as solid line.

The turnover rates calculated per total metal atom and per exposed surface atom basis are summarized in Table 3-2 showing that higher catalytic activity is obtained for small particles on per metal loading basis, as *a priori* expected solely on their higher surface-to-volume ratio. However, the activity of this catalyst dropped by about 30% after the first 10 min of reaction. The drop in activity coincides with the region where a fine change in particle shape, without

indication of sintering takes place. Similar distinct changes in catalytic performance following changes in particle morphology were reported for example for small Cu and Ag nanoparticles<sup>[25, 49]</sup>, however some coking of Pt cannot be fully excluded. A stable ethene conversion of 0.12% and 0.08% was determined for small and large Pt particles, respectively, in good accord with the results obtained on ~15 nm sized Pt particles tested under similar conditions.<sup>[56]</sup> The Pt metal loading based ethane turnover rates were 22 molecules Pt atom<sup>-1</sup> s<sup>-1</sup> (95 molecules Pt (exposed)<sup>-1</sup> s<sup>-1</sup>) after 4 min and 15 molecules Pt atom<sup>-1</sup> s<sup>-1</sup> (63 molecules Pt (exposed)<sup>-1</sup> s<sup>-1</sup>) after 10 min of reaction for small particles. In contrast, large particles had a constant turnover rate of 12 molecules Pt atoms<sup>-1</sup> s<sup>-1</sup> (53 molecules Pt (exposed)<sup>-1</sup> s<sup>-1</sup>). The latter value is comparable with that reported for about 15 nm large Pt particles.<sup>[56]</sup>

The GISAXS study during the deuterium-ethene reaction showed that small Pt particles on *n*-type GaN changed their shape reversibly, while large particles were not affected. The decreased lateral diameter of small particles in reactant gas atmosphere is attributed to rearrangements of particle facets. Altered surface energy might be caused by adsorbed carbon species that were left on the Pt surface during reaction.<sup>[57, 58]</sup> Similar dynamic shape transformations were observed from GISAXS during the epoxidation of propene on size-selected silver nanocatalysts by Vajda *et al.*<sup>[25]</sup> It was suggested that propene ligands might alter the surface energy of the particles and the strength of interaction to the support.

**Table 3-2.** Ethene conversion, ethane turnover rate, total and estimated surface Pt atoms for Pt nanoparticles on *n*-type GaN.

Pt particles	Ethene conversion / %	Total Pt atoms × 10 <sup>-11</sup> / mol <sup>(c)</sup>	Turnover rate / ethane molecules × total Pt atoms <sup>-1</sup> s <sup>-1</sup>	Surface Pt atoms × 10 <sup>-12</sup> / mol <sup>(c)</sup>	Turnover rate / ethane molecules × surface Pt atoms <sup>-1</sup> s <sup>-1</sup>
small	0.18 <sup>(a)</sup>	2.2	22 <sup>(a)</sup>	5.2	95 <sup>(a)</sup>
	0.12 <sup>(b)</sup>		15 <sup>(b)</sup>		63 <sup>(b)</sup>
large	0.08	1.4	12	3.0	53

<sup>(a)</sup> After 4 min of reaction (peak). <sup>(b)</sup> After 10 min of reaction (steady-state). <sup>(c)</sup> Estimate of the number of total atoms in the nanoparticles. A hemispherical particle shape was assumed for small particles and a flat cuboid for large particles, and the volume and surface area calculated from the average height and diameter of particles determined by GISAXS (*cf.* Table 3-1) (The area of the particle base inaccessible to reactant molecules was not taken into consideration). The number of atoms on the surface of the particles was calculated by taking into consideration the 2.77 Å Pt-Pt distance in Pt(111) of a fcc structure.

The catalytic activity observed is in good agreement with the activity of a Pt nanoparticle array reported by Grunes *et al.*<sup>[56]</sup> A turnover frequency of 354 molecules Pt atoms<sup>-1</sup> s<sup>-1</sup> was found for this Pt particle array prepared by electron beam lithography. It is interesting to note

of the small Pt particles deactivated at the beginning of the reaction, but it was concluded that the deactivation was unrelated to particle sintering. Thus, we tentatively attribute the deactivation to changes in faceting of the particles.

The possibility to simultaneously detect GISAXS as well as X-ray fluorescence allows for the measurement of grazing incidence X-ray absorption spectra such as XANES and extended X-ray absorption fine structure (EXAFS).<sup>[59]</sup> Although EXAFS was not employed in this study, future work on the Pt particle on GaN will involve EXAFS, as this will enable us to exactly determine the amount of oxygen in the platinum nanoparticles. An example of such an experiment performed in the same experimental setup is illustrated in Figure 3-1, in which a normalized and background corrected quick EXAFS scan of oxidized Pt<sub>10</sub> nanoclusters on MgO is presented. Depending on the required data quality, *i.e.*, signal-to-noise ratio, the recording time can be varied. In the measurement of Figure 3-1 a quick EXAFS is shown with a recording time of only 14 min per scan already providing valuable information about the Pt-O bond distance (0.203 nm) and the coordination number (2.7), which were obtained by estimated fitting of the Fourier transform of the EXAFS in R-space with Artemis.<sup>[32]</sup>

### 3.4 Conclusion

In the presented study, Pt nanoparticles with two different sizes of 1.8 nm and 6.7 nm supported on *n*-type GaN surfaces were studied by combined *in situ* GISAXS, GIXANES, and TPRx during reduction and deuterium-ethene reaction. Particle size analysis was complemented by *ex situ* methods such as TEM and AFM. The model catalysts resisted sintering during reduction and hydrogenation reaction at 373 K as well as at stability test with temperatures reaching 673 K. However, the deuterium and deuterium-ethene atmosphere at 373 K had a significant impact on the shape of the smaller Pt particles, which dynamically responded to changes in their environment. Small Pt particles as well as large Pt particles showed catalytic activity in deuteration of ethene with turnover rates comparable to literature values.<sup>[56]</sup> The small particles exhibited a deactivation period in the first 10 min of reaction that was not related to particle sintering or particle shape changes, but most likely to changes in the morphology of the particles.<sup>[49]</sup> The decrease in the white line intensity with increasing temperature during the reaction on small particles reflects an increase in the electron density

of the particles. This suggests a charge transfer that occurred by thermal induction of the support material. The control of this energy input by *e.g.* illumination in the semiconductor bandgap region could help to alter the electron density on the metal particle and to realize catalysis on demand.

The research on small metal particles for catalysis has been of broad interest among others due to the large fraction of surface atoms that drive surface reactions. But for structure-sensitive reactions such as isomerization or hydrogenolysis<sup>[60]</sup> both the size and shape of the Pt particles are crucial for their activity and selectivity. Our study revealed dynamic changes in the particle shape of small particles in deuterium and deuterium-ethene gas mixtures that may be responsible for the varying catalytic performance. This dynamic structural/morphological change of small nanoparticles under reaction conditions should be considered not only in studies of structure-sensitive reactions, but also in reactions, in which adsorption of one of the reactants can cause a dynamic structural disorder of the surface and/or affect the morphology of the whole particle.<sup>[24, 25, 48, 49, 61-63]</sup> The change in particle shape, along with the potential restructuring of the catalyst-support interface, may also alter the electronic structure of small particle and its interaction (including charge transfer) with the support during the course of the catalytic reaction. On the other hand, size- and shape-selective synthesis of large particles could also help for a better understanding of structure-sensitive reactions, because the shape of the large particles was not affected by deuterium and the deuterium-ethene mixture.

In brief, the combination of surface-sensitive *in situ* GISAXS and GIXANES with TPRx proved to be a powerful method to study the effect of particle size, shape, and oxidation state of model catalyst as illustrated on the example of semiconductor-supported Pt catalysts under realistic reaction conditions.

### 3.5 References

- [1] A. Stierle, A. M. Molenbroek, *MRS Bull.* **2007**, 32, 1001.
- [2] P. L. J. Gunter, J. W. Niemantsverdriet, F. H. Ribeiro, G. A. Somorjai, *Catal. Rev. Sci. Eng.* **1997**, 39, 77.
- [3] S. E. Deutsch, J. T. Miller, K. Tomishige, Y. Iwasawa, W. A. Weber, B. C. Gates, *J. Phys. Chem.* **1996**, 100, 13408.
- [4] E. Bus, R. Prins, J. A. van Bokhoven, *Phys. Chem. Chem. Phys.* **2007**, 9, 3312.
- [5] M. G. O'Brien, A. M. Beale, S. D. M. Jacques, B. M. Weckhuysen, *Top. Catal.* **2009**, 52, 1400.
- [6] J. A. van Bokhoven, C. Louis, J. T. Miller, M. Tromp, O. V. Safonova, P. Glatzel, *Angew. Chem. Int. Edit.* **2006**, 45, 4651.
- [7] V. V. Kaichev, I. P. Prosvirin, V. I. Bukhtiyarov, H. Unterhalt, G. Rupprechter, H. J. Freund, *J. Phys. Chem. B* **2003**, 107, 3522.
- [8] B. C. Gates, H. Knoezinger, F. C. Jentoft, *Advances in Catalysis, Vol. 52*, Academic Press., **2009**.
- [9] G. C. Bond, *Chem. Soc. Rev.* **1991**, 20, 441.
- [10] M. M. Koebel, L. C. Jones, G. A. Somorjai, *J. Nanopart. Res.* **2008**, 10, 1063.
- [11] G. W. Busser, J. G. van Ommen, J. A. Lercher, *J. Phys. Chem. B* **1999**, 103, 1651.
- [12] T. Teranishi, M. Hosoe, T. Tanaka, M. Miyake, *J. Phys. Chem. B* **1999**, 103, 3818.
- [13] A. Y. Stakheev, L. M. Kustov, *Appl. Catal. A-Gen.* **1999**, 188, 3.
- [14] G. M. Schwab, J. Block, W. Müller, D. Schultze, *Naturwissenschaften* **1957**, 44, 582.
- [15] J. C. Frost, *Nature* **1988**, 334, 577.
- [16] G. M. Schwab, G. Mutzbauer, *Naturwissenschaften* **1959**, 46, 13.
- [17] F. Solymosi, I. Tombacz, M. Kocsis, *J. Catal.* **1982**, 75, 78.
- [18] W. Langenbeck, D. Nehring, H. Dreyer, *Z. Anorg. Allg. Chem.* **1960**, 304, 37.
- [19] W. Langenbeck, D. Nehring, H. Dreyer, H. Fuhrmann, *Z. Anorg. Allg. Chem.* **1962**, 314, 167.
- [20] W. Schottky, *Z. Phys.* **1939**, 113, 367.
- [21] V. P. Zhdanov, *Surf. Sci.* **2002**, 512, L331.
- [22] J. Y. Park, G. A. Somorjai, *J. Vac. Sci. Technol. B* **2006**, 24, 1967.
- [23] M. Ali, V. Cimalla, V. Lebedev, H. Romanus, V. Tilak, D. Merfeld, P. Sandvik, O. Ambacher, *Sens. Actuator B-Chem.* **2006**, 113, 797.
- [24] Y. Lei, F. Mehmood, S. Lee, J. P. Greeley, B. Lee, S. Seifert, R. E. Winans, J. W. Elam, R. J. Meyer, P. C. Redfern, D. Teschner, R. Schlögl, M. J. Pellin, L. A. Curtiss, S. Vajda, *Science* **2010**, 328, 224.
- [25] S. Vajda, S. Lee, K. Sell, I. Barke, A. Kleibert, V. von Oeynhausen, K.-H. Meiwes-Broer, A. F. Rodriguez, J. W. Elam, M. M. Pellin, B. Lee, S. Seifert, R. E. Winans, *J. Chem. Phys.* **2009**, 131, 121104.
- [26] B. Lee, S. Seifert, S. J. Riley, G. Tikhonov, N. A. Tomczyk, S. Vajda, R. E. Winans, *J. Chem. Phys.* **2005**, 123, 074701.
- [27] S. Lee, L. M. Molina, M. J. Lopez, J. A. Alonso, B. Hammer, B. Lee, S. Seifert, R. E. Winans, J. W. Elam, M. J. Pellin, S. Vajda, *Angew. Chem. Int. Edit.* **2009**, 48, 1467.

- [28] G. Renaud, R. Lazzari, C. Revenant, A. Barbier, M. Noblet, O. Ulrich, F. Leroy, J. Jupille, Y. Borensztein, C. R. Henry, J. P. Deville, F. Scheurer, J. Mane-Mane, O. Fruchart, *Science* **2003**, *300*, 1416.
- [29] J. R. Levine, L. B. Cohen, Y. W. Chung, P. Georgopoulos, *J. Appl. Crystallogr.* **1989**, *22*, 528.
- [30] A. Guinier, G. Fournet, C. B. Walker, K. L. Yudowitch, *Small Angle Scattering of X-rays*, Wiley: New York, **1955**.
- [31] J. E. Penner-Hahn, *Coord. Chem. Rev.* **1999**, *192*, 1101.
- [32] B. Ravel, M. Newville, *J. Synchrotron Radiat.* **2005**, *12*, 537.
- [33] R. M. Rioux, H. Song, J. D. Hoefelmeyer, P. Yang, G. A. Somorjai, *J. Phys. Chem. B* **2005**, *109*, 2192.
- [34] S. Schäfer, S. A. Wyrzgol, Y. Wang, J. A. Lercher, M. Stutzmann, *Phys. Status Solidi C* **2010**, *7*, 411.
- [35] I. Horcas, R. Fernandez, J. M. Gomez-Rodriguez, J. Colchero, J. Gomez-Herrero, A. M. Baro, *Rev. Sci. Instrum.* **2007**, *78*, 013705.
- [36] Y. Y. Yeo, L. Vattuone, D. A. King, *J. Chem. Phys.* **1997**, *106*, 392.
- [37] C. Revenant, F. Leroy, R. Lazzari, G. Renaud, C. R. Henry, *Phys. Rev. B* **2004**, *69*, 035411.
- [38] M. Harada, K. Saijo, N. Sakamoto, H. Einaga, *Colloid Surf. A-Physicochem. Eng. Asp.* **2009**, *345*, 41.
- [39] I. E. Beck, V. V. Kriventsov, D. P. Ivanov, V. I. Zaikovsky, V. I. Bukhtiyarov, *Nucl. Instrum. Meth. A* **2009**, *603*, 108.
- [40] F. W. Lytle, P. S. P. Wei, R. B. Gregor, G. H. Via, J. H. Sinfelt, *J. Chem. Phys.* **1979**, *70*, 4849.
- [41] J. Bartolome, F. Bartolome, L. M. Garcia, E. Roduner, Y. Akdogan, F. Wilhelm, A. Rogalev, *Phys. Rev. B* **2009**, *80*, 014404.
- [42] D. E. Ramaker, B. L. Mojet, M. T. G. Oostenbrink, J. T. Miller, D. C. Koningsberger, *Phys. Chem. Chem. Phys.* **1999**, *1*, 2293.
- [43] R. E. Winans, S. Vajda, B. Lee, S. J. Riley, S. Seifert, G. Y. Tikhonov, N. A. Tomczyk, *J. Phys. Chem. B* **2004**, *108*, 18105.
- [44] S. Vajda, R. E. Winans, J. W. Elam, B. Lee, M. J. Pellin, S. Seifert, G. Y. Tikhonov, N. A. Tomczyk, *Top. Catal.* **2006**, *39*, 161.
- [45] R. E. Winans, S. Vajda, G. E. Ballentine, J. W. Elam, B. Lee, M. J. Pelline, S. Seifert, G. Y. Tikhonov, N. A. Tomczyk, *Top. Catal.* **2006**, *39*, 145.
- [46] S. Vajda, M. J. Pellin, J. P. Greeley, C. L. Marshall, L. A. Curtiss, G. A. Ballentine, J. W. Elam, S. Catillon-Mucherie, P. C. Redfern, F. Mehmood, P. Zapol, *Nat. Mater.* **2009**, *8*, 213.
- [47] T. Wang, C. Lee, L. D. Schmidt, *Surf. Sci.* **1985**, *163*, 181.
- [48] P. Nolte, A. Stierle, N. Y. Jin-Phillipp, N. Kasper, T. U. Schulli, H. Dosch, *Science* **2008**, *321*, 1654.
- [49] P. L. Hansen, J. B. Wagner, S. Helveg, J. R. Rostrup-Nielsen, B. S. Clausen, H. Topsøe, *Science* **2002**, *295*, 2053.
- [50] C. R. Henry, *Prog. Surf. Sci.* **2005**, *80*, 92.

- [51] Z. L. Wang, J. M. Petroski, T. C. Green, M. A. El-Sayed, *J. Phys. Chem. B* **1998**, *102*, 6145.
- [52] A. P. Markusse, B. F. M. Kuster, D. C. Koningsberger, G. B. Marin, *Catal. Lett.* **1998**, *55*, 141.
- [53] M. Katsikini, T. D. Moustakas, E. C. Paloura, *J. Synchrotron Radiat.* **1999**, *6*, 555.
- [54] F. W. Lytle, R. B. Gregor, E. C. Marques, D. R. Sandstrom, G. H. Via, J. H. Sinfelt, *J. Catal.* **1985**, *95*, 546.
- [55] M. G. Samant, M. Boudart, *J. Phys. Chem.* **1991**, *95*, 4070.
- [56] J. Grunes, J. Zhu, E. A. Anderson, G. A. Somorjai, *J. Phys. Chem. B* **2002**, *106*, 11463.
- [57] P. S. Cremer, G. A. Somorjai, *J. Chem. Soc. Faraday T.* **1995**, *91*, 3671.
- [58] P. S. Cremer, X. C. Su, Y. R. Shen, G. A. Somorjai, *Catal. Lett.* **1996**, *40*, 143.
- [59] D. C. Koningsberger, B. L. Mojet, G. E. van Dorssen, D. E. Ramaker, *Top. Catal.* **2000**, *10*, 143.
- [60] G. A. Somorjai, *Abstr. Pap. Am. Chem. Soc.* **1985**, *189*, 79.
- [61] F. Tao, S. Dag, L. W. Wang, Z. Liu, D. R. Butcher, H. Bluhm, M. Salmeron, G. A. Somorjai, *Science* **2010**, *327*, 850.
- [62] M. A. Newton, C. Belver-Coldeira, A. Martinez-Arias, M. Fernandez-Garcia, *Nat. Mater.* **2007**, *6*, 528.
- [63] G. Renaud, R. Lazzari, F. Leroy, *Surf. Sci. Rep.* **2009**, *64*, 255.



# Chapter 4

## Platinum Nanoparticles on Gallium Nitride Surfaces: The Effect of Semiconductor Doping on Nanoparticle Reactivity

### Abstract

The electronic control of catalytic activity via the electronic metal-support interaction is investigated on novel hybrid systems containing platinum nanoparticles supported on *n*- and *p*-type gallium nitride (GaN). High-pressure photoemission spectroscopy was used to study *in situ* oxidation and reduction on the particles. The results revealed a significant influence of the underlying wide bandgap semiconductor on the chemical composition and oxygen affinity of the supported particles under X-ray illumination. As-prepared cuboctahedral platinum particles on *n*-type GaN showed a higher amount of oxidized surface atoms than particles on *p*-type GaN. Upon oxygen exposure, an immediate oxidation of particles supported on *n*-type GaN was observed, whereas only little oxidation was recorded for particles on the *p*-type surface. Consequently, these experiments demonstrate that the platinum chemical state is affected under X-ray irradiation by the type of GaN doping. The strong particle-support interaction is consistent with the charge transfer of X-ray photo-generated free carriers at the semiconductor-particle interface and suggests that GaN is a promising wide bandgap support material for photocatalysis and electronic control of catalysis.

## 4 Platinum Nanoparticles on Gallium Nitride Surfaces: The Effect of Semiconductor Doping on Nanoparticle Reactivity

### 4.1 Introduction

The rational synthesis of photocatalysts is challenging by the conversion of photon energy into a catalytically active species due to the selective charge transfer and the application of this input for the modification of catalytic activity and selectivity. Such control requires the use of semiconducting supports combined with catalytically active metal nanoparticles, yielding advanced concepts of Green Chemistry for the development of efficient catalysts with low consumption of energy and resources. Solid catalysts are widely used in heterogeneous catalyzed reactions and numerous studies have been devoted to understand and control the metal particle properties in accordance with their performance in catalysis. The effect of the particle size and shape on their catalytic activity and selectivity has been investigated in multipath reactions<sup>[1-5]</sup> and metal-support interactions have been studied for several oxidic supports<sup>[6, 7]</sup>. For instance, methanol decomposition was tested on Pt particles supported on reducible ( $\text{CeO}_2$ ,  $\text{TiO}_2$ ) and non-reducible ( $\text{SiO}_2$ ,  $\text{ZrO}_2$ ,  $\text{Al}_2\text{O}_3$ ) oxides, with the highest activity obtained on the  $\text{ZrO}_2$  support.<sup>[8]</sup> A flattening of the particles was observed on  $\text{ZrO}_2$ , while only weak interactions were obtained for  $\text{SiO}_2$ -supported particles. Strong metal-support interaction (SMSI) was observed for metal particles supported on  $\text{TiO}_2$ , where particle encapsulation occurred after a high-temperature treatment.<sup>[9]</sup> Although some oxidic supports exhibit semiconducting properties, the effect and potential impact of an underlying semiconductor is rarely discussed. For photocatalysis, the wide bandgap semiconductors  $\text{TiO}_2$  and  $\text{ZnO}$  were extensively studied, which are similar to  $\text{GaN}$  in terms of bandgap and band positions. Thus, both  $\text{GaN}$  and  $\text{TiO}_2$  have been investigated for water splitting or light harvesting.<sup>[10-13]</sup> However, the *p*-type doping remains difficult for metal oxides like  $\text{ZnO}$  or  $\text{TiO}_2$  due to their high background *n*-type conductivity. In contrast,  $\text{GaN}$  is one of the few wide bandgap semiconductors that is available with controlled, electronic *n*- and *p*-type doping. With the Pt work function (5.7 eV) being located approximately in the center of the  $\text{GaN}$  bandgap ( $E_G = 3.4$  eV) (Figure 4-1), Pt- $\text{GaN}$  hybrid structures provide a rare combination for the investigation of the effect of charge transfer on the semiconductor doping. Thermal, electrical, or optical excitation can adjust the charge density of the  $\text{GaN}$  surface and thus,  $\text{GaN}$  may be a suitable substrate that influences the catalytic activity of supported particles by its electronic activation.

GaN is thermally and chemically stable, and decomposition is not observed up to 1123 K.<sup>[14]</sup> A thin oxygen adlayer is typically present on the GaN surface under ambient conditions.<sup>[15, 16]</sup> Oxygen saturation coverages have been determined experimentally and theoretically to be 0.4-0.9 ML for ordered GaN(0001) surfaces, where oxygen has been found to bind only to Ga atoms without contribution of O-N bonds.<sup>[17-19]</sup> Upon oxidation, the formation of intermediate GaO<sub>x</sub> species was reported to be present prior to stoichiometric Ga<sub>2</sub>O<sub>3</sub>. An electrically insulating oxide on the GaN surface can only be grown at temperatures above 975 K.<sup>[20, 21]</sup>

Pt-GaN compounds have been reported as Schottky diodes for the detection of small molecules like hydrogen and the monitoring of a hot electron chemicurrent upon the exothermic CO oxidation.<sup>[22-24]</sup> The surface band bending by Schottky contact formation is determined by the Fermi level alignment of the metal and semiconductor, providing an electric field for the separation of photo-generated electron-hole pairs and the driving force of free carriers to the interface. However, for the understanding of the complex chemical and electrical interaction at the Pt-GaN interface, both the particle and semiconductor properties must be considered. The direct comparison of Pt particles on electronically active *n*- and *p*-type GaN surfaces allows the discrimination of photo-induced charge transfer from other energy dissipation channels like hot electron or phonon generation.

Kinetic experiments have provided the evidence for an electronically controlled catalytic performance of Pt particles in the hydrogenation of ethene to ethane via light stimulation of the underlying *n*- and *p*-type GaN support (consider Chapter 5). Here, we have performed a comparative study on the interactions between Pt particles and *n*- and *p*-type GaN surfaces during reduction and oxidation using *in situ* high-pressure photoelectron spectroscopy (HP-XPS). The chemical composition of the Pt particles and the GaN supports are discussed in terms of the semiconductor band alignment. A charge transfer model under X-ray radiation is presented, elucidating the observed differences of the Pt oxidation behavior on *n*- and *p*-type GaN. Considerations of the Pt-GaN system are highly relevant for other semiconductor-nanoparticle compounds used in photocatalysis.

## 4.2 Experimental

### 4.2.1 Sample Preparation

Monodisperse, size- and shape-selected Pt particles were prepared either by the polyol process using silver nitrate to achieve cuboctahedral or cubic geometry, or by the reduction of the Pt

precursor with alcohol.<sup>[2, 25]</sup> Poly(*N*-vinylpyrrolidone) (PVP) was used as the protecting shell to avoid clustering in solution.

Small Pt particles with an average size of 2.0 nm were synthesized by the reduction of chloroplatinic acid with 1-propanol.<sup>[25]</sup> An aqueous solution (bidistilled water > 18.2 MΩ-cm, 20 ml) containing chloroplatinic acid solution (0.057 mmol, 8 wt.% in water) and PVP (2.0 mmol monomer) was stirred at 373 K for 2 h before 1-propanol (130 ml) was added as reduction agent. The solvent was evaporated in vacuum after 48 h at 373 K and the residue was re-dispersed in ethanol (20 ml).

Larger Pt particles of cubic and cuboctahedral shape with an average size of 8 nm (7.6 nm for cubes, and 8.1 nm for cuboctahedra) were prepared by the polyol process.<sup>[2]</sup> Ethylene glycol solutions of PVP (1.125 mmol monomer, 3 ml) and chloroplatinic acid (0.094 mmol, 1.5 ml) were alternately added to silver nitrate ( $1 \times 10^{-3}$  mmol for cubes, and  $5.5 \times 10^{-3}$  mmol for cuboctahedra) dissolved in ethylene glycol (2.5 ml) every 30 s for 17 min at 473 K. Subsequently, the mixture was refluxed at 473 K for 5 min. Precipitated silver chloride was separated by centrifugation (4000 rpm, 283 K, 30 min) and the particles were settled from the supernatant by adding acetone (23 ml) and separated by centrifugation (3000 rpm, 283 K, 5 min). The precipitate was dispersed in ethanol (3 ml) in an ultrasonic bath (15 min) and *n*-hexane (9 ml) was added to wash out residual silver ions. Finally, the particles were separated again by centrifugation (3000 rpm, 283 K, 5 min). The washing procedure was repeated for additional two times before the final particle re-dispersion in ethanol (3 ml).

The average particle size in ethanol was determined by transmission electron microscopy (TEM, JEOL JEM-2010) at an acceleration voltage of 120 keV before the deposition onto the GaN surfaces.

MOCVD-grown GaN thin films (3 μm) were used as nanoparticle support, with net carrier concentrations (300 K) of  $n = 2 \times 10^{18} \text{ cm}^{-3}$  for *n*-type and  $p = 5 \times 10^{17} \text{ cm}^{-3}$  for *p*-type GaN. These GaN surfaces exhibit Ga-face crystal polarity along the [0001] axis, resulting in high chemical and mechanical stability due to low surface defect concentrations.<sup>[26-28]</sup> To avoid sample charging during photoemission experiments, ohmic contacts were evaporated onto two edges of all GaN samples (Ti/Al 30/70 nm on *n*-type, Ni/Au 20/20 nm on *p*-type) and annealed at 775 K for 5 min prior to particle deposition.<sup>[29, 30]</sup> The surface morphologies of the annealed reference samples were analyzed with atomic force microscopy (AFM), revealing smooth surfaces with atomic grown steps (Figure 4-10 (a, d)). All substrates were cleaned in acetone (ultrasonic bath, 10 min) and rinsed with 2-propanol. After cleaning, Pt dispersions

with a defined metal concentration in ethanol ( $6.2 \times 10^{-4} \text{ mol l}^{-1}$  Pt for 2.0 nm particles and  $2.2 \times 10^{-3} \text{ mol l}^{-1}$  Pt for large cubic and cuboctahedral particles) were pipetted onto the GaN surfaces and spin-coated at 3000 rpm for 60 s. The samples were heated to 360 K for 5 min to evaporate excess solvent. The remaining PVP-capping was removed by oxygen plasma with an oxygen pressure of 1.4 mbar at 200 W for 5 min (TePla 100-E, Technics Plasma GmbH). To increase the adhesive forces between particles and the GaN surfaces, the samples were moderately heated to 425 K for 15 min in nitrogen atmosphere (100 mbar).<sup>[31, 32]</sup> The complete removal of PVP fragments after the oxygen plasma treatment was verified by the absence of any peaks related to organic fragments from PVP in thermal desorption spectra up to 800 K.<sup>[31]</sup>

The distribution of the deposited nanoparticles on GaN surfaces was characterized by AFM (Veeco Multimode, Nanoscope V) in tapping mode. The average number of particles per  $\text{cm}^2$  was used to calculate the total number of Pt atoms, as well as the fraction of Pt surface atoms on the particle (in percentage of a monolayer, %ML), with respect to an atom density of  $1.5 \times 10^{15} \text{ cm}^{-2}$  for Pt(111).<sup>[33]</sup> It was assumed that the deposited particles are truncated and only two thirds of the surface atoms contribute to the chemically active surface area. The number of Pt atoms per particle and the number of Pt surface atoms were determined with the consideration of the individual particle geometry (consider calculations described in 2.2.2).<sup>[34]</sup>

Two sets of samples were used for the experiments presented in this work. The first set contained as-prepared small, spherical and large, cubic and cuboctahedral particles after oxygen plasma treatment on both *n*- and *p*-type GaN. From these samples, the GaN surfaces with cuboctahedral particles were used for *in situ* reduction experiments. The second set of samples based on cuboctahedral particles was reduced *ex situ* in flowing hydrogen (1 bar) at 775 K for 3 h and were used afterwards for the *in situ* oxidation. These samples were stored and transported in nitrogen atmosphere without exposure to air.

#### 4.2.2 High-Pressure X-ray Photoemission Spectroscopy

All *in situ* high-pressure XPS measurements were performed at the ISSS beamline at BESSY II (Helmholtz-Zentrum Berlin). XPS can be performed at the mbar pressure range using a differentially pumped electrostatic lens system.<sup>[35]</sup> The ISSS setup consists of a loadlock and

a high-pressure XPS analysis chamber with a base pressure of  $1 \times 10^{-7}$  mbar. The differentially pumped electrostatic lens system was used to maintain a high count rate by reducing photoelectron scattering at high pressures. A sapphire sample holder allows for laser heating during the measurements. The sample was clamped between stainless steel plates for sufficient grounding and optical access to the sample was provided by a 3 mm diameter hole in the top plate. The HP-XPS setup is described in more detail by Salmeron and Schlögl and Knop-Gericke *et al.*<sup>[36, 37]</sup> We performed the measurements at a constant photoelectron kinetic energy of 270 eV by adjusting the incident monochromatic photon energy with respect to the analyzed core level binding energy. The constant kinetic energy of the photoelectrons provided a material depth of 8 Å for all analyzed species.<sup>[38]</sup> Detailed spectra were collected for O1s, N1s, C1s, Pt4f, and Ga3d core levels, using the CASA XPS software for quantitative analysis of peak positions, line widths, and relative peak areas.<sup>[39]</sup> The raw spectra were fitted with Gaussian-Lorentzian functions and a Shirley background was subtracted prior to peak fitting to account for energy loss processes, e.g. the inelastic scattering of photoelectrons.<sup>[40]</sup> Asymmetric Doniach-Sunjic functions with asymmetry factors of 0.008-0.01 were applied for the fitting of Pt4f core level spectra (Table 4-4). Spin-orbit coupling results in a Pt4f doublet structure with a peak separation of 3.3 eV and a branching intensity ratio of 0.75 between Pt 4f<sub>7/2</sub> and Pt 4f<sub>5/2</sub>. The full width at half maximum (FWHM) was restricted to  $1.0 \pm 0.1$  eV for all Pt species in the spectrum. The total Pt coverage was determined from the Pt/Ga element ratio (Equation 4-1), taking into account the respective energy dependent ionization cross section and the incident photon flux (Table 4-1).<sup>[41, 42]</sup>

$$\frac{Pt}{Ga} = \frac{A_{Pt4f} \sigma_{Ga3d} \varphi_{Ga3d}}{A_{Ga3d} \sigma_{Pt4f} \varphi_{Pt4f}} \quad (\text{Equation 4-1})$$

With Pt4f and Ga3d peak areas  $A$ , ionization cross sections  $\sigma$ , and the incident photon flux  $\varphi$ .

**Table 4-1.** Energy dependent photon flux and ionization cross sections for Ga3d and Pt4f core levels.<sup>[41, 42]</sup>

Core level	Photon energy/ eV	Photon flux $\times 10^{10} / \text{s}^{-1}$	Cross section / b
Ga3d	285	4.32	2.04
Pt4f	365	1.72	5.03

In the first experiment, the impact of the X-ray irradiation on the *n*- and *p*-type samples was analyzed by continuous measurements at room temperature in vacuum over 5 h. In the following experiment, the oxidation state of the particles with different shapes was

investigated under X-ray irradiation as a function of the GaN support doping. Pt4f core level spectra were acquired from the first sample set, the as-prepared samples, at room temperature in vacuum, at room temperature in hydrogen, and during *in situ* reduction with hydrogen at 800 K. Additionally, a Pt foil treated with oxygen plasma (1.4 mbar oxygen, 200 W, 5 min) was measured at room temperature in vacuum for the comparison of Pt oxidation states and the chemical composition with as-prepared Pt-GaN samples. Using the second set of samples (*ex situ* reduced), the *in situ* oxidation of the Pt particles was investigated at 725 K in oxygen atmosphere. The gas pressure was adjusted to 0.5 mbar during all high-pressure experiments.

For a correct interpretation of the XPS spectra of the samples based on the wide bandgap semiconductor, several physical quantities need to be considered (Figure 4-1). The Fermi level of the semiconductor is aligned with the Fermi level of the XPS detector upon annealing of the ohmic contact on the GaN support. Thus, the binding energy is defined by the difference of the surface core level energy and the Fermi level of the semiconductor. The positions of the conduction and valence band at the semiconductor surface differ from that in the bulk material by an upward band bending for *n*-type and a downward band bending for *p*-type GaN. This difference is described by the Schottky barrier.

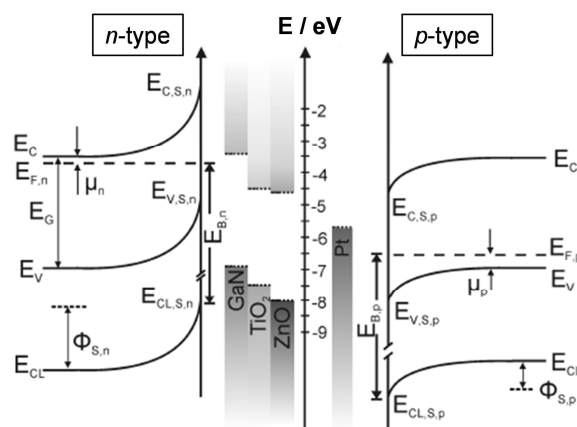


**Figure 4-1.** Energetic positions of GaN, TiO<sub>2</sub>, and ZnO bandgaps, GaN band bending in *n*- and *p*-type, and Pt work function (bandgap  $E_G$ , energy of core level, valence, and conduction band  $E_{CL}$ ,  $E_V$ ,  $E_C$ , Fermi level  $E_F$ , difference of Fermi level and band edge  $\mu$ , core level electron binding energy  $E_B$ , and Schottky barrier height  $\Phi_S$ ).

The binding energies for *n*- and *p*-type samples are defined by Equation 4-2.<sup>[43]</sup> For heavily doped GaN, the Fermi level is approximately equal to the energetic position of the donor and acceptor level in the *n*- and *p*-type sample, respectively. The measured offset in binding energies for *n*- and *p*-type GaN is derived from these considerations (Equation 4-3).<sup>[43]</sup>

$$E_{B,n} = E_{F,n} - E_{CL} - \Phi_{S,n} \quad \text{and} \quad E_{B,p} = E_{F,p} - E_{CL} - E_{S,p} \quad (\text{Equation 4-2})$$

$$\begin{aligned} \Delta E_B &= E_{B,n} - E_{B,p} = E_{F,n} - E_{F,p} - \Phi_{S,n} - \Phi_{S,p} \\ &= E_G - \mu_n - \mu_p - \Phi_{S,n} - \Phi_{S,p} \end{aligned} \quad (\text{Equation 4-3})$$

Where  $E_{B,n}$  and  $E_{B,p}$  are the binding energies,  $E_{F,n}$  and  $E_{F,p}$  the Fermi levels,  $\Phi_{S,n}$  and  $\Phi_{S,p}$  the Schottky barrier heights,  $\mu_n$  and  $\mu_p$  the carrier activation energies of *n*- and *p*-type GaN, respectively,  $E_{CL}$  the core level energy, and  $E_G$  the GaN bandgap.

The carrier activation energy is determined to be 22 meV for *n*-type and 170 meV for *p*-type GaN.<sup>[44, 45]</sup> Using typical Schottky barrier heights of 1.1 eV for Pt on *n*-type and 0.5 eV for Pt on *p*-type GaN, the binding energy offset was calculated to be 1.6 eV, which is in fairly good agreement with the shift of the Pt4f core level binding energy observed experimentally within this work (Figure 4-7 (a, d)).<sup>[46, 47]</sup> Upon contact, the mechanism includes the Fermi level alignment of GaN and Pt by the charge redistribution at the interface in thermal equilibrium.<sup>[48, 49]</sup> Therefore, the offset in the core level binding energies must be observed for the deposited particles due to the alignment of the Fermi levels.<sup>[49]</sup>

To verify the absence of a thick insulating oxygen layer due to the exposure of the samples to air, the oxygen coverage on GaN was investigated from Ga3d, N1s, and O1s core level spectra (Figure 4-2). The Ga3d core levels confirmed the presence of a very thin native oxide and an intermediate GaO<sub>x</sub> species. The N1s core level spectrum exhibited only one species, which led to the exclusion of an oxygen binding to the N atom. The O1s spectra contained at least two species, Ga-O bonds and adsorbed OH.

The oxygen coverage was determined for solvent-cleaned surfaces (acetone, 15 min ultrasonic bath, rinsed with 2-propanol), oxygen plasma treated samples (1.4 bar oxygen, 200 W, 5 min), *in situ* reduced and oxidized GaN samples at room temperature, as well as elevated temperatures (Table 4-2).<sup>[31]</sup> The calculation of the oxygen coverage will be explained in more detail in the following. A total volume of  $9.6 \times 10^{-12} \text{ cm}^3$  was probed in XPS, which results from a beam spot size of  $150 \times 80 \text{ }\mu\text{m}$  and a photoelectron escape depth of 8 Å. Using a Ga-N bond length of 1.95 Å and an atomic density of  $8.8 \times 10^{22} \text{ cm}^{-3}$ , the probed volume corresponds to four atomic layers with  $4 \times 10^{11}$  Ga atoms in total.<sup>[50, 51]</sup> One monolayer of oxygen corresponds to the total number of Ga atoms in one atomic layer, as oxygen is solely bound to Ga atoms and not to N atoms (Figure 4-2). The total oxygen coverage was calculated from relative Ga3d peak areas that contribute to Ga-N or Ga-O bonds. Notably, the calculated values present an upper limit estimation, as the Ga-N peak is underestimated due to the oxygen adlayer, which reduces the photoelectron intensity from underlying layer.



An increase in oxygen coverage due to the oxygen plasma treatment was not observed for the *n*-type surface. Only a slight reduction of the oxygen coverage was determined for *p*-type GaN after the *in situ* reduction experiment in hydrogen, while the *n*-type surface composition remained constant. The oxygen coverages during the *in situ* oxidation showed only minor changes for both GaN surfaces. Consequently, the oxygen adlayer consisted of 1 ML on the *n*-type and 2 ML on the *p*-type surface and did not affect the transport of charges over the metal-support interface.

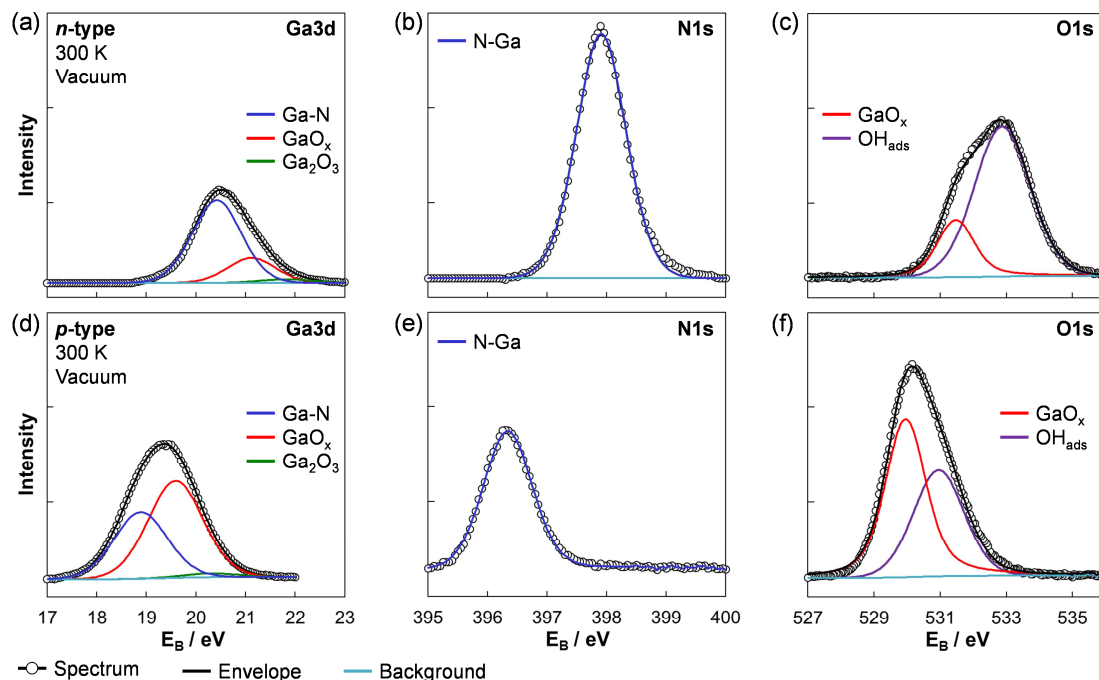


**Figure 4-2.** (a, d) Ga3d, (b, e) N1s, and (c, f) O1s core level spectra for Pt cuboctahedra on (a-c) *n*-type and (d-f) *p*-type GaN at 300 K in vacuum.

**Table 4-2.** Oxygen coverages for *n*- and *p*-type GaN samples at various treatments. All coverages are given in monolayers (ML) with an uncertainty of  $\pm 0.3$  ML.<sup>[31]</sup>

GaN Surfaces	Experimental conditions	Oxygen adlayer / ML	
		<i>n</i> -type	<i>p</i> -type
solvent-cleaned	RT, vac	1.4	-
O <sub>2</sub> plasma	RT, vac	1.4	-
<i>in situ</i> reduction	RT, vac (initial/final)	1.1/1.1	2.4/1.8
<i>in situ</i> oxidation	RT/725 K, vac (initial)	1.3/0.8	2.1/1.9
	725 K, 5/15/25 min O <sub>2</sub>	1.2/1.0/1.0	1.9/1.7/1.8
	725 K, vac (final)	1.1	2.0
	775 K, vac	1.2	2.1
	RT, vac (final)	1.3	2.2

### 4.3 Results

The spin-coating of monodisperse spherical (2.0 nm), cuboctahedral (8.1 nm), and cubic (7.6 nm) Pt particles onto GaN surfaces shows a highly reproducible, homogeneous, and stable particle distribution without agglomeration (Figure 4-3). Although spin-coating does not produce ordered nanoparticle arrays, it is a suitable method to prepare model catalysts with low particle coverage below one particle monolayer for the study of the particle-support interaction.

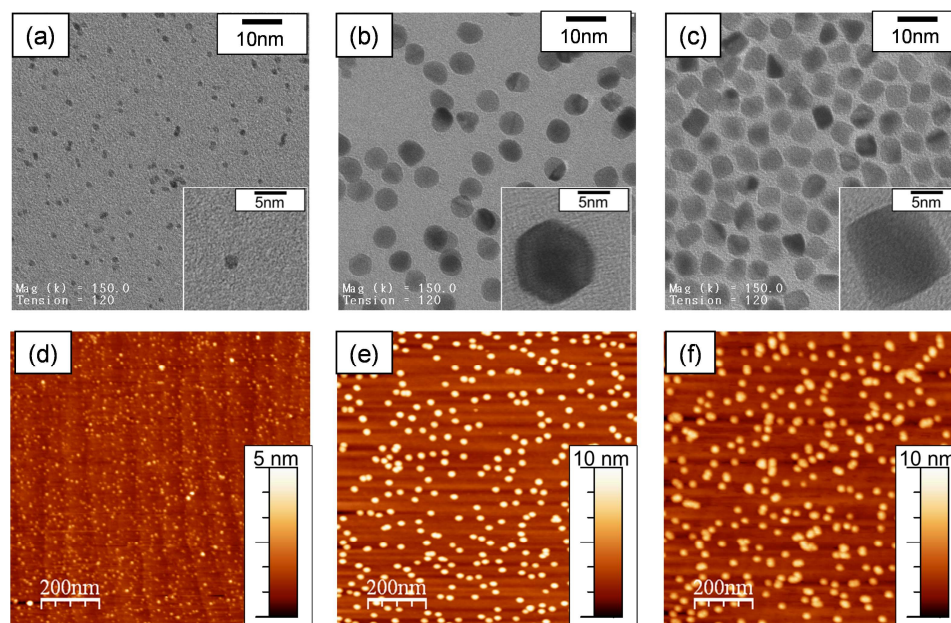


**Figure 4-3.** (a-c) TEM micrographs of PVP-protected Pt nanoparticles in ethanol solution with (a) spherical (2.0 nm), (b) cuboctahedral (8.1 nm), and (c) cubic (7.6 nm) particle geometry. (d-f) AFM images ( $1 \mu\text{m}^2$ ) of Pt nanoparticles deposited on *n*-type GaN with (d) spherical, (e) cuboctahedral, and (f) cubic particle shape.

The total number of Pt on the surface was assessed from the particle diameter analyzed with TEM and the areal density of particles on the GaN support that was determined from AFM. The total Pt coverage was 2 %ML for small, spherical and 16 %ML for large, cuboctahedral and cubic particles on *n*-type GaN, while slightly higher values were obtained for particles on the *p*-type surface, 3 %ML for spheres and 17 %M for cuboctahedra and cubes (Table 4-3). However, considering one particle size and the experimental error, identical coverage of Pt was achieved on both surfaces. The fraction of Pt surface atoms was 1-2 %ML for small, spherical, 3 %ML for large, cuboctahedral, and 4 %ML for large, cubic particles on *n*- and *p*-type GaN. The coverages were evaluated independently using data from AFM and XPS (Pt/Ga element ratio) for cuboctahedral particles. Only the surface atoms contribute to the

coverage in the case of AFM, whereas the XPS data yields information about all Pt atoms with the photoelectron escape depth of 8 Å, resulting in twice as high Pt surface coverage (Table 4-3). Considering this, the calculated coverages are in very good agreement and the following discussion applies for Pt atoms at or in close vicinity of the particle surface.

**Table 4-3.** Total Pt coverage and surface Pt coverage of spherical, cuboctahedral, and cubic nanoparticles on *n*- and *p*-type GaN, the Pt/Ga element ratio of as-prepared and reduced cuboctahedra on *n*- and *p*-type GaN, and the root mean square of blank *n*- and *p*-type surfaces.

Particle shape	GaN	Total Pt coverage <sup>(a)</sup> / %ML	Surface Pt coverage <sup>(a)</sup> / %ML	Pt/Ga ratio / %		rms <sup>(b)</sup> / nm
				300 K, vac	800 K, H <sub>2</sub>	
Spherical (2.0 nm)	<i>n</i> -type	2.0 ± 0.2	1.2 ± 0.1	-	-	0.25
	<i>p</i> -type	2.5 ± 0.3	1.5 ± 0.2	-	-	0.75
Cuboctahedral (8.1 nm)	<i>n</i> -type	15.9 ± 2.5	3.1 ± 0.5	6.3	6.8	0.25
	<i>p</i> -type	16.8 ± 4.6	3.2 ± 0.9	7.1	7.7	0.75
Cubic (7.6 nm)	<i>n</i> -type	16.1 ± 7.1	3.5 ± 1.6	-	-	0.25
	<i>p</i> -type	16.8 ± 1.1	3.7 ± 0.2	-	-	0.75

<sup>(a)</sup> The coverage was calculated from the particle size determined with TEM and the number of particles on the substrate analyzed with AFM assuming the individual shape and a truncation of one third of the particle.

<sup>(b)</sup> Root mean square determined from 5 × 5 μm AFM images.

For the correct spectrum evaluation of the particles, the Pt4f core level spectrum of an oxygen plasma treated Pt foil was compared to that of cuboctahedral Pt particles supported on *n*-type GaN at room temperature in vacuum (Figure 4-4). The Pt4f core level spectra were deconvoluted into four components, which were assigned to metallic platinum Pt<sup>0</sup> at the lowest binding energy of 71.3 eV (foil) and 71.8 eV (particles). The three oxidized species Pt<sup>ox</sup> were located at core level shifts (CLSs) of +0.8 eV, +1.7 eV, and +2.8 eV in the case of the Pt foil, and +0.9 eV, +1.8 eV, and +2.9 eV for the cuboctahedral Pt particles with respect to Pt<sup>0</sup>. These species were attributed to Pt atoms with chemisorbed oxygen, Pt<sup>Chem-O</sup>, Pt<sup>2+</sup>, and Pt<sup>4+</sup>, respectively.<sup>[40, 52, 53]</sup> The same assignment was applied for the deconvolution of the spectra obtained for different Pt-GaN samples of *n*- and *p*-type. A CLS of 0.5 eV to higher binding energy was observed for Pt particles on *n*-type GaN in comparison to the Pt foil, which was supposed to result from the different zero point of the Fermi edge of the underlying GaN support.<sup>[54]</sup> Not only the core level binding energy, but also the chemical composition differed between the foil and the particle sample (Figure 4-4 (c)). The oxygen plasma caused an oxidation of both samples with a pronounced contribution of Pt<sup>4+</sup> for the Pt foil, whereas only a minor fraction of Pt<sup>4+</sup> was observed on the particles. The most abundant

species on the *n*-type GaN-supported particles was Pt<sup>Chem-O</sup>. The altered oxidation behavior was assigned to the presence of different surface atoms and facets that were exposed on the Pt foil and sub-10 nm cuboctahedral particles.<sup>[55, 56]</sup> Additionally, under oxygen plasma conditions, UV light may also be formed that is able to optically excite the GaN support, which would vary the Pt particle oxidation due to strong metal-support interactions.

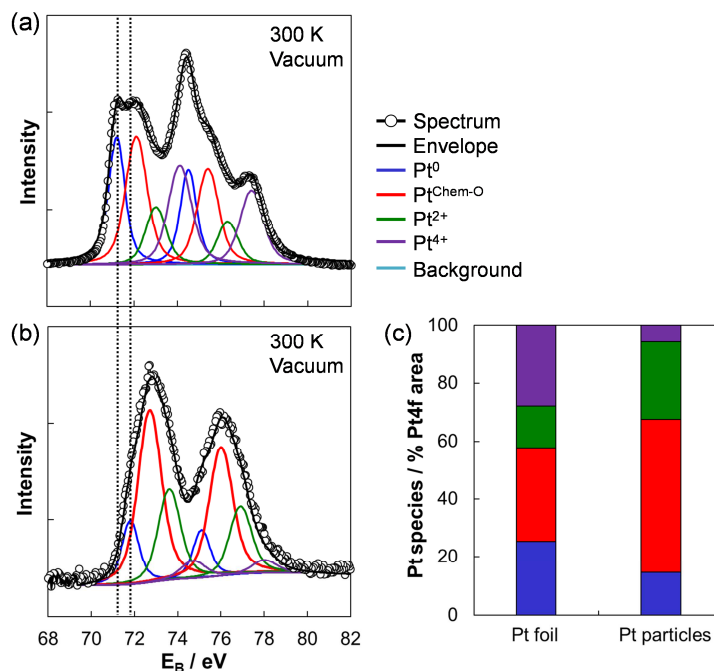


**Figure 4-4.** Pt4f core level spectra of (a) Pt foil and (b) Pt cuboctahedra on *n*-type GaN at 300 K in vacuum with spectra deconvolution into Pt<sup>0</sup>, Pt<sup>Chem-O</sup>, Pt<sup>2+</sup>, and Pt<sup>4+</sup>. Both samples were treated with oxygen plasma before XPS measurement. (c) The corresponding fractions of each Pt species of the spectra (% of Pt4f peak area).

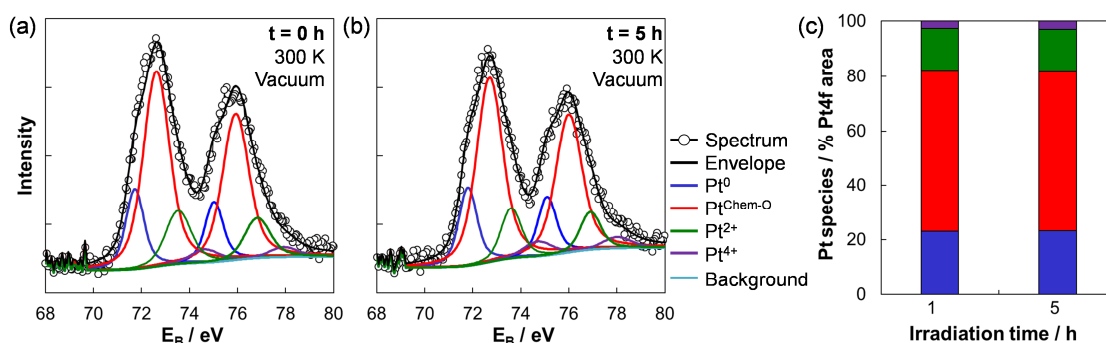


**Figure 4-5.** Stability of Pt4f core level spectra of Pt cuboctahedra on *n*-type GaN over time under X-ray irradiation for (a) *t* = 0 h and (b) *t* = 5 h at 300 K in vacuum. (c) The corresponding fractions of each Pt species of the spectra (% of Pt4f peak area).

Before performing *in situ* experiments to compare *n*- and *p*-type samples, alterations in the sample composition under continuous X-ray irradiation had to be excluded. Therefore, Pt4f core level spectra of Pt cuboctahedra on *n*- and *p*-type GaN were measured at room temperature in vacuum over a time period of 5 h at a single location on the sample (Figure 4-5, exemplary shown for the *n*-type sample). Beam-induced changes were observed neither in CLSs nor in the chemical composition of Pt, resulting in a constant stability of the samples against the damage by X-rays.

Although the Pt4f core level spectra were not altered during X-ray irradiation, except for their intensity, the deposition of carbon species onto the sample was verified in the C1s core level, as well as in the C1s/Ga3d element ratio (Figure 4-6). The carbon evolution occurred with increasing X-ray irradiation time, which could not be prevented due to the relative high base pressure of the experimental chamber ( $1 \times 10^{-7}$  mbar).

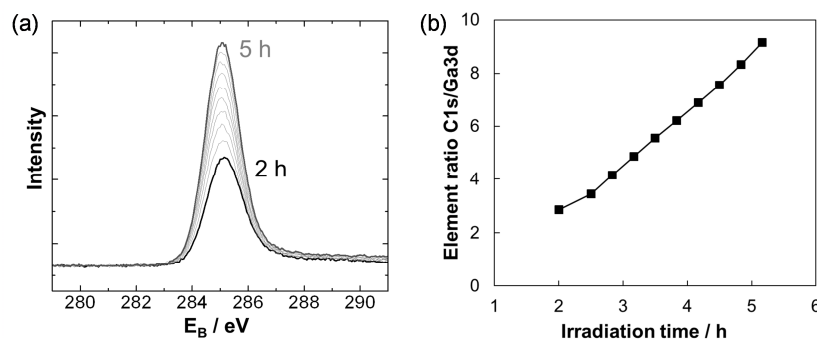


**Figure 4-6.** Carbon deposition onto the sample (Pt cuboctahedra on *n*-type GaN) during the beam damage experiment (a) evaluated from C1s core level spectra and (b) the corresponding element ratios C1s/Ga3d over time under X-ray irradiation at 300 K in vacuum.

The effect of the chemical composition of as-prepared Pt cuboctahedra at room temperature in vacuum and hydrogen was evaluated with respect to the GaN doping (Figure 4-7 (a, b) and (d, e)). Again, four Pt species were observed in the Pt4f core level spectra with Pt<sup>0</sup> at a binding energy of 71.8 eV in vacuum and 71.4 eV in hydrogen at 300 K for the *n*-type sample, whereas the absolute positions of Pt<sup>0</sup> was located at lower binding energy (70.5 eV in vacuum and 70.1 eV in hydrogen at 300 K) for the *p*-type sample (Table 4-4). The relative CLSs of the Pt<sup>ox</sup> components were determined to be +0.9 eV, +1.8 eV, and +2.9 eV for particles on *n*-type GaN and +0.8 eV, +1.6 eV, and +2.8 eV for cuboctahedra on the *p*-type support with respect to the Pt<sup>0</sup> peak position. Moreover, the fraction of Pt<sup>0</sup>/Pt<sup>total</sup> was 28% for particles on

the *p*-type, and only 16% on the *n*-type GaN (Figure 4-7 (g)). Upon hydrogen inlet, the fraction of Pt<sup>0</sup> immediately increased to 45% for particles on *p*-type, but only to 30% for particles on *n*-type GaN. In both cases, the Pt4f core level spectra were dominated by the Pt<sup>Chem-O</sup> and Pt<sup>2+</sup> species with a smaller contribution from Pt<sup>4+</sup>. However, for *p*-type GaN-supported particles, the Pt<sup>Chem-O</sup> and Pt<sup>2+</sup> species were less pronounced compared to the *n*-type sample, and Pt<sup>4+</sup> was not observed upon hydrogen exposure on *p*-type.

**Table 4-4.** Absolute binding energies ( $E_B$ ) of Pt<sup>0</sup> and relative core level shifts (CLS) of Pt<sup>Chem-O</sup>, Pt<sup>2+</sup>, and Pt<sup>4+</sup> for as-prepared and *in situ* oxidized Pt nanoparticles on *n*- and *p*-type GaN evaluated from Pt4f core level spectra. Doniach-Sunjic functions with asymmetry factor  $\alpha$  and convolution factor  $n$  were used for peak fitting.

Substrate		$E_B(\text{Pt}^0)$ / eV	CLS(Pt <sup>Chem-O</sup> ) / eV	CLS(Pt <sup>2+</sup> ) / eV	CLS(Pt <sup>4+</sup> ) / eV
<i>n</i> -type	As-prepared	71.8 <sup>(a)</sup> /71.4 <sup>(b)</sup>	+ 0.9	+ 1.8	+ 2.9
	Oxidized	71.3	+ 1.1	+ 2.2	+ 3.7
<i>p</i> -type	As-prepared	70.5 <sup>(a)</sup> /70.1 <sup>(b)</sup>	+ 0.8	+ 1.6	+ 2.8
	Oxidized	70.0	+ 0.8	+ 1.6	+ 2.8
Doniach-Sunjic ( $\alpha, n$ )		(0.008, 190)	(0.010, 250)	(0.020, 300)	(0.020, 300)

<sup>(a)</sup> Pt4f core level spectrum in vacuum. <sup>(b)</sup> Pt4f core level spectrum in hydrogen.

In summary, the oxygen plasma treatment for the removal of PVP results generally in highly oxidized Pt particles on both *n*- and *p*-type GaN. Interestingly, the extent of oxidation and the corresponding CLSs vary strongly with the GaN doping and are higher for Pt particles on the *n*-type surface under X-ray illumination. The variations in Pt composition are more pronounced in hydrogen atmosphere. These results suggest that the electronic doping of the GaN support plays a noticeable role in the particle-support interaction when irradiated with X-rays.

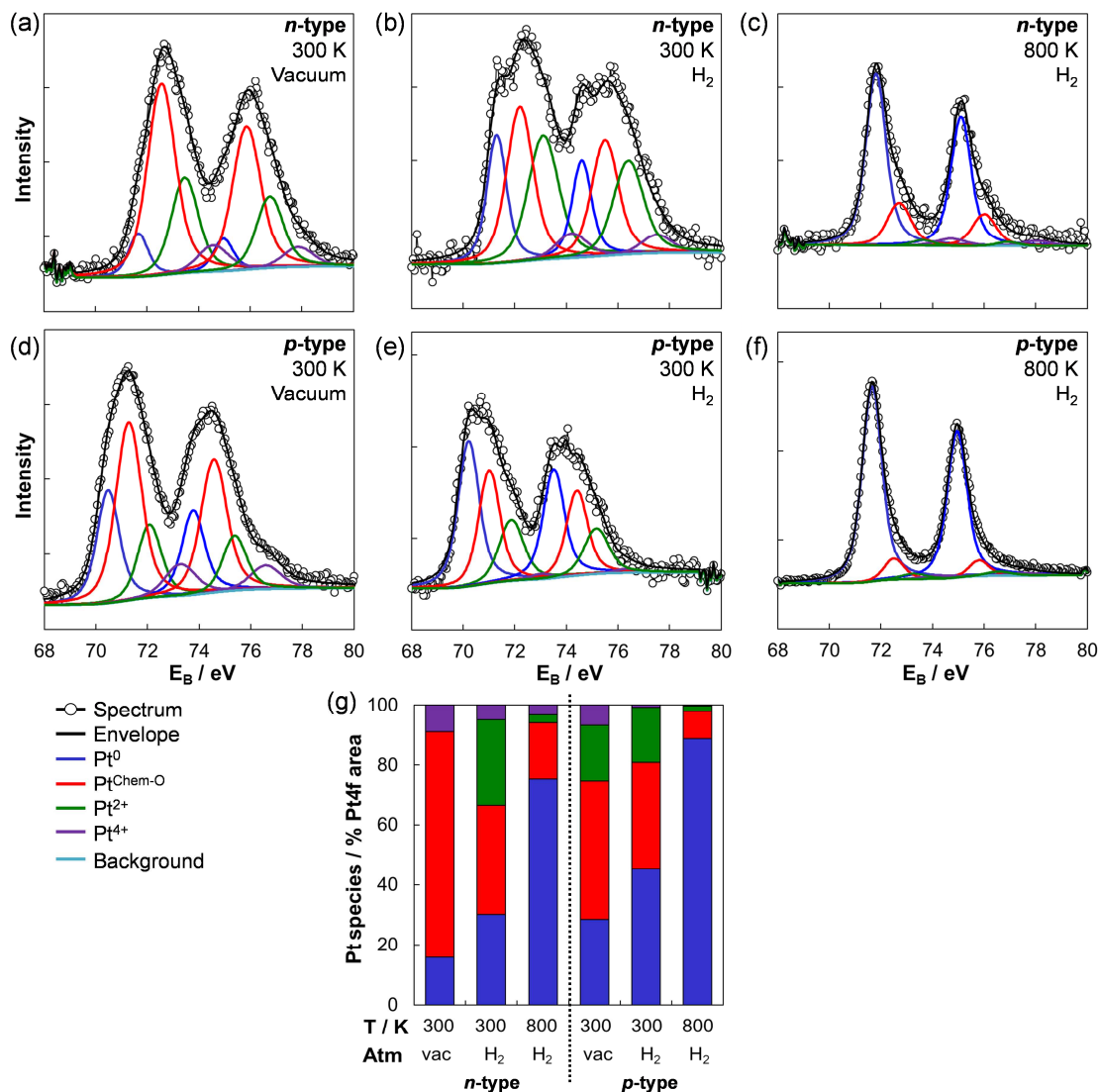


**Figure 4-7.** Pt4f core level spectra of cuboctahedral Pt nanoparticles supported on *n*-type (a-c) and *p*-type GaN (d-f) at 300 K in vacuum (a, d), at 300 K in hydrogen (0.5 mbar) (b, e), and at 800 K in hydrogen (0.5 mbar) (c, f), respectively. (g) Evaluation of the Pt fractions of each species (% of Pt4f peak area) for the spectra (a-f).

The different oxidation properties of Pt on *n*- and *p*-type GaN were consistent for various Pt particle sizes and shapes (Figure 4-8, spectra exemplarily shown for *p*-type samples). For small, spherical, as well as large, cuboctahedral and cubic particles, the Pt<sup>0</sup> contribution was always lower on for the *n*-type sample. From these spectra, it is clearly visible that the kind of particle synthesis, the amount of PVP (three times higher amount of polymer for capping of small spherical particles), and the particle size as well as geometry determine the oxidation degree during the oxygen plasma treatment. Nevertheless, the effect from the underlying *n*- or *p*-type GaN support was still detectable.



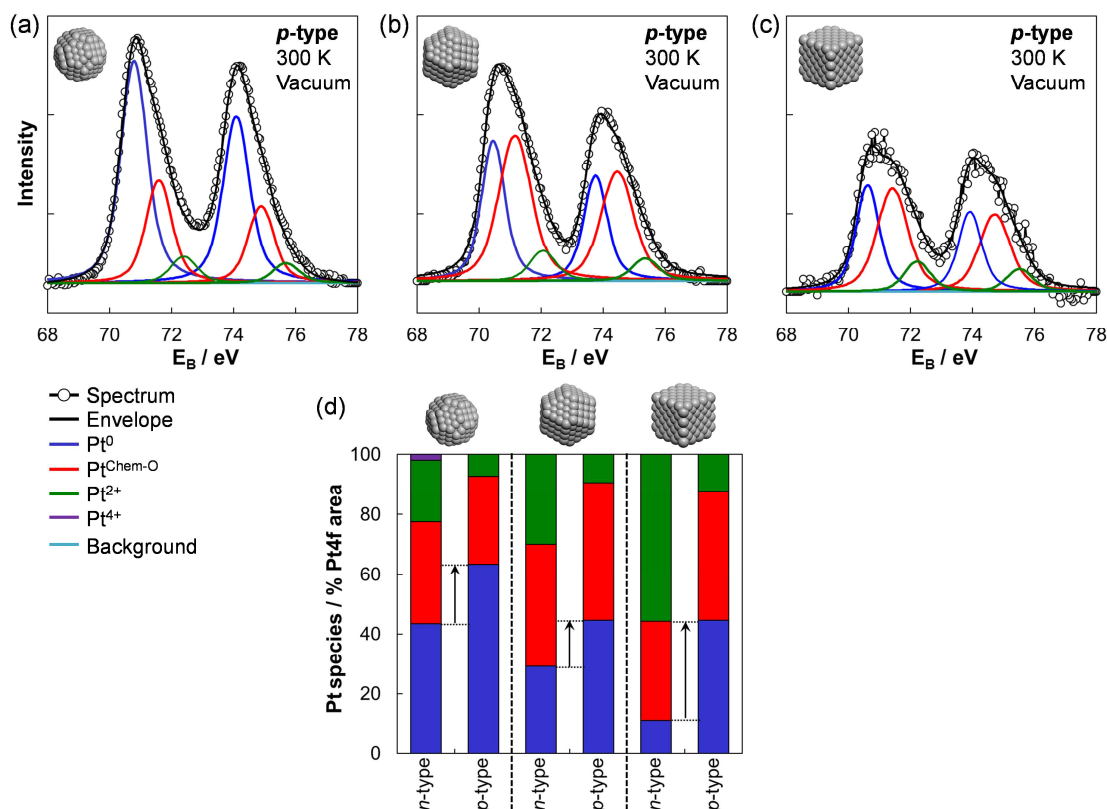


**Figure 4-8.** Pt4f core level spectra exemplarily shown for Pt nanoparticles on *p*-type GaN with (a) spherical, (b) cuboctahedral, and (c) cubic particle geometry at 300 K in vacuum. (d) The corresponding fractions of each Pt species of the spectra (% of Pt4f peak area) of the different particle shapes on *n*- and *p*-type GaN.

In subsequent photoemission experiments, *in situ* reduction in hydrogen and *in situ* oxidation in oxygen were performed to gain further insight into the effect of the semiconductor on the nanoparticles under reaction conditions. For the reduction experiment, the first sample set (as-prepared samples) was heated in hydrogen (0.5 mbar) from room temperature to 800 K. Pt4f core level spectra after reduction at 800 K revealed a significant decrease of all  $Pt^{ox}$  components for both *n*- and *p*-type GaN surfaces (Figure 4-7 (c, f)). The fraction of  $Pt^0$  increased to 88% for particles on *p*-type GaN, and to 75% for the *n*-type sample. In both cases, solely the  $Pt^{Chem-O}$  component contributed to  $Pt^{ox}$ , while the  $Pt^{2+}$  and  $Pt^{4+}$  species disappeared nearly completely, especially for the *p*-type support. Additional Pt species were not evolved as a result of thermal treatment. The possible detachment of particles from the GaN surface was determined by the calculation of Pt/Ga element ratios before and after *in situ* reduction. The total amount of deposited Pt was found to be 6-7% (Table 4-3), which shows that Pt was not lost during the thermal treatment in hydrogen atmosphere.



The *in situ* oxidation experiment was performed to further investigate changes in Pt chemical activity due to a possible charge transfer between the particles and the underlying GaN support under X-ray illumination (Figure 4-9 (a)). For this experiment, the second sample set was used, which was previously reduced at 775 K in hydrogen for 3 h, yielding initial Pt<sup>0</sup> fractions of 69% and 78% for Pt cuboctahedra on *n*- and *p*-type GaN, respectively.

The temperature was increased to 725 K in vacuum resulting in comparable Pt<sup>0</sup> fractions at 725 K and room temperature. Upon oxygen exposure at 725 K, only small changes in the Pt composition were detected for cuboctahedra on *p*-type GaN and the amount of Pt<sup>0</sup> decreased to a minimum of 68%. The CLSs of the evolving Pt<sup>ox</sup> peaks relative to Pt<sup>0</sup> were identical to the positions for as-prepared *p*-type samples (Table 4-4). In contrast to the particles on *p*-type GaN, the Pt<sup>0</sup> fraction of particles on *n*-type GaN dropped immediately after oxygen inlet to 30%. The CLSs of the Pt<sup>ox</sup> species were shifted to higher values compared to as-prepared *n*-type samples (Table 4-4). Furthermore, the Pt<sup>4+</sup> component contributed significantly to Pt<sup>ox</sup> for particles on *n*-type GaN. Although the high pressure caused very low count rates and hence, a higher uncertainty in peak fitting, the qualitative differences between Pt4f core levels of the *n*- and *p*-type samples are clearly resolved (Figure 4-9 (b, c)). After 80 min of oxidation, the samples were heated to 775 K in vacuum and the particles were reduced thermally to their initial composition. Two interesting points arise from this experiment. First, the particle affinity towards oxygen and oxidation is much higher on the *n*-type than on the *p*-type support under X-ray irradiation. Second, the CLSs of Pt<sup>ox</sup> species relative to Pt<sup>0</sup> are larger for particles on *n*-type GaN for the *in situ* oxidation with oxygen under X-ray illumination than for oxygen plasma preparation in the absence of X-rays.

The AFM characterization after the *ex situ* reduction at 775 K in hydrogen and *in situ* oxidation at 725 K in oxygen showed no significant particle sintering (Figure 4-10). However, some Ostwald ripening was detected for particles on *n*-type GaN, whereas some agglomerates were observed for particles on the *p*-type surface after the oxidation experiment during X-ray photoemission. Due to the high stability of the Pt-GaN samples, effects from aggregation and sample damage could be excluded to contribute to the observed differences in the particles' oxidation and reduction behavior with X-ray illumination on *n*- and *p*-type GaN.

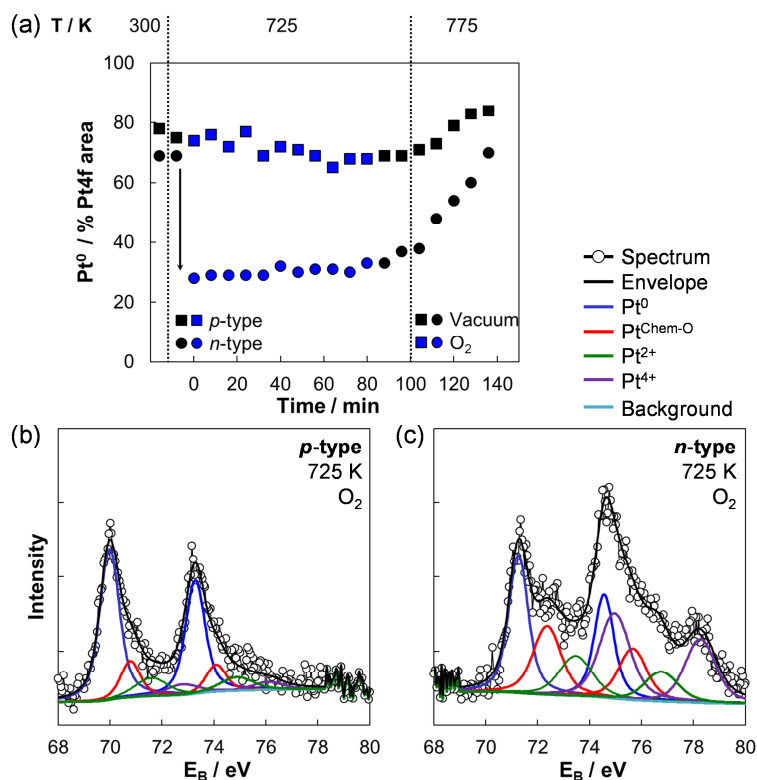


**Figure 4-9.** (a) Pt<sup>0</sup> fraction (% of Pt4f peak area) of Pt cuboctahedra on *n*- and *p*-type GaN before, during, and after oxidation with oxygen (0.5 mbar, 725 K) and during further heating in vacuum (775 K). The corresponding Pt4f core level spectra of (b) *n*-type and (c) *p*-type sample after 1 h in oxygen are shown as an example.

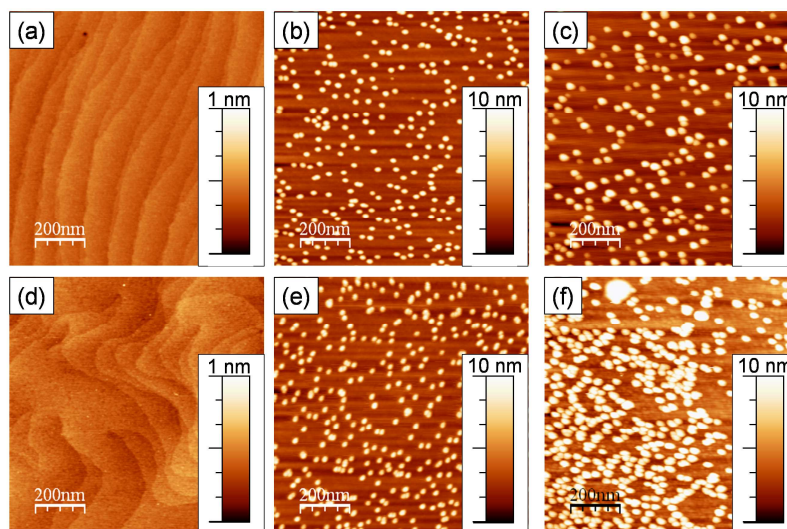


**Figure 4-10.** AFM images (1  $\mu\text{m}^2$ ) of (a) *n*-type and (d) *p*-type GaN surfaces before particle deposition, as-prepared Pt cuboctahedra on (b) *n*-type and (e) *p*-type GaN before XPS, and identical particle samples of (c) *n*-type and (f) *p*-type after *ex situ* reduction (775 K, 3 h, H<sub>2</sub>) and *in situ* oxidation (725 K, 80 min, O<sub>2</sub>, X-rays).

## 4.4 Discussion

The catalysts based on *n*- and *p*-type GaN were prepared with defined Pt particle sizes and geometries, and with a reproducible particle monolayer on the semiconductor surface. The GaN-supported Pt nanoparticle composition was found to be stable against X-ray-induced changes that allowed a detailed photoemission study of the particle behavior during *in situ* reduction and oxidation at elevated temperature. The comparison of the Pt foil with cuboctahedral Pt particles on *n*-type GaN, which were both oxidized by the oxygen plasma, was used to identify the present Pt species in accordance to their binding energy shifts. Four components were found in the Pt4f core level spectra of both samples (Figure 4-4), providing an accurate quantitative analysis of peak areas and core level shifts of each Pt species. The first doublet was attributed to metallic Pt and the obtained binding energies for Pt<sup>0</sup> at room temperature in vacuum (Table 4-4) are in reasonable agreement with literature values (70.7 eV to 71.6 eV) for Pt cuboctahedra on *n*- and *p*-type GaN. A positive shift of +1.3 eV to higher binding energy was recorded in the Pt4f core level spectra of the *n*-type sample with respect to the binding energy of Pt<sup>0</sup> measured for particles on *p*-type GaN (Table 4-4). This shift can be explained by considering the electronic structure of the semiconductor.<sup>[57]</sup> The Fermi level of the sufficiently grounded semiconductor is referenced to that of the detector during XPS measurements (Figure 4-11 (a)). The recorded core level binding energies are analyzed with respect to the semiconductor Fermi level.<sup>[54]</sup> This is also true for the deposited metal particles, because they are only electrically contacted through the semiconductor support (Figure 4-1). Compared to the metal foil core level spectra, this creates a different situation for the interpretation of CLSs for semiconductor-supported particles. Therefore, the relative shift in the absolute Pt4f binding energy originates from energetic differences between the Fermi levels in *n*- and *p*-type GaN, rather than from a chemical shift. The energetic difference of the bulk Fermi level positions of 3.0 eV between *n*- and *p*-type GaN is reduced by the surface band bending due to Fermi level pinning at the GaN surface, which can lead to the observed shift of +1.3 eV. An absolute Pt<sup>0</sup> binding energy shift of -0.4 eV was detected for both *n*- and *p*-type GaN samples at room temperature in hydrogen atmosphere (Table 4-4). As this shift was not accompanied by a binding energy shift of the N1s core level (not shown), it cannot be assigned to a change in GaN surface band bending. Consequently, the negative shift of the binding energy is identified as a chemical shift related to the adsorption of hydrogen on the Pt particles. The second doublet was assigned to a chemisorbed oxygen species, Pt<sup>Chem-O</sup>, due to its CLS of +0.9 eV and +0.8 eV for the *n*- and *p*-type GaN

sample, respectively. This assignment is supported by Kim *et al.*<sup>[52]</sup> and Butcher *et al.*<sup>[53]</sup>, who reported CLSs of +0.7 eV for chemisorbed oxygen on Pt(110) and +0.6 eV on Pt(111). Both authors proposed the formation of chemisorbed oxygen on Pt to be caused by the X-ray-induced oxygen dissociation upon oxygen inlet. Additionally, chemisorbed oxygen species on metallic gold have been explained by the same mechanism.<sup>[58]</sup> However, the Pt<sup>Chem-O</sup> component appears in our experiments prior to *in situ* oxygen exposure and thus, we relate its origin to the treatment with oxygen plasma, which removes the capping PVP shell from the particles. The third component exhibited a CLS of +1.8 eV for the *n*-type and +1.6 eV for the *p*-type sample, which was identified to be Pt<sup>2+</sup> in PtO.<sup>[52]</sup> The fourth doublet correlated with Pt<sup>4+</sup> in PtO<sub>2</sub> and CLSs of +2.9 eV and +2.8 eV were found for Pt on *n*- and *p*-type GaN, respectively.<sup>[40, 52]</sup> It has to be noted that the use of different asymmetry factors for peak fitting can delete the Pt<sup>4+</sup> species from the Pt4f core level spectra, but the overall background does not allow higher values for asymmetry. Therefore, we conclude that the fourth doublet is essential for the appropriate spectrum deconvolution. The magnitudes of CLSs can be slightly different than reported values due to effects from Pt particle size and the support. Moreover, the nature of the Pt<sup>ox</sup> component and thus, the oxidation behavior is strongly dependent on the specific metal facets, as well as on structural inhomogeneities on the particle surface like steps, kinks, and edges.<sup>[7, 59]</sup>

The comparison of Pt4f core level spectra of as-prepared Pt cuboctahedra on *n*- and *p*-type GaN at room temperature in vacuum shows a much larger fraction of oxidized Pt components for particles supported on *n*-type than for those supported on *p*-type GaN (Figure 4-7 (a, d)). This difference is even more pronounced when hydrogen is introduced at room temperature (Figure 4-7 (b, e)). Both experiments indicate that oxygen is stronger bound to Pt particles on *n*-type GaN than to particles on the *p*-type surface under X-ray illumination. Consequently, we conclude that a strong nanoparticle-support interaction exists that is affected by the GaN doping, altering the particles' affinity towards oxygen. Particle sintering was excluded to be the origin of the observed effect due to the homogeneous particle distribution on the GaN surfaces analyzed by AFM (Figure 4-10). In addition to that, both the *n*- and *p*-type samples were prepared under identical conditions and differ only in their electrical doping.

However, given the known interactions between metal particles and oxidic supports, e.g. TiO<sub>2</sub>, effects from adsorbed oxygen on the GaN surface has to be considered. A higher coverage with oxygen is expected on the *p*-type surface due to the higher surface roughness compared to *n*-type GaN, which was determined from AFM (Figure 4-10 (a, d)). Anyhow, the adsorption energy of oxygen should be very similar on both surfaces. Only a thin oxygen

adlayer is expected to be present in the range of 0.8 ML, which exhibits possible electron tunneling.<sup>[19]</sup> A reduction mechanism has been proposed for particles on TiO<sub>2</sub>, which describes the X-ray-induced formation of oxygen vacancies and a subsequent oxygen spillover from the particles to the support.<sup>[60, 61]</sup> A comparable particle reduction process was excluded to contribute to the observed behavior on *n*- and *p*-type GaN, because the particles were not reduced by the X-ray beam within 5 h (Figure 4-5).

In order to explain the observed differences in the Pt particle surface composition on *n*- and *p*-type GaN, we propose a mechanism considering the GaN band alignment at the Pt-GaN interface. The Fermi level of Pt or rather the metal work function of 5.7 eV is located approximately in the center of the GaN bandgap (3.4 eV). At the Pt-GaN interface, the valence and conduction bands of the semiconductor are bent upwards for *n*-type and downwards for *p*-type GaN, as a result of surface defects and the Schottky barrier formation with Pt. Due to this band alignment, a charge transfer mechanism is plausible and can be used to describe the observed particle-support interaction. Free charge carriers are photo-generated within the space charge region upon X-ray illumination due to measuring. Therefore, free holes are driven to the *n*-type GaN surface, whereas free electrons accumulate at the *p*-type surface (Figure 4-11 (b, c)). Due to the energetic alignment of Pt with GaN in contact, recombination of electrons from the particles with holes from the *n*-type GaN is expected under illumination. Likewise, a transfer of electrons from the *p*-type support to the particles is assumed, when irradiated with X-rays. Due to the charge transfer at the interface under illumination, a reduced net charge on Pt particles on *n*-type GaN would be expected, while Pt particles on *p*-type GaN would exhibit an increased net charge. A similar charge transfer process was previously applied to describe the photo-degradation of organic monolayers on GaN.<sup>[62]</sup> Consequently, we propose that the observed altered chemical properties of the Pt particles on *n*- and *p*-type GaN under X-ray illumination originate from this mechanism.

In order to evaluate the validity of this charge transfer model, *in situ* reduction and oxidation experiments were performed with Pt cuboctahedral particles on GaN. During the temperature increase to 800 K in hydrogen, the fraction of oxidized Pt compounds diminished for particles on both *n*- and *p*-type GaN (Figure 4-7 (c, f)). The higher oxidized components, Pt<sup>2+</sup> and Pt<sup>4+</sup>, disappeared, while only Pt<sup>Chem-O</sup> remained in the Pt4f core level spectra. An alloy formation between Ga and Pt was not observed at 800 K, as no additional peaks evolved in the spectrum. Although the particles were reduced in hydrogen on both GaN surfaces at the same conditions, the amount of oxidized Pt species was higher for particles on *n*-type than on *p*-type GaN, which supports the charge transfer mechanism described above. The

decomposition of the GaN substrate was excluded at reduction temperature of 800 K, because GaN is thermally stable up to 1250 K.<sup>[14]</sup> However, the presence of hydrogen at 800 K reduces the oxygen adlayer in the case of *p*-type GaN, while it remains constant for the *n*-type surface (Table 4-2). The Pt coverage was evaluated before and after the *in situ* reduction to investigate a possible particle detachment from the support, which may occur by the modified surface composition. But we can exclude this process due to only slight increase of the Pt/Ga element ratio at 800 K, determined from the core level spectra (Table 4-3). The increased Pt/Ga element ratio is attributed to the removal of contaminates during reduction, resulting in an increase of the exposed Pt surface area.

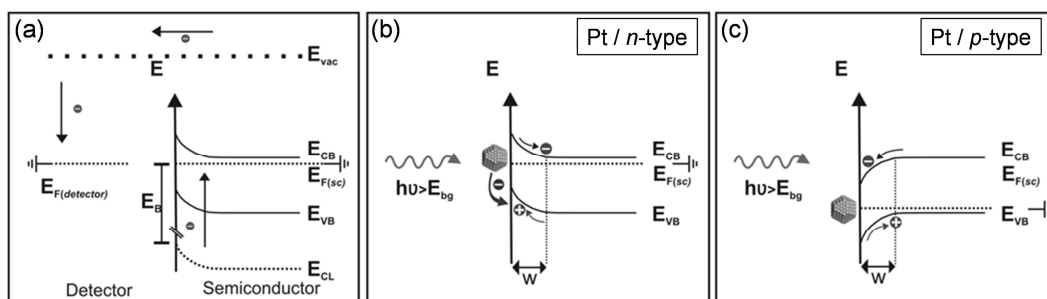


**Figure 4-11.** (a) Illustration of the energetic alignment of an *n*-type semiconductor with the spectrometer and the detection of the sample's photoelectrons with Fermi levels  $E_F$ , energy of valence and conduction band  $E_{VB}$ ,  $E_{CB}$ , energy of the core level  $E_{CL}$ , and the binding energy  $E_B$  of the core level electron. The alignment of Pt nanoparticles on *n*-type (b) and *p*-type GaN (c) shows the possible photo-induced charge transfer mechanism under X-ray irradiation ( $h\nu$ ).

The *in situ* oxidation experiments further verifies the changes in the oxidation properties of the particles in dependency on the GaN doping. *Ex situ* reduced samples were used for these measurements, which yielded a high amount of Pt<sup>0</sup> with the typical differences in composition for *n*- and *p*-type GaN. The *in situ* oxidation occurred under X-ray illumination due to the simultaneous collection of core level spectra. Assuming the charge transfer model under illumination, we expect a significantly changed reactivity of the particles on *n*- and *p*-type GaN. An immediate oxidation of particles on *n*-type GaN was observed upon oxygen exposure, whereas almost no changes in the Pt chemical composition were detected for particles on the *p*-type surface (Figure 4-9). Again, this difference in the oxidation behavior of the Pt particles on *n*- and *p*-type GaN under X-ray irradiation is in excellent agreement with the proposed charge transfer model. Therefore, we suppose that Pt nanoparticles exhibit fewer electrons on *n*-type GaN under illumination than on *p*-type GaN, which is a result of the recombination situation at the Pt-GaN interface. Consequently, the Pt particles supported on

*n*-type GaN should provide a higher affinity for the electronegative oxygen molecules, as observed in the experiment.

## 4.5 Conclusion

Monodisperse, size- and shape-selected Pt nanoparticles supported on electrically doped GaN surfaces are shown to be very suitable model hybrid structures to explore photo-stimulated changes of the particles' chemical properties. *In situ* reduction and oxidation in a high-pressure XPS setup revealed a strong doping-dependent particle-support interaction, which significantly increased the affinity of the particles towards oxygen, when applied to the *n*-type GaN surface. Generally, the Pt particles on *n*-type GaN exhibit a higher amount of atoms in a higher oxidation state under X-ray irradiation. In addition, the exposure to oxygen at high temperature under X-ray illumination led to the immediate oxidation of the particles supported on *n*-type GaN, which is in contrast to particles of the *p*-type sample. We propose a model for the photo-induced charge transfer across the particle-semiconductor interface, which involves the recombination of minority charge carriers from *n*-type GaN with electrons from Pt. This work highlights the impact of semiconductor support materials and suggests that GaN is a promising support for (photo)catalysis.

## 4.6 References

- [1] T. S. Ahmadi, Z. L. Wang, T. C. Green, A. Henglein, M. A. El-Sayed, *Science* **1996**, 272, 1924.
- [2] H. Song, F. Kim, S. Connor, G. A. Somorjai, P. D. Yang, *J. Phys. Chem. B* **2005**, 109, 188.
- [3] C.-K. Tsung, J. N. Kuhn, W. Huang, C. Aliaga, L.-I. Hung, G. A. Somorjai, P. Yang, *J. Am. Chem. Soc.* **2009**, 131, 5816.
- [4] G. A. Somorjai, J. Y. Park, *Top. Catal.* **2008**, 49, 126.
- [5] G. A. Somorjai, H. Frei, J. Y. Park, *J. Am. Chem. Soc.* **2009**, 131, 16589.
- [6] H. J. Freund, *Surf. Sci.* **2002**, 500, 271.
- [7] B. R. Cuenya, *Thin Solid Films* **2010**, 518, 3127.
- [8] J. R. Croy, S. Mostafa, J. Liu, Y. Sohn, H. Heinrich, B. R. Cuenya, *Catal. Lett.* **2007**, 119, 209.
- [9] L. K. Ono, B. Yuan, H. Heinrich, B. R. Cuenya, *J. Phys. Chem. C* **2010**, 114, 22119.
- [10] S. U. M. Khan, M. Al-Shahry, W. B. Ingler, *Science* **2002**, 297, 2243.

- [11] K. Fujii, M. Ono, Y. Iwaki, K. Sato, K. Ohkawa, T. Yao, *J. Phys. Chem. C* **2010**, *114*, 22727.
- [12] B. O'Regan, M. Grätzel, *Nature* **1992**, *353*, 737.
- [13] B. K. Kang, Y. H. Song, S. M. Kang, Y. C. Choi, D. K. Lee, S.-W. Kim, D. H. Yoon, *J. Electrochem. Soc.* **2011**, *158*, H693.
- [14] O. Ambacher, M. S. Brandt, R. Dimitrov, T. Metzger, M. Stutzmann, R. A. Fischer, A. Miehr, A. Bergmaier, G. Dollinger, *J. Vac. Sci. Technol. B* **1996**, *14*, 3532.
- [15] K. Prabhakaran, T. G. Andersson, K. Nozawa, *Appl. Phys. Lett.* **1996**, *69*, 3212.
- [16] I. Shalish, Y. Shapira, L. Burstein, J. Salzman, *J. Appl. Phys.* **2001**, *89*, 390.
- [17] V. M. Bermudez, *J. Appl. Phys.* **1996**, *80*, 1190.
- [18] O. Janzen, C. Hahn, W. Mönch, *Eur. Phys. J. B* **1999**, *9*, 315.
- [19] T. K. Zywietz, J. Neugebauer, M. Scheffler, *Appl. Phys. Lett.* **1999**, *74*, 1695.
- [20] O. Weidemann, E. Monroy, E. Hahn, M. Stutzmann, M. Eickhoff, *Appl. Phys. Lett.* **2005**, *86*, 083507.
- [21] G. Steinhoff, *Group III-nitrides for bio- and electrochemical sensors*, Technische Universität München: Ph.D. Thesis, **2008**.
- [22] M. Ali, V. Cimalla, V. Lebedev, H. Romanus, V. Tilak, D. Merfeld, P. Sandvik, O. Ambacher, *Sensor Actuat. B-Chem.* **2006**, *113*, 797.
- [23] J. Schalwig, G. Müller, U. Karrer, M. Eickhoff, O. Ambacher, M. Stutzmann, L. Görgens, G. Dollinger, *Appl. Phys. Lett.* **2002**, *80*, 1222.
- [24] J. Y. Park, G. A. Somorjai, *J. Vac. Sci. Technol. B* **2006**, *24*, 1967.
- [25] G. W. Busser, J. G. van Ommen, J. A. Lercher, *J. Phys. Chem. B* **1999**, *103*, 1651.
- [26] M. Stutzmann, J. A. Garrido, M. Eickhoff, M. S. Brandt, *Phys. Status Solidi A* **2006**, *203*, 3424.
- [27] S. S. Dhesi, C. B. Stagarescu, K. E. Smith, D. Doppalapudi, R. Singh, T. D. Moustakas, *Phys. Rev. B* **1997**, *56*, 10271.
- [28] B. J. Kowalski, R. J. Iwanowski, J. Sadowski, J. Kanski, I. Grzegory, S. Porowski, *Surf. Sci.* **2002**, *507-510*, 186.
- [29] J.-K. Ho, C.-S. Jong, C. C. Chiu, C.-N. Huang, C.-Y. Chen, K.-K. Shih, *Appl. Phys. Lett.* **1999**, *74*, 1275.
- [30] D. Qiao, Z. F. Guan, J. Carlton, S. S. Lau, G. J. Sullivan, *Appl. Phys. Lett.* **1999**, *74*, 2652.
- [31] S. Schäfer, *Gallium nitride for the electronic control of catalytic activity*, Ph.D. Thesis, Walter Schottky Institut, Technische Universität München, **2012**.
- [32] Y. Wang, *Preparation and Properties of Platinum Nanoparticles on Wide Bandgap Semiconductor Surfaces*, Master's Thesis, Walter Schottky Institute, Technische Universität München, **2009**.
- [33] Y. Y. Yeo, L. Vattuone, D. A. King, *J. Chem. Phys.* **1997**, *106*, 392.
- [34] R. E. Benfield, *J. Chem. Soc. Faraday T.* **1992**, *88*, 1107.
- [35] D. F. Ogletree, H. Bluhm, G. Lebedev, C. S. Fadley, Z. Hussain, M. Salmeron, *Review Of Scientific Instruments* **2002**, *73*, 3872.
- [36] M. Salmeron, R. Schlögl, *Surf. Sci. Rep.* **2008**, *63*, 169.
- [37] A. Knop-Gericke, E. Kleimenov, M. Hävecker, R. Blume, D. Teschner, S. Zafeirotos, R. Schlögl, V. I. Bukhtiyarov, V. V. Kaichev, I. P. Prosvirin, A. I. Nizovskii, H.



- Bluhm, A. Barinov, P. Dudin, M. Kiskinova, *Chapter 4 X-ray Photoelectron Spectroscopy for Investigation of Heterogeneous Catalytic Processes*, Vol. 52, Academic Press, **2009**.
- [38] M. P. Seah, W. A. Dench, *Surf. Interface Anal.* **1979**, 1, 2.
- [39] N. Fairley, *Casa XPS 2.3*, Casa XPS software Ltd, **2005**.
- [40] L. K. Ono, J. R. Croy, H. Heinrich, B. R. Cuenya, *J. Phys. Chem. C* **2011**, 115, 16856.
- [41] J. J. Yeh, I. Lindau, *Atom. Data Nucl. Data* **1985**, 32, 1.
- [42] J. J. Yeh, *Atomic Calculation of Photoionization Cross-Sections and Asymmetry Parameters*, Routledge: New York, **1993**.
- [43] E. A. Kraut, R. W. Grant, J. R. Waldrop, S. P. Kowalczyk, *Phys. Rev. B* **1983**, 28, 1965.
- [44] W. Götz, N. M. Johnson, C. Chen, H. Liu, C. Kuo, W. Imler, *Appl. Phys. Lett.* **1996**, 68, 3144.
- [45] W. Götz, N. M. Johnson, J. Walker, D. P. Bour, R. A. Street, *Appl. Phys. Lett.* **1996**, 68, 667.
- [46] K. Suzue, S. N. Mohammad, Z. F. Fan, W. Kim, O. Aktas, A. E. Botchkarev, H. Morkoc, *J. Appl. Phys.* **1996**, 80, 4467.
- [47] T. Mori, T. Kozawa, T. Ohwaki, Y. Taga, S. Nagai, S. Yamasaki, N. Asami, N. Shibata, M. Koike, *Appl. Phys. Lett.* **1996**, 69, 3537.
- [48] W. Schottky, *Z. Phys.* **1939**, 113, 367.
- [49] V. P. Zhdanov, *Surf. Sci.* **2002**, 512, L331.
- [50] A. L. Rosa, J. Neugebauer, *Surf. Sci.* **2006**, 600, 335.
- [51] C. Liu, A. Wenzel, B. Rauschenbach, E. Alves, A. D. Sequeira, N. Franco, M. F. da Silva, J. C. Soares, X. J. Fan, *Nucl. Instrum. Meth. B* **2001**, 178, 200.
- [52] Y. S. Kim, A. Bostwick, E. Rotenberg, P. N. Ross, S. C. Hong, B. S. Mun, *J. Chem. Phys.* **2010**, 133, 034501.
- [53] D. R. Butcher, M. E. Grass, Z. Zeng, F. Aksoy, H. Bluhm, W.-X. Li, B. S. Mun, G. A. somorjai, Z. Liu, *J. Am. Chem. Soc.* **2011**, 133, 20319.
- [54] G. Ecke, M. Niebelschütz, R. Kosiba, U. Rossow, V. Cimalla, J. Liday, P. Vogrincic, J. Pezoldt, V. Lebedev, O. Ambacher, *J. Electr. Eng.* **2006**, 57, 354.
- [55] A. Panchenko, M. T. M. Koper, T. E. Shubina, S. J. Mitchell, E. Roduner, *J. Electrochem. Soc.* **2004**, 151, A2016.
- [56] N. Seriani, F. Mittendorfer, *J. Phys-Condens. Mat.* **2008**, 20, 184023.
- [57] S. M. Sze, K. K. Ng, *Physics of Semiconductor Devices*, John Wiley & Sons, Inc.: Hoboken, New Jersey, **2007**.
- [58] J. M. Gottfried, K. J. Schmidt, S. L. M. Schroeder, K. Christmann, *Surf. Sci.* **2002**, 511, 65.
- [59] N. Seriani, F. Mittendorfer, *J. Phys-Condens. Mat.* **2008**, 20, 184023.
- [60] L. K. Ono, B. R. Cuenya, *J. Phys. Chem. C* **2008**, 112, 4676.
- [61] P. Jiang, S. Porsgaard, F. Borondics, M. Köber, A. Caballero, H. Bluhm, F. Besenbacher, M. Salmeron, *J. Am. Chem. Soc.* **2010**, 132, 2858.
- [62] J. Howgate, S. J. Schoell, M. Hoeb, W. Steins, B. Baur, S. Hertrich, B. Nickel, I. D. Sharp, M. Stutzmann, M. Eickhoff, *Adv. Mater.* **2010**, 22, 2632.

# Chapter 5

## Optoelectronic Control of the Catalytic Reactivity of GaN-Supported Pt Nanoparticles

### Abstract

Supported metal nanoparticles constitute an important group of catalysts, their properties being intrinsically controlled by the identity of the metal, the terminating surfaces of the particles and the influence of the support in withdrawing or donating electrons. If the support is a semiconductor, then band bending and the associated charge transfer at the metal-support interface provide a new channel for tuning electronic properties beyond the effects of coordinatively unsaturated sites provided by isolated metal particles. Supporting identical Pt particles on epitaxially grown *n*- and *p*-type GaN, we show that optical excitation of the wide bandgap support by UV light induces a controlled doping-dependent charge transfer between the support and the metal particles. The impact of this on catalytic reactivity is demonstrated using the structure-insensitive hydrogenation of ethene. The interfacial charge exchange between the optically excited semiconductor and the supported metal particles not only enables an external control of catalytic activity, but also a quantitative evaluation of the electronic impact of the semiconductor support on the metal. An increase of the electron density on Pt nanoparticles for *p*-type GaN increases the rate of ethene hydrogenation, while that rate is decreased by decreasing the electron density for Pt particles on *n*-type GaN. The fact that the same metal particles were supported on two chemically identical semiconducting carriers with the possibility to electronically tune the charge exchange via substitutional doping enabled us to quantitatively relate the electronic modification of the Pt particles to their catalytic properties. This has yielded new basic understanding of electronic metal-support interactions and opens up the possibility of electronically tuned catalyst properties.

## 5 Optoelectronic Control of the Catalytic Reactivity of GaN-Supported Pt Nanoparticles

### 5.1 Introduction

Whereas we begin to understand the intrinsic catalytic properties of metals and the role of coordinatively unsaturated surface metal atoms<sup>[1]</sup>, the more indirect electronic effects of the support on metal particles are still challenging to assess and to quantify. This is because the support not only influences the electronic state but also shape and size of the supported particles.<sup>[2, 3]</sup> This makes it difficult to deconvolute changes of catalytic reactivity due to metal morphology from purely electronic effects caused by charge transfer between the support and the catalyst.

To demonstrate the consequence of a controlled electronic alteration of the support on metal particles in the absence of particle size effects, we report here a novel experiment using two semiconducting catalyst supports with identical chemical properties (*n*- and *p*-type GaN), in which opposite electronic effects can be stimulated by irradiation with above bandgap UV light. For this purpose Pt particles of identical size and shape distributions were deposited on these two supports and used for the hydrogenation of ethene to ethane in the presence or absence of UV light. The metal particles were prepared in colloidal suspension by anchoring and protecting them in poly(*N*-vinylpyrrolidone) polymer.<sup>[4]</sup> The addition of AgNO<sub>3</sub> directed the particle growth in the poly(*N*-vinylpyrrolidone)-containing polyol solution towards a dominant portion of 88% of Pt cuboctahedra with a size of 9 nm, exhibiting solely Pt(100) and Pt(111) faces (Figure 5-1 (g-i)).<sup>[4]</sup>

Apart from being one of only two wide bandgap semiconductors (SiC and GaN), which can be efficiently doped both *n*- and *p*-type, gallium nitride also features a direct bandgap of 3.4 eV with a strong optical absorption and a very favorable alignment of the conduction and valence band edges with the Fermi energy of Pt and other catalytically active metals.<sup>[5, 6]</sup> As shown in Figure 5-2 (a), the Fermi level of Pt is located close to the middle of the GaN bandgap. The well-documented formation of a Schottky contact between GaN and Pt leads to re-distribution of charges and the formation of a built-in space charge region at the interface, which is depleted of electrons in the case of *n*-type GaN and of positively charged holes in the case of *p*-type GaN (Figure 5-2 (c, d)).<sup>[7, 8]</sup> After thermal equilibrium is achieved, further transfer of charge carriers between Pt and GaN requires energy to overcome the Schottky barrier. Such Pt/GaN Schottky contacts have been investigated recently in the oxidation of

CO to detect a ballistic electron transfer across the metal/semiconductor interface.<sup>[9]</sup> Electron transfer with the underlying GaN was induced in this case by the exothermic reaction of CO on Pt particles. A similar behavior was observed for Pt on *n*-type TiO<sub>2</sub>.<sup>[10]</sup> An enhancement in the rate of CO oxidation was also detected for photocatalysis based on *n*-type TiO<sub>2</sub> doped with fluorine.<sup>[11]</sup>

Thus, the working hypothesis for the experiments described here was that the unique combination of the wide bandgap and the bipolar doping properties of GaN would enable us to achieve a systematic control of electron transfer between GaN and Pt, leading to new and unexpected catalytic properties of the latter. Electron transfer differs from the traditional strong metal-support interaction (SMSI) effect, which arises from the reversible decoration of metal particles by the reducible supports.<sup>[3]</sup> The GaN used in this case is chemically stable under the chosen conditions and has an identical crystal structure for the case of *n*- and *p*-type doping (Figure 5-1 (a, d)).<sup>[5]</sup> This allows the direct comparison of the particle reactivity altered by the accumulation of opposite charge carriers on the *n*- or *p*-type GaN surface. Due to the preparation procedure of the catalysts and their storage in air, nonstoichiometric natural oxides of 1-2 monolayers (ML) were found on the *n*- and *p*-type GaN surfaces under reducing and oxidizing conditions, respectively (Chapter 4). However, these thin oxide adlayers are transparent to electron transfer<sup>[12]</sup> that is well established through previous studies of macroscopic Pt/GaN Schottky diodes fabricated from GaN epilayers with a natural oxide.<sup>[13]</sup>

## 5.2 Results and Discussion

The deposition of the shape-selected monodisperse Pt particles was performed via spin-coating with a polymer-protected metal sol resulting in a homogeneously distributed layer of particles, which did not sinter at reaction conditions or at high temperature (Figure 5-1 (b, e) and (c, f), Chapter 3). An oxygen plasma was used after deposition to remove the protecting polymer coating. The Pt particles were also oxidized by the plasma treatment. This was verified by a thorough XPS analysis of the different Pt oxidation states (Pt<sup>0</sup>, Pt<sup>2+</sup>, Pt<sup>4+</sup>). Only 12% of the Pt atoms were zero-valent on *n*-type GaN, while on *p*-type GaN 24% Pt atoms remained fully reduced (Chapter 4). The varying fractions of reduced and oxidized Pt on *n*- and *p*-type GaN after reduction in H<sub>2</sub> at high temperature as well as dedicated *in situ* XPS

oxidation experiments revealed a higher affinity of Pt towards oxygen for Pt particles on *n*-type GaN than for *p*-type samples (Chapter 4).

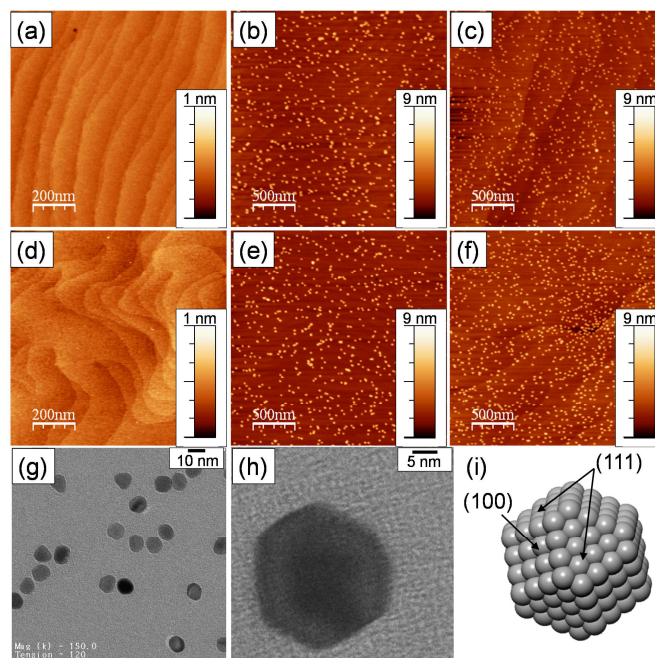


**Figure 5-1.** (a-f) AFM images of *n*- (a) and *p*-type (d) GaN reference surfaces, as well as Pt particle containing *n*- (b, c) and *p*-type (e, f) samples before (b, e) and after (c, f) its catalytic performance in ethene hydrogenation. The particle height and Pt coverage were determined to be 7-8 nm and 8-9 %ML, respectively, and remained constant after catalytic testing. (g-h) TEM micrographs of Pt particles ( $8.9 \pm 0.7$  nm, 88% cuboctahedra) in solution before deposition onto GaN surfaces. (i) The cuboctahedra exhibit mainly Pt(111) and Pt(100) facets.

Based on these results, we propose a photo-induced charge transfer occurring under illumination with above bandgap light ( $h\nu > 3.4$  eV,  $\lambda < 365$  nm) (Chapter 4). By such a UV irradiation, electron-hole pairs are excited and separated close to the surface, depending on the type of doping of the GaN support. The upward band bending occurring in *n*-type GaN leads to the diffusion of photo-generated electrons into the bulk of the support while holes are accumulated at the surface (Figure 5-2 (e)). In this case, we expect recombination of electrons from Pt with the photo-generated holes at the surface of *n*-type GaN, yielding electron-deficient Pt particles. The net positive charge of the Pt particles will re-distribute over the particle surface in order to maintain a zero internal electrical field.<sup>[14]</sup> Conversely, in the case of *p*-type GaN samples, photo-excited electrons are transferred through the Pt/*p*-type GaN interface to the Pt particles due to the downward surface band bending (Figure 5-2 (f)). As a consequence, the Pt surface becomes electron-rich under illumination of the *p*-type GaN

support. The different light-induced electron densities of the particles on the *n*- and *p*-type GaN surfaces provide a plausible explanation for the altered oxygen affinity of *n*- and *p*-type samples in our previous XPS experiments (Chapter 4).

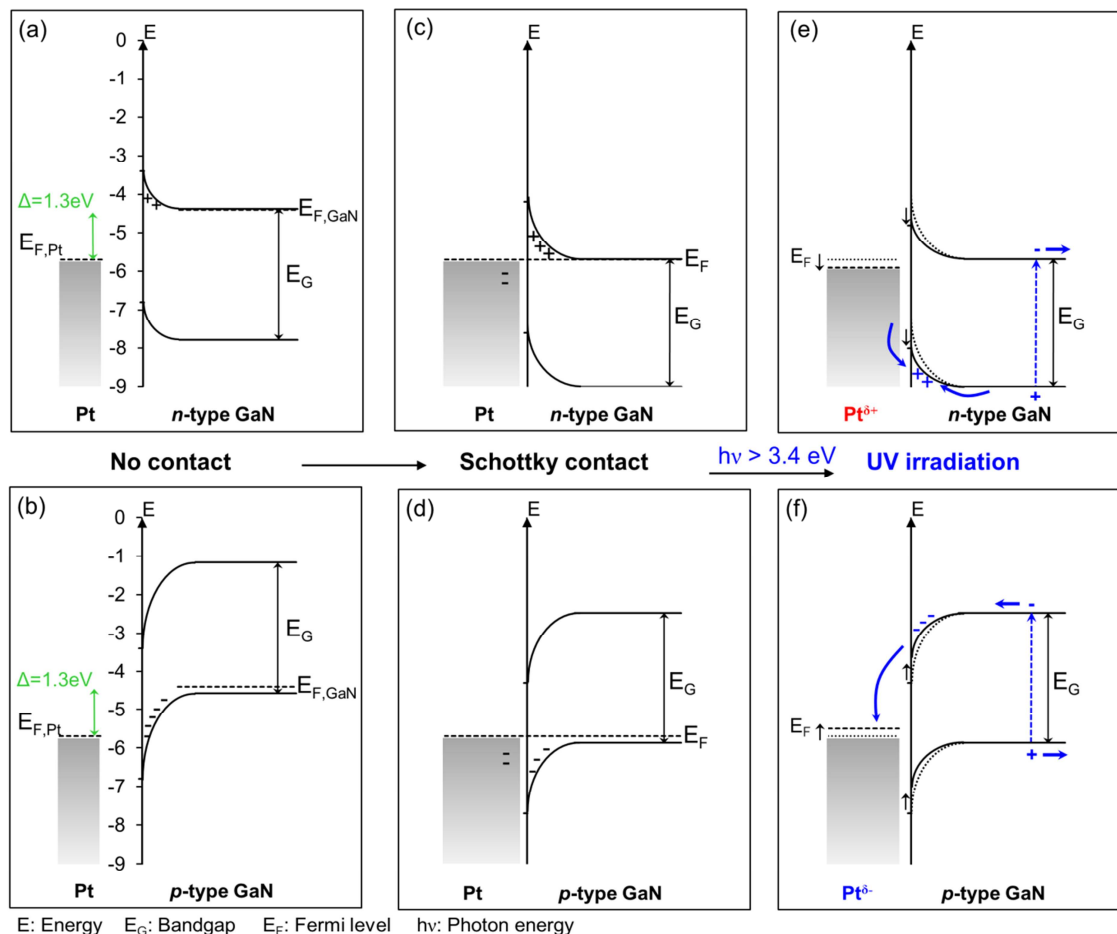


**Figure 5-2.** (a-b) Fermi level of Pt and *n*- (a) and *p*-type (b) GaN bandgap<sup>[8]</sup>. (c-d) Schottky contact between Pt and GaN in thermal equilibrium with upward and downward band bending for *n*- (c) and *p*-type (d) GaN. Due to the Fermi level pinning at the GaN surface, electrons are transferred from *n*- and *p*-type GaN to Pt. (e-f) Charge distribution during illumination of *n*- (e) and *p*-type (f) GaN. Irradiation leads to non-equilibrium at the interface, with holes accumulating at the *n*-type surface facilitating charge recombination with electrons from Pt, and interfacial electron transfer for the *p*-type GaN. The charge carrier accumulation leads to a potential drop at the surface, denoted as surface photovoltage, causing band flattening (dashed to solid lines).

The impact of these different charge transfer reactions on the catalytic properties of Pt nanoparticles on *n*- and *p*-type GaN supports was investigated and quantified for the hydrogenation of ethene to ethane in a recirculating reactor (Figure 5-3), comparing the various reaction rates with and without irradiation with 254 nm UV light. Without

illumination, Pt on *n*- and *p*-type GaN showed the same catalytic activity within the experimental uncertainty (Figure 5-4 (a, b)). Under UV light, however, the two types of catalysts exhibited a characteristically different behavior: the Pt nanoparticle reactivity **increased** for the *p*-type GaN support, but **decreased** for the *n*-type GaN support. The observed photo-induced changes in reactivity were at least a factor of two in both cases. This was quantified in the conversion rates expressed as turnover frequencies (TOFs) at different temperatures between 335-355 K (Figure 5-4 (a, b)). Notably, the catalytic reactivity of the particles responded immediately to switching on or off the UV light (Figure 5-4 (a), small insets), indicating correspondingly fast electron transfer processes at the Pt/GaN interfaces.

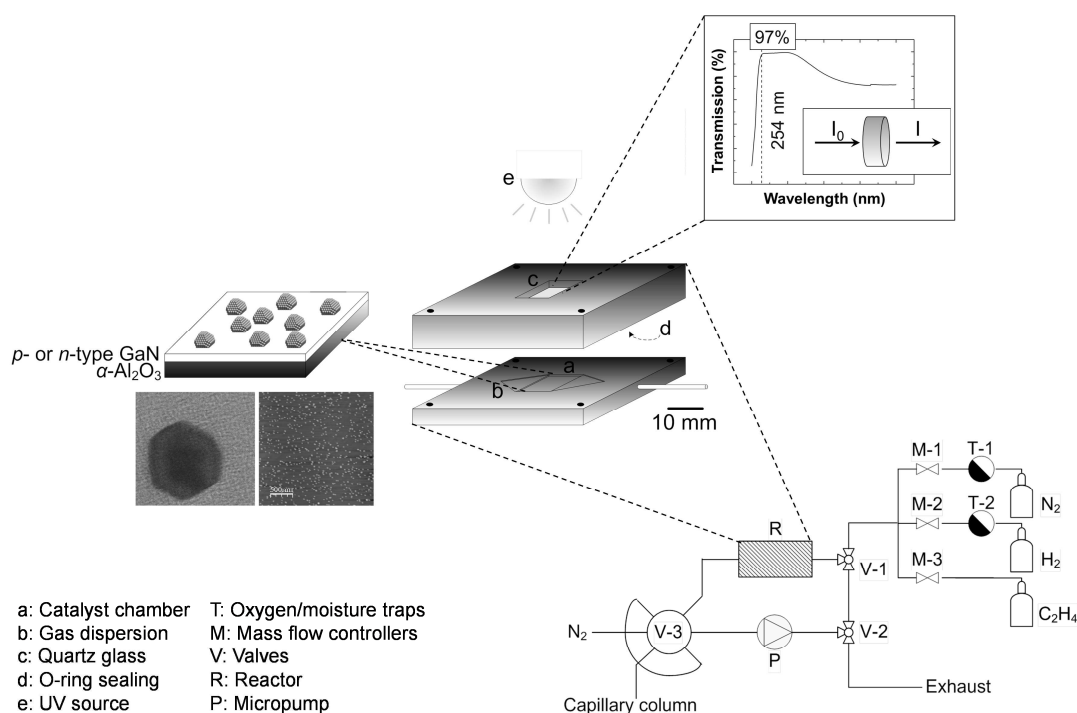


**Figure 5-3.** The flow scheme of the reaction setup shows possible operation in continuous and recycle mode by switching both valves V-1 and V-2. Sampling and analysis by gas chromatography was achieved by loading the gas mixture onto the capillary column by switching valve V-3 three times per hour. The sandwich-like, stainless steel reactor included the sample and facilitated optical excitation of the catalyst through the quartz glass window, which showed 97% transparency for UV light of wavelength 254 nm in the transmission spectrum.

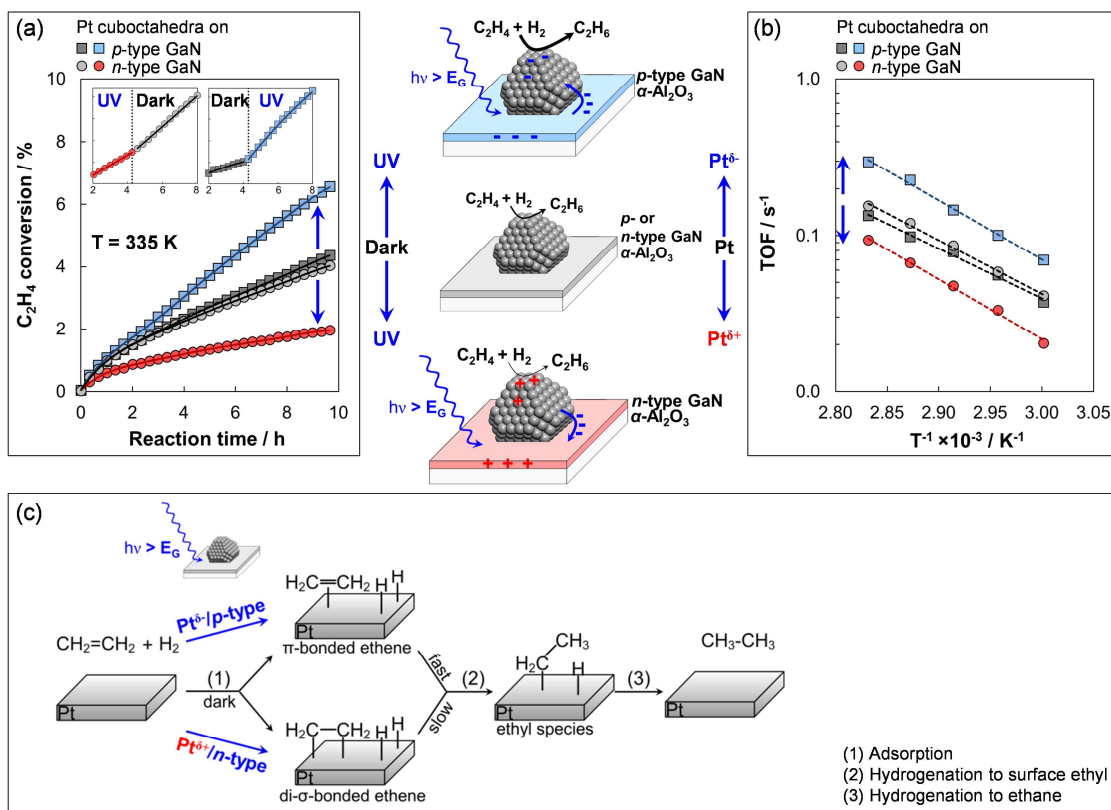


**Figure 5-4.** (a) Ethene conversion during gas recirculation and (b) temperature-dependent TOFs over the *n*- and *p*-type catalyst with and without UV irradiation. A deactivation was observed within the first two hours. The particles showed similar reactivity in dark, whereas an increased and decreased activity was detected for the *p*- and *n*-type catalyst in UV light, respectively, which is supposed to originate from the charge transfer mechanism under illumination. (c) Proposed reaction mechanism with and without UV light. The pathway via  $\pi$ - and di- $\sigma$ -bonded ethene was proposed to be dominant for the *p*- and *n*-type sample, respectively, under UV irradiation.

The experimentally observed changes in reactivity are in accordance with the proposed charge transfer under illumination described above (Figure 5-2 (e, f) and Chapter 4). Without UV light irradiation, the transfer of electrons between Pt and *n*- or *p*-type GaN upon Schottky contact formation can be estimated to about 30 electrons per particle, both for *n*- and *p*-type GaN (calculation described in 5.4.5, Table 5-1). Upon illumination of the catalysts a further transfer of charge carriers in steady state occurs. This can be estimated to about 70 holes per particle in the case of the *n*-type and additional 30 electrons per particle in the case of the *p*-type GaN sample (calculation described in 5.4.5, Table 5-1), explaining the inverse effect of illumination on the catalytic reactivity of the supported particles. Consequently, an increase in the hydrogenation rate was observed for electron-rich particles (*p*-type sample), while for electron-deficient particles (*n*-type sample) the reaction rate decreased.



**Table 5-1.** Descriptions of the Pt-GaN catalysts.

Specification	Unit	Details	Pt cuboctahedra (8.9 nm) <sup>(a)</sup> on	
			<i>n</i> -type GaN	<i>p</i> -type GaN
Oxygen adlayer <sup>(b)</sup>	ML ( $\pm 0.3$ )	-	1.1	2.4
Particle height <sup>(c)</sup>	nm ( $\pm 0.6$ )	before/after reaction	7.0/7.2	7.4/7.8
		averaged	7.1	7.6
Pt coverage <sup>(d)</sup>	%ML ( $\pm 1.1$ )	before/after reaction	7.4/7.6	8.7/9.4
		averaged	7.5	9.0
Surface Pt sites <sup>(d)</sup>	%ML ( $\pm 0.2$ ) atoms cm <sup>-2</sup>	-	1.3	1.6
		-	$2.0 \times 10^{13}$	$2.4 \times 10^{13}$
E <sub>a,app</sub>	kJ mol <sup>-1</sup> ( $\pm 3.0$ )	dark	66	61
		UV	74	73
Charge carrier transfer <sup>(e)</sup>	carriers	dark	36 (e <sup>-</sup> added to particle)	36 (e <sup>-</sup> added to particle)
		UV	70 (holes at interface)	28 (e <sup>-</sup> at interface)

<sup>(a)</sup> Size in solution (TEM). <sup>(b)</sup> From Ga3d core level spectra of similar samples (Chapter 4). <sup>(c)</sup> Size on GaN surface (AFM). <sup>(d)</sup> The coverage was calculated (in %ML, with 1 ML =  $1.5 \times 10^{15}$  Pt atoms cm<sup>-2</sup>)<sup>[15]</sup> from particle size (TEM) and number of atoms (or surface atoms) of a cuboctahedral particle (assumption of 17 atomic shells) using the particle density on the GaN surface (AFM).<sup>[16]</sup> <sup>(e)</sup> The detailed calculation of transferred charges is described in 5.4.5.

These changes in the reaction rates are attributed to variations in the stabilization of particular ethene surface species (Figure 5-4 (c)). Overall adsorbed ethene is hydrogenated to ethane by reacting with surface metal-hydride.<sup>[17-19]</sup> Ethene is adsorbed in two configurations on Pt, as di- $\sigma$ - or as  $\pi$ -bonded species.<sup>[20, 21]</sup> The  $\pi$ -bound ethene is the key intermediate for hydrogenation, while reaction via the di- $\sigma$ -bound ethene is slow.<sup>[22-24]</sup>

Without UV illumination, the similar electronic properties of Pt nanoparticles supported on *n*- or *p*-type GaN will give rise to similar equilibria of the different forms of adsorbed ethene and, hence, to similar ethene hydrogenation rates. In contrast, considering the  $\sigma$ -donor/ $\pi$ -acceptor interactions between Pt and ethene under UV illumination, electron-deficient particles are expected to prefer ethene adsorption in di- $\sigma$ -coordination, whereas  $\pi$ -bonded ethene species would be favored on electron-rich particles (Figure 5-4 (c)), which explains a lower activity of Pt particles on *n*-type and a higher activity on *p*-type GaN (Figure 5-4 (a, b)).

### 5.3 Conclusion

The present results demonstrate that the characteristic effects which can be induced by optoelectronic electron or hole injection into metal particles on semiconductor supports can be

used to dynamically control their catalytic reactivity. The controlled and quantifiable effect of this *in situ* light-induced tuning of catalytic reactivity opens new pathways for controlling catalytic activity and presumably also selectivity via light. In particular, the favorable optoelectronic properties of GaN<sup>[25]</sup>, as well as its biocompatibility<sup>[26-28]</sup>, open great potential for semiconductor device technology as well as biocatalysis.

## 5.4 Methods

### 5.4.1 Model Catalyst Preparation

Colloidal Pt particles in solution were synthesized by the polyol process described by Song *et al.*<sup>[4]</sup> For cuboctahedral Pt particle geometry,  $5.5 \times 10^{-3}$  mmol of AgNO<sub>3</sub> (> 99% Sigma-Aldrich) was used in ethylene glycol ( $\geq 99.5\%$  Fluka) prior to the addition of solutions containing PVP (1.125 mmol monomer,  $M_w = 55\,000$  g mol<sup>-1</sup>, Sigma-Aldrich) and H<sub>2</sub>PtCl<sub>6</sub> (0.094 mmol, 8 wt.% in H<sub>2</sub>O, Sigma-Aldrich). The alternate addition of the Pt precursor and the polymer was finished after 17 min, resulting in sub-10 nm cuboctahedra. After the particle separation with acetone ( $\geq 99.5\%$  Sigma-Aldrich) followed by centrifugation and washing procedure with ethanol (99% Fluka) and 1-hexane (Sigma-Aldrich) the particles were dispersed in ethanol with a Pt concentration of 31.3 mmol l<sup>-1</sup>. As semiconductor supports, MOCVD-grown GaN of *n*-type (Si donor concentration  $n = 2 \times 10^{18}$  cm<sup>-3</sup>, Lumilog Group St Gobain Crystals) and *p*-type (Mg acceptor concentration  $p = 5 \times 10^{17}$  cm<sup>-3</sup>, Fraunhofer Institute of Applied Solid State Physics, Freiburg, Germany) were used. The substrates were washed in acetone (ultrasonic bath, 10 min) and rinsed with 2-propanol ( $\geq 99.5\%$  Fluka) before Pt particles in ethanol (50  $\mu$ l,  $1.2 \times 10^{-4}$  mmol) were deposited on the GaN surface via spin-coating (3000 rpm, 60 s). Excess solvent was evaporated by heating the samples to 360 K for 5 min in ambient atmosphere, whereas oxygen plasma (1.4 mbar O<sub>2</sub>, 200 W, 5 min, TePla 100-E, Technics Plasma GmbH) was applied to remove the PVP-capping from the particles. The samples were finally heated to 425 K in vacuum for 15 min to increase the adhesive forces between particles and substrate.

### 5.4.2 Transmission Electron and Atomic Force Microscopy (TEM, AFM)

Solutions of PVP-protected Pt particles in ethanol were drop-cast onto carbon-coated Cu grids (Quantifoil Micro Tools GmbH) for the analysis with TEM (JEOL JEM-2010, 120 keV). The average particle sizes and the fractions of different particle shapes were evaluated from at least 250 particles. The GaN surfaces functionalized with the particles were analyzed with AFM and images ( $1 \times 1 \mu\text{m}$ , 256 data points per line, 1 Hz) were acquired with a Veeco Multimode AFM (Nanoscope IIIa SPM controller) in tapping mode using AFM probes with a tip radius  $< 7 \text{ nm}$  (204-497 kHz,  $10\text{-}130 \text{ N m}^{-1}$ , Nanosensors). The average particle height and the areal particle distributions on the GaN surface were evaluated (WSxM software<sup>[29]</sup>, Table 5-1). The number of particles per GaN area was used to calculate the Pt coverage in percentage of a monolayer (%ML) ( $1 \text{ ML} = 1.5 \times 10^{15} \text{ cm}^{-2}$  Pt atoms for Pt(111)). For this calculation, the number of atoms per particle and the number of atoms on the particle surface were determined according to the model equations of Benfield<sup>[16]</sup> with the assumption of 17 atomic shells. Due to the particle truncation by the contact to the GaN support, two thirds of the particle was supposed to be exposed, resulting in a hypothetical number of surface Pt atoms that are catalytically active. The surface Pt coverage of the catalyst was used to normalize the activity towards ethene hydrogenation.

### 5.4.3 Batch-operated Recycle Reactor Setup for Ethene Hydrogenation

A recirculating reactor was constructed for batch operation to test the catalytic performance of Pt-GaN catalysts with low metal coverage in the hydrogenation of ethene to ethane, facilitating experiments with and without optical excitation of the samples (Figure 5-3). The catalyst was mounted into a sandwich-like, stainless steel reactor with a quartz glass window (broadband antireflection coating, LINOS Photonics). The gas was dispersed over the catalyst with a V-shaped unit towards the catalyst chamber. The chamber depth was similar to the GaN thickness ( $333 \mu\text{m}$ ) and the gas was flushed over the surface functionalised with Pt particles. The inner surface of the top plate and the quartz glass stabilization contained channels for o-rings, which were pressed by screws for sealing. An adapted heater unit (Ultramic600 Heater, Watlow) allowed reactor heating from the back side with a temperature deviation on the sample surface of maximum 1.5%. The gas flux was adjusted via mass flow controllers (Bronkhorst) and directed through the catalyst chamber, the six-port valve

integrated into the gas chromatograph (HP 6890 Series), the piezoelectric membrane pump (mp5, Bartels Mikrotechnik), and finally into the exhaust during continuous operation, while the gas was recirculated into the catalyst chamber in recycle mode. The optical excitation of the catalyst was performed with a UV lamp (254 nm, 6 W,  $600 \mu\text{W cm}^{-2}$ , Benda) during kinetic experiments under illumination. Differential reactor conditions without concentration gradients along the catalyst were achieved for the kinetic study with and without UV irradiation. Mass transport limitations by film diffusion of reactants from the gas phase onto the metal surface were not observed within the used temperature range. In a typical experiment, the sample was mounted into the reactor chamber and flushed with  $\text{N}_2$  (1 bar, 350 K, 15 min). For catalyst activation,  $\text{H}_2$  (1 bar) was introduced, while heating the sample to 425 K (temperature ramp of  $1 \text{ K min}^{-1}$ ). After reduction at 425 K for 6 h, the reactor was cooled down to reaction temperature (335-355 K) in  $\text{H}_2$  and gas chromatographic analysis was started (HP-PLOT  $\text{Al}_2\text{O}_3$  KCl capillary column,  $50 \text{ m} \times 0.32 \text{ mm} \times 5 \mu\text{m}$ , 320 K). The kinetic data were collected with decreasing temperature (355-335 K, steps of 5 K) and afterwards again at 355 K. This procedure was performed in dark and in UV light for the *n*- and *p*-type catalysts. The recirculation was applied at constant reactant flow by switching valves and turning on the micropump (250 Hz, 250 V). The UV lamp was additionally switched on during illumination experiments. Reference samples of *n*- and *p*-type GaN were prepared using exactly the same conditions and treatments as for samples functionalised with particles, including spin-coating of PVP in ethanol ( $50 \mu\text{l}$ ,  $1.4 \times 10^{-6} \text{ mol}$ ), oxygen plasma and heating in vacuum. A small concentration of ethane was detected for an empty reactor chamber, which was less than 3% of the particles' activity. The background reaction was subtracted from that of the catalysts for all data shown within this study. The conversion of ethene to ethane was evaluated from ethane accumulation curves during recycling and TOFs of ethane accumulation were determined for each temperature for ethene conversions below 10% (consider chapter 2.4.1 for detailed calculation). The apparent activation energies were graphically identified from Arrhenius plots (Table 5-1).

#### 5.4.4 Kinetic Data Evaluation

The catalytic activity of Pt particles on *n*- or *p*-type GaN in the hydrogenation of ethene to ethane ( $\text{C}_2\text{H}_4 + \text{H}_2 \rightarrow \text{C}_2\text{H}_6$ ) was evaluated comparing the ethene conversions and turnover frequencies for the ethane production with and without UV light irradiation in the temperature

range of 335-355 K. The time ( $t$ )-dependent conversion ( $X$ ) of ethene to ethane was determined via the concentration ( $c$ ) of formed ethane (Equation 2-35). The number of accumulated ethane molecules ( $N_{acc}$ ) was normalized to the number of particle surface Pt atoms ( $N_{surface}$ ), resulting in temperature-dependent turnover frequencies ( $TOFs$ ) (Equation 2-36). The recycle reactor volume ( $V_R$ ), the reaction rate ( $r$ ), and the Avogadro constant ( $N_A$ ) were used to calculate the number of accumulated ethane molecules from the obtained product accumulation curves (Equation 2-37). The linearization of the Arrhenius equation was used for the graphical determination of the apparent activation energies ( $E_{a,app}$ , Table 5-1) in the measured temperature range ( $T$ ) with the pre-exponential factor ( $A_0$ ) and the universal gas constant ( $R$ ) (Equation 2-38).

### 5.4.5 Charge transfer to Pt nanoparticles on GaN

The maximum amount of charge which can be transferred to the Pt nanoparticles in the dark and during illumination of the GaN support is determined by the electrical capacitance  $C = 4\pi\epsilon\epsilon_0r$  of individual particles and the energy position of the Pt Fermi level within the bandgap of GaN.  $\epsilon$  is the effective dielectric constant of the support/nanoparticle interface and  $r$  is the radius of a spherical nanoparticle. Adding an additional charge to the nanoparticle leads to an increase of the Coulombic energy by  $e^2/2C$ . Thus, the change in potential energy associated with the transfer of  $N$  electrons or holes to a given Pt particle is  $\Delta E = N e^2/(8\pi\epsilon\epsilon_0r)$ . For a radius of  $r = 4 \text{ nm}$  and an effective dielectric constant of  $\epsilon = 1 \dots 10$ , the charging energy  $\Delta E$  of the nanoparticles will vary between 0.18 eV per electron for  $\epsilon = 1$  and 0.018 eV per electron for  $\epsilon = 10$ . Since the effective dielectric constant for the GaN/Pt nanoparticle heterostructure is not known, we assume an effective average value of  $\epsilon = 5$  for this case. With this assumption, the charging energy would amount to 36 meV per electron or hole added to a Pt particle with a radius of 4 nm.

Without illumination, the Fermi level position at the natural surface of GaN is determined by surface states and metal-induced gap states (MIGS) close to the center of the GaN band gap. As a consequence, the Schottky barrier height of Schottky diodes for most metals on  $n$ -type GaN is around  $0.9 \pm 0.1 \text{ eV}$ , including Pt Schottky diodes.<sup>[30]</sup> For  $p$ -type GaN, the barrier heights are around  $0.6 \pm 0.1 \text{ eV}$ .<sup>[31]</sup> Therefore, the simple model for Schottky diodes

according to Zhdanov<sup>[14]</sup> is not valid for GaN. Instead, the Fermi level at the GaN surface has been found to be pinned approximately 1 eV below the conduction band (i.e. 4.4 eV below the vacuum level and 2.4 eV above the GaN valence band), both, for *n*- and *p*-type GaN grown by MOCVD.<sup>[32]</sup> With a work function of 5.7 eV for Pt, the Fermi level of the nanoparticles is 1.3 eV below this pinning energy (Figure 5-2 (a, b)). Upon contact, electrons will be transferred from the GaN support to the nanoparticles to equilibrate the Fermi level positions. According to the estimate above, this will require  $1.3/0.036 = 36$  **electrons** per Pt nanoparticle, independent of the type of doping (Figure 5-2 (c, d)). This is about one order of magnitude more than what is obtained based on the model of Zhdanov<sup>[14]</sup>, and about one order of magnitude less than expected from the model of Ionides and Verykios<sup>[33]</sup>. Also, this is in agreement with our observation that the catalytic activity of the GaN/Pt system in the dark does not depend significantly on the doping of the GaN support (cf. Figure 5-4 (a, b)).

Upon illumination with UV light, excess charge carriers are generated and separated in the band bending region close to the surface (Figure 5-2 (e, f)). The amount of charge separation can be deduced from the photoconductivity of an illuminated sample compared to the conductivity of the same sample in the dark. For *n*-type GaN supports with a doping level of  $n = 2 \times 10^{18} \text{ cm}^{-3}$ , we observe a relative change of the conductivity of  $\Delta\sigma/\sigma = + 10^{-3}$  under equivalent illumination conditions of GaN without the Pt particles. This corresponds to an illumination-induced increase of the majority carrier density in the bulk of the GaN wafer by  $\Delta n = 2 \times 10^{15} \text{ cm}^{-3}$  for standard illumination conditions. With a GaN film thickness of  $d = 3 \mu\text{m}$ , the steady state areal density of the photo-generated counter charges at the GaN surface then follows as  $d \times \Delta n = 6 \times 10^{11} \text{ cm}^{-2}$  of holes. The effective lifetime of photo-induced charge carriers under these conditions obtained from transient photoconductivity measurements is less than about 50 ms, so that a lower limit for the steady state optical generation rate of minority carriers at the surface is  $1.2 \times 10^{13} \text{ cm}^{-2} \text{ s}^{-1}$ .

Charging of the Pt nanoparticles will stop once the Fermi level of the charged nanoparticles is higher than the conduction band for *p*-type GaN or lower than the valence band for *n*-type GaN. This allows an additional transfer of  $1/0.036 = 28$  **electrons** into each nanoparticle for *p*-type GaN, whereas  $2.5/0.036 = 70$  **holes** can be maximally transferred into each particle on *n*-type GaN. Note that for bulk GaN/Pt Schottky diodes it has been observed that the Schottky barrier height is decreased significantly by the presence of molecular hydrogen.<sup>[34]</sup>

This effect has been explained by the catalytic dissociation of H<sub>2</sub> by Pt or Pd plus the formation of an interfacial O<sup>-</sup>-H<sup>+</sup> dipole layer with the natural surface oxide of GaN.<sup>[35]</sup> Since the experiments described in this work necessarily require a large partial pressure of hydrogen, this observation could also be of relevance here. However, it is not known to what extent a similar effect will also be valid for a GaN surface with a small coverage of Pt nanoparticles and how this will influence the charge transfer between GaN and the nanoparticles. Therefore, we have neglected this point in the present discussion.

Since the areal density of Pt nanoparticles on the GaN surface is about  $2 \times 10^{11} \text{ cm}^{-2}$ , a transfer of 50 electrons per particle requires an integrated photo-generated surface charge density of  $1 \times 10^{13} \text{ cm}^{-2}$ . For the optical generation rate of surface charges calculated above ( $1.2 \times 10^{13} \text{ cm}^{-2} \text{ s}^{-1}$ ), the complete charge transfer should be finished within about one second of illumination time.

## 5.5 References

- [1] I. Chorkendorff, J. W. Niemantsverdriet, *Concepts of Modern Catalysis and Kinetics*, WILEY-VCH Verlag GmbH & Co. KGaA: Weinheim, **2003**.
- [2] Q. Fu, T. Wagner, *Surf. Sci. Rep.* **2007**, *62*, 431.
- [3] M. Englisch, A. Jentys, J. A. Lercher, *J. Catal.* **1997**, *166*, 25.
- [4] H. Song, F. Kim, S. Connor, G. A. Somorjai, P. D. Yang, *J. Phys. Chem. B* **2005**, *109*, 188.
- [5] S. Nakamura, M. Senoh, T. Mukai, *Jpn. J. Appl. Phys.* **1991**, *30*, L1708.
- [6] C. I. Wu, A. Kahn, *J. Vac. Sci. Technol. B* **1998**, *16*, 2218.
- [7] W. Schottky, *Z. Phys.* **1939**, *113*, 367.
- [8] C. Kittel, *Introduction to Solid State Physics*, John Wiley & Sons, Inc.: New York, **2005**.
- [9] J. Y. Park, G. A. Somorjai, *J. Vac. Sci. Technol. B* **2006**, *24*, 1967.
- [10] A. Hervier, J. R. Renzas, J. Y. Park, G. A. Somorjai, *Nano Lett.* **2009**, *9*, 3930.
- [11] L. R. Baker, A. Hervier, H. Seo, G. Kennedy, K. Komvopoulos, G. A. Somorjai, *J. Phys. Chem. C* **2011**, *115*, 16006.
- [12] Q. Z. Liu, S. S. Lau, *Solid State Electron.* **1998**, *42*, 677.
- [13] O. Weidemann, E. Monroy, E. Hahn, M. Stutzmann, M. Eickhoff, *Appl. Phys. Lett.* **2005**, *86*, 083507.
- [14] V. P. Zhdanov, *Surf. Sci.* **2002**, *512*, L331.
- [15] Y. Y. Yeo, L. Vattuone, D. A. King, *J. Chem. Phys.* **1997**, *106*, 392.
- [16] R. E. Benfield, *J. Chem. Soc. Faraday T.* **1992**, *88*, 1107.
- [17] I. Horiuti, M. Polanyi, *T. Faraday Soc.* **1934**, *30*, 1164.

- [18] J. E. Rekoske, R. D. Cortright, S. A. Goddard, S. B. Sharma, J. A. Dumesic, *J. Phys. Chem.* **1992**, *96*, 1880.
- [19] R. D. Cortright, S. A. Goddard, J. E. Rekoske, J. A. Dumesic, *J. Catal.* **1991**, *127*, 342.
- [20] R. M. Rioux, J. D. Hoefelmeyer, M. Grass, H. Song, K. Niesz, P. Yang, G. A. Somorjai, *Langmuir* **2008**, *24*, 198.
- [21] E. Bus, D. E. Ramaker, J. A. van Bokhoven, *J. Am. Chem. Soc.* **2007**, *129*, 8094.
- [22] P. S. Cremer, X. C. Su, Y. R. Shen, G. A. Somorjai, *Catal. Lett.* **1996**, *40*, 143.
- [23] T. Ohtani, J. Kubota, J. N. Kondo, C. Hirose, K. Domen, *J. Phys. Chem. B* **1999**, *103*, 4562.
- [24] K. Maeda, K. Domen, *Chem. Mater.* **2010**, *22*, 612.
- [25] F. A. Ponce, D. P. Bour, *Nature* **1997**, *386*, 351.
- [26] M. Stutzmann, J. A. Garrido, M. Eickhoff, M. S. Brandt, *Phys. Status Solidi A* **2006**, *203*, 3424.
- [27] J. Howgate, S. J. Schoell, M. Hoeb, W. Steins, B. Baur, S. Hertrich, B. Nickel, I. D. Sharp, M. Stutzmann, M. Eickhoff, *Adv. Mater.* **2010**, *22*, 2632.
- [28] B. Baur, G. Steinhoff, J. Hernando, O. Purrucker, M. Tanaka, B. Nickel, M. Stutzmann, M. Eickhoff, *Appl. Phys. Lett.* **2005**, *87*, 263901.
- [29] I. Horcas, R. Fernandez, J. M. Gomez-Rodriguez, J. Colchero, J. Gomez-Herrero, A. M. Baro, *Rev. Sci. Instrum.* **2007**, *78*, 013705.
- [30] U. Karrer, O. Ambacher, M. Stutzmann, *Appl. Phys. Lett.* **2000**, *77*, 2012.
- [31] T. Mori, T. Kozawa, T. Ohwaki, Y. Taga, S. Nagai, *Appl. Phys. Lett.* **1996**, *69*, 3537.
- [32] J. P. Long, V. M. Bermudez, *Phys. Rev. B* **2002**, *66*, 121308.
- [33] T. Ioannides, X. E. Verykios, *J. Catal.* **1996**, *161*, 560.
- [34] B. P. Luther, S. D. Wolter, S. E. Mohny, *Sens. Actuators B* **1999**, *56*, 164.
- [35] O. Weidemann, M. Hermann, G. Steinhoff, H. Wingbrant, A. L. Spetz, M. Stutzmann, M. Eickhoff, *Appl. Phys. Lett.* **2003**, *83*, 773.



# *Chapter 6*

## **Summary & Zusammenfassung**

## 6 Summary & Zusammenfassung

### 6.1 Summary

Due to the world's increasing energy demand, the chemical industry requires processes within Green Chemistry with low consumption on energy and reduced waste production. Heterogeneous catalyzed reactions exhibit an optimal solution by high atom efficiency and product selectivity. However, high efficiency requires a rational development of heterogeneous catalysts with optimal catalytic properties, which are tunable for the respective chemical reaction. In particular, nanocatalysts exhibit small metal particle sizes and increase the active surface for reaction. The combination of such small particles with suitable supporting materials expands the possibilities in catalyst synthesis. The support can interact with the particles electronically or geometrically, implementing unique properties for catalysis. The controlled activation of the catalysts *in situ*, during reaction, is challenging for catalysis on demand.

In this work, the possibility of *in situ* tunable catalytic properties of model nanocatalysts has been studied and an altered performance in ethene hydrogenation, as well as a different behavior during reduction and oxidation has been found with the photo-activation of the catalyst. To achieve these observations, a suitable model hybrid system was developed that showed low complexity of the metal-support interface and simultaneously was treated under same conditions like industrially used catalysts (wet chemical synthesis and handling in ambient air). The choice of platinum nanoparticles allowed the controlled synthesis of size- and shape-selected particles, which are catalytically active in various reactions like hydrogenation. Epitaxially-grown gallium nitride (GaN) was used as a non-oxidic, semiconducting wide bandgap support that is available with controlled electronic doping in *n*- and *p*-type, in contrast to the oxidic semiconductor materials titania and zinc oxide. Additionally, GaN is commercially utilized in optoelectronic semiconductor technology. Thus, the model catalysts based on Pt nanoparticles supported on highly doped GaN surfaces provide the application for electronic devices or integrated microstructured reactors.

The Pt-GaN interface forms a Schottky contact with the electronic alignment between the metal work function and the Fermi levels of *n*- and *p*-type GaN, where the Pt work function lies 1.3 eV below the pinned Fermi level of *n*- and *p*-type GaN. In thermal equilibrium, an

upwards band bending of the valence and conduction band occurs for *n*-type GaN, whereas both bands bend downwards in the case of *p*-type GaN. Due to the Fermi level alignment electrons are transferred from the *n*- and *p*-type surface to the Pt particles. The change of charge on Pt is therefore equal for *n*- and *p*-type GaN and an alteration of the catalytic activity of the particles for reaction is not expected. In contrast, the activation of the underlying GaN support by illumination with photons that excite electrons above the bandgap causes a huge difference in the charge distribution at the Pt-GaN interface. Electron-hole pairs are formed upon light excitation and the minority charge carriers drift towards the surface. Minority charges are holes in *n*-type and electrons in *p*-type semiconductor. At the Pt-GaN interface, charge recombination of electrons from Pt with accumulated holes of *n*-type GaN is supposed. For Pt on the *p*-type surface, electron transfer from the *p*-type GaN to Pt is proposed upon illumination. This charge transfer is supposed to affect the catalytic properties of Pt under irradiation, which was tested for X-ray and UV light illumination under reduction, oxidation, and hydrogenation conditions.

To verify this charge transfer model under illumination, both the Pt nanoparticles and the GaN surfaces had to be well-defined. The particle synthesis could be controlled to prepare monodisperse, size- and shape-selected Pt nanoparticles, which were characterized with transmission electron microscopy. The particles contained a polymer-shell of poly(*N*-vinylpyrrolidone) (PVP) to prevent agglomeration of particles in solution. Small particles with a size of 2 nm were synthesized by the reduction of the Pt precursor with 1-propanol. Large Pt particles were prepared by the polyol method using silver nitrate as shape-directing agent to achieve cubic, cuboctahedral, and octahedral particles with a size of around 10 nm. The GaN surfaces were analyzed with X-ray photoemission spectroscopy and oxygen coverages of 1 ML (monolayer) and 2 ML were found on *n*- and *p*-type GaN, respectively. The thin oxygen adlayer allows the transfer of electrons across the Pt-GaN interface by electron tunneling. The PVP-protected Pt particles were applied onto both *n*- and *p*-type GaN via spin-coating, resulting in a homogenous particle distribution on the surfaces. The Pt-GaN model catalysts were characterized with atomic force microscopy that enables the calculation of the Pt coverage. The Pt coverage could be controlled by the Pt concentration in solution, as well as by the spin-coating rotation speed and was typically 2 %ML for small and 16-17 %ML for large particles on GaN. The polymer was subsequently removed by oxygen plasma without sintering of the particles, which normally occurs by thermal polymer removal.

The heating of the model catalysts to moderate temperature of 425 K increased the adhesive forces between the particles and the GaN surface.

As the model catalysts were studied under reaction conditions, i.e. exposure to gaseous atmosphere at elevated temperatures, the particle stability on the GaN surface had to be investigated with *in situ* small-angle X-ray scattering and X-ray absorption spectroscopy in grazing incidence mode. These data showed that small (2 nm) and large (7 nm) Pt particles on *n*-type GaN were resistant against sintering at high temperature of 673 K. However, a rounding of edges for large particles was observed at 573 K. In hydrogen, as well as in deuterium-ethene atmosphere, a dynamic response of small particles to the presence of gas molecules was monitored, which was assigned to molecule adsorption on the particle surface followed by a change in the nanoparticle shape. In contrast to the small particles, large particles did not change their geometry under the same conditions. X-ray absorption spectra revealed the reduction of small nanoparticles during the hydrogenation of ethene with deuterium, while large particles appeared unchanged and completely reduced.

To monitor electronic changes on the Pt particle surface, as well as on the GaN surfaces under reaction conditions, *in situ* high-pressure X-ray photoelectron spectroscopy (HP-XPS) was used, which is a surface-sensitive method in contrast to X-ray absorption spectroscopy. Thereby, synchrotron radiation was required to resolve the Pt4f core level spectra. Various Pt nanoparticle sizes and shapes on *n*- and *p*-type GaN were measured after preparation and showed significant differences, which result from the underlying support doping. Pt particles on *n*-type GaN exhibited always a higher amount of oxidized Pt species after synthesis, as well as after reduction with hydrogen. The fraction of metallic Pt was only 16% for Pt cuboctahedra (8.1 nm) on *n*-type GaN and 28% for the same particles on *p*-type GaN after preparation measured at room temperature in vacuum. After *in situ* reduction in hydrogen at 800 K, the particles were not completely reduced, containing 88% and 75% Pt<sup>0</sup> for particles on *n*- and *p*-type GaN, respectively. The *in situ* oxidation experiment with *ex situ* reduced samples (78% Pt<sup>0</sup> on *p*-type and 69% Pt<sup>0</sup> on *n*-type) confirmed the different chemical composition of the particles on *n*- and *p*-type GaN under illumination with X-rays. The Pt particles on the *n*-type surface were immediately oxidized (only 30% Pt<sup>0</sup>) upon oxygen inlet at 725 K, whereas Pt particles on *p*-type GaN remained at their initial reduced level (68% Pt<sup>0</sup>). The XPS study supports the charge transfer model under illumination, because the X-ray irradiation during the measurements caused the excitation of the underlying GaN support, changing the affinity of the nanoparticles towards oxygen.

Reaction experiments with and without illumination of the model catalysts should definitely prove the altered catalytic reactivity of the Pt particle surface by photo-activation of the GaN support. Therefore, the samples were tested in the hydrogenation of ethene to ethane in a batch-operated recycle reactor that facilitates irradiation with UV light (254 nm) through a quartz glass window. The same catalytic activity was found for Pt cuboctahedra (8.9 nm) on both *n*- and *p*-type GaN without illumination (ethene conversion of 5% at 335 K after 10 h). Upon irradiation with UV light, an enhanced reactivity towards ethane production was detected for *p*-type GaN-supported Pt particles (ethene conversion of 7% at 335 K after 10 h). In contrast to the *p*-type sample, a lower hydrogenation activity under illumination was determined for Pt nanoparticles on the *n*-type surface (ethene conversion of 2% at 335 K after 10 h). Considering the charge transfer mechanism at the Pt-GaN interface under illumination, the Pt particles appear electron-deficient on *n*-type GaN, whereas Pt is electron-rich on the *p*-type surface. The different electronic properties of the particle surface with and without illumination was proposed to change the portions of di- $\sigma$ - and  $\pi$ -bound ethene due to altered  $\sigma$ -donor and  $\pi$ -acceptor interactions between Pt and ethene. The reaction mechanism of ethene hydrogenation describes a fast reaction pathway via the  $\pi$ -bonded ethene, while the pathway via di- $\sigma$ -bonded ethene is very slow. The reaction enhancement for the *p*-type sample via the  $\pi$ -bound ethene species and the reaction retardation for the *n*-type sample via the di- $\sigma$ -bound ethene under illumination are consistent with the reaction mechanism of the hydrogenation.

Consequently, this proof of principle study reveals the potential to actively manipulate catalytic properties of semiconductor-supported metal nanoparticles on demand. We are convinced that this effect works for various reactions as well, e.g. for CO oxidation, the selective hydrogenation of unsaturated aldehydes and nitriles. The electronic modification of the nanoparticle surface by the illumination of the underlying semiconductor support should impact the particles' reactivity in reactions, where electronic effects change the product yield or distribution.

## 6.2 Zusammenfassung

Aufgrund des weltweit zunehmenden Energiebedarfs benötigt die chemische Industrie Prozesse im Bereich der „Grünen Chemie“ mit niedrigem Verbrauch an Energie und reduzierter Abfallproduktion. Heterogen katalysierte Reaktionen stellen eine optimale Lösung mit hoher Atomeffizienz und Produktselektivität dar. Allerdings erfordert die hohe Effizienz eine rationale Entwicklung von heterogenen Katalysatoren mit optimalen katalytischen Eigenschaften, die auf die einzelne chemische Reaktion abgestimmt sind. Speziell weisen Nanokatalysatoren eine kleine Metallpartikelgröße auf und erhöhen die aktive Oberfläche für die Reaktion. Die Kombination solcher kleinen Partikel mit geeigneten Trägermaterialien erweitert die Möglichkeiten in der Katalysatorsynthese. Der Träger kann mit den Partikeln elektronisch oder geometrisch wechselwirken und führt besondere Eigenschaften für die Katalyse ein. Die kontrollierte Aktivierung der Katalysatoren *in-situ*, während der Reaktion, ist eine Herausforderung für die abrufbare Katalyse.

In dieser Arbeit wurde die Möglichkeit der *in-situ* einstellbaren katalytischen Eigenschaften von Modellnanokatalysatoren untersucht und eine modifizierte Effizienz wurde in der Ethenhydrierung ebenso wie ein verändertes Verhalten während der Reduktion und Oxidation mit der Photoaktivierung des Katalysators gefunden. Um solche Beobachtungen zu erhalten wurde ein geeignetes Modellhybridsystem entwickelt, das eine niedrige Komplexität der Metall-Träger-Grenzfläche zeigte und gleichzeitig unter denselben Bedingungen wie ein industriell genutzter Katalysator behandelt wurde (nasschemische Synthese und Handhabung an Raumluft). Die Wahl von Platin-Nanopartikeln erlaubte die geregelte Synthese von größen- und formselektierten Partikeln, die in vielen Reaktionen wie der Hydrierung katalytisch aktiv sind. Epitaktisch gewachsenes Galliumnitrid (GaN) wurde als nicht-oxidischer, halbleitender Träger mit weiter Bandlücke verwendet, der im Gegensatz zu den oxidischen Halbleitermaterialien Titanoxid oder Zinkoxid mit kontrollierter elektronischer Dotierung in *n*- und *p*-Typ verfügbar ist. Zusätzlich wird GaN kommerziell in der optoelektronischen Halbleitertechnologie verwendet. Daher bieten Modellkatalysatoren basierend auf Pt-Nanopartikeln geträgert auf hoch-dotierten GaN-Oberflächen den Einsatz in elektronischen Bauelementen oder integrierten mikrostrukturierten Reaktoren.

Die Pt-GaN-Grenzfläche bildet mit der elektronischen Ausrichtung der Metallaustrittsarbeit und den Fermienergieebenen von *n*- und *p*-Typ GaN einen Schottkykontakt aus, wobei die Pt-

Austrittsarbeit 1,3 eV unter dem gepinnten Fermi-niveau von *n*- und *p*-Typ GaN liegt. Im thermischen Gleichgewicht tritt eine aufsteigende Bandverbiegung des Valenz- und Leitungsbands für *n*-Typ GaN auf, während sich beide Bänder im Fall von *p*-Typ GaN abwärts biegen. Aufgrund der Ausrichtung der Fermi-niveaus werden Elektronen von der *n*- und *p*-Typ Oberfläche auf die Pt-Partikel übertragen. Die Änderung der Ladung am Pt ist daher für *n*- und *p*-Typ GaN gleich und eine Veränderung der katalytischen Aktivität der Partikel für die Reaktion wird nicht erwartet. Im Gegensatz dazu bewirkt die Aktivierung des darunterliegenden GaN-Trägers durch Beleuchtung mit Photonen, die Elektronen über die Bandlücke anregen, einen enormen Unterschied in der Ladungsverteilung an der Pt-GaN-Grenzfläche. Elektron-Loch-Paare bilden sich unter Lichtanregung aus und Minoritätsladungsträger driften zur Oberfläche. Die Minoritätsladungen sind Löcher im *n*-Typ und Elektronen im *p*-Typ Halbleiter. An der Pt-GaN-Grenzfläche wird eine Ladungsrekombination von Elektronen vom Pt mit akkumulierten Löchern des *n*-Typ GaNs vorausgesetzt. Für Pt an der *p*-Typ Oberfläche wird ein Elektronentransfer vom *p*-Typ GaN auf das Pt unter Beleuchtung angenommen. Es wird vermutet, dass dieser Ladungstransfer die katalytischen Eigenschaften des Pt unter Bestrahlung beeinflusst, was für Röntgen- und UV-Licht-Beleuchtung unter Reduktions-, Oxidations- und Hydrierungsbedingungen getestet wurde.

Um dieses Ladungstransfermodell unter Beleuchtung zu bestätigen, mussten sowohl die Pt-Nanopartikel als auch die GaN-Oberflächen gut definiert sein. Die Partikelsynthese konnte so gesteuert werden, dass monodisperse, größen- und formselektierte Pt-Nanopartikel präpariert wurden, die mit Transmissionselektronenmikroskopie charakterisiert wurden. Die Partikel enthielten eine Polymerhülle von Poly(*N*-vinylpyrrolidon) (PVP) um das Agglomerieren der Partikel in Lösung zu vermeiden. Kleine Partikel mit einer Größe von 2 nm wurden durch die Reduktion der Pt-Vorstufe mit 1-Propanol synthetisiert. Große Pt-Partikel wurden mit der Polyolmethode hergestellt und Silbernitrat wurde als formgebende Komponente verwendet um kubische, kuboktaedrische und oktaedrische Partikel mit einer Größe von etwa 10 nm zu erreichen. Die GaN-Oberflächen wurden mittels Röntgen-Photoemissionsspektroskopie analysiert und Sauerstoffbedeckungen von 1 ML (Monolage) und 2 ML wurden jeweils für *n*- und *p*-Typ GaN gefunden. Die dünne Sauerstoffschicht erlaubt den Transfer von Elektronen entlang der Pt-GaN-Grenzfläche aufgrund von Elektronentunneln. Die PVP-geschützten Pt-Partikel wurden sowohl auf *n*- als auch auf *p*-Typ GaN durch Spin-Coating aufgebracht, wodurch eine homogene Partikelverteilung auf der Oberfläche erzielt wurde. Die Pt-GaN-

Modellkatalysatoren wurden durch Rasterkraftmikroskopie charakterisiert, was die Berechnung der Pt-Bedeckung ermöglichte. Die Pt-Bedeckung konnte sowohl durch die Pt-Konzentration in Lösung als auch durch die Spin-Coating-Rotationsgeschwindigkeit kontrolliert werden und betrug typischerweise 2 %ML für kleine und 16-17 %ML für große Partikel auf GaN. Das Polymer wurde anschließend durch Sauerstoffplasma ohne Sintern der Partikel, das normalerweise bei thermischer Polymerentfernung auftritt, entfernt. Das Aufheizen der Modellkatalysatoren auf moderate Temperaturen von 425 K erhöhte die adhäsiven Kräfte zwischen den Partikeln und der GaN-Oberfläche.

Da die Modellkatalysatoren unter Reaktionsbedingungen, d. h. unter Einwirkung von Gasatmosphäre bei hohen Temperaturen, untersucht wurden, musste die Partikelstabilität auf der GaN-Oberfläche mit *in-situ* Kleinwinkel-Röntgenstreuung und Röntgen-Absorptionsspektroskopie unter streifendem Einfall geprüft werden. Diese Daten zeigten, dass kleine (2 nm) und große (7 nm) Pt-Partikel auf *n*-Typ GaN resistent gegen das Sintern bei hoher Temperatur von 673 K waren. Allerdings wurde das Abrunden der Kanten von großen Partikeln bei 573 K beobachtet. Sowohl in Wasserstoff- als auch in Deuterium-Ethen-Atmosphäre wurde eine dynamische Reaktion kleiner Partikel auf die Anwesenheit von Gasmolekülen beobachtet, das der Moleküladsorption auf der Partikeloberfläche gefolgt von einer Änderung der Nanopartikelform zugeordnet wurde. Im Gegensatz zu den kleinen Partikeln änderten große Partikel ihre Geometrie unter denselben Bedingungen nicht. Röntgen-Absorptionsspektren zeigten die Reduktion von kleinen Nanopartikeln während der Hydrierung von Ethen mit Deuterium, während große Partikel unverändert und vollständig reduziert erschienen.

Um die elektronischen Änderungen an der Pt-Partikeloberfläche und auch an den GaN-Oberflächen unter Reaktionsbedingungen zu beobachten, wurde die *in-situ* Hochdruck-Röntgen-Photoemissionsspektroskopie (HR-XPS) verwendet, die im Gegensatz zur Röntgen-Absorptionsspektroskopie eine oberflächen-sensitive Methode darstellt. Dabei war Synchrotronstrahlung erforderlich um die Pt4f-Kernniveaus aufzulösen. Verschiedene Pt-Nanopartikelgrößen und -formen auf *n*- und *p*-Typ GaN wurden nach der Präparation gemessen und zeigten signifikante Unterschiede, die aus der darunterliegenden Trägerdotierung resultierten. Pt-Partikel auf *n*-Typ GaN wiesen sowohl nach der Synthese als auch nach Reduktion mit Wasserstoff immer einen höheren Anteil an oxidierten Pt-Spezies auf. Der Anteil an metallischem Pt war nur 16% für Pt-Kuboktaeder (8.1 nm) auf *n*-Typ GaN



und 28% für dieselben Partikel auf *p*-Typ GaN nach der Synthese und gemessen bei Raumtemperatur im Vakuum. Nach der *in-situ* Reduktion in Wasserstoff bei 800 K wurden die Partikel nicht vollständig reduziert und enthielten jeweils 88% und 75% Pt<sup>0</sup> für Partikel auf *n*- und *p*-Typ GaN. Das *in-situ* Oxidationsexperiment mit *ex-situ* reduzierten Proben (78% Pt<sup>0</sup> auf *p*-Typ und 69% Pt<sup>0</sup> auf *n*-Typ) bestätigte die unterschiedliche chemische Zusammensetzung der Partikel auf *n*- und *p*-Typ GaN unter Beleuchtung mit Röntgenstrahlen. Die Pt-Partikel auf der *n*-Typ Oberfläche wurden sofort nach dem Sauerstoffeinlass bei 725 K oxidiert (nur 30% Pt<sup>0</sup>), während die Pt-Partikel auf *p*-Typ GaN bei ihrem ursprünglichen Reduktionsniveau blieben (68% Pt<sup>0</sup>). Die XPS-Studie unterstützt das Ladungstransfermodell unter Beleuchtung, da die Röntgen-Bestrahlung während des Messens die Anregung des darunterliegenden GaN-Trägers verursacht und die Affinität der Nanopartikel zu Sauerstoff verändert.

Reaktionsexperimente mit und ohne Beleuchtung der Modellkatalysatoren sollte die veränderte katalytische Reaktivität der Pt-Partikeloberfläche bei Photoaktivierung des GaN-Trägers eindeutig beweisen. Deshalb wurden die Proben in der Hydrierung von Ethen zu Ethan in einem absatzweise-betriebenen Kreislaufreaktor getestet, der die Bestrahlung mit UV-Licht (254 nm) durch ein Quarzglasfenster ermöglichte. Dieselbe katalytische Aktivität wurde für Pt-Kuboktaeder (8.9 nm) sowohl auf *n*-Typ als auch auf *p*-Typ GaN ohne Beleuchtung gefunden (Ethenumsatz von 5% bei 335 K nach 10 h). Unter Bestrahlung mit UV-Licht wurde eine verbesserte Reaktivität bezüglich der Ethanproduktion für *p*-Typ GaN-geträgerte Pt-Partikel detektiert (Ethenumsatz von 7% bei 335 K nach 10 h). Im Gegensatz zu der *p*-Typ Probe wurde eine niedrigere Hydrierungsaktivität für Pt-Nanopartikel auf der *n*-Typ Oberfläche unter Beleuchtung bestimmt (Ethenumsatz von 2% bei 335 K nach 10 h). Unter Berücksichtigung des Ladungstransfermechanismus an der Pt-GaN-Grenzfläche unter Beleuchtung scheinen die Pt-Partikel elektronenarm auf *n*-Typ GaN zu sein, während das Pt elektronenreich auf der *p*-Typ Oberfläche ist. Es wurde vermutet, dass die unterschiedlichen elektronischen Eigenschaften der Partikeloberfläche mit und ohne Beleuchtung die Anteile des di- $\sigma$ - und  $\pi$ -gebundenen Ethens aufgrund der modifizierten  $\sigma$ -Donor- und  $\pi$ -Akzeptor-Wechselwirkungen zwischen Pt und Ethen ändern. Der Reaktionsmechanismus der Ethenhydrierung beschreibt einen schnellen Reaktionsweg über das  $\pi$ -gebundene Ethen, während der Pfad über das di- $\sigma$ -gebundene Ethen sehr langsam ist. Die Reaktionsbeschleunigung für die *p*-Typ Probe über die  $\pi$ -gebundene Ethenspezies und die

Reaktionsabbremmung für die *n*-Typ Probe über das di- $\sigma$ -gebundene Ethen unter Beleuchtung ist konsistent mit dem Reaktionsmechanismus der Hydrierung.

Infolgedessen macht diese Grundlagenuntersuchung das Potenzial der aktiven Manipulation katalytischer Eigenschaften von Halbleiter-geträgerten Metallnanopartikel auf Abruf deutlich. Wir sind davon überzeugt, dass dieser Effekt auch für verschiedene Reaktionen funktioniert, z. B. für die CO Oxidation, die selektive Hydrierung von ungesättigten Aldehyden und Nitrilen. Die elektronische Modifikation der Nanopartikeloberfläche durch die Beleuchtung des darunterliegenden Halbleiter-Trägers sollte die Reaktivität der Partikel in Reaktionen beeinflussen, in denen elektronische Effekte die Produktausbeute oder -verteilung verändern.

# *Chapter 7*

## **Outlook**

## 7 Outlook

### 7.1 Outlook

The proof of principle described in this work showed that the catalytic activity of size- and shape-selected Pt particles supported on GaN is affected by the semiconductor electronic *n*- or *p*-type doping under illumination with above bandgap light. Alterations in the electronic properties of the particles upon irradiation were verified by *in situ* HP-XPS (Chapter 4), as well as by the catalytic performance in ethene hydrogenation (Chapter 5). Based on the results in this work as well as the work of Schäfer<sup>[1]</sup>, a charge transfer model was proposed that describes strong metal-support interaction by the charge re-distribution at the Pt-GaN interface under illumination. Furthermore, the samples were very stable against sintering at high temperatures (Chapter 3), as well as against the exposure to reducing and oxidizing gas. The Pt particles and the Pt-GaN interface were well-defined by the preparation methods, resulting in highly reproducible and homogeneous model catalysts.

Using the basic knowledge of the Pt-GaN hybrid structures, variation in the metal nanoparticles is possible, which may extend the understanding of the metal-GaN interface by the use of defined nanoparticle sizes and geometries, as well as particles of metals with different work functions. Pt and Rh particles can be synthesized with preparation methods that control the nanoparticle size and shape selectively (Figure 7-1 (a-c), (e-g)).<sup>[2-7]</sup> Large Pt particles of around 10 nm with cubic, cuboctahedral, and octahedral shape were applied in this work. A continuative study may include Rh particles of e.g. cubic geometry with comparable particle sizes. Small Ni particles, which are not only catalytically active in hydrogenation reactions but also in e.g. dry reforming, can also be prepared with sizes below 5 nm.<sup>[8]</sup> An interesting situation for the metal-GaN interaction, as well as for the reactivity in catalysis may be achieved by bimetallic particles with different work functions for each metal, like Pt-Co particles.<sup>[9]</sup>

An advanced opportunity to extend the GaN surface area for nanocatalysts with high metal particle loadings is demonstrated by the use of GaN nanowires grown on silica surfaces. GaN nanowires provide optimized crystal properties with ideal structure and a very low density of defects.<sup>[10, 11]</sup> The controlled vapor deposition of the metals allows the preparation of well-defined nanowires with *n*- and *p*-type doping, as well as with *p-n* junctions. First spin-coating

experiments of small and large Pt particles showed the successful deposition of the particles onto the various types of nanowires (Figure 7-2).

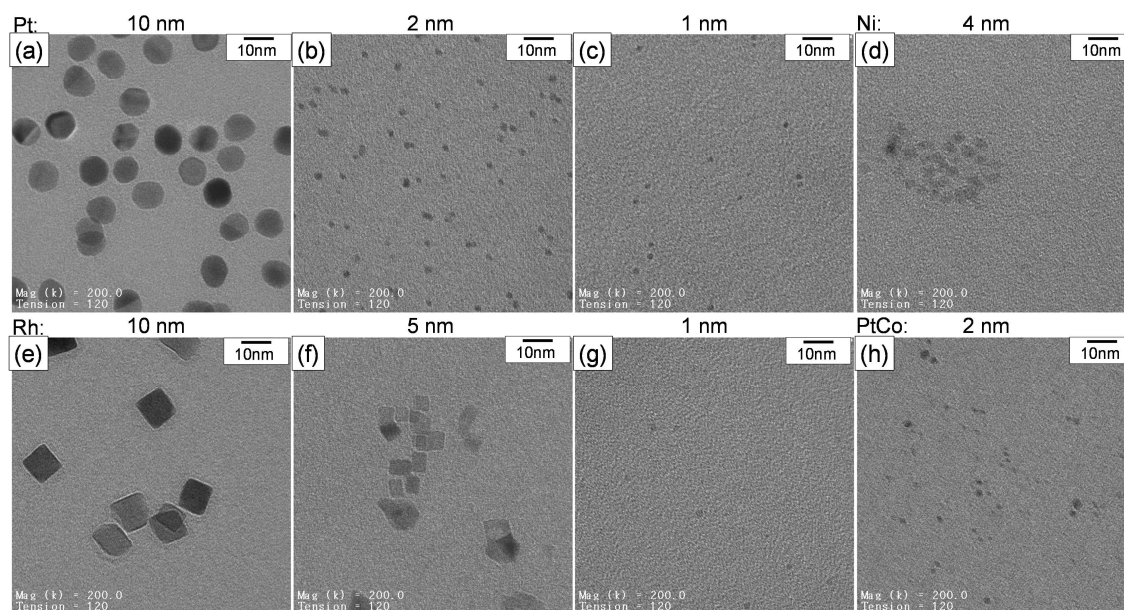


**Figure 7-1.** TEM micrographs of (a-c) Pt nanoparticles (cuboctahedra of 10 nm, spheres of 2 nm and 1 nm), (d) Ni nanoparticles (spheres of 4 nm), (e-g) Rh nanoparticles (cubes of 10 nm and 5 nm, spheres of 1 nm), and (h) bimetallic PtCo nanoparticles (spheres of 2 nm).

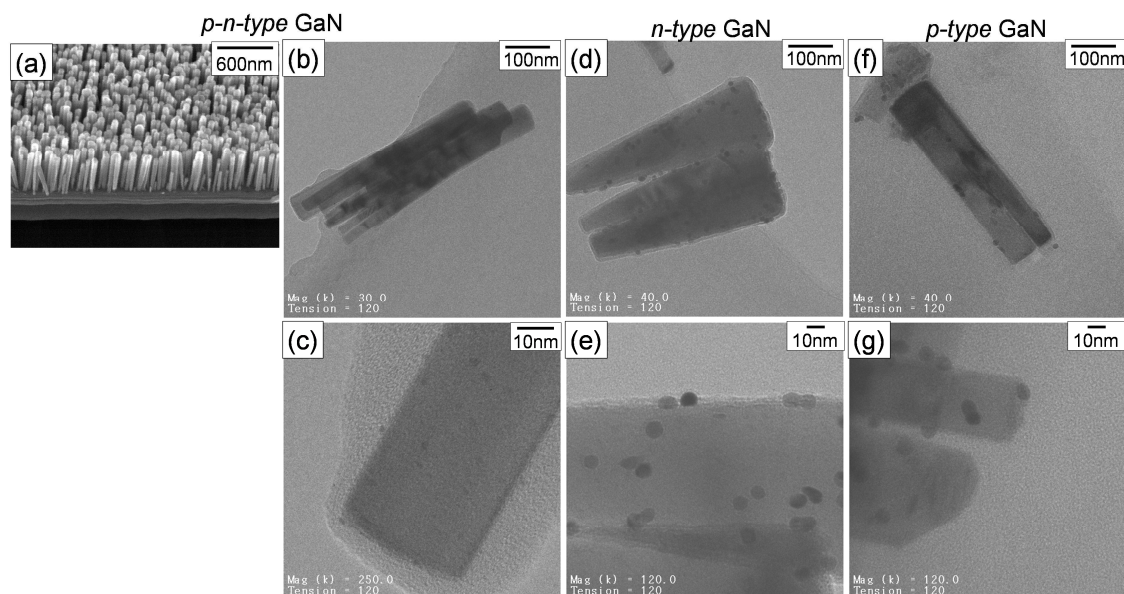


**Figure 7-2.** (a) SEM of *p-n*-type GaN nanowires grown on silica surface, (b-g) TEM of (b, c) spherical Pt nanoparticles (2 nm) on *p-n*-type, cuboctahedral Pt nanoparticles (8 nm) on (d, e) *n*-type and (f, g) *p*-type GaN.

The application of different wide bandgap semiconductors may show the possibility of bandgap engineering for the use of direct sunlight for an optical excitation of the underlying support. A new photocatalyst consisting of a solid solution of GaN and ZnO is currently studied for the hydrogen evolution from overall water splitting.<sup>[12, 13]</sup> The GaN:ZnO powders exhibit a bandgap of below 3 eV and were found to be efficient for water splitting under irradiation with light of wavelengths  $> 400$  nm.

The charge transfer mechanism under irradiation of the GaN support and its effect on the nanoparticle reactivity in ethene hydrogenation may also be valid for other reactions. This was indicated by *in situ* HP-XPS experiments during the oxidation of CO (Figure 7-3).<sup>[11]</sup> Pt cuboctahedra (8.1 nm) on *n*- and *p*-type GaN were heated stepwise from room to reaction temperature in a gas mixture of CO and O<sub>2</sub> (1:1, 0.5 mbar). The particle surface was reduced during the course of CO oxidation due to the consumption of adsorbed oxygen by CO. The particles on the *p*-type surface were found to be reduced at lower temperature compared to the *n*-type catalyst, which showed the different oxygen affinity of particles on *n*- and *p*-type GaN under X-ray irradiation. These results are consistent with *in situ* reduction and oxidation experiments in Chapter 4, confirming the proposed charge transfer model under illumination.

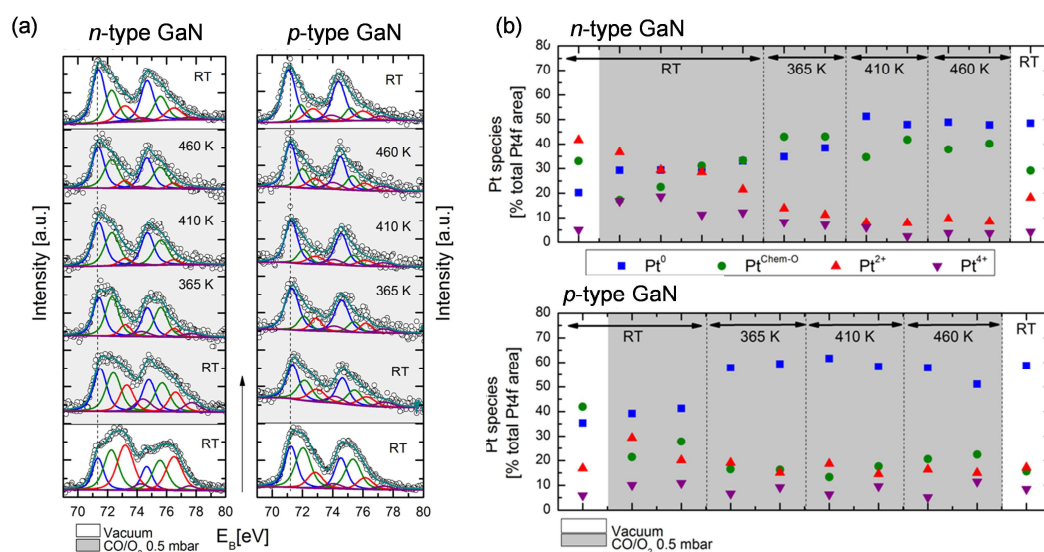


**Figure 7-3.** (a) Pt4f core level spectra during *in situ* CO oxidation (0.5 mbar CO/O<sub>2</sub>) measured with increasing temperature from 300 K to 460 K, and after cooling at 300 K in vacuum for Pt cuboctahedra (8.1 nm) on *n*- and *p*-type GaN. (b) Evaluation of the Pt fractions of each species (% of Pt4f peak area) for the spectra (a).

The described transfer of electronic charges across the metal-semiconductor interface upon illumination affected the nanoparticles' reactivity significantly in a measurable range (Chapter 5). Therefore, we assume huge differences in the product selectivity with the catalyst illumination during the hydrogenation of crotonaldehyde, for example. The hydrogenation of crotonaldehyde yields in two products, butyraldehyde and crotyl alcohol, where butyraldehyde is thermodynamically and kinetically favored. However, crotyl alcohol is the desired compound for the use in fine chemicals industry. It was found that the selectivity towards crotyl alcohol is dependent on the exposed Pt nanoparticle facets and thus, on the different electronic properties of Pt.<sup>[14]</sup> Therefore, an alteration in the product selectivity can be expected upon illumination of Pt-GaN model catalysts.

Consequently, the new approach used in this work institutes an advanced research area in photocatalysis for various applications.

## 7.2 References

- [1] S. Schäfer, *Gallium nitride for the electronic control of catalytic activity*, Ph.D. Thesis, Walter Schottky Institut, Technische Universität München, **2013**.
- [2] G. W. Busser, J. G. van Ommen, J. A. Lercher, *J. Phys. Chem. B* **1999**, *103*, 1651.
- [3] H. Song, F. Kim, S. Connor, G. A. Somorjai, P. D. Yang, *J. Phys. Chem. B* **2005**, *109*, 188.
- [4] R. M. Rioux, H. Song, J. D. Hoefelmeyer, P. Yang, G. A. Somorjai, *J. Phys. Chem. B* **2005**, *109*, 2192.
- [5] Y. W. Zhang, M. E. Grass, J. N. Kuhn, F. Tao, S. E. Habas, W. Y. Huang, P. D. Yang, G. A. Somorjai, *J. Am. Chem. Soc.* **2008**, *130*, 5868.
- [6] J. D. Hoefelmeyer, K. Niesz, G. A. Somorjai, T. D. Tilley, *Nano Lett.* **2005**, *5*, 435.
- [7] S. M. Humphrey, M. E. Grass, S. E. Habas, K. Niesz, G. A. somorjai, T. D. Tilley, *Nano Lett.* **2007**, *7*, 785.
- [8] G. G. Couto, J. J. Klein, W. H. Schreiner, D. H. Mosca, A. J. A. de Oliveira, A. J. G. Zarbin, *J. Colloid Interf. Sci.* **2007**, *311*, 461.
- [9] I. I. E. Markovits, *Synthesis and characterization of polymer-stabilized bimetallic nanoparticles and their application in catalysis*, Master's Thesis, Lehrstuhl für Technische Chemie II, Technische Universität München, **2010**.
- [10] F. Furtmayr, M. Vielemeyer, M. Stutzmann, J. Arbiol, S. Estrade, F. Peiro, J. R. Morante, M. Eickhoff, *J. Appl. Phys.* **2008**, *104*, 034309.
- [11] F. Furtmayr, M. Vielemeyer, M. Stutzmann, A. Laufer, B. K. Meyer, M. Eickhoff, *J. Appl. Phys.* **2008**, *104*, 074309.
- [12] K. Maeda, K. Domen, *Chem. Mater.* **2011**, *22*, 612.
- [13] K. Maeda, T. Takata, M. Hara, N. Saito, Y. Inoue, H. Kobayashi, K. Domen, *J. Am. Chem. Soc.* **2005**, *127*, 8286.
- [14] M. Englisch, A. Jentys, J. A. Lercher, *J. Catal.* **1997**, *166*, 25.



## **8 Curriculum Vitae**

Sonja Agnes Wyrzgol was born in Groß Strehlitz, Poland, Upper Silesia on September 14<sup>th</sup> 1982. At the end of 1988, she moved with her family to Straubing, Germany and visited there the Gymnasium der Ursulinen-Schulstiftung from 1993 to 2002, when she graduated and received her Abitur, the general qualification for university entrance. In October 2002, she started her chemistry studies at the Technische Universität München with the major study field of catalysis and reaction engineering. During her studies, she performed her industrial practical in oxidation catalysis at Süd-Chemie AG, Heufeld, Germany in August and September 2006. She completed her studies with the diploma thesis entitled “Low-Temperature Water-Gas Shift Catalysts with Ionic Liquid Mediated Metal Nanoparticles” in the group of Prof. Johannes A. Lercher (Lehrstuhl für Technische Chemie II, TUM). After her graduation in 2008 as Diplom-Chemikerin Univ., which she “passed with distinction”, she joined the research group of Prof. Johannes A. Lercher for her PhD thesis and received a scholarship by the International Graduate School of Science and Engineering, IGSSE. Her PhD project was focused on the electronic control of catalytic properties, where she cooperated with the group of Prof. Martin Stutzmann (Experimental Semiconductor Physics II, Walter Schottky Institute, TUM).

From October 2008 to March 2009, she attended the course on “Fundamental Aspects and Common Principles on Catalysis” of the South German Catalysis Institute in Ulm, Germany with certificate. In February 2009, she participated in the winter school “Advanced Course on Catalysis: From Molecular to Reactor Design” in Villars, Switzerland with certificate. Within the transferable skills training of IGSSE, she attended various courses like “Academic Presentation Skills” in 2008, “Scientific Paper Writing & Publishing” and “Time- and Self-management” in 2009, and the “Advanced Course on Scientific Paper Writing” in 2010. Furthermore, she worked at the research group of Prof. Günther Rupprechter (Institute of Material Chemistry, Vienna University of Technology, Vienna, Austria) during her stay abroad from January 2011 to March 2011, where she dealt with sum frequency generation spectroscopy.

In addition to her research work at TUM, she visited the synchrotron facility “Deutsches Elektronen-Synchrotron, DESY”, Hamburg, Germany in August 2007, the “European Synchrotron Radiation Facility, ESRF”, Grenoble, France in October 2008, the “Advanced

Photon Source, APS”, Argonne, USA in August 2009, and the “Berliner Elektronenspeicherring-Gesellschaft für Synchrotronstrahlung, BESSY”, Berlin, Germany in July 2010, May 2011, and March 2012, where she performed X-ray absorption spectroscopy, small-angle X-ray scattering, and X-ray photoelectron spectroscopy.

During her PhD thesis, she was responsible for teaching students in practical work (practical of technical chemistry, TUM) from winter semester 2008 to summer semester 2011. Furthermore, she supervised students during their research practical, as well as during their Bachelor’s or Master’s thesis.

In March 2012, she finished the practical work on her PhD and started her professional working life at the OBTEGO AG, Altheim, Germany in April 2012, where she is responsible for the direction of research and development as well as quality management in the field of surface protection systems for the construction industry.

## 9 List of Publications

**2013** S. A. Wyrzgol, S. Schäfer, A. Winnerl, A. Jentys, M. Stutzmann, J. A. Lercher. “Optoelectronic control of the catalytic reactivity of GaN-supported Pt nanoparticles“, *Science* (ready for submission).

S. Schäfer, S. A. Wyrzgol, J. A. Lercher, M. Stutzmann, I. D. Sharp, “Charge transfer across the GaN/Pt nanoparticle interface in electrolyte“, *ChemCatChem*, **2013**, DOI:10.1002/cctc.201300070.

**2012** S. Schäfer, S. A. Wyrzgol, R. Caterino, A. Jentys, S. J. Schoell, M. Hävecker, A. Knop-Gericke, J. A. Lercher, I. D. Sharp, M. Stutzmann. “Platinum Nanoparticles on Gallium Nitride Surfaces: The Effect of Semiconductor Doping on Nanoparticle Reactivity”, *J. Am. Chem. Soc.*, **2012**, *134*, 12528-12535.

**2010** S. A. Wyrzgol, S. Schäfer, S. Lee, B. Lee, M. Di Vece, X. Li, S. Seifert, R. E. Winans, M. Stutzmann, J. A. Lercher, S. Vajda. “Combined TPRx, in situ GISAXS and GIXAS studies of model semiconductor-supported platinum catalysts in the hydrogenation of ethene“, *Phys. Chem. Chem. Phys.*, **2010**, *12*, 5585-5595.

S. Schäfer, S. A. Wyrzgol, Y. Wang, J. A. Lercher, M. Stutzmann. “Platinum nanoparticles deposited on wide-bandgap semiconductor surfaces for catalytic applications“, *Phys. Status Solidi C*, **2010**, *7*, 411-414.

R. Knapp, S. A. Wyrzgol, M. Reichelt, T. Hammer, H. Morgner, T. E. Müller, J. A. Lercher. “Corrugated ionic liquid surfaces with embedded polymer stabilized platinum nanoparticles”, *J. Phys. Chem. C*, **2010**, *114*, 13722-13729.

R. Knapp, S. A. Wyrzgol, A. Jentys, J. A. Lercher. “Water-gas shift catalysts based on ionic liquid mediated supported Cu nanoparticles“, *J. Catal.*, **2010**, *276*, 280-291.

## 10 List of Presentations

- 2012 15<sup>th</sup> International Congress on Catalysis**, “The Effect of Gallium Nitride Doping on Platinum Nanoparticle Oxidation Behavior”, S. A. Wyrzgol, S. Schäfer, I. D. Sharp, A. Jentys, A. Knop-Gericke, R. Schlögl, M. Stutzmann, J. A. Lercher, July 2012, Munich, Germany, poster presentation.
- 2011 MRS Spring Meeting**, “Combined TPRx, *in situ* GISAXS and GIXAS Study of GaN-supported Pt Model Catalysts”, S. A. Wyrzgol, S. M. Schäfer, X. Li, M. Stutzmann, S. Lee, M. Di Vece, S. Vajda, J. A. Lercher, April 2011, San Francisco, USA, oral presentation.
- 44. Jahrestreffen Deutscher Katalytiker**, “Catalytically Active Metal Nanoparticles on Wide Bandgap Semiconductor Surfaces”, S. A. Wyrzgol, S. Schäfer, A. Jentys, M. Stutzmann, S. Vajda, J. A. Lercher, March 2011, Weimar, Germany, poster presentation.
- 2010 2<sup>nd</sup> TUM Nanomagnetik Workshop**, “Catalytically active metal nanoparticles on semiconductor devices“, S. A. Wyrzgol, S. Schäfer, X. Li, M. Stutzmann, J. A. Lercher, January 2010, Munich, Germany, oral presentation.
- 43. Jahrestreffen Deutscher Katalytiker**, “Catalytically active metal nanoparticles on semiconductor devices“, S. A. Wyrzgol, S. Schäfer, X. Li, M. Stutzmann, J. A. Lercher, March 2010, Weimar, Germany, poster presentation.
- 4<sup>th</sup> IGSSE Forum**, “Catalytically active metal nanoparticles on wide-band gap semiconductor surfaces“, S. A. Wyrzgol, S. Schäfer, M. Stutzmann, J. A. Lercher, June 2010, Raitenhaslach, Burghausen, Germany, oral presentation.
- 2009 42. Jahrestreffen Deutscher Katalytiker**, “Catalytically active metal nanoparticles on semiconductor devices - Electronic control of catalytic properties“, S. A. Wyrzgol, X. Li, J. A. Lercher, March 2009, Weimar, Germany, poster presentation.
- 2008 2<sup>nd</sup> IGSSE Forum**, “Electronic control of catalytic properties“, S. A. Wyrzgol, S. Schäfer, X. Li, M. Eickhoff, M. Stutzmann, J. A. Lercher, June 2008, Raitenhaslach, Burghausen, Germany, poster presentation.